AD-A249 284

ARO 23762.6-EG-F

Turbomachinery Laboratory

Department of Aerospace Engineering
The Pennsylvania State University

EXPLICIT NAVIER-STOKES COMPUTATION OF TURBOMACHINERY FLOWS

A Ph.D. Thesis in
Aerospace Engineering

By
ROBERT F. KUNZ

Advised by
B. LAKSHMINARAYANA

DISTRIBUTION STATEMENT A
Approved for public release;
[illegible]

DTIC
ELECTE
APR 29 1992
S D
3

PennState

92-11225

92 4 27 456

PSU TURBO R 9201

EXPLICIT NAVIER-STOKES COMPUTATION OF TURBOMACHINERY FLOWS

A Ph.D. Thesis in
Aerospace Engineering

By
ROBERT F. KUNZ

Advised by
B. LAKSHMINARAYANA

Supported by

UNITED STATES ARMY RESEARCH OFFICE FELLOWSHIP
GRANT NO. DAAL 03-86-G-0044
MONITOR: T. DOLIGALSKI

TURBOMACHINERY LABORATORY
DEPARTMENT OF AEROSPACE ENGINEERING
THE PENNSYLVANIA STATE UNIVERSITY
UNIVERSITY PARK, PA 16802

JANUARY 1992

REPORT DOCUMENTATION PAGE

Form Approved
OMB No. 0704-0188

Public reporting burden for this collection of information is estimated to average 1 hour per response, including the time for reviewing instructions, searching existing data sources, gathering and maintaining the data needed, and completing and reviewing the collection of information. Send comments regarding this burden estimate or any other aspect of this collection of information, including suggestions for reducing this burden, to Washington Headquarters Services, Directorate for Information Operations and Reports, 1215 Jefferson Davis Highway, Suite 1204, Arlington, VA 22202-4302, and to the Office of Management and Budget, Paperwork Reduction Project (0704-0188), Washington, DC 20503.

1. AGENCY USE ONLY *(Leave blank)*

2. REPORT DATE
January 1992

3. REPORT TYPE AND DATES COVERED
Final Report Aug. 1, 1986 to Dec. 31, 1991

4. TITLE AND SUBTITLE
Explicit Navier-Stokes Computation of Turbomachinery Flows

5. FUNDING NUMBERS
DAAL 03-86-G-0044

6. AUTHOR(S)
R. Kunz and B. Lakshminarayana

7. PERFORMING ORGANIZATION NAME(S) AND ADDRESS(ES)
Department of Aerospace Engineering
The Pennsylvania State University
153J Hammond Building
University Park, PA 16802

8. PERFORMING ORGANIZATION REPORT NUMBER
PSU Turbo R 9201

9. SPONSORING/MONITORING AGENCY NAME(S) AND ADDRESS(ES)
U. S. Army Research Office
P. O. Box 12211
Research Triangle Park, NC 27709-2211

10. SPONSORING/MONITORING AGENCY REPORT NUMBER
ARO 23762.6-EG-F

11. SUPPLEMENTARY NOTES
The view, opinions and/or findings contained in this report are those of the author(s) and should not be construed as an official Department of the Army position, policy, or decision, unless so designated by other documentation.

12a. DISTRIBUTION/AVAILABILITY STATEMENT
Approved for public release; distribution unlimited.

12b. DISTRIBUTION CODE

13. ABSTRACT *(Maximum 200 words)*

A new three-dimensional explicit Navier-Stokes procedure has been developed for computation of turbomachinery flows. Several numerical strategies and modelling techniques have been developed and incorporated which enable convergent and accurate predictions of high Reynolds number flowfields across a wide range of Mach numbers. These include incorporation of a compressible low Reynolds number form of the turbulence transport model and other physical and solution parameters, eigenvalue and local velocity artificial dissipation scalings, a compact flux evaluation procedure and a hybrid low Reynolds number k-e/algebraic Reynolds stress model. Detailed stability and order of magnitude analyses are performed on the discrete system of seven governing equations. Conclusions are drawn concerning the influence of system rotation and turbulence transport source terms, implicit source term treatment and the coupling of the discrete mean flow equation system to the turbulence model equations and its effect on the stability of the numerical scheme. Three-dimensional validation is provided by the results of an incompressible curved duct flow computation. A high Reynolds number axial rotor flow, for which extensive experimental data is also available, was computed. A backswept transonic centrifugal compressor flow, for which L2F meridional passage velocity measurements are available, is computed. Full Navier-Stokes solutions are presented which are shown to capture detailed viscous dominated flow features, including tip clearance and curvature induced and rotation induced secondary motions, with good accuracy.

14. SUBJECT TERMS
Computational Fluid Dynamics, Turbomachinery

15. NUMBER OF PAGES
221

16. PRICE CODE

17. SECURITY CLASSIFICATION OF REPORT	18. SECURITY CLASSIFICATION OF THIS PAGE	19. SECURITY CLASSIFICATION OF ABSTRACT	20. LIMITATION OF ABSTRACT
UNCLASSIFIED	UNCLASSIFIED	UNCLASSIFIED	UL

ABSTRACT

A new three-dimensional explicit Navier-Stokes procedure has been developed for computation of turbulent turbomachinery flows. Several numerical strategies and modelling techniques have been developed and incorporated which enable convergent and accurate predictions of high Reynolds number flowfields across a wide range of Mach numbers. These include incorporation of a compressible low Reynolds number form of the k-ε turbulence model in a fully explicit fashion, appropriate stability bound treatment of the transport turbulence model and other physical and solution parameters, eigenvalue and local velocity artificial dissipation scalings, a compact flux evaluation procedure and a hybrid low Reynolds number k-ε / algebraic Reynolds stress model.

The derivation of the governing transport equations and the numerical discretization procedures are provided for three dimensions, although two-dimensional computations are also considered. A compact central finite difference flux evaluation scheme, is introduced. This scheme allows for the straightforward application of boundary conditions often attributed to finite volume formulations, and eliminates the metric singularity at the interface between solid and periodic boundaries.

Detailed stability and order of magnitude analyses are performed on the discrete system of seven governing equations. The results of these analyses and corroborative numerical experiments are provided. Conclusions are drawn concerning the influence of system rotation and turbulence transport source terms, grid clustering, effective diffusivity, artificial dissipation, convective acceleration terms, implicit source term treatment and the coupling of the discrete mean flow equation system to the turbulence model equations on the stability of the numerical scheme. Notable is the conclusion that, contrary to general perception, turbulence model source terms themselves do not adversely affect the stability of the numerical scheme used, for many low Reynolds number forms, provided that certain constraints are met. Applicability of these results to explicit multigrid and implicit time marching schemes is discussed.

The highly stretched grids, required to resolve near wall flow physics in high Reynolds number turbomachinery flow computations, give rise to important artificial dissipation issues. Accordingly, alternative local velocity and flux Jacobian eigenvalue scalings are provided for the dissipation operators. It is illustrated that such scalings are required for convergent and accurate solutions of these flows.

A hybrid k-ε / algebraic Reynolds stress model (ARSM) has been developed. This hybrid approach reconciles the near wall damping provided by the low Reynolds number k-ε model with the high Reynolds number form ARSM. The accuracy of this approach is validated for a simple shear layer, and the numerical stability of the model is analyzed and verified.

Two-dimensional results are provided for a supersonic compressor cascade operating at unique incidence condition and a low-subsonic double circular arc compressor cascade. Detailed comparison of the numerical solution with experimental results is provided. Shock structure, boundary layer and wake physics are well predicted, providing validation of the numerical and turbulence modelling approaches.

Three-dimensional validation is provided by the results of an incompressible curved duct flow computation, for which wall static pressure and LDA primary and secondary velocity measurements are available. A high Reynolds number axial rotor flow, for which extensive experimental data is also available, was computed. This large scale computation is shown to capture rotational inviscid, blade and endwall boundary layer and

wake flow physics, including spanwise mixing effects, with good accuracy.

Finally, a backswept transonic centrifugal compressor flow, for which L2F meridional passage velocity measurements are available, is computed. Such flows are the most complex that exist in turbomachines. Full Navier-Stokes solutions are presented which are shown to capture detailed viscous dominated flow features, including tip clearance and curvature induced and rotation induced secondary motions, with good accuracy. Relative helicity is used to help interrogate these computational results, and it is found that this parameter is very useful in providing insight into the secondary motions in these machines. Results of impeller flowfield calculations using the hybrid model with and without the influence of system rotation are also provided and interpreted.

Accession For
NTIS GRA&I ☑
DTIC TAB ☐
Unannounced ☐
Justification____
By____
Distribution/
Availability Codes
Dist | Avail and/or Special
A-1
3

TABLE OF CONTENTS

LIST OF FIGURES ix

LIST OF TABLES xxiii

NOMENCLATURE xxiv

ACKNOWLEDGEMENTS xxx

Chapter 1 INTRODUCTION 1

Chapter 2 THEORETICAL FORMULATION 20

2.1 Favre Averaged Governing Equations 20

- 2.1.1 Mean Flow Equations 20
- 2.1.2 Eddy Diffusivity Approximations 22
- 2.1.3 Turbulence Transport Model 24
- 2.1.4 Algebraic Reynolds Stress Model 27

2.2 Transformation of Governing Equations to Generalized Coordinates 30

Chapter 3 DEVELOPMENT AND ANALYSIS OF NUMERICAL PROCEDURES 35

3.1 Discretized Governing Equations 35

- 3.1.1 Spatial Discretization, Flux Evaluation 36
- 3.1.2 Explicit Numerical Procedure 39

3.1.3 Boundary and Initial Conditions 43

3.2 Artificial Dissipation 46

3.2.1 Eigenvalue Scaling 47

3.2.2 Local Velocity Scaling 55

3.3 Stability and Order of Magnitude Analyses of Discretized Equations 61

3.3.1 Treatment of Mean Flow and Turbulence Transport Systems 62

3.3.2 Vector VonNeumann Procedure 63

3.3.3 Order of Magnitude Analyses 72

3.3.3.1 Rotation Source Terms 73

3.3.3.2 Turbulence Model Source Terms 75

3.3.3.3 Physical and Artificial Dissipation 85

3.3.4 Stability Boundary 89

3.4 Numerical Implementation and Stability of Algebraic Reynolds Stress Model 92

3.5 Computational Considerations 98

Chapter 4 PREDICTION OF TWO-DIMENSIONAL INTERNAL AND CASCADE FLOWS 99

4.1 Turbulent Flat Plate Boundary Layer Flow - Turbulence Model Validation 99

4.2 Turbulent Flow Through a Supersonic Compressor Cascade Operating at Unique Incidence Condition 103

4.3 Turbulent Flow Through a Subsonic Cascade of Double Circular Arc Profiles with Flow Reversal 117

Chapter 5 PREDICTION OF THREE-DIMENSIONAL INTERNAL AND TURBOMACHINERY FLOWS 125

5.1 Turbulent Flow in a 90° Bending Duct of Square Cross-section 125

5.2 Subsonic Compressor Rotor Operating at Peak Pressure Rise Coefficient 131

Chapter 6. TRANSONIC CENTRIFUGAL COMPRESSOR COMPUTATIONS 154

6.1. Background 154

6.2. Flowfield Calculation Using the k-ε Model 165

6.3. Flowfield Calculation Using the Hybrid k-ε / ARS Model 186

Chapter 7 CONCLUSIONS AND RECOMMENDATIONS 197

REFERENCES 205

APPENDIX. NONCONSERVATIVE JACOBIAN MATRICES AND FOURIER MATRIX FOR HYPERBOLIC STABILITY 216

Figure 3.6 Comparison of predicted skin friction coefficient, along the suction surface of a subsonic double circular arc cascade, with and without velocity scaling of artificial dissipation. 60

Figure 3.7 Comparison of convergence rates for rotating (solid) and stationary (dashed) rotor passage flow with and without inclusion of rotation terms in local timestep evaluations. 74

Figure 3.8 Convergence histories for turbulent flat plate flow computations. Baldwin and Lomax (1978) model (solid line) and present k-ε model (dashed line). 81

Figure 3.9 Comparison of a) convergence histories, b) converged boundary layer velocity and local turbulence intensity profiles at a location on the suction surface for fine grid cascade computations. Results for three different source and dissipation term treatments are compared. 83

Figure 3.10 Regions of computational domain where $\Delta t_v < \Delta t_c$ for a) fine grid and b) coarse grid rotor flow calculations at convergence (annular grid slice near midspan). 87

Figure 3.11 Percentage of grid points for which $\Delta t_v < \Delta t_c$ as a function of iteration number for coarse grid rotor flow computation. 88

LIST OF FIGURES

Figure 2.1 Coordinate Transformation Representation 31

Figure 3.1 Two-dimensional representation of periodic leading edge grid topology in physical and computational space. Fluxes evaluated at X. Dashed lines represent grid in periodic adjacent passage. 37

Figure 3.2 Stability boundary of Runge-Kutta scheme used in this thesis. The curve represents the contour $|g(Z)| = 1.0$, where Z is the complex Fourier symbol, $Z = X + iY$ of any discretized scalar equation at a particular wave number, and g is the amplification factor arising from a 1-D scalar VonNeumann linear stability analysis of the given scheme applied to this discretized equation. 41

Figure 3.3 Amplification factor, $|g|$, vs. error phase, ϕ, plot for RK4 scheme applied to scalar advection equation. For comparison, the $|g|$ vs. ϕ curve for the Lax-Wendroff scheme is also included. 42

Figure 3.4 Artificial dissipation local velocity scaling function used in this thesis. 57

Figure 3.5 Effect of artificial dissipation velocity scaling on law-of-the-wall predictions for a turbulent flat plate flow computation. Standard law-of-the-wall relations (solid lines) and computed values (symbols). 58

Figure 3.12 Comparison of convergence rates for several operating Von Neumann numbers with (solid) and without (dashed) inclusion of artificial dissipation terms in timestep computations. 90

Figure 3.13 Location of numerical operating point, (CFL_{op}, Ω_{op}), for full scale cascade and rotor flow computations, plotted in the complex Z plane with the stability boundary for the RK4 scheme used. Corresponding convergence histories for these two calculations are also included. 91

Figure 3.14 Blending function for hybrid turbulence model. 96

Figure 3.15 Convergence histories for turbulent flat plate flow computations. Low Reynolds number k-ε model (alternating long dash-short dash), high Reynolds number ARSM model (solid), hybrid model, blending function, equation [3.63] used (short dash). 97

Figure 4.1 Law-of-the-wall predictions for a turbulent flat plate flow computation. Crossing curves represent standard law-of-the-wall relations. Low Reynolds number k-ε model (alternating long dash-short dash), high Reynolds number ARSM model (solid), hybrid model (short dash). 102

Figure 4.2 Turbulent kinetic energy distributions for a turbulent flat plate flow. Experimental data due to Klebanoff (1954) (symbols). Computations using low Reynolds number k-ϵ model (alternating long dash-short dash), high Reynolds number ARSM model (solid), hybrid model (short dash). 102

Figure 4.3 Boundary layer Reynolds normal stress distributions for a turbulent flat plate flow. Experimental data due to Klebanoff (1954): streamwise intensity (++++ symbols), plate normal intensity (oooo symbols), crossflow intensity (xxxx symbols). Computations using hybrid model (solid line). 104

Figure 4.4 129 x 100 computational grid for the PAV-1.5 cascade. For clarity, only every other grid line is shown in both ξ and η directions. 106

Figure 4.5 Convergence history for PAV-1.5 cascade computation. 108

Figure 4.6 Shock wave pattern for PAV - 1.5 cascade. Divergence of velocity contours (-300 to -4800 by -500 [s^{-1}]). In this diagram, the top two passages show computed contours. The bottom passage is the shock wave pattern deduced from flow visualization and L2F measurements, adapted from Schreiber (1988). 110

Figure 4.7 Isentropic blade surface Mach numbers and shock structure identification for PAV-1.5 cascade computation. Calculated (solid line) and experimental values (symbols). 111

Figure 4.8 Total pressure ratio profile 0.09 chord downstream of trailing edge for PAV-1.5 cascade computation. Calculated (solid line) and experimental values (symbols). 112

Figure 4.9 Local boundary layer velocity and turbulence intensity profiles at four chord locations along the suction and pressure surfaces for the PAV-1.5 cascade computation. Locations a, b, c, d correspond to .25, .50, .75, .90 chord, respectively. The hash marks correspond to the estimated boundary layer thicknesses reported by Schreiber (1988). 114

Figure 4.10 Total pressure loss coefficients at several cascade operating points. Calculated (solid symbols) and experimental values (open symbols). 116

Figure 4.11 129 x 85 Computational grid for the ARL DCA cascade. 118

Figure 4.12 Convergence history for ARL DCA cascade computation. 120

Figure 4.13 Pressure coefficient for ARL DCA cascade computation. Calculated (solid line) and experimental values (symbols). 121

Figure 4.14 Boundary layer profiles at three chord locations along the suction surface for the ARL DCA cascade computation. Calculated (solid line) and experimental values (symbols). 122

Figure 4.15 Local turbulence intensity profiles at three chord locations along the suction surface for the ARL DCA cascade computation. Calculated (solid line) and experimental values (symbols). 124

Figure 5.1 81 x 21 x 41 Computational grid and notation for incompressible duct flow computation. 127

Figure 5.2 Convergence history for incompressible duct flow computation. 129

Figure 5.3 Streamwise static pressure coefficient distribution at several locations along symmetry plane for incompressible duct flow computation. Calculated (solid line) and experimental values (symbols). 130

Figure 5.4 Contours of normalized streamwise velocity, V_s/V_b, for incompressible duct flow computation. Experimental contours, reproduced from Taylor et al. (1981), appear on bottom side of each cross section. Computed contours appear on top. See Figure 5.1 for notation. 132

Figure 5.5 Secondary velocities at various streamwise stations for incompressible duct flow computation. a) Computed secondary velocity vectors [solid lines indicate location of traverses in b)]. b) Scaled radial velocities, V_r/V_b, at five radial locations. Calculated (solid line) and experimental values (symbols). See Figure 5.1 for notation. 133

Figure 5.6 Computational grid and configuration details for PSU rotor flow computation. a) 89 x 45 x 45 computational grid. b) detail of "thin blade" tip clearance gap at midchord. c) hub-leading edge detail showing relative flow velocities at stationary-rotating hub interface in relative frame. 135

Figure 5.7 Convergence history for PSU rotor flow computation. 137

Figure 5.8 Blade to blade axial velocity distribution (W_x/U) for PSU rotor flow, at four spanwise locations. Laser velocimeter measurements due to Popovski and Lakshminarayana (1986) (symbols) and computed distributions (solid lines). 139

Figure 5.9 Suction surface streamwise boundary layer velocity distribution ($W_s/W_{s\ edge}$) for PSU rotor flow, at four spanwise locations. Rotating hot wire measurements due to Lakshminarayana and Popovski (1987) (symbols) and computed distributions (solid lines). 140

Figure 5.10 Suction surface radial boundary layer velocity distribution ($W_r/W_{s\ edge}$) for PSU rotor flow, at four spanwise locations. Rotating hot wire measurements due to Lakshminarayana and Popovski (1987) (symbols) and computed distributions (solid lines). 141

Figure 5.11 Wake axial velocity distribution ($W_x/W_{x\ edge}$) for PSU rotor flow, at three spanwise locations. Five hole probe measurements due to Prato (1990) (symbols) and computed distributions (solid lines). 143

Figure 5.12 Wake tangential velocity distribution ($W_\theta/W_{\theta\ edge}$) for PSU rotor flow, at three spanwise locations. Five hole probe measurements due to Prato (1990) (symbols) and computed distributions (solid lines). 144

Figure 5.13 Wake radial velocity distribution ($W_r/W_{x\ edge}$) for PSU rotor flow, at three spanwise locations. Five hole probe measurements due to Prato (1990) (symbols) and computed distributions (solid lines). 145

Figure 5.14 Passage averaged (mass weighted) values of a) axial velocity and b) flow angle downstream of PSU rotor passage. Averaged five hole probe measurements due to Prato (1990) (symbols) and computed distributions (solid lines). 147

Figure 5.15 Computed contours of relative stagnation pressure loss coefficient, $C_{p\ loss}$, at a) trailing edge, and b) exit plane of computational domain. 148

Figure 5.16 Loss coefficient distributions for General Electric Low Speed Research Compressor. This figure is reproduced from Adkins and Smith (1982). 150

Figure 5.17 Passage averaged (mass weighted) relative stagnation pressure loss coefficient, $C_{p\ loss}$, a) in the near wake and b) .66 chord downstream of hub trailing edge. Averaged five hole probe measurements due to Prato (1990) (symbols) and computed distributions (solid lines). 151

Figure 6.1 Impeller wheel tested experimentally by Krain (1988), and investigated computationally in this chapter. This figure was reproduced from Krain (1988). 155

Figure 6.2 Periphery of computational grid used in numerical simulation studies, showing impeller and diffuser sections of centrifugal compressor stage. 156

Figure 6.3 Performance maps for Krain impeller, indicating computed operating point. This figure was adapted from Krain (1988). 157

Figure 6.4 Meridional view of 59 x 27 x 27 computational grid for Krain impeller computation. Streamwise grid indexing and location of experimental laser planes are indicated for reference. 159

Figure 6.5 Cross stream views of 59 x 27 x 27 computational grid for Krain impeller computation. a) Impeller inlet grid slice, b) grid slice near impeller exit and c) tip gap detail at inlet grid plane. 160

Figure 6.6 Qualitative representation of secondary motions present in a centrifugal compressor impeller. a) Sense of curvature and rotation induced motions and b) qualitative sketch of pressure surface crossflow arising from axial to radial turning of the meridional flow. 162

Figure 6.7 Convergence history for Krain impeller flow computation. 166

Figure 6.8 Shroud static pressure distribution. Experimentally obtained time averaged static pressure tap measurements (symbols), circumferentially averaged computed values (solid line). 167

Figure 6.9 Meridional velocity profiles at L2F data acquisition Plane I. Experimental measurements (symbols), computed values (solid line). 168

Figure 6.10 Meridional velocity profiles at L2F data acquisition Plane II. Experimental measurements (symbols), computed values (solid line). 169

Figure 6.11 Computed normalized relative helicity contours at solution grid slice corresponding to L2F data acquisition Plane III. 171

Figure 6.12 Meridional velocity profiles at L2F data acquisition Plane III. Experimental measurements (symbols), computed values (solid line). 172

Figure 6.13 Meridional velocity contours at L2F data acquisition Plane III. Experimental contours (top), computed contours (bottom). 174

Figure 6.14 Computed normalized relative helicity contours at solution grid slice corresponding to L2F data acquisition Plane IV. 175

Figure 6.15 Meridional velocity profiles at L2F data acquisition Plane IV. Experimental measurements (symbols), computed values (solid line). 176

Figure 6.16 Meridional velocity contours at L2F data acquisition Plane IV. Experimental contours (top), computed contours (bottom). 177

Figure 6.17 Qualitative representation of physical phenomena contributing to the formation of the wake flow region. a) Representative sketch adapted from Eckardt (1976) and b) computed normalized relative helicity at 68 % chord. 178

Figure 6.18 Computed normalized relative helicity contours at solution grid slice corresponding to L2F data acquisition Plane V. 180

Figure 6.19 Meridional velocity profiles at L2F data acquisition Plane V. Experimental measurements (symbols), computed values (solid line). 181

Figure 6.20 Meridional velocity contours at L2F data acquisition Plane V. Experimental contours (top), computed contours (bottom). 182

Figure 6.21 Computed normalized relative helicity contours at solution grid slice corresponding to L2F data acquisition Plane V. 183

Figure 6.22 Meridional velocity profiles at L2F data acquisition Plane VI. Experimental measurements (symbols), computed values (solid line). 184

Figure 6.23 Meridional velocity contours at L2F data acquisition Plane VI. Experimental contours (top), computed contours (bottom). 185

Figure 6.24 Convergence history for the three computations presented. Features labelled a and b correspond to solution restarts using alternate turbulence models. 187

Figure 6.25 Converged hybrid model solution contours of y^+ on a grid slice at 75 % chord. The precise location of $y^+_{match} = 200$, the value used in the hybrid solutions, is indicated. 189

Figure 6.26 Meridional velocity profiles at L2F data acquisition Plane IV. Comparison of solutions using three turbulence models : low Reynolds number k-ε model (solid), hybrid model, $R_{ij} = 0$ (long dash), hybrid model, $R_{ij} \neq 0$ (short dash). 190

Figure 6.27 Near wall relative crossflow velocity profiles at 90 % chord. a) midspan on suction surface, b) midspan on pressure surface, c) mid passage on hub. Comparison of solutions using three turbulence models : low Reynolds number k-ε model (square), hybrid model, $R_{ij} = 0$ (circle), hybrid model, $R_{ij} \neq 0$ (triangle). 191

Figure 6.28 Predicted skin friction coefficient vs. dimensionless streamwise distance along shroud. Comparison of solutions using three turbulence models: low Reynolds number k-ε model (solid), hybrid model, $R_{ij} = 0$ (long dash), hybrid model, $R_{ij} \neq 0$ (short dash). 193

Figure 6.29 Computed normalized relative helicity contours on a solution grid slice at 68 % chord. Comparison of solutions using two turbulence models: low Reynolds number k-ε model (bottom), hybrid model, $R_{ij} \neq 0$ (top). 194

LIST OF TABLES

Table 4.1. Comparison of Performance Parameters for PAV-1.5 Cascade 115

Table 4.2. Comparison of Performance Parameters for ARL-DCA Cascade 123

Table 5.1. Comparison of Performance Parameters for Penn State Compressor Rotor 153

Table 6.1. Comparison of Performance Parameters for Transonic Centrifugal Compressor Stage 186

Table 6.2. Comparison of Predicted Performance Parameters for Transonic Centrifugal Compressor Stage, Using Different Turbulence Models 195

NOMENCLATURE

a	Speed of sound
A	Flux Jacobian, duct cross-sectional area
AVDR	Axial Velocity Density Ratio ($= \dfrac{\int \rho_2 V_{2x}\, dn}{\int \rho_1 V_{1x}\, dn}$)
$\widehat{A}_i, \widehat{S}_i, \widehat{T}_i, \widehat{D}_i$	Nonconservative flux and source Jacobians (Defined in Appendix A)
c	Local chord length
c_p, c_v	Specific heat at constant pressure and volume
CFL_{op}	Operational Courant Number (defined in Chapter 3)
C_f	Skin friction coefficient
C_p	Pressure coefficient ($= \dfrac{p - p_{ref}}{\frac{1}{2}\rho_\infty V_b^2}$)
$C_{p\ loss}$	Relative stagnation pressure loss coefficient ($= \dfrac{p^*_{inlet}(r) - p^*_{local}}{\frac{1}{2}\rho_\infty U^2}$)
$C_\mu, C_1, C_2, \mathfrak{D}, \mathfrak{E}, R_T$	Turbulence modelling parameters
D	Artificial dissipation operator, duct height
D_e	Dean number ($= \left(\dfrac{.5D}{R_c}\right)^{1/2} R_e$)
e	Internal energy per unit mass
e_{0R}	Energy transport variable ($= e + W^2/2 - \omega^2 r^2/2$)
E, F, G	Flux vectors
g, G	Amplification factor, matrix
h_0	Stagnation enthalpy
H	Normalized relative helicity

I	Rothalpy ($e + W^2/2 - \omega^2 r^2/2 + p$)
i, j, k	Streamwise, pitchwise, spanwise grid indices
ile, ite	Streamwise grid index at leading and trailing edges
J	Metric Jacobian
k	Turbulent kinetic energy
k_e	Effective conductivity
l	Wall proximity length scale
L	Turbulence length scale
M	Mach number
$\dot{m}$	Mass flow rate
n	Pitchwise coordinate (= 0, 1 at suction, pressure side in passage, = 0 at wake centerline downstream of passage)
N_s	Specific speed ($\phi^{1/2}/\psi^{3/4}$)
$O(\ )$	Order of magnitude
p	Static pressure
p_0	Stagnation pressure
p^*	Relative stagnation pressure ($= p + \rho W^2/2$)
P	Matrix polynomial function, Production of turbulent kinetic energy Scaling matrix for nonconservative formulation (defined in Appendix A)
P_{ij}	ARSM production by mean strain rate tensor
$Pr_l, Pr_t, Pr_k, Pr_\varepsilon$	Prandtl numbers
q_i	Cartesian components of heat transfer rate vector
Q	Primary transport variable vector
r	Radial coordinate (measured from machine axis)
R	Gas constant Residual vector

$R_{c\ inner}$, $\overline{R_c}$	Inner and average duct radius of curvature
R_e	Reynolds number
R_{ij}	ARSM production by system rotation tensor
s	Chordwise coordinate (= 0, 1 at leading, trailing edges)
S	Source term vector
$S_{4\xi}$, $S_{4\eta}$, $S_{4\zeta}$	Artificial dissipation scale factors
t	Time
	Local blade spacing
T	Static temperature
	Turbulence intensity
T_{ij}	ARSM modelling tensor
u^*	Friction velocity
u, v, w	Relative cartesian velocities
U, U_{local}	Blade tip speed, local blade speed
U, V, W	Contravariant velocities
v_θ	Absolute tangential velocity
v_x, $\overline{v}_x$	Axial velocity, mass averaged axial velocity
V	Magnitude of total absolute velocity
V_b	Bulk velocity ($= \int V_s dA/A$)
W	Magnitude of total relative velocity
w_θ	Relative tangential velocity
x, y, z	Relative cartesian coordinates
Z	Fourier matrix of spatial discretization
α	Exponent in artificial dissipation scaling function
α_k	Weighting factor in time integration scheme
β_1, β_2	Incidence and deviation angles

γ	Specific heat ratio
δ_{ij}	Kronecker delta
$\delta_{\xi\xi}$, $\delta_{\eta\eta}$, $\delta_{\xi\xi\xi\xi}$, $\delta_{\eta\eta\eta\eta}$	2nd and 4th central differencing operators
δ_1, δ_2	Displacement and momentum thickness
Δt	Local timestep
$\Delta \bar{x}_i$	$(\Delta x, \Delta y, \Delta z)^T$
∇	Gradient operator
ε	Isotropic component of turbulent kinetic energy dissipation rate
ε^+	Actual dissipation rate nondimensinalized in inner varaibles ($\varepsilon^+ = \nu\varepsilon/u^{*4}$)
ε_{ijk}	Alternating tensor
$\bar{\eta}$	Total to total efficiency
κ_2, κ_4	Artificial dissipation constants
λ	Eigenvalue
μ_l, μ_t, μ_e	Molecular, turbulent, effective viscosity
ν	Kinematic viscosity
ν_{ij}	Pressure monitoring parameter for artificial dissipation
$\bar{\xi}_i$	$(\xi, \eta, \zeta)^T$
ξ, η, ζ	Curvilinear coordinates
η	Efficiency
$\vec{\zeta}$	Relative vorticity vector
ρ	Density
	Spectral radius
σ_i	Artificial dissipation scaling factors
σ_2, σ_4	Artificial dissipation weighting functions
τ_{ij} (τ_{xx}, τ_{xy}, etc...)	Cartesian components of stress tensor
τ_w	Wall shear stress
ϕ	General scalar, phase of error mode

$\bar{\phi}$	Flow coefficient (defined with Table 1)
$\bar{\psi}$	Pressure rise coefficient (defined with Table 1)
ω	Total pressure loss coefficient
	Machine rotation rate (s^{-1})
Ω_{op}	Operational VonNeumann Number (defined in Chapter 3)

Superscripts and Subscripts

b	Bulk
c	Convective
edge	Boundary layer or wake edge value
hub	Value at hub
i, j	Grid indices in streamwise and pitchwise directions respectively
inlet	Value at inlet to computational domain
is	Isentropic
l	Laminar
local	Local value
m	Cascade mean value (average of inlet and outlet quantities)
match	Matching condition for hybrid model
merid	Meridional ($W_{merid} = (W_x^2 + W_r^2)^{1/2}$)
o	Stagnation
ps	Value at pressure surface
r	Radial
ref	Reference
s	Streamwise

s''_{ij}	Fluctuating strain rate tensor ($=\frac{1}{2}\left(\frac{\partial u''_i}{\partial x_j}+\frac{\partial u''_j}{\partial x_i}\right)$)
shroud	Value at machine shroud surface (k=nk)
ss	Value at suction surface
S_{ij}	Mean strain rate tensor ($=\frac{1}{2}\left(\frac{\partial \tilde{u}_i}{\partial x_j}+\frac{\partial \tilde{u}_j}{\partial x_i}\right)$)
t	Turbulent
tt	Total to total
tip	Value at blade tip (k=nktip)
v	Viscous
w	Wall
x	Axial
θ	Cascade pitchwise direction
∞	Inlet freestream
1	Cascade or rotor inlet
2	Cascade or rotor exit
^	Quantity scaled by metric Jacobian
'	Fluctuating quantity in time averaging
"	Fluctuating quantity in density averaging
~	Density-weighted time-averaged quantity
-	Time averaged quantity
	Mass averaged quantity (when used in performance parameter definitions)

ACKNOWLEDGMENTS

I would like to thank Professor Budugur Lakshminarayana, my thesis advisor, for providing invaluable advice and encouragement to me during my Ph.D. program, and for helping to provide focus to my thesis work.

The author was supported by a United States Army Research Office Fellowship, through the Grant DAAL 03-86-G-0044, monitored by Dr. T. L. Doligalski. The author wishes to acknowledge NASA for providing the supercomputing resources at the National Aerodynamic Simulation Facility at NASA Ames Research Center.

Professors Dulikravich, Merkle and Morris, the other members of my thesis committee, have all given me individual guidance in their primary areas of expertise, as they have related to my thesis work. Their contributions are appreciated.

Several colleagues, Dr. Rod Chima, Dr. Stuart Connell, Dr. Garth Hobson, Dr. Kevin Kirtley and Dr. Seungsoo Lee, have provided technical assistance to me during the course of code development, turbulence model implementation and turbomachinery flowfield computations. The many conversations I had with these individuals during the last two years were invaluable, and are gratefully acknowledged.

Surely, no individual has endured the rigors of my thesis program with more empathy than my loving wife, Carolyn. Without her emotional support and continuous understanding, my studies would have been far more difficult.

CHAPTER 1

INTRODUCTION

Computation of viscous flows by numerical solution of the Navier-Stokes equations has become increasingly feasible due to improvements in numerical algorithms, and to the ever-increasing speed and memory of digital computers. The most up to date CFD codes available today are capable of calculating steady 3-D viscous flows about entire vehicles, and even unsteady viscous flows in 3-D turbomachinery stages. However, despite the rapid advance towards exploiting the power of computers now available, some serious limitations of these codes have yet to be adequately resolved. Surely the most profound of these limitations is the lack of accurate, general turbulence models. Secondary to this, but of much concern, is the role of artificial dissipation in Navier-Stokes calculations.

The flowfield in all turbomachines is characterized by significant rotational inviscid phenomena, arising from stagnation enthalpy and pressure gradients due to shaft work, flow turning and compressibility effects. Consequently, a great deal of the physics in these machines can be analyzed with inviscid methods. For this reason, inviscid solution procedures have advanced to the point, and are efficient enough, that they are today used routinely in turbomachinery design.

Alternatively, viscous flow phenomena play a dominant role in many parameters of interest to the engineer. Specifically, machine performance parameters such as efficiency, maximum pressure rise/drop and attainable mass flow rates are strongly influenced by viscous effects. The developing boundary layers on blade and endwall surfaces give rise to losses and blockage. The convection and diffusion of blade row wakes and some spanwise mixing effects are viscous phenomena which play important roles in multistage machines. Also of large concern, especially in turbines and centrifugal machines, are secondary motions which arise due to the turning and rotation of shear layers in these machines. The direct effect of apparent stresses, due to flowfield turbulence, is a factor in all turbomachines since Reynolds numbers are characteristically large. The physics of tip clearance vortices, localized flow reversal, rotating stall, surge and choking are all intimately tied to viscous flow effects. In order to develop a further understanding of these phenomena, nothing short of analyses that incorporate the full Reynolds averaged Navier-Stokes equations are sufficient.

The engineer needs analysis tools which are 1) accurate, 2) versatile, 3) relatively easy to use on a routine basis, and 4) fast/efficient. Unfortunately, for these very reasons, the current state of the art does not allow for detailed Navier-Stokes analysis in the turbomachinery design environment. At present, high Reynolds number, three-dimensional turbomachinery passage flows have been computed by a number of researchers using on the order of 10^5 grid points, but the central memory and CPU run time requirements for such calculations are large. Also, even grids of this size are not adequate to provide grid converged, detailed viscous flow predictions. The state of the art seems to be, rather, the reasonable prediction of global three-dimensional vorticity distributions at design and off design conditions. Also, in addition to accuracy limitations imposed by practical grid size constraints, simple turbulence models and the inescapable presence of artificial dissipation introduce additional inaccuracies.

Pre-processing, including grid generation and flow initialization, can be daunting and time-consuming tasks for complex turbomachinery configurations. Application of Navier-Stokes flow solvers themselves generally require an experienced analyst, with detailed understanding of the physical models and/or numerical procedures incorporated in these codes. Lastly, postprocessing large scale solutions can take days of an analyst's time to extract useful design information. So, in short, Navier-Stokes methodologies currently fail on several counts, from an engineer's standpoint. For this reason, there is currently a great deal of research to improve the usefulness of these methods, with emphasis on turbulence and other physical modeling, incorporation of efficient algorithms and improved computer architectures, and the use of full scale simulation studies to develop an understanding of particular physical processes in turbomachines [see recent paper by Leylek and Wisler (1990), for an good example of this last item)].

The purpose of this thesis is to develop a new explicit, three-dimensional Navier-Stokes methodology for turbomachinery flowfield prediction. In accordance with the need to address the items mentioned above, emphasis has been placed on 1) incorporation of a low Reynolds number two-equation turbulence model in an explicit numerical solution procedure, 2) comprehensive investigation of the stability of the procedure, including the influence of various geometric and flowfield parameters on numerical stability, with emphasis on the turbulence model, 3) investigation of the role of artificial dissipation in the accuracy and stability of viscous flow computations on highly stretched grids, 4) simulation of a variety of complex two- and three-dimensional turbomachinery flows, across a wide range of Mach numbers, including a transonic centrifugal compressor, with the goal of using the flow solution to provide a detailed understanding of the viscous physical mechanisms in these machines.

In three-dimensional Navier-Stokes calculations of steady state turbomachinery flowfields, both explicit and implicit time-marching procedures have been implemented by a number of researchers. As mentioned above, high Reynolds number turbomachinery passage flows have been computed by a number of researchers using on the order of 10^5

grid points [See recent publications by Bansod and Rhie (1990), Chima and Yokota (1988), Choi and Knight (1989), Walker and Dawes (1989), Hah and Wennerstrom (1990), Hobson and Lakshminarayana (1990), Kirtley et al. (1990), Leylek and Wisler (1990), Moore and Moore (1990), Subramaniam (1989), Warfield and Lakshminarayana (1989), for example].

The comparative performance of implicit and explicit numerical schemes, in three-dimensional steady flow computations is not definitive. Both explicit and implicit procedures generally incorporate local timestepping, where estimated optimum timesteps are used. For explicit schemes, this corresponds to operational Courant-Friedrichs-Lewy (1928), or CFL, numbers just below that allowed for numerical stability ($\cong 2.8$ for standard four-stage Runge-Kutta schemes). In multidimensional problems, implicit time-marching schemes are generally factored in nature, and factorization gives rise to optimum local CFL numbers of the same order (in three-dimensions, typical *optimum* CFL numbers of approximately 5 have been reported for LU schemes [Yokota and Caughey (1987)] and approximately 10 for ADI schemes [Merkle (1988), for example]). Since local timesteps are monotonically related to local distances between grid points, the performance of both implicit and explicit schemes suffer on the highly clustered grids required for high Reynolds number flow computations.

There are several other considerations involved in the choice between implicit and explicit schemes, including the availability of steady state acceleration schemes. Multigrid procedures have been used for explicit Euler calculations with great success (Ni (1982), for example) and with some success in implicit computations [Yokota and Caughey (1987), for example]. Implicit residual smoothing (IRS) schemes can provide approximately a factor of two in CPU times savings in explicit procedures, but the performance of both multigrid and IRS schemes are very sensitive to the grid stretching required in viscous flow computations[see Radespiel et al. (1990)].

Explicit algorithms, and some implicit algorithms, are fully vectorizable, giving rise to rapid (CPU seconds)/(grid point * iteration) performance on advanced vector computer architectures. Explicit procedures can be more easily rendered close to 100 % parallelizable, so application to the massively parallel architectures, which are now emerging, is appropriate. Modified implicit solvers, though, have recently been shown [Wake and Egolf (1991))], to provide efficient execution rates on such machines, as well.

Lastly, the nature of the discrete equation set being solved should be considered in choosing a particular numerical scheme (or a temporal discretization procedure for certain terms). Specifically, implicit treatment may improve damping properties when applied to discrete transport equations with source terms. In summary, it is currently not clear whether implicit or explicit procedures are uniformly more efficient in viscous three-dimensional turbomachinery computations.

An explicit numerical procedure of the Runge-Kutta class has been chosen in this thesis. This scheme is preferred in this work for several reasons. First, the numerical formulation is somewhat simpler than for implicit schemes, which is helpful from a code development standpoint, when complications due to additional physical modelling and application to turbomachinery configurations is required. Second, Runge-Kutta schemes are more efficient [Jameson et al. (1981)] and naturally less dissipative than other explicit schemes (central and upwind difference; see Figure 3.2 and accompanying discussion), allowing the user to control more precisely levels of artificial dissipation which may corrupt solution accuracy. Furthermore, a number of researchers have successfully applied Runge-Kutta procedures in viscous three-dimensional turbomachinery computations [see Chima and Yokota (1988), Kirtley et al. (1990), Subramaniam (1989) for example]. Lastly, as will be shown, the procedures developed in this thesis have been very successful, which in retrospect, ultimately justifies their choice.

Due to the wide range of length scales associated with turbulent motions in high Reynolds number turbomachinery flows, models which require closure approximations for the time averaged governing equations will be required for computation of these flows for many years.

Closure models can be broadly classified into first order and second order closures. In first order closures, the Reynolds stresses (second order correlations) are modelled as functions of gradients of the mean velocity field. Models which fall under this classification are commonly referred to as eddy viscosity models, and include algebraic and one-equation mixing length models, and two-equation models. In second order closures, the transport equations for the Reynolds stresses themselves are treated, where the third order correlations are expressed in terms of mean flow quantities and the Reynolds stresses themselves. Models which fall under this classification include algebraic Reynolds stress models (ARSM) and full Reynolds stress models (FRSM).

The first and simplest of turbulence models is the mixing length model of Prandtl (1925). This model assumes that characteristic time scales of turbulent transport by eddy motion are of the same order as time scales of the local mean flow. In simple shear layers, where only one mean strain rate and Reynolds shear stress component are dominant, the model takes the following form :

$$-\rho\overline{u_1' u_2'} = \mu_t \frac{\partial U_1}{\partial x_2} = C\rho L^2 \left|\frac{\partial U_1}{\partial x_2}\right| \qquad [1.1]$$

where an eddy viscosity has been introduced, following Boussinesq (1877), who proposed that the turbulent shear stresses can be modelled as being linearly related to mean strain rate as molecular stresses are in a Newtonian fluid. In equation [1.1], L, represents a local "mixing length," which must be prescribed by a combination of analytical and empirical results, and C is an empirical constant. The accuracy of mixing length models depend on the accuracy of the mixing length prescription. In simple two-dimensional shear layers, local mixing length distributions are well established, but the evaluation of L becomes difficult in non-simple shear layers, most especially in internal flows such as turbomachinery. Also, the mean strain only provides a good representation of the turbulence time scale when the Reynolds stress production and dissipation are approximately in balance. Additionally, transport and history effects on local turbulence structure are neglected in mixing length models. Regardless of these shortcomings, extensions of equation [1.1] to multidimensional problems have been very popular. In such approaches, a tensor form extension of the Boussinesq approximation is employed :

$$-\rho\overline{u_i'u_j'} = 2\mu_t S_{ij} - \frac{2}{3}\rho k \delta_{ij} \qquad [1.2]$$

where S_{ij} is the mean strain rate tensor, and k is the turbulent kinetic energy. The very popular two-layer model of Baldwin and Lomax (1978) falls in this class, where the last term in equation [1.2] is neglected, and the eddy viscosity is algebraically related to the mixing length in a fashion analogous to equation [1.1].

If the turbulence kinetic energy, k, is known locally, then time scale arguments similar to those justifying the mixing length hypothesis yield :

$$\mu_t = C_\mu \rho k^{1/2} L \qquad [1.3]$$

where now $k^{1/2}$ is taken as a velocity scale representative of the turbulence eddy transport. In one equation models, a differential transport equation is solved for k, but the mixing length is still prescribed algebraically. These models have been popular in external flow computations, where mixing length prescriptions are not as ambiguous as in internal flows (King (1987), for example).

It was mentioned that the specification of a local mixing length is difficult in turbomachinery flows where shear layers can be highly three dimensional, local flow reversal can exist (in which case equation [1.1] provides that $-\overline{u_1^{'}u_2^{'}} \rightarrow 0$ at locations within the separation zone where $\frac{\partial U_1}{\partial x_2} \rightarrow 0$), and solid boundary proximity can be ambiguous. For these reasons, two-equation models, which solve conceptually a transport equation for the turbulence length scale, have been used extensively. A variety of two-equation models exist, all of them have in common that the characteristic local turbulence velocity and length scales, $k^{1/2}$, L, can be extracted from the two transport variables. The most well known of these is the k-ε model, which is based on the pioneering work of a number of researchers including Jones (1971) and Launder and Spalding (1974). The underlying assumption of these models, is that, at high enough local turbulence Reynolds number, $R_T \equiv \frac{\sqrt{k}\,L}{\nu}$, the rate of change of local turbulence kinetic energy is equal to the energy dissipated in the small scales (local equilibrium assumption). Since the dynamics of the large scale turbulence motions can be characterized by velocity and length scales, $k^{1/2}$ and L, dimensional analysis provides that

$$\varepsilon = \varepsilon(k,L) = C\,\frac{k^{3/2}}{L} \qquad [1.4]$$

where the dissipation rate is defined here as $\varepsilon \equiv \nu\,\overline{\frac{\partial u_i^{'}}{\partial x_j}\frac{\partial u_i^{'}}{\partial x_j}}$, which is the homogeneous component of the total dissipation rate (see discussion in Chapter 2). Accordingly, we have $L = C\frac{k^{3/2}}{\varepsilon}$, and invoking equation [1.3], the Prandtl-Kolmogorov relation for eddy viscosity becomes :

$$\mu_t = C_\mu \rho \frac{k^2}{\varepsilon} \qquad [1.5]$$

where C_μ is an empirical constant.

Launder and Spalding (1974) provided the so-called standard high Reynolds number k-ε model and recommended empirically obtained values for the modelling constants which appear. In order to account for near wall effects, where the high Reynolds number form of the k and ε equations are not valid, Launder and Spalding (1974) introduced wall functions which incorporate assumed near wall log-law velocity profiles. Accordingly, wall functions are applied at the first grid point off of the wall which, for consistency, should lie in the inertial sublayer (nominally $30 < y^+_2 < 300$). Boundary conditions on k and ε which assume local equilibrium (production of k = dissipation) are also applied at this location. Wall functions have the advantage that significant computer resource savings can be realized since near wall physics need not be resolved explicitly. This has kept wall functions popular, even in state-of-the-art three-dimensional turbomachinery flow solvers (Leylek and Wisler (1990), Bansod and Rhie (1990), for example).

However, since wall functions rely on the assumption of a locally logarithmic velocity distribution and the local equilibrium of the turbulence, their accurate applicability is severely restricted. Specifically, in locally separated flows, no log-law region exists, and in three-dimensional flows, secondary motions (say spanwise flows) often extend well into the inner layer, giving rise to skewed boundary layer profiles. Additionally, implicit in the use of wall functions is that blade boundary layers are fully turbulent. Lastly, application of wall functions in turbomachinery configurations gives rise to several ambiguities, including leading edge and blade-endwall intersection treatment and wake centerline treatment. For these reasons, the wall function approach is not adopted in the present work.

Low Reynolds number forms of the k-ε model directly model near-wall influences on the turbulence structure by modifying the k and ε equations. Specifically, they are distinguished from high Reynolds number forms in that several modelling parameters which account for the proximity of solid boundaries are accounted for (see Patel et al. (1985) for example). Specifically, molecular viscosity is retained in the diffusion terms, model constants in the dissipation rate equation are factored with near wall modification functions, and in some cases near wall source functions are incorporated to model directly the behavior of the dissipation rate near the wall (refer to equations [2.10] - [2.12]). The eddy viscosity, and thereby conceptually the Reynolds stresses, are also damped as the wall is approached in a fashion consistent with Van Driest (1956) damping. Specifically, the Prandtl-Kolmogorov relation is modified as :

$$\mu_t = f_\mu C_\mu \rho \frac{k^2}{\varepsilon} \tag{1.6}$$

where f_μ provides appropriate exponential damping as the wall is approached.

Low Reynolds number models have the advantage that near wall boundary layer skew due to secondary motions can be resolved. This is important in flows such as centrifugal compressors, where significant cross flow velocity components can exist very close to the wall (refer to results in Chapter 6). These models can be applied in an unambiguous fashion in complex geometries (all that is needed is an appropriate wall proximity length scale prescription; see Chapter 2). This is important especially at turbomachinery boundaries such as the interface between rotating and stationary portions of a hub, a stationary blade adjacent to a rotating (in the relative frame) shroud, and the interface between solid and periodic boundaries, such as at leading and trailing edges and tip clearance gaps. In the opinion of the author, the use of wall functions along these boundaries would be difficult and inappropriate. Lastly, low Reynolds number k-ε models can model the influence of freestream turbulence on turbulence transition (Jones and Launder (1972) for example), albeit only if the modelled flow is such that transition is strongly influenced by local freestream intensity.

The improvements in prediction accuracy which can be obtained using two-equation models over mixing length models is well documented. For example, the k-ε model has been shown to provide better predictions than algebraic models for flows with adverse pressure gradient [Kirtley and Lakshminarayana (1985)] and for 2-D shock-boundary layer flow on curved surfaces [Degrez and VanDromme (1985)]. However, there are still well acknowledged deficiencies [see Lakshminarayana (1986] and Speziale (1989), for example) associated with the use of two-equation models. Such models are eddy viscosity models, and as such invoke the Boussinesq approximation which implies that the Reynolds stress tensor is aligned with the mean strain rate tensor. Accordingly, eddy viscosity models cannot predict secondary flows of the second kind, which are induced by Reynolds intensity anisotropies, and are present even in unidirectional flows (see further discussion in Chapter 5, Section 1). Also, eddy viscosity models cannot account for component Reynolds stress relaxation/amplification effects; instead they predict instantaneous return to isotropy in the absence of local mean strain. Another criticism of these models, is that unless empirically modified, they cannot account for the influence of local streamline curvature and system rotation on local turbulence structure.

Full Reynolds stress models (FRSM) of the form proposed by Launder et al. (1975) :

$$\frac{D\overline{u_i^{'}u_j^{'}}}{Dt} = \left\{C_s\frac{\partial}{\partial x_k}\left(\frac{k}{\varepsilon}\overline{u_k^{'}u_l^{'}}\frac{\partial\overline{u_i^{'}u_j^{'}}}{\partial x_l}\right)\right\} + \left\{-\overline{u_i^{'}u_k^{'}}\frac{\partial u_j}{\partial x_k} - \overline{u_j^{'}u_k^{'}}\frac{\partial u_i}{\partial x_k}\right\}$$

$$+\left\{-C_1\frac{\varepsilon}{k}\left(\overline{u_i^{'}u_j^{'}} - \frac{2}{3}\delta_{ij}k\right) - \gamma\left(P_{ij} - \frac{2}{3}P\delta_{ij}\right) + \phi_{ij,w}\right\} + \left\{-\frac{2}{3}\delta_{ij}\varepsilon\right\} \qquad [1.7]$$

or :

Convection = {Diffusion, D_{ij}} + {Production by mean strain rate, P_{ij}}

+ {Pressure strain} + {Dissipation}

can in principle account for the eddy viscosity modelling deficiencies alluded to above. In these closures, the modelled transport equations for the six individual Reynolds stress components, equation [1.7], are solved, along with an equation for turbulence energy dissipation rate. Various FRSM have been shown to account correctly for Reynolds stress anisotropy phenomena and amplification/relaxation effects, and account intrinsically for curvature and rotation effects since fluctuating momentum balance information is incorporated in the exact equations (see Gibson and Rodi (1978) and Launder et al. (1987) for example). Currently, however, the use of FRS closures has been limited to simple flows wherein reduced forms of the models and less computationally intensive numerical schemes are applicable. This is due to the computational intensity of solving seven transport equations, each of which contain complicated source terms, in addition to the mean flow equations.

Rodi (1976) proposed an approximation which reduces the modelled incompressible full Reynolds stress (FRS) equations to algebraic form. Specifically, he presented the FRSM of Launder et al. (1975), equation [1.7], and proposed the following approximation :

$$\frac{D\overline{u_i'u_j'}}{Dt} - D_{ij} = \frac{\overline{u_i'u_j'}}{k}\left(\frac{Dk}{Dt} - D_k\right) = \frac{\overline{u_i'u_j'}}{k}(P - \varepsilon) \qquad [1.8]$$

where D_k represents the viscous diffusion term in the turbulence kinetic energy equation (1/2 the trace of equation [1.7]). This approximation assumes that the convective and diffusive transport of individual Reynolds stress components are locally proportional to transport of turbulent kinetic energy, the constant of proportionality being the local ratio of the Reynolds stress component to the turbulent kinetic energy. This simplification reduces the system of six non-linear Reynolds stress partial differential equations to a system of six non-linear algebraic equations in the six unknown stresses. The advantage to such an approach is that solution of the algebraic systems should be less computationally intensive, though solution of a 6 x 6 system of non-linear algebraic equations at every grid point, at every iteration, can be computationally intensive. Also, transport equations for k and ε must be solved in order to provide the values which appear in equation [1.8].

In this thesis, a low Reynolds number form of the k-ε model is used. The particular model chosen is a three-dimensional, compressible extension to a model proposed by Chien (1982). This model was one of four low Reynolds number models deemed to perform well in the prediction of a variety shear layer flows, in a recent review article by Patel et al. (1985). The formulation for this model is presented in equations [2.10] - [2.12]. Also, a hybrid low Reynolds number k-ε/high Reynolds number ARS model has been developed and applied. One of the goals of this thesis work has been to compute the flow in a centrifugal compressor. It was felt that for adequate resolution of the strong secondary motions in such machines, a low Reynolds number k-ε model would be significantly more appropriate than a mixing length model or a high Reynolds number form with wall functions. Application of the model adopted to the complex geometries in impellers, and all turbomachinery applications, is relatively straightforward. Additionally, as second order closures are adopted in the code, transport equations for k and/or ε need to be solved anyway, so the implementation, stability and application results presented in this thesis are directly relevant to incorporation of ARS and FRS closures.

The flow in centrifugal compressors and pumps provide one of the most challenging problems available to internal flow aerodynamicists. The complex three-dimensional physics in all of these machines has defied accurate prediction to date. The real flow in an impeller is drastically different from the desirable inviscid flow arising from the influence of curvature and rotation on rotor streamtubes in the absence of shear. A dominant boundary layer separation, or "wake" appears in many radial and mixed flow centrifugals, which alters strikingly the flow structure in the radial section of the impeller. A variety of strong secondary flows develop and interact due to the influence of centrifugal and coriolis forces on blade and endwall shear layers. Curvature and rotation also influence local turbulence intensity levels, thereby affecting the structure of developing boundary layers. Tip clearance flows and unsteady impeller-diffuser interactions introduce additional anomalies to an already complex passage flow. Additionally, there can be compressibility effects, even shock surfaces in the passage. Regions of flow reversal can be present at off design operation. In short, the complete physics involved are highly complex, and therefore, Navier-Stokes analyses to date have provided only qualitative accuracy.

Full Navier-Stokes procedures have been implemented to compute centrifugal compressor flows by several researchers recently (refer to Dawes (1988), Choi and Knight (1989), Goto (1990), Bansod and Rhie (1990), Hah and Krain (1989), Dorney and Davis (1990)). Most of these researchers have extracted qualitative comparison with experimentally obtained pressure distributions, and typically provide reasonable performance parameter trends (with varying mass flow rate or tip clearance gap for instance). Very popular is the use of solution contour plots of meridional velocity and relative stagnation pressure, and cross flow velocity vector plots. Such numerical simulation results provide insight into the variety of complex flow phenomena which exist in these machines, and substantiate the ability of Navier-Stokes procedures to qualitatively model these physics. However, direct comparison of predicted mean internal passage flow properties to measured results are consistently not provided, since quantitatively, predictions are generally poor. Additionally, only two of these works (Choi and Knight (1989), Hah and Krain (1989)) have adopted the degree of turbulence modelling complexity of a low Reynolds number two-equation model.

In the last chapter of this thesis, the results and interpretation of a transonic impeller computation is provided. Direct comparisons of predicted meridional velocities are made with L2F measurements due to Krain (1988). Relative helicity density is introduced as an excellent parameter for interpretation of secondary flow development. Extensive physical interpretation is provided for a solution in which the low Reynolds number k-ε model is used. Additionally, results using a hybrid low Reynolds number k-ε/ARS model are presented which indicate that although meridional mean flow is not significantly influenced by the modelling choice, cross flows, wall shear stress and machine performance parameters are.

The choice of an explicit numerical procedure in conjunction with a low Reynolds number k-ε model is not without its consequences. Specifically, nearly as well documented as the accuracy advantages of using low Reynolds number form k-ε models over algebraic eddy viscosity models, are the perceived numerical disadvantages, and thereby the unpopularity, of implementing two-equation models in time-marching Navier-Stokes procedures (Coakley (1983), for example). For these reasons, algebraic eddy viscosity models are often used to approximate the apparent stresses in CFD codes, since these models have little computational overhead and do not adversely affect the stability of the scheme. When transport models are used, the numerical stiffness associated with implicit and explicit computation of the Navier-Stokes and turbulence transport equations on the highly stretched grids required by low Reynolds number two-equation models has prompted researchers to adopt a variety of strategies to obtain convergent solutions. Wall functions (Eliasson (1988), Grasso and Speziale (1989), Holmes and Connell (1989) for instance), require less near wall grid clustering and bridge much of the inner region of the boundary layer, where turbulence source terms are large. Liu (1987) has used a hybrid approach, where an algebraic Van-Driest damping model is used to model the near-wall physics, thereby also relieving these two stability constraints. Pointwise implicit source term treatment has been used in implicit (Coakley (1983), Sahu and Danberg (1986), Martelli and Michelassi (1990)) and explicit (Liu (1987), Gerolymos (1990), Mavriplis and Martinelli (1991)) codes. Common to all of these approaches is their success in predicting a variety of complex turbulent flows in convergent fashion. In addition, most of these researchers cite the need for ad hoc stabilization procedures in the early stages of iteration where source terms can be very large if the flow is initialized in a simple fashion.

The above considerations have motivated the comprehensive stability investigation provided in Chapter 3 of this thesis, in which the stability of the turbulence model is one of the emphasized items. The author is familiar with two attempts in the literature to analyze the stability of the discrete k-ε equations. Liu (1987), analyzed the 2D "uncoupled" (see terminology discussion in Chapter 3), two-equation k-ε system and provided an expression for a local timestep based on implicit source term treatment using a 2-stage Runge-Kutta procedure. Eliasson (1988) provided a VonNeumann analysis of the coupled five equation incompressible 2D Navier-Stokes/k-ε system. In his work, the influence of turbulence production on the stability of the scheme was neglected. Eliasson thereby obtained the result that the remaining dissipation terms effectively provide damping to the scheme. He reconciles this result with the observation that it is not necessary to add fourth order artificial dissipation to the k or ε equations, which has also been the experience of this author. Though this neglect of production with respect to dissipation in the stability analysis may be useful when using wall functions, as Eliasson did, it was felt that it would not be appropriate to adopt this simplification in the present work. In Chapter 3, much more general stability results are obtained than by these authors, and numerical verification studies are performed to corroborate these analyses.

The explicit flow solver used for the numerical studies included in this thesis was written and developed by the author and is described briefly here. The code is a structured H-grid, explicit, compressible, 3D, full Navier-Stokes flow solver which incorporates a compressible low Reynolds number k-ε model. Inlet characteristic boundary conditions, system rotation and periodic boundaries are available to accommodate turbomachinery applications. Euler and periodic boundaries consistent with either rectilinear or annular geometries are available. The modified eigenvalue and velocity artificial dissipation scalings presented in Chapter 3 are implemented. An algebraic Reynolds stress model which may be hybrid with the low Reynolds number k-ε model is available in the code. Code performance issues are discussed in Chapter 3.

In Chapter 2, the governing equations for the mean flow and turbulence models are provided. Chapter 3 provides details of the spatial and temporal discretization procedures used. This includes the introduction of a compact central finite difference flux evaluation scheme which eliminates the metric singularity at the interface between solid and periodic boundaries, often attributed to finite difference procedures. Also included in Chapter 3 are extensive analyses and discussion of artificial dissipation issues which arise in the high Reynolds number viscous flow computations of interest in this thesis. The motivation and stability implications of numerically coupling the turbulence transport equations to the mean flow equations are then analyzed and discussed. Next, a vector VonNeumann analysis of the seven discrete, numerically coupled governing equations is undertaken, and some local stability results obtained. Order of magnitude arguments and numerical verification experiments are applied to these results from which some conclusions of relevance to the engineering analyst are drawn. ARSM numerical implementation and stability results, as well as overall code performance issues are also presented in Chapter 3.

Chapter 4 provides turbulence modelling validation and two-dimensional cascade computations. Results and interpretation are included for a supersonic compressor cascade operating at unique incidence, and a low subsonic double-circular-arc cascade with mean flow reversal. The flowfields within each of these have been investigated experimentally, and these results are used for comparison. In Chapter 5, the three-dimensional methodology is applied to a turbulent duct flow for which CFD validation-quality experimental data is available. Also, results of a large scale three-dimensional compressor rotor flow computation are presented. This Navier-Stokes solution is compared with a variety of rotor and wake flowfield measurements, and extensive interpretation is provided. As mentioned above, Chapter 6 details the computation of a centrifugal compressor flowfield using the present method.

Chapter 7 summarizes the conclusions arrived at in this thesis. The range and applicability of the methodologies presented are also discussed there, as are limitations and suggestions for further study.

CHAPTER 2

THEORETICAL FORMULATION

2.1 Favre Averaged Governing Equations

In the present development, the density-weighted time-averaging developed by Favre (1965) is used. This decomposition has advantages in flow computations with variable density (see Jones (1980)). Specifically, the averaged governing equations are of simpler form and the physical interpretation of terms in the equations is clearer than when conventional time averaging is used. Reynolds (time) averaging, defined for a scalar, ϕ, as

$$\phi = \bar{\phi} + \phi' \text{ , where } \bar{\phi} = \lim_{t \to \infty} \frac{1}{t} \int_{t_0}^{t_0+t} \phi \, ds \qquad [2.1]$$

is used for pressure, density, molecular stress tensor and molecular heat flux vector. Favre (density-weighted time) averaging, defined for scalar, ϕ, as

$$\phi = \tilde{\phi} + \phi'' \text{ , where } \tilde{\phi} = \frac{\overline{\rho\phi}}{\bar{\rho}} \text{ ,} \qquad [2.2]$$

is used for velocity components, internal energy, turbulent kinetic energy and turbulent energy dissipation rate.

2.1.1 Mean Flow Equations

Applying the density-weighted time-averaging procedure to the continuity, momentum and energy equations allows one to write the five mean flow equations in conservation form, in cartesian tensor notation, as :

$$\frac{\partial \bar{\rho}}{\partial t} + \frac{\partial}{\partial x_j}\left(\bar{\rho}\tilde{u}_j\right) = 0$$

$$\frac{\partial\left(\bar{\rho}\tilde{u}_i\right)}{\partial t} + \frac{\partial}{\partial x_j}\left(\bar{\rho}\tilde{u}_i\tilde{u}_j\right) = -\frac{\partial \bar{p}}{\partial x_i} + \frac{\partial}{\partial x_i}\tau_{ij} - \bar{\rho}\varepsilon_{ijk}\omega_j\varepsilon_{klm}\omega_l x_m - \bar{\rho}2\varepsilon_{ijk}\omega_j\tilde{u}_k$$

$$\frac{\partial\left(\bar{\rho}\tilde{e}_{0R}\right)}{\partial t} + \frac{\partial}{\partial x_j}\left(\bar{\rho}\tilde{I}\tilde{u}_j\right) = \frac{\partial}{\partial x_j}\left(\tilde{u}_j\tau_{ij} - q_i\right) \qquad [2.3]$$

where the effective stress tensor and effective heat flux vector are given by :

$$\tau_{ij} = \tau_{lij} - \overline{\rho u_i'' u_j''} \quad ,$$

$$q_i = q_{il} + \overline{\rho u_i'' e''} \quad . \qquad [2.4]$$

with :

$$\tau_{lij} = \mu_l\left[\left(\frac{\partial \tilde{u}_i}{\partial x_j} + \frac{\partial \tilde{u}_j}{\partial x_i}\right) - \frac{2}{3}\delta_{ij}\frac{\partial \tilde{u}_k}{\partial x_k}\right]$$

$$q_{il} = -\ \gamma\frac{\mu_l}{Pr_l}\frac{\partial \tilde{e}}{\partial x_i}. \qquad [2.5]$$

All velocity components in equations [2.3] - [2.5] are relative to a reference frame rotating with constant angular velocity, ω_i (s^{-1}). In the following developments, ω is taken, without loss of generality, to be coincident with the x-axis. The particular choice of energy variable, $\bar{\rho}\tilde{e}_{0R} = \bar{\rho}\tilde{e} + \bar{\rho}\tilde{W}^2/2 - \bar{\rho}\omega^2 r^2/2$, has the advantage that for the inviscid only problem, the steady state converged energy equation reduces to a statement of conservation of rothalpy, $\tilde{I}$, along streamlines. The apparent body force terms, which arise in the momentum equations due to system rotation, are linear in relative velocity, and therefore do not introduce additional stresses due to the density-weighted time-averaging procedure. In the derivation of equation [2.3], it has been assumed that the time averaged molecular stress tensor and the molecular heat flux vector are equivalent to their density-weighted time averaged values. This approximation should be a good one since, compared to turbulent diffusion, molecular diffusion is only significant near solid boundaries, where local Mach number and hence density fluctuations are small. For the compressible flows considered in this thesis, a perfect gas equation of state is provided as $\bar{p} = \bar{\rho} R \tilde{T}$, where $\tilde{T} = \frac{1}{c_v}\left(\tilde{e}_{0R} - \frac{\tilde{W}^2}{2} + \frac{\omega^2 r^2}{2}\right)$. It is further noted that by definition of the energy transport variable used, $e_{0R} \equiv e + \frac{W^2}{2} - \frac{\omega^2 r^2}{2}$, Favre averaging gives rise to a turbulence energy term, ie. $\tilde{e}_{0R} \equiv c_v \tilde{T} + \frac{\tilde{W}^2}{2} + \tilde{k} - \frac{\omega^2 r^2}{2}$, where turbulent kinetic energy is defined as $\tilde{k} \equiv \frac{\frac{1}{2}\overline{\rho u_i'' u_i''}}{\bar{\rho}}$. Strictly, this term should be accomodated in pressure and temperature terms in the inviscid flux vectors in the momentum equation and in the viscous flux vectors in the energy equation. These terms are usually neglected in the literature and in this thesis, though Wilcox (1991) has pointed out that these terms become important above local Mach numbers near 3.

2.1.2 Eddy Diffusivity Approximations

Equations [2.3] contain unknown correlated fluctuation quantities which arise from averaging the nonlinear convection operators in the momentum and energy equations. Eddy viscosity models employ a Boussinesq (1877) approximation, where the Reynolds stress tensor, $-\rho u_i'' u_j''$, is assumed to be linearly proportional to the strain rate tensor :

$$-\overline{\rho u_i'' u_j''} = \mu_t\left[\left(\frac{\partial \tilde{u}_i}{\partial x_j} + \frac{\partial \tilde{u}_j}{\partial x_i}\right) - \frac{2}{3}\delta_{ij}\frac{\partial \tilde{u}_k}{\partial x_k}\right] - \frac{2}{3}\delta_{ij}\bar{\rho}\tilde{k} \qquad [2.6]$$

where an eddy viscosity, μ_t, has been introduced. This is one of the approaches taken in the present work.

Analogous to assuming a linear relationship between apparent stress and velocity gradient, a gradient diffusion hypothesis is adopted which assumes a linear relationship between apparent heat flux, $\overline{\rho u_i'' e''}$, and internal energy gradient :

$$\overline{\rho u_i'' e''} = -\gamma\, \mu_{t\ \mathrm{energy}} \frac{\partial \tilde{e}}{\partial x_i},$$

or introducing a turbulent Prandtl number, $Pr_t = \mu_t/\mu_{t\ \mathrm{energy}}$,

$$\overline{\rho u_i'' e''} = -\gamma \frac{\mu_t}{Pr_t}\frac{\partial \tilde{e}}{\partial x_i} \qquad [2.7]$$

The effective stress tensor and effective heat flux vector provided in equation [2.4] can now be written :

$$\tau_{ij} = \tau_{lij} - \overline{\rho u_i'' u_j''} = (\mu_l + \mu_t)\left[\left(\frac{\partial \tilde{u}_i}{\partial x_j} + \frac{\partial \tilde{u}_j}{\partial x_i}\right) - \frac{2}{3}\delta_{ij}\frac{\partial \tilde{u}_k}{\partial x_k}\right] - \frac{2}{3}\delta_{ij}\bar{\rho}\tilde{k},$$

$$q_i = q_{il} + \overline{\rho u_i'' e''} = -c_p\left(\frac{\mu_l}{Pr_l} + \frac{\mu_t}{Pr_t}\right)\frac{\partial \tilde{T}}{\partial x_i}, \qquad [2.8]$$

where $\tilde{e}$ has been replaced by $c_v\tilde{T}$. In the present work, air is used as the working fluid in all test cases. Accordingly, the laminar Prandtl number, Pr_l, is set to 0.72. The turbulent Prandtl number, Pr_t, is set to a value of 0.91 (Cebici (1970) for example).

To close the system of governing equations, [2.3], it remains to obtain the spatial distribution of eddy viscosity and turbulent kinetic energy.

2.1.3 Turbulence Transport Model

In low Reynolds number k-ε turbulence models, the eddy viscosity is obtained from the Prandtl-Kolmogorov relation :

$$\mu_t = \frac{C_\mu f_\mu \bar{\rho}\, \tilde{k}^2}{\tilde{\varepsilon}} \qquad [2.9]$$

where the turbulent kinetic energy is defined as $\tilde{k} \equiv \frac{\frac{1}{2}\overline{\rho u_i'' u_i''}}{\bar{\rho}}$, the homogeneous component of the turbulence energy dissipation rate is defined as $\tilde{\varepsilon} \equiv \frac{\overline{\nu \rho \frac{\partial u_i''}{\partial x_j} \frac{\partial u_i''}{\partial x_j}}}{\bar{\rho}}$, $C_\mu \equiv 0.09$ (obtained empirically (Launder ans Spalding (1974))) and f_μ is a damping function to accommodate the direct influence of solid boundary proximity on the local turbulence structure.

In general, low-Reynolds number forms of the k-ε model can be Favre averaged and cast in conservation form for compressible flows as (see Coakley (1983), Narayan (1991) for example) :

$$\frac{\partial\left(\widetilde{\overline{\rho k}}\right)}{\partial t} + \frac{\partial}{\partial x_j}\left(\widetilde{\overline{\rho k}}\tilde{u}_j\right) = \frac{\partial}{\partial x_j}\left[\left(\mu + \frac{\mu_t}{Pr_k}\right)\frac{\partial \tilde{k}}{\partial x_j}\right] + P - \widetilde{\overline{\rho \varepsilon}} + \mathbf{D}$$

$$\frac{\partial\left(\widetilde{\overline{\rho \varepsilon}}\right)}{\partial t} + \frac{\partial}{\partial x_j}\left(\widetilde{\overline{\rho \varepsilon}}\tilde{u}_j\right) = \frac{\partial}{\partial x_j}\left[\left(\mu + \frac{\mu_t}{Pr_\varepsilon}\right)\frac{\partial \tilde{\varepsilon}}{\partial x_j}\right] + \left(f_1 C_1 P - f_2 C_2 \widetilde{\overline{\rho \varepsilon}}\right) + \mathbf{E} \qquad [2.10]$$

where production of turbulent kinetic energy is defined as :

$$P = -\overline{\rho u_i'' u_j''}\frac{\partial \tilde{u}_i}{\partial x_j} = \left\{\mu_t\left[\left(\frac{\partial \tilde{u}_i}{\partial x_j} + \frac{\partial \tilde{u}_j}{\partial x_i}\right) - \frac{2}{3}\delta_{ij}\frac{\partial \tilde{u}_k}{\partial x_k}\right] - \frac{2}{3}\delta_{ij}\widetilde{\overline{\rho k}}\right\}\frac{\partial \tilde{u}_i}{\partial x_j} \qquad [2.11]$$

and Pr_k, Pr_ε, f_1, f_2, C_1, C_2, $\mathcal{D}$, and $\mathcal{E}$ are modelling parameters.

The particular form of low Reynolds number model used in the code was originally devised by Chien (1982) for incompressible flow. For this model, the constants and functions in equations [2.9] and [2.10] are given by :

$$Pr_k = 1.0\ ,\ Pr_\varepsilon = 1.3$$

$$f_\mu = 1 - \exp(-.0115y^+)\ ,\ f_1 = 1\ ,\ f_2 = 1 - \frac{2}{9}\exp(-R_T^2/36)$$

$$C_\mu = 0.09\ ,\ C_1 = 1.35\ ,\ C_2 = 1.80$$

$$\mathcal{D} = -\frac{2\mu_l\tilde{k}}{l^2}\ ,\ \mathcal{E} = -\frac{2\mu_l\tilde{\varepsilon}}{l^2}\exp(-.5y^+)$$

$$R_T = \frac{\bar{\rho}\,\tilde{k}^2}{\mu_l\tilde{\varepsilon}}\ ,\ y^+ = \frac{\bar{\rho}\,l u^*}{\mu_l}\ ,\ u^* = \sqrt{\frac{\bar{\tau}_w}{\bar{\rho}}} \qquad [2.12]$$

In turbomachinery blade row computations, ξ corresponds to the streamwise coordinate, η to the pitchwise coordinate, and ζ to the spanwise coordinate. The wall proximity length scale, l, used in equations [2.12], accounts for the influence of adjacent walls (such as blade-endwall corners), and is defined as $l = \dfrac{1}{\dfrac{1}{l_{\eta\ ss}} + \dfrac{1}{l_{\eta\ ps}} + \dfrac{1}{l_{\zeta\ hub}} + \dfrac{1}{l_{\zeta\ shroud}}}$, where l_η and l_ζ are absolute distances from solid boundaries in the two crossflow directions. Upstream and downstream of blade rows, l_η is replaced by absolute distance from leading or trailing edge, respectively. In tip clearance gap regions, $l_{\zeta\ hub}$ is replaced by $l_{\zeta\ tip}$.

In high Reynolds number k-ε models, the dissipation variable, $\tilde{\varepsilon}$, is the dissipation rate in homogeneous turbulence, $\tilde{\varepsilon} \equiv \dfrac{\overline{\nu\rho \dfrac{\partial u_i''}{\partial x_j} \dfrac{\partial u_i''}{\partial x_j}}}{\bar{\rho}}$. The transport variable, $\tilde{\varepsilon}$, used in Chien's and certain other low Reynolds number k-ε models is the isotropic component of the dissipation. As discussed by Jones and Launder (1972), at high local Reynolds numbers, the non-isotropic component of dissipation is negligible, so the model remains valid in these regions. Near a solid wall, however, the dissipation is not negligible, though the isotropic component of the dissipation goes to zero. The term, $\mathcal{D}$, accounts for the non-zero value of total dissipation near the wall, so that the model also remains valid near solid boundaries, but the convenience of specifying an $\tilde{\varepsilon} = 0$ Dirichlet condition is retained. Specifically, then, $\mathcal{D}$ represents viscous diffusion of turbulence kinetic energy at the wall, which is in balance with dissipation there. Some numerical stability implications of this choice of dissipation variable are presented in Chapter 3.

Since the k-ε equations have been cast in compressible form, the direct influence of the dilitation terms in equations [2.8] and [2.11] are incorporated. However, the other modelling assumptions invoked in this thesis are essentially those for incompressible flow. Specifically, terms in the unmodelled ε equation which contain density fluctuation terms, ρ', are neglected. The unmodelled, Favre averaged $\tilde{\varepsilon}$ equation is extremely complicated due to the presence of many terms which contain density fluctuations. Jones (1980) points out that the physical interpretation of exact terms in the incompressible ε equation are not helpful in modelling the equation. He argues that there is, then, little point in trying to model the much more complicated exact equation, with varying density. Accordingly, most efforts to date to model the $\tilde{\varepsilon}$ equation, in compressible flows, have retained standard incompressible modelling.

For the density-weighted time-averaged turbulent kinetic energy equation, several researchers have chosen to explicitly model some of the extra terms which arise due to the Favre averaging procedure. Specifically, VanDromme (1983) and Grasso and Speziale (1989) have modelled some or all of the extra pressure work correlation terms, dilitation, and density fluctuation terms which arise in the exact Favre averaged $\tilde{k}$ equation, to account for extra strain effects in mixing layer flows where buoyancy effects are important, and in supersonic adverse pressure gradient flows. Though the framework for incorporation of these types of corrections is available in a code using the Favre averaging procedure, no such modelling is employed in this work.

Stability implications and validation of the low Reynolds number k-ε model are provided in Chapters 3 and 4 respectively.

Anticipation of the computation of a centrifugal compressor flow (Chapter 6) required that no thin layer approximations be made in either the mean flow or turbulence transport equations.

2.1.4 Algebraic Reynolds Stress Model (ARSM)

A class of ARS models, [Rodi (1976), Galmes and Lakshminarayana (1984), Andersson and Nilsen (1989), for example] can be derived by application of equation [1.8] to modelled FRS models such as that given in equation [1.7], yielding the following general algebraic expressions for the six individual Reynolds stress components :

$$-\overline{u_i' u_j'} = -\frac{2}{3}\delta_{ij}k - kT_{ij}$$

where

$$T_{ij} = \frac{R_{ij}(C_r - C_3) + (P_{ij} - 2P\delta_{ij}/3)(1-C_2) + \phi_{ij,w}}{P + \varepsilon(C_1-1)}, \quad R_{ik} = -2\omega_p(\varepsilon_{ipj}\overline{u'_k u'_j} - \varepsilon_{kpj}\rho\overline{u'_i u'_j})$$

$$P_{ij} = (-\overline{u'_i u'_k}\frac{\partial u_j}{\partial x_k} - \overline{u'_j u'_k}\frac{\partial u_i}{\partial x_k}), \quad 2P = P_{ii} \qquad [2.13]$$

and the parameters C_r, C_1, C_2, C_3, $\phi_{ij,w}$ arise from the pressure strain correlation modelling in the particular FRSM chosen. R_{ij}, the production by rotation tensor, arises when the Reynolds stress transport equations are derived in a rotating coordinate system of angular velocity vector, ω_p.

A number of researchers [Launder et al. (1975), Galmes and Lakshminarayana (1984), Shih and Lumley (1986), Launder et al. (1987) for example] have proposed near wall modelling for FRS or ARS closures, which account for the influence of the wall on the pressure strain correlation, $\phi_{ij,w}$ (the so called "echo effect," which accounts for the damping of the wall normal velocity fluctuation and redistribution of its energy in the other two intensities), and/or very near wall viscous damping effects. In practical numerical computations, wall functions are often used in both FRS [Shih and Lumley (1986), Launder et al. (1987)] and ARS [Warfield and Lakshminarayana (1987), Zhang and Lakshminarayana (1990)] models to bridge the near wall region, thereby avoiding the necessity for viscous near wall modelling. Near wall pressure-strain modelling, though, is retained in boundary layer code computations using FRSM by Shih and Lumley (1986) and Launder et al. (1987), and an ARS version of Shih and Lumley's model due to Zhang and Lakshminarayana (1990). For full-scale Navier-Stokes computations of the type performed by Warfield and Lakshminarayana (1987) and of interest in this thesis, these terms are not retained, for two reasons. Firstly, available models for $\phi_{ij,w}$ involve many very complicated terms (Shih and Lumley (1986), Launder et al. (1987), for example). In full Navier-Stokes implementation, the computation of this term alone would significantly burden the overall CPU performance of the method. The second reason for the neglect of this near wall pressure strain term is its implicit incorporation in the hybrid modelling approach presented below.

In this thesis, a hybrid low Reynolds number k-ε model/high Reynolds number ARSM approach has been devised. In the fully turbulent region ($y^+ = O(10^2)$), a compressible extension to the high Reynolds number form of the ARSM due to Galmes and Lakshminarayana (1984) is adopted :

$$-\overline{\rho u_i'' u_j''} = -\frac{2}{3}\delta_{ij}\rho k - \rho k T_{ij}$$

where

$$T_{ij} = \frac{R_{ij}(2-C_2)/2 + (P_{ij} - 2P\delta_{ij}/3)(1-C_2)}{P + \rho\varepsilon(C_1-1)}, \quad R_{ik} = -2\omega_p(\,\varepsilon_{ipj}\overline{\rho u_k'' u_j''} - \varepsilon_{kpj}\overline{\rho u_i'' u_j''}\,)$$

$$P_{ij} = (-\overline{\rho u_i'' u_k''}\frac{\partial u_j}{\partial x_k} - \overline{\rho u_j'' u_k''}\frac{\partial u_i}{\partial x_k}), \quad 2P = P_{ii} \qquad [2.14]$$

where $C_1 = 1.5$, $C_2 = 0.6$.

In the near wall region (viscous sublayer and overlap regions), the low-Reynolds number form employed previously is used. This hybrid approach has the advantage that no near wall modelling is explicitly required for the ARSM used, but the influence of extra strain rates on Reynolds stress distributions are accommodated.

The matching point for the hybrid model is chosen as $y^+_{match} = 200$. The justification for this choice is as follows. As pointed out by Patel et al. (1985), the near wall shear stress damping provided by the f_μ functions in low Reynolds number k-ε formulations are designed to model the direct influence of molecular viscosity on the

Reynolds shear stresses. However, since Reynolds stresses are also damped due to the pressure-strain correlation ($\phi_{ij,w}$ above), and the damping constants in the f_μ function are obtained by empirical matching of simple shear flow data (Chien (1982)), f_μ implicitly accounts for near wall pressure strain, though it is only appropriately correlated for the viscous damping effects. In light of this and the choice in the present work to neglect near wall pressure strain modelling in the ARSM used, y^+_{match} was chosen as 200 since for Chien's model, f_μ has nearly reached its freestream value of 1.0 at this location ($f_\mu(y^+ = 200) = .90$).

The effective stress tensor then becomes for the ARSM :

$$\tau_{ij} = \mu_l \left[\left(\frac{\partial u_i}{\partial x_j} + \frac{\partial u_j}{\partial x_i} \right) - \frac{2}{3} \delta_{ij} \frac{\partial u_k}{\partial x_k} \right] \qquad - \rho k T_{ij} \qquad - \frac{2}{3} \delta_{ij} \rho k \qquad [2.15]$$

Equation [2.15] is used to evaluate viscous fluxes in the momentum and energy equations. The gradient diffusion approximation, equation [2.7], is retained for the heat flux terms in the energy equation. Stability implications and validation of the hybrid model are provided in Chapters 3 and 4, respectively.

2.1.5 Transformation of Governing Equations to Generalized Coordinates

In general, three-dimensional flow problems of engineering interest have physical boundaries which can be very complex. It is convenient in these circumstances to map the physical coordinates to a rectilinear computational space, (x, y, z) --> (ξ, η, ζ), as shown in Figure 2.1. In this thesis, such a transformation to generalized body fitted coordinates is applied to the seven governing equations [2.3], [2.10]. The resulting coupled, Favre (x, y, z) --> (ξ, η, ζ)

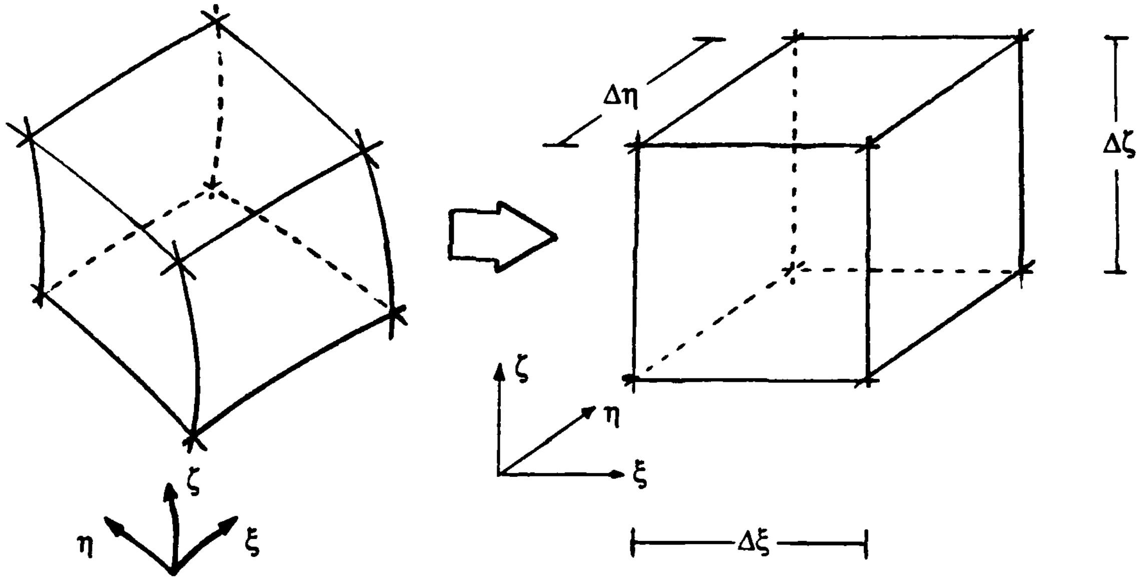
Δη
Δζ
ζ
η
ξ
Δξ
ζ
η
ξ

Figure 2.1 Coordinate Transformation Representation

averaged, three-dimensional, continuity, momentum, energy and k and ε equations can be written in conservative form in generalized body fitted coordinates as :

$$\frac{\partial \hat{Q}}{\partial t} + \left(\frac{\partial \hat{E}_c}{\partial \xi} + \frac{\partial \hat{F}_c}{\partial \eta} + \frac{\partial \hat{G}_c}{\partial \zeta} \right) = \left(\frac{\partial \hat{E}_v}{\partial \xi} + \frac{\partial \hat{F}_v}{\partial \eta} + \frac{\partial \hat{G}_v}{\partial \zeta} \right) + \hat{S} \qquad [2.16]$$

where

$$\hat{Q} = \frac{1}{J} \begin{pmatrix} \overline{\rho} \\ \overline{\rho}\tilde{u} \\ \overline{\rho}\tilde{v} \\ \overline{\rho}\tilde{w} \\ \overline{\rho}\widetilde{e_{0R}} \\ \overline{\rho}\tilde{k} \\ \overline{\rho}\tilde{\varepsilon} \end{pmatrix}, \quad \hat{E}_c = \frac{1}{J} \begin{pmatrix} \overline{\rho}\widetilde{U} \\ \overline{\rho}\tilde{u}\widetilde{U}+\xi_x\overline{p} \\ \overline{\rho}\tilde{v}\widetilde{U}+\xi_y\overline{p} \\ \overline{\rho}\tilde{w}\widetilde{U}+\xi_z\overline{p} \\ (\overline{\rho}\widetilde{e_{0R}}+\overline{p})\widetilde{U} \\ \overline{\rho}\tilde{k}\widetilde{U} \\ \overline{\rho}\tilde{\varepsilon}\widetilde{U} \end{pmatrix}, \quad \hat{F}_c = \frac{1}{J} \begin{pmatrix} \overline{\rho}\widetilde{V} \\ \overline{\rho}\tilde{u}\widetilde{V}+\eta_x\overline{p} \\ \overline{\rho}\tilde{v}\widetilde{V}+\eta_y\overline{p} \\ \overline{\rho}\tilde{w}\widetilde{V}+\eta_z\overline{p} \\ (\overline{\rho}\widetilde{e_{0R}}+\overline{p})\widetilde{V} \\ \overline{\rho}\tilde{k}\widetilde{V} \\ \overline{\rho}\tilde{\varepsilon}\widetilde{V} \end{pmatrix}, \quad \hat{G}_c = \frac{1}{J} \begin{pmatrix} \overline{\rho}\widetilde{W} \\ \overline{\rho}\tilde{u}\widetilde{W}+\zeta_x\overline{p} \\ \overline{\rho}\tilde{v}\widetilde{W}+\zeta_y\overline{p} \\ \overline{\rho}\tilde{w}\widetilde{W}+\zeta_z\overline{p} \\ (\overline{\rho}\widetilde{e_{0R}}+\overline{p})\widetilde{W} \\ \overline{\rho}\tilde{k}\widetilde{W} \\ \overline{\rho}\tilde{\varepsilon}\widetilde{W} \end{pmatrix}$$

$$\hat{E}_v = \frac{1}{J} \cdot \begin{pmatrix} 0 \\ \xi_x\tau_{xx}+\xi_y\tau_{yx} + \xi_z\tau_{zx} \\ \xi_x\tau_{xy}+\xi_y\tau_{yy} + \xi_z\tau_{zy} \\ \xi_x\tau_{xz}+\xi_y\tau_{yz} + \xi_z\tau_{zz} \\ \xi_x(\tilde{u}\tau_{xx}+\tilde{v}\tau_{xy}+\tilde{w}\tau_{xz}-q_x)+\xi_y(\tilde{u}\tau_{yx}+\tilde{v}\tau_{yy}+\tilde{w}\tau_{yz}-q_y)+\xi_z(\tilde{u}\tau_{zx}+\tilde{v}\tau_{zy}+\tilde{w}\tau_{zz}-q_z) \\ \left[\mu_l+\frac{\mu_t}{Pr_k}\right]\left[(\nabla\xi\cdot\nabla\xi)\frac{\partial\tilde{k}}{\partial\xi}+(\nabla\xi\cdot\nabla\eta)\frac{\partial\tilde{k}}{\partial\eta}+(\nabla\xi\cdot\nabla\zeta)\frac{\partial\tilde{k}}{\partial\zeta}\right] \\ \left[\mu_l+\frac{\mu_t}{Pr_\varepsilon}\right]\left[(\nabla\xi\cdot\nabla\xi)\frac{\partial\tilde{\varepsilon}}{\partial\xi}+(\nabla\xi\cdot\nabla\eta)\frac{\partial\tilde{\varepsilon}}{\partial\eta}+(\nabla\xi\cdot\nabla\zeta)\frac{\partial\tilde{\varepsilon}}{\partial\zeta}\right] \end{pmatrix}$$

$$\hat{F}_v = \frac{1}{J} \cdot \begin{pmatrix} 0 \\ \eta_x\tau_{xx}+\eta_y\tau_{yx} + \eta_z\tau_{zx} \\ \eta_x\tau_{xy}+\eta_y\tau_{yy} + \eta_z\tau_{zy} \\ \eta_x\tau_{xz}+\eta_y\tau_{yz} + \eta_z\tau_{zz} \\ \eta_x\left(\tilde{u}\tau_{xx}+\tilde{v}\tau_{xy}+\tilde{w}\tau_{xz}-q_x\right)+\eta_y\left(\tilde{u}\tau_{yx}+\tilde{v}\tau_{yy}+\tilde{w}\tau_{yz} -q_y\right)+\eta_z\left(\tilde{u}\tau_{zx}+\tilde{v}\tau_{zy}+\tilde{w}\tau_{zz} -q_z\right) \\ \left[\mu_l+\frac{\mu_t}{Pr_k}\right]\left[\left(\nabla\eta\cdot\nabla\xi\right)\frac{\partial\tilde{k}}{\partial\xi}+\left(\nabla\eta\cdot\nabla\eta\right)\frac{\partial\tilde{k}}{\partial\eta}+\left(\nabla\eta\cdot\nabla\zeta\right)\frac{\partial\tilde{k}}{\partial\zeta}\right] \\ \left[\mu_l+\frac{\mu_t}{Pr_\varepsilon}\right]\left[\left(\nabla\eta\cdot\nabla\xi\right)\frac{\partial\tilde{\varepsilon}}{\partial\xi}+\left(\nabla\eta\cdot\nabla\eta\right)\frac{\partial\tilde{\varepsilon}}{\partial\eta}+\left(\nabla\eta\cdot\nabla\zeta\right)\frac{\partial\tilde{\varepsilon}}{\partial\zeta}\right] \end{pmatrix}$$

$$\hat{G}_v = \frac{1}{J} \cdot \begin{pmatrix} 0 \\ \zeta_x\tau_{xx}+\zeta_y\tau_{yx} + \zeta_z\tau_{zx} \\ \zeta_x\tau_{xy}+\zeta_y\tau_{yy} + \zeta_z\tau_{zy} \\ \zeta_x\tau_{xz}+\zeta_y\tau_{yz} + \zeta_z\tau_{zz} \\ \zeta_x\left(\tilde{u}\tau_{xx}+\tilde{v}\tau_{xy}+\tilde{w}\tau_{xz}-q_x\right)+\zeta_y\left(\tilde{u}\tau_{yx}+\tilde{v}\tau_{yy}+\tilde{w}\tau_{yz} -q_y\right)+\zeta_z\left(\tilde{u}\tau_{zx}+\tilde{v}\tau_{zy}+\tilde{w}\tau_{zz} -q_z\right) \\ \left[\mu_l+\frac{\mu_t}{Pr_k}\right]\left[\left(\nabla\zeta\cdot\nabla\xi\right)\frac{\partial\tilde{k}}{\partial\xi}+\left(\nabla\zeta\cdot\nabla\eta\right)\frac{\partial\tilde{k}}{\partial\eta}+\left(\nabla\zeta\cdot\nabla\zeta\right)\frac{\partial\tilde{k}}{\partial\zeta}\right] \\ \left[\mu_l+\frac{\mu_t}{Pr_\varepsilon}\right]\left[\left(\nabla\zeta\cdot\nabla\xi\right)\frac{\partial\tilde{\varepsilon}}{\partial\xi}+\left(\nabla\zeta\cdot\nabla\eta\right)\frac{\partial\tilde{\varepsilon}}{\partial\eta}+\left(\nabla\zeta\cdot\nabla\zeta\right)\frac{\partial\tilde{\varepsilon}}{\partial\zeta}\right] \end{pmatrix}$$

$$\hat{S} = \frac{1}{J}\begin{pmatrix} 0 \\ 0 \\ \rho\omega(y\omega+2\tilde{w}) \\ \rho\omega(z\omega-2\tilde{v}) \\ 0 \\ P - \overline{\rho\tilde{\varepsilon}} + \mathcal{D} \\ \left(C_1f_1P - C_2f_2\overline{\rho\tilde{\varepsilon}}\right)\frac{\tilde{\varepsilon}}{\tilde{k}} + \mathcal{E} \end{pmatrix}. \qquad [2.17]$$

Components of the effective stress tensor, τ_{ij}, are defined in equations [2.8] and [2.15]. Metric terms in equations [2.17] are defined by

$$\begin{pmatrix} \xi_x & \eta_x & \zeta_x \\ \xi_y & \eta_y & \zeta_y \\ \xi_z & \eta_z & \zeta_z \end{pmatrix} = J \begin{pmatrix} y_\eta z_\zeta - z_\eta y_\zeta & y_\zeta z_\xi - z_\zeta y_\xi & y_\xi z_\eta - z_\xi y_\eta \\ x_\zeta z_\eta - z_\zeta x_\eta & x_\xi z_\zeta - z_\xi x_\zeta & x_\eta z_\xi - z_\eta x_\xi \\ x_\eta y_\zeta - y_\eta x_\zeta & x_\zeta y_\xi - y_\zeta x_\xi & x_\xi y_\eta - y_\xi x_\eta \end{pmatrix},$$

where the metric Jacobian

$$J = \det \begin{vmatrix} \xi_x & \xi_y & \xi_z \\ \eta_x & \eta_y & \eta_z \\ \zeta_x & \zeta_y & \zeta_z \end{vmatrix} \qquad [2.18]$$

In this thesis, equation [2.16], is solved numerically subject to appropriate boundary conditions, as detailed in the next chapter. For notational simplicity, averaging superscripts will be dropped hereafter.

CHAPTER 3

DEVELOPMENT AND ANALYSIS OF NUMERICAL PROCEDURES

3.1 Discretized Governing Equations

The numerical solution of the system of equations [2.16] subject to appropriate boundary conditions, is the topic of this chapter. The spatial and temporal discretization procedures adopted are presented first. An extensive discussion of artificial dissipation, including accuracy and stability implications on highly stretched grids, and the scalings incorporated is provided in section 3.2. Boundary and initial conditions for the turbomachinery flow computations of interest in this thesis are presented.

In the third section of this chapter, a comprehensive numerical stability analysis of the discrete, coupled system of seven governing equations is presented. Order of magnitude arguments are presented for flow and geometric properties typical of internal flows, including turbomachinery applications, to ascertain the relative importance of grid stretching, rotation and turbulence source terms and effective diffusivity on the stability of the scheme. It is demonstrated through both analysis and corroborative numerical experiments that 1) it is quite feasible to incorporate, efficiently, a two equation k-ε turbulence model in an explicit time marching scheme, provided certain numerical stability constraints are enforced; 2) the role of source terms due to rotation on the stability of the numerical scheme is negligible for rotation numbers typical of turbomachinery flow calculations; 3) the direct role of source terms in the turbulence transport equations on the stability of the explicit numerical scheme is negligible, except in the earliest stages of iteration (a result which is contrary to that generally perceived); 4) there is no advantage to numerically coupling the two equation model system to the mean flow equation system, in regard to convergence or accuracy; 5) for some flow configurations, including turbomachinery blade rows, it is useful to incorporate the influence of artificial dissipation in the prescription of a local timestep; and 6) explicit implementation of an algebraic Reynolds stress model (ARSM) is intrinsically stable provided that the discrete two-equation transport model which provides the necessary values of k and ε is itself stable.

3.1.1 Spatial Discretization, Flux Evaluation

A finite difference discretization (for evaluation of inviscid and viscous fluxes), which avoids the metric singularity at the interface between periodic and solid wall boundaries (i.e. H-grid leading and trailing edges) that occurs in standard finite difference approaches, has been adopted. This scheme, presented here, removes the ambiguity in metric evaluation at such boundaries, and results in a more compact differencing molecule at all grid points. In the present discussion, a two-dimensional formulation is presented for the purpose of brevity and clarity.

Consider a two-dimensional flux evaluation in the computational plane shown in Figure 3.1. When evaluating fluxes in the ξ direction, the derivatives $\frac{\partial \hat{E}_c}{\partial \xi}$, $\frac{\partial \hat{E}_v}{\partial \xi}$, may be discretized to second order as

$$\frac{\partial \hat{E}}{\partial \xi} = \frac{\hat{E}_{i+1,j} - \hat{E}_{i-1,j}}{2} \quad \text{or} \quad \frac{\partial \hat{E}}{\partial \xi} = \hat{E}_{i+1/2,j} - \hat{E}_{i-1/2,j} \qquad [3.1]$$

where $\Delta\xi \equiv 1$. The former gives rise to a 13 point differencing molecule in two-dimensions (33 point in three-dimensions) for the viscous fluxes.

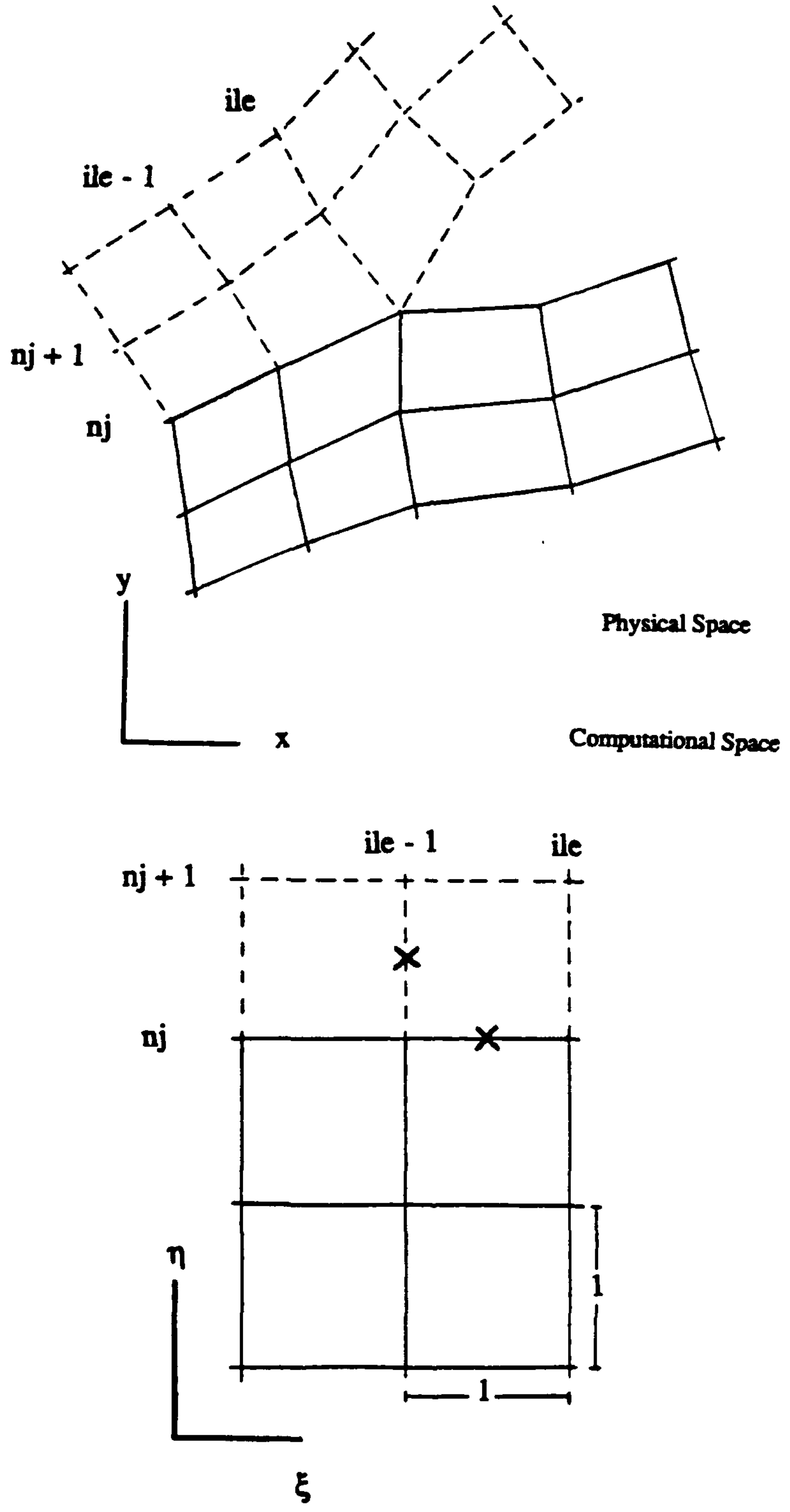
ile
ile - 1
nj + 1
nj
y
x
Physical Space
Computational Space
ile - 1
ile
nj + 1
nj
X
X
η
1
1
ξ

Figure 3.1 Two-dimensional representation of periodic leading edge grid topology in physical and computational space. Fluxes evaluated at X. Dashed lines represent grid in periodic adjacent passage.

Referring again to Figure 3.1, evaluation of $\widehat{E}_{c\ i+1/2,j}$ and $\widehat{E}_{v\ i+1/2,j}$ require values of the transport variables, pressure and effective diffusivities at i+1/2. These are obtained unambiguously by averaging values at i and i+1. However, if the metric terms required at i+1/2 are averaged in the same fashion, the metric ambiguity problem mentioned above manifests itself. To see this consider the evaluation of $\widehat{E}_{i+1/2,j}$ at ile-1 as illustrated in Figure 3.1. Straightforward averaging of metrics requires values of ξ_x, ξ_y, η_x and η_y at ile, where

$$\xi_x = Jy_\eta\ ,\ \xi_y = -Jx_\eta\ ,\ \eta_x = -Jy_\xi\ ,\ \eta_y = Jx_\xi\ ,\ J = \frac{1}{x_\xi y_\eta - x_\eta y_\xi} \qquad [3.2]$$

Here, x_ξ and y_ξ are not uniquely defined at i = ile, because either the suction or pressure side branch can be considered in evaluating $\frac{\partial}{\partial\xi}$. This difficulty is avoided, in the present technique, in that all metrics used in flux computations are evaluated halfway between grid points in the computational domain. Once again referring to Figure 3.1, at i+1/2, we have the metric quantities as defined in equation [3.2], where discretization at i+1/2 is given as :

$$\begin{aligned} x_{\xi\ i+1/2,j} &= x_{i+1,j} - x_{i,j}\ ,\ y_{\xi\ i+1/2,j} = y_{i+1,j} - y_{i,j} \\ x_{\eta\ i+1/2,j} &= .25^*(x_{i+1,j+1} - x_{i+1,j-1} + x_{i,j+1} - x_{i,j-1}) \\ y_{\eta\ i+1/2,j} &= .25^*(y_{i+1,j+1} - y_{i+1,j-1} + y_{i,j+1} - y_{i,j-1}) \end{aligned} \qquad [3.3]$$

Expressions similar to equation [3.3] are used to evaluate fluxes in the η and ζ directions at j+1/2 and k+1/2 respectively. This discretization is second order accurate. Extension of this procedure to three dimensions is straightforward.

The present approach requires more storage for metric terms than if the fluxes are computed on the grid vertices themselves (13 point molecule), however, the accuracy, convenient application of boundary conditions and numerical stability of the scheme, all suffer by using the larger differencing molecule when evaluating dissipation fluxes, so only the second form in equation [3.1] was considered. Specifically, the truncation error associated with discretizing the viscous fluxes on a uniform cartesian grid using a thirteen point scheme is $O(4\Delta x^{2}) + O(4\Delta y^{2})$ as compared to $O(\Delta x^{2}) + O(\Delta y^{2})$ for the nine point molecule, consistent with the truncation error of the convective fluxes. It is also easier and more consistent to apply cyclic differencing along periodic boundaries and Neumann conditions near the intersection of periodic and solid boundaries with the more compact differencing molecule. In addition, it can be shown (Merkle (1988)) that using the larger differencing molecule is equivalent to using the more compact form with added negative dissipation, that is, a destabilizing term.

3.1.2 Explicit Numerical Procedure

The numerical technique used for temporal discretization in the present studies incorporates a standard 4-stage Runge-Kutta scheme as first applied to Euler calculations by Jameson et al. (1981),

$$\begin{aligned} \hat{Q}^{1} &= \hat{Q}^{n} + \frac{1}{4}\Delta t\, \hat{R}(\hat{Q}^{n}) \\ \hat{Q}^{2} &= \hat{Q}^{n} + \frac{1}{3}\Delta t\, \hat{R}(\hat{Q}^{1}) \\ \hat{Q}^{3} &= \hat{Q}^{n} + \frac{1}{2}\Delta t\, \hat{R}(\hat{Q}^{2}) \\ \hat{Q}^{n+1} &= \hat{Q}^{n} + \Delta t\, \hat{R}(\hat{Q}^{3}) \end{aligned} \qquad [3.4]$$

Here, the residual, $\hat{R}$, is defined according to

$$\hat{R} = -\left(\frac{\partial \hat{E}_c}{\partial \xi} + \frac{\partial \hat{F}_c}{\partial \eta} + \frac{\partial \hat{G}_c}{\partial \zeta}\right) + \left(\frac{\partial \hat{E}_v}{\partial \xi} + \frac{\partial \hat{F}_v}{\partial \eta} + \frac{\partial \hat{G}_v}{\partial \zeta}\right) + \hat{S} \qquad [3.5]$$

Viscous and source terms are evaluated prior to the first stage, convective terms are computed at every stage. The scheme is first order accurate in time. The stability region for the scheme is shown in Figure 3.2.

The curve in Figure 3.2 represents the contour $|g(z)| = 1.0$, where z is the value of the complex Fourier symbol of any discretized scalar equation at a particular wave number, and g is the amplification factor arising from a 1-D scalar VonNeumann linear stability analysis of the given scheme applied to this discretized equation.

In Figure 3.3, an amplification factor vs. error phase plot is presented for this scheme applied to a scalar advection equation with a CFL number of $2\sqrt{2}$. Also, for comparison, the g vs. ϕ plot for a Lax-Wendroff scheme (1960) is presented where a typical CFL number of 0.85 was used. These CFL numbers are representative of those used in three-dimensional Navier-Stokes computations using the Lax-Wendroff scheme (Davis (1991)) and Runge-Kutta schemes. This diagram illustrates that the Runge-Kutta scheme provides no high wave number damping, whereas the Lax-Wendroff scheme intrinsically damps high wave number errors. This illustrates one of the characteristics of Runge-Kutta procedures. Specifically, artificial dissipation must be purposefully added to the scheme for stability, conceptually giving the user more control of its levels.

To accelerate the solution to steady state, locally varying timesteps are computed based on a linear stability analysis of the discretized Navier-Stokes equations. This linear stability analysis of the discrete coupled 7 x 7 system, is presented in section 3.3 of this chapter, and provides the following local timestep specification :

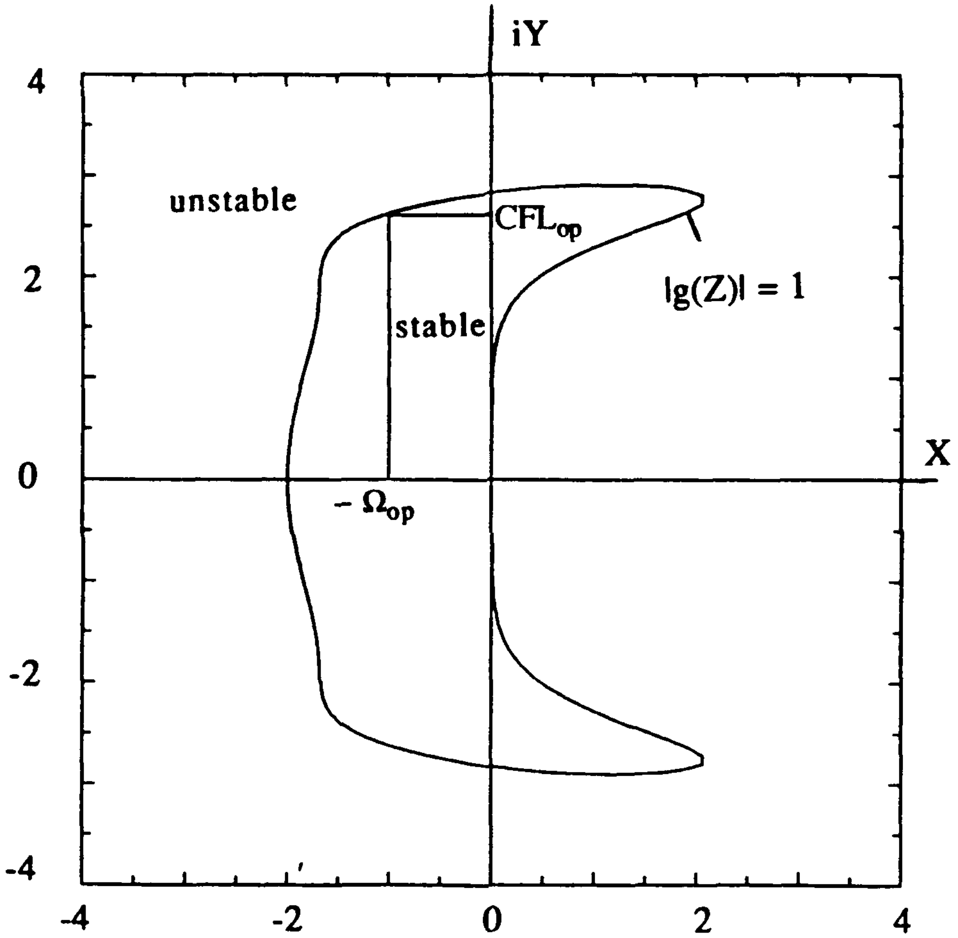

Figure 3.2 Stability boundary of Runge-Kutta scheme used in this thesis. The curve represents the contour $|g(Z)| = 1.0$, where Z is the complex Fourier symbol, $Z = X + iY$ of any discretized scalar equation at a particular wave number, and g is the amplification factor arising from a 1-D scalar VonNeumann linear stability analysis of the given scheme applied to this discretized equation.

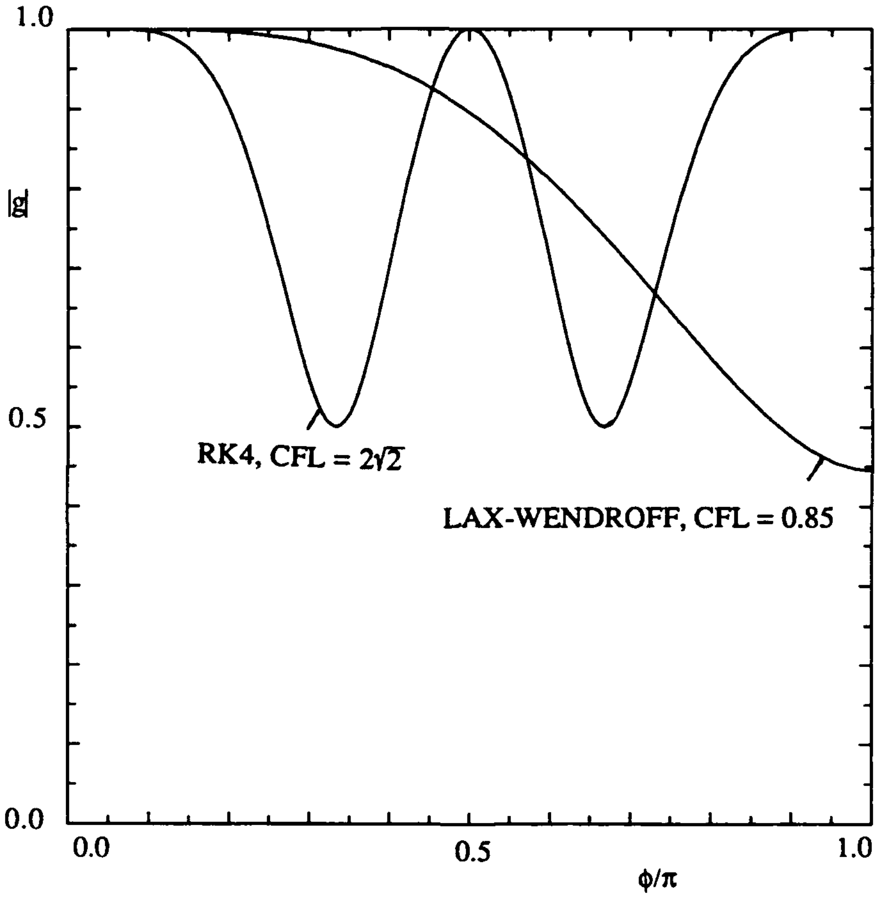

Figure 3.3 Amplification factor, |g|, vs. error phase, ϕ, plot for RK4 scheme applied to scalar advection equation. For comparison, the |g| vs. ϕ curve for the Lax-Wendroff scheme is also included.

$$\Delta t = \mathrm{MIN}\left[\Delta t_c\,,\Delta t_v\right] =$$

$$\mathrm{MIN}\Bigg[\frac{\mathrm{CFL_{op}}}{|U| + |V| + |W| + a\sqrt{(\nabla\xi\cdot\nabla\xi) + (\nabla\eta\cdot\nabla\eta) + (\nabla\zeta\cdot\nabla\zeta)}}\,,$$

$$\frac{\Omega_{op}}{\begin{array}{c}\frac{4\gamma}{\rho}\left(\frac{\mu_l}{\mathrm{Pr}_l} + \frac{\mu_t}{\mathrm{Pr}_t}\right)\left[(\nabla\xi\cdot\nabla\xi) + (\nabla\eta\cdot\nabla\eta) + (\nabla\zeta\cdot\nabla\zeta)\right] + \\ \frac{1}{3\rho}(\mu_l + \mu_t)\left[\begin{array}{c}\sqrt{(\nabla\xi\cdot\nabla\xi)(\nabla\eta\cdot\nabla\eta)} + \\ \sqrt{(\nabla\xi\cdot\nabla\xi)(\nabla\zeta\cdot\nabla\zeta)} + \sqrt{(\nabla\eta\cdot\nabla\eta)(\nabla\zeta\cdot\nabla\zeta)}\end{array}\right] \\ - 16(\sigma_\xi + \sigma_\eta + \sigma_\zeta)\end{array}}\Bigg] \qquad [3.6]$$

Here, $\mathrm{CFL_{op}}$ and Ω_{op} are input parameters corresponding to operational CFL and VonNeumann numbers chosen to ensure stability, and σ_ξ, σ_η and σ_ζ are general artificial dissipation scale factors, several possible forms of which are discussed in the next section. The first term in the brackets in equation [3.6] arises from the convection operators, the latter terms correspond to physical and artificial dissipation. The influence of machine rotation, turbulence quantities and nonorthogonality metrics do not appear in this stability specification, as justified by an order of magnitude analysis carried out in section 3.3 of this chapter.

3.1.3 Boundary and Initial Conditions

Along blade surfaces, the no-slip condition is imposed upon the velocities, pressure is extrapolated from adjacent grid points, and density is computed based on specified wall temperature or heat transfer rate. Also, turbulent kinetic energy and dissipation rate are set to zero along solid boundaries, as discussed in section 2.1.3.

Considering the ξ direction only, the inviscid form of equation [2.16], can be written, in the absolute frame, in nonconservative form as $\frac{\partial Q}{\partial t} = -J\hat{A}\frac{\partial Q}{\partial \xi}$, where $\hat{A}$ is the 7 x 7 flux Jacobian of vector $\hat{E}_c$, $\hat{A} = \frac{\partial \hat{E}_c}{\partial Q}$. The eigenvalues of $\hat{A}$ are $U, U, U, U, U, U + a\sqrt{\nabla\xi \cdot \nabla\xi}, U - a\sqrt{\nabla\xi \cdot \nabla\xi}$. This requires that for subsonic inlet flow six boundary conditions should be specified. Likewise, for subsonic exit flow one boundary condition should be specified.

Accordingly, at subsonic inflow boundaries, total temperature profile and constant values of turbulent kinetic energy and dissipation rate are specified. Following Kirtley et al. (1990), for the subsonic rotor flow computation presented in Chapter 5, and for the transonic centrifugal compressor computation presented in Chapter 6, inlet flow angles and the axial component of mass flux are specified, and the static pressure is extrapolated along η = constant grid lines from the interior of the computational domain. This allows the user to impose a desired operating flow coefficient almost exactly, without having to adjust exit static pressure so as to pass the appropriate mass flow to match the flow coefficient. For all other calculations, either flow angle or crossflow velocity components and total pressure profile are specified, and the R^- characteristic, $R^- \equiv V - \frac{2c}{\gamma - 1}$, is extrapolated along η = constant grid lines from the interior of the computational domain. Specifically, designating subscripts 1 and 2 for grid planes at and adjacent to the inlet boundary :

$$V_1 = \frac{(\gamma - 1)(R_2^-)^2 + \sqrt{2(1-\gamma)(R_2^-)^2 + 4(\gamma + 1)c_p T_{0\,2}}}{(\gamma + 1)} \qquad [3.7]$$

a result which is easily obtained using the definitions of total temperature and the left running Riemann variable.

At subsonic outflow boundaries, static pressure is specified and relative velocity components, entropy, ρk and $\rho\varepsilon$ are extrapolated along η = constant grid lines. For annular geometries, a simplified radial equilibrium equation :

$$\frac{\partial p}{\partial r} = \rho \frac{v_\theta{}^2}{r} \qquad [3.8]$$

is used to integrate a specified hub exit static pressure in the radial direction to provide the exit pressure distribution. Along periodic boundaries, values of the flowfield variables are prescribed along periodic "ghost" grid points and this information is used when discretizing derivatives in the η direction.

The constant values of ρk and $\rho\varepsilon$, which are imposed at the inflow boundary, are based on specified freestream turbulence intensity and length scale,

$$T_{u\infty} = \frac{\sqrt{\frac{2}{3}k_\infty}}{V_\infty}, \quad L_\infty = \frac{C_\mu k_\infty^{3/2}}{\varepsilon_\infty} \qquad [3.9]$$

Typically , the freestream length scale is set between .001 and .01 times the blade spacing, as this scale is of the same order as the largest eddy motions, i.e. the thickness of the boundary layers which develop along the blades and endwalls.

The flowfield is initialized using an inviscid quasi-1D analysis to provide uniform initial velocity profiles along each ξ = constant grid line. In situations where this simple initialization strategy has proven to be insufficient, alternative procedures are detailed in the following chapters.

3.2 Artificial Dissipation

When central difference schemes, which do not inherently damp high wave number errors, are applied to hyperbolic problems, the addition of artificial dissipation is required to damp high wave number disturbances. These disturbances can be introduced into linear problems through inconsistent boundary condition treatment or machine roundoff error. In non-linear problems, such disturbances can be introduced through aliasing of sub-grid scale non-linear disturbances, to lower, resolvable wave numbers. Even for viscous flow calculations, artificial dissipation must be introduced into the scheme because the physical viscous terms are only effective in damping frequencies at higher wave numbers than can be resolved on practical grids.

In the present work, artificial dissipation is added to the five discretized mean flow equations [3.5] as :

$$\hat{R} = -\left(\frac{\partial \hat{E}_c}{\partial \xi} + \frac{\partial \hat{F}_c}{\partial \eta} + \frac{\partial \hat{G}_c}{\partial \zeta}\right) + \left(\frac{\partial \hat{E}_v}{\partial \xi} + \frac{\partial \hat{F}_v}{\partial \eta} + \frac{\partial \hat{G}_v}{\partial \zeta}\right) + D(Q) + \hat{S} \qquad [3.10]$$

Here, D(Q) represents a mixed 2nd and 4th order nonconservative artificial dissipation operator similar to that devised by Jameson et al. (1981) :

$$D(Q) = D_\xi(Q) + D_\eta(Q) + D_\zeta(Q)$$

$$D_\xi(Q) = S_{2\xi}\delta_{\xi\xi}Q + S_{4\xi}\delta_{\xi\xi\xi\xi}Q$$

$$D_\eta(Q) = S_{2\eta}\delta_{\eta\eta}Q + S_{4\eta}\delta_{\eta\eta\eta\eta}Q$$

$$D_\zeta(Q) = S_{2\zeta}\delta_{\zeta\zeta}Q + S_{4\zeta}\delta_{\zeta\zeta\zeta\zeta}Q \qquad [3.11]$$

The fourth order operators are included to damp high wave number errors and the second order operators are included to improve shock capturing.

As pointed out by Pulliam (1986), artificial dissipation terms should operate on physical values of the flowfield variables, that is, $D(Q)$, as in equations [3.11], not $D(\hat{Q})$. This is required since in general, regions of smoothly varying flowfield properties can occur in regions of non-smooth grid distribution. Accordingly, the scale factors, S, in equations [3.11] should be scaled by the inverse of the metric Jacobian, J.

In addition to the above consistency requirement on the dissipation scaling, artificial dissipation should always be reduced to levels adequate to stabilize a scheme without altering the accuracy of the solution. For the computation of viscous flows on highly stretched grids, this requirement is a sensitive matter.

3.2.1 Eigenvalue Scaling

If flux split differencing is used for the convection operators, an inherent amount of artificial dissipation is introduced. It can be easily shown that flux split differencing schemes are equivalent to central differencing schemes with appropriately added artificial dissipation. Since Runge-Kutta schemes are intrinsically less dissipative than upwind schemes, it is attractive to purposefully add artificial dissipation to these schemes in a way as to provide the stability and shock capturing advantages of upwind schemes, while retaining control of its levels. Accordingly, flux split approaches can be used to "guide" the development of central difference artificial dissipation schemes [Pulliam (1986)], leading to what is referred to in this thesis as eigenvalue scaling.

By way of example, Pulliam (1986) shows that second order Steger-Warming (1981) flux vector splitting applied to the convection operator, $\frac{\partial E_c}{\partial x}$, is equivalent to a central difference plus a fourth order difference operating on Q. The coefficient of this operator is the flux Jacobian matrix, A (where $E_c = AQ$). This suggests the use of the spectral radius of matrix A as a scale factor in artificial dissipation operators applied to central difference schemes.

In explicit local time stepping schemes applied to inviscid problems, local timesteps are generally computed such that they are inversely proportional to the spectral radius of A, $\rho(A)$, or in multi-dimensions, some linear combination of the spectral radii of the several flux Jacobians. For this reason, most early workers (see Jameson et al. (1981) for example) scaled dissipation operators by $\rho(A) + \rho(B)$ (for two-dimensional Euler computations; $F_c = BQ$), or equivalently, by $\frac{1}{\Delta t}$ where $\Delta t = \frac{\Delta t_x \Delta t_y}{\Delta t_x + \Delta t_y}$. Here, Δt_x and Δt_y are inversely proportional to $\rho(A)$ and $\rho(B)$ respectively. From a flux split point of view, this says that the artificial dissipation is proportional to the propagation speed of the characteristic which limits the maximum stable local timestep. This approach has been widely used in multidimensional central difference inviscid flow computations where grids are relatively uniform.

For high Reynolds number flows, very highly stretched grids must be used to resolve body normal gradients in near wall regions. If the artificial dissipation terms in both the ξ and η directions are scaled by the local timestep on grids which are highly stretched in the η direction, excessive dissipation is introduced in the ξ direction. This effect is discussed by Caughey and Turkel (1988) and Swanson and Turkel (1987). This excessive dissipation may reduce accuracy and convergence rates in viscous flow computations. Martinelli (1987) recently devised a flux Jacobian eigenvalue scaling of the artificial dissipation terms which alleviates this problem. Since the present technique is primarily used to compute viscous flows on highly stretched grids, anisotropic dissipation scaling factors similar to those used by Martinelli are incorporated. In his two-dimensional work, Martinelli provided the following form for the scale factors in equation [3.11] (where the present finite difference notation is used) :

$$S_{2\xi} = \frac{\sigma_{2\xi}}{J}\left[\frac{1}{\Delta t_{c\xi}}\left(1 + \left(\frac{\Delta t_{c\xi}}{\Delta t_{c\eta}}\right)^{\alpha}\right)\right], \; S_{2\eta} = \frac{\sigma_{2\eta}}{J}\left[\frac{1}{\Delta t_{c\eta}}\left(1 + \left(\frac{\Delta t_{c\eta}}{\Delta t_{c\xi}}\right)^{\alpha}\right)\right]$$

$$S_{4\xi} = \frac{\sigma_{4\xi}}{J}\left[\frac{1}{\Delta t_{c\xi}}\left(1 + \left(\frac{\Delta t_{c\xi}}{\Delta t_{c\eta}}\right)^{\alpha}\right)\right], \; S_{4\eta} = \frac{\sigma_{4\eta}}{J}\left[\frac{1}{\Delta t_{c\eta}}\left(1 + \left(\frac{\Delta t_{c\eta}}{\Delta t_{c\xi}}\right)^{\alpha}\right)\right] \qquad [3.12]$$

Here, $\Delta t_{c\xi}$, $\Delta t_{c\eta}$, are timesteps corresponding to unit CFL limit for the inviscid one-dimensional problem in each direction,

$$\Delta t_{c\xi} = \frac{1}{|U| + a\sqrt{(\nabla\xi \cdot \nabla\xi)}}, \; \Delta t_{c\eta} = \frac{1}{|V| + a\sqrt{(\nabla\eta \cdot \nabla\eta)}} \qquad [3.13]$$

and $\sigma_{2\xi}$, $\sigma_{2\eta}$, $\sigma_{4\xi}$, $\sigma_{4\eta}$ are scalar coefficients discussed below.

The choice of unit CFL scaling in the numerator of equation [3.13] ensures that the steady state solution will be independent of the operational CFL number used to compute local timesteps. If $\alpha = 1$, equation [3.12] reduces to standard isotropic scaling. As mentioned above, this introduces excessive dissipation in the ξ direction in regions where the grid is stretched in the η direction. If $\alpha = 0$, the scaling becomes purely anisotropic. If the grid is very highly stretched in the η direction, such scaling may not provide enough dissipation in the ξ direction, resulting in reduced convergence rates. For intermediate values of α between 1/2 and 2/3, Martinelli (1987) and Swanson and Turkel (1987) have shown good convergence rates for Euler and Navier-Stokes calculations on highly clustered grids.

Careful examination of the scaling in equation [3.12], shows that if the coefficient, α, is reduced to zero (towards purely anisotropic scaling), local levels of artificial dissipation do decrease in the direction opposite that in which the grid is clustered, consistent with the arguments presented above. However, the dissipation levels in the direction of clustering actually increase. To see this, consider a two-dimensional grid element, stretched in the η direction, of aspect ratio 100. If this element lies within the boundary layer, where local velocity is small, the spectral radii of the flux Jacobians can be approximated by :

$$\rho(\hat{A}) = |U| + a\sqrt{\nabla\xi\cdot\nabla\xi} \cong a\sqrt{\nabla\xi\cdot\nabla\xi},\ \rho(\hat{B}) = |V| + a\sqrt{\nabla\eta\cdot\nabla\eta} \cong a\sqrt{\nabla\eta\cdot\nabla\eta}$$

The scaling [3.12] provides for $\alpha = 1$ (isotropic) :

$$S_\xi \cong a\sqrt{\nabla\xi\cdot\nabla\xi} + a\sqrt{\nabla\eta\cdot\nabla\eta} \cong 100\ \mathrm{K}$$

$$S_\eta \cong a\sqrt{\nabla\xi\cdot\nabla\xi} + a\sqrt{\nabla\eta\cdot\nabla\eta} \cong 100\ \mathrm{K}$$

where K is some constant, proportional to a constant length scale in the physical domain and the local speed of sound. If a purely anisotropic scaling is introduced, $\alpha = 0$:

$$S_\xi \cong 2a\sqrt{\nabla\xi\cdot\nabla\xi} \cong 2\ \mathrm{K}$$

$$S_\eta \cong 2a\sqrt{\nabla\eta\cdot\nabla\eta} \cong 200\ \mathrm{K}$$

that is, S_η doubles in magnitude, which substantiates the above argument. It has been the experience of the author, that in three-dimensional viscous computations, it is crucial to incorporate very low values of α, in order to obtain stable solutions ($\alpha = 0.1$ was used for the rotor flow computation presented in Chapter 5, for example). Accordingly, Martinelli's scaling, equation [3.12], has been modified and extended to three-dimensions in this work as follows :

$$S_{2\xi} = \frac{\sigma_{2\xi}}{J}\left[\frac{1}{\Delta t_{c\xi}}\left(1 + \frac{\Delta t_{c\xi}}{\Delta t_{c\eta}} + \frac{\Delta t_{c\xi}}{\Delta t_{c\zeta}}\right)^{\alpha}\right], \; S_{2\eta} = \frac{\sigma_{2\eta}}{J}\left[\frac{1}{\Delta t_{c\eta}}\left(1 + \frac{\Delta t_{c\eta}}{\Delta t_{c\xi}} + \frac{\Delta t_{c\eta}}{\Delta t_{c\zeta}}\right)^{\alpha}\right],$$

$$S_{2\zeta} = \frac{\sigma_{2\zeta}}{J}\left[\frac{1}{\Delta t_{c\eta}}\left(1 + \frac{\Delta t_{c\zeta}}{\Delta t_{c\xi}} + \frac{\Delta t_{c\zeta}}{\Delta t_{c\eta}}\right)^{\alpha}\right]$$

$$S_{4\xi} = \frac{\sigma_{4\xi}}{J}\left[\frac{1}{\Delta t_{c\xi}}\left(1 + \frac{\Delta t_{c\xi}}{\Delta t_{c\eta}} + \frac{\Delta t_{c\xi}}{\Delta t_{c\zeta}}\right)^{\alpha}\right], \; S_{4\eta} = \frac{\sigma_{4\eta}}{J}\left[\frac{1}{\Delta t_{c\eta}}\left(1 + \frac{\Delta t_{c\eta}}{\Delta t_{c\xi}} + \frac{\Delta t_{c\eta}}{\Delta t_{c\zeta}}\right)^{\alpha}\right],$$

$$S_{4\zeta} = \frac{\sigma_{4\zeta}}{J}\left[\frac{1}{\Delta t_{c\eta}}\left(1 + \frac{\Delta t_{c\zeta}}{\Delta t_{c\xi}} + \frac{\Delta t_{c\zeta}}{\Delta t_{c\eta}}\right)^{\alpha}\right] \qquad [3.14]$$

where :

$$\Delta t_{c\xi} = \frac{1}{|U| + a\sqrt{(\nabla\xi\cdot\nabla\xi)}}, \; \Delta t_{c\eta} = \frac{1}{|V| + a\sqrt{(\nabla\eta\cdot\nabla\eta)}}, \; \Delta t_{c\zeta} = \frac{1}{|W| + a\sqrt{(\nabla\zeta\cdot\nabla\zeta)}} \qquad [3.15]$$

If this scaling is applied to the example provided above, for $\alpha = 1$:

$$S_\xi \cong a\sqrt{\nabla\xi\cdot\nabla\xi} + a\sqrt{\nabla\eta\cdot\nabla\eta} \cong 100\ \mathrm{K}$$

$$S_\eta \cong a\sqrt{\nabla\xi\cdot\nabla\xi} + a\sqrt{\nabla\eta\cdot\nabla\eta} \cong 100\ K$$

identical to the original scaling, but for $\alpha = 0$:

$$S_\xi \cong a\sqrt{\nabla\xi\cdot\nabla\xi} \cong\ K$$

$$S_\eta \cong a\sqrt{\nabla\eta\cdot\nabla\eta} \cong 100\ K$$

That is, the modified anisotropic eigenvalue scaling, does not increase levels of dissipation in the direction of grid stretching. This modified scaling, published originally in Kunz and Lakshminarayana (1990) has been adopted by Chima (1991), who has also found this scaling to provide a "good distribution of dissipative terms in each direction", in three-dimensional viscous flow calculations.

If no shocks are anticipated in the flowfield, the scalar coefficients, σ, in equations [3.14] are defined as $\sigma_{4\xi} = \sigma_{4\eta} = \sigma_{4\zeta} = -\ \kappa_4$, where typically $\kappa_4 \cong 0.02$. If shocks are anticipated in the flowfield (see the supersonic cascade results in Chapter 4), a composite dissipation operator devised by Jameson et al. (1981) is used to turn off locally the fourth order central difference dissipation and turn on a second order central difference dissipation operator. In this case, the scalar coefficients, σ, in equations [3.14] take the following form :

$$\sigma_{2\xi} = \kappa_2\ \mathrm{MAX}\left(\nu_{\xi_{i+1,\ j,\ k}}, \nu_{\xi_{i,\ j,\ k}}, \nu_{\xi_{i-1,\ j,\ k}}\right)$$

$$\sigma_{4\xi} = -\ \mathrm{MAX}\left(0,\ \kappa_4 - \sigma_{2\xi}\right) \qquad [3.16]$$

where the dissipation "sensor" ν, is a normalized second derivative of pressure that is very small except in the immediate vicinity of shocks and stagnation points :

$$\nu_{\xi i,\, j,\, k} = \frac{\left| p_{i+1,\, j,\, k} - 2\, p_{i,\, j,\, k} + p_{i-1,\, j,\, k} \right|}{p_{i+1,\, j,\, k} + 2\, p_{i,\, j,\, k} + p_{i-1,\, j,\, k}} \qquad [3.17]$$

Here, $\kappa_2 \cong 0.25$, $\kappa_4 \cong 0.02$. Expressions similar to equations [3.16] and [3.17] are used in the η and ζ directions. When shocks are not anticipated in the flowfield, κ_2 is set equal to zero so that fourth difference artificial dissipation only is added to the mean flow.

The dissipation scaling issues presented so far are essentially inviscid in nature, in that eigenvalues of the inviscid flux Jacobians only are considered. As the computational grid in a Navier-Stokes solution is refined, smaller and smaller scales can be resolved. Eventually, the small length scales associated with nonlinear disturbances introduced by convection operators in the governing equations (shocks for instance) can be resolved, and the gradients that these disturbances give rise to can be effectively damped by physical dissipation. Accordingly, it is desirable that any variable artificial dissipation scaling should have the property that as the grid is refined, artificial dissipation goes to zero. This item is considered here; again a two-dimensional formulation is adopted for clarity.

If a cartesian physical grid is considered, with $\Delta x \cong \Delta y$, $\nabla\xi \cdot \nabla\xi = \xi_x^2$, $\nabla\eta \cdot \nabla\eta = \eta_y^2$ (ξ coincident with x-axis, η coincident with y-axis), then the scaling factors proposed in equations [3.14] take on the following forms for isotropic ($\alpha = 1$, subscript i) and anisotropic ($\alpha = 0$, subscript a) scalings :

$$S^0_{i\xi} = \frac{|U| + |V| + a\sqrt{\nabla\xi \cdot \nabla\xi} + a\sqrt{\nabla\eta \cdot \nabla\eta}}{J} = \Delta y_0(|u|+a) + \Delta x_0(|v|+a)$$

$$S^0_{i\eta} = \Delta y_0(|u|+a) + \Delta x_0(|v|+a)$$

$$\begin{aligned} S^0_{a\xi} &= \Delta y_0(|u|+a) \\ S^0_{a\eta} &= \Delta x_0(|v|+a) \end{aligned} \qquad [3.18]$$

where superscript 0 denotes the grid under consideration. If the grid is doubled n times in the η direction, with $n >> 1$, as would be representative near a solid boundary in a viscous flow computation, then denoting the refined grid by superscript 1, the scale factors become :

$$\begin{aligned} S^1_{i\xi} &= \Delta y_1(|u|+a) + \Delta x_0(|v|+a) = \frac{1}{2^n}\Delta y_0(|u|+a) + \Delta x_0(|v|+a) \cong \Delta x_0(|v|+a) \\ S^1_{i\eta} &\cong \Delta x_0(|v|+a) \\ S^1_{a\xi} &\cong \frac{1}{2^n}\Delta y_0(|u|+a) \\ S^1_{a\eta} &\cong \Delta x_0(|v|+a) \end{aligned} \qquad [3.19]$$

So clearly, as the grid is refined in one direction only, both isotropic and anisotropic scale factors remain finite as the grid is refined infinitely. However, $\delta_{\eta\eta\eta\eta}Q$ --> 0 as Δy --> 0, because, unlike the fourth derivative of a function Q, which may be large if Q is exponential in nature, the fourth difference stencil applied to Q will always tend to zero as the grid is refined for any continuous function Q. So the eigenvalue scaled artificial dissipation operators do have the desirable property that artificial dissipation goes to zero as the grid is refined, even if in only one direction, as is typical in high Reynolds number viscous flow computations.

A problem arises in viscous flow computations though, because the rate at which artificial dissipation goes to zero with grid refinement may not be adequate to keep levels of artificial dissipation significantly less than the physical dissipation very near a solid boundary. This is probably not surprising since all of the scalings presented are based on inviscid considerations only. This observation warrants additional boundary layer scaling such that artificial dissipation remain significantly less than physical dissipation through most of the boundary layer.

3.2.2 Local Velocity Scaling

Another scaling issue is important in the computation of viscous flows. Near solid boundaries, the viscous fluxes in the momentum equation are quite large and are themselves adequate to provide smoothing. As discussed above, in these same regions, second and fourth derivatives of the transport variables can be quite large leading to large values of artificial dissipation there. This phenomenon, which has been observed by several other researchers (Davis et al. (1986) and Swanson and Turkel (1987) for instance), can give rise to very large nonphysical values of total dissipation in the near wall region. It has been the experience of the present author, that in the momentum equations, the ratio of artificial to physical dissipation, i.e. $\hat{R}_{art}/\hat{R}_{phys}$, where $\hat{R}_{art} = D(Q)$, $\hat{R}_{phys} = \left(\frac{\partial \hat{E}_v}{\partial \xi} + \frac{\partial \hat{F}_v}{\partial \eta} + \frac{\partial \hat{G}_v}{\partial \zeta}\right)$, can be as high as $O(10^1)$, in the very near wall region if the grid is highly stretched locally! The accuracy implications of this are self-evident. Personal experience, and that of others (Kirtley (1990), Weiss (1991)), have shown non-physical overshoots of nearwall velocity profiles in converged viscous flow solutions on highly stretched grids, when artificial dissipation operators which incorporate inviscid flow physics in their formulation, are used.

In this thesis, a geometric decay function is used to control the levels of artificial dissipation in near wall regions, in order to reduce the magnitude of numerical to physical smoothing to acceptable levels. Specifically, the scaling functions in equations [3.14] are multiplied by a normalized square of the local velocity, $(W/W_{ref})^2$, for the momentum equations :

$$\widehat{D}'(Q) = \mathrm{MIN}\left[\left(\frac{W_{local}}{W_{ref}}\right)^2,\ 1\right]\widehat{D}(Q) \qquad [3.20]$$

In Figure 3.4, this scaling function is plotted as a function of W/W_{ref}. As shown below, this additional local velocity scaling can greatly improve solution accuracy for the high Reynolds number viscous flow computations of interest in this thesis.

To illustrate the above considerations in a quantitative fashion, a series of numerical experiments were undertaken.

In Chapter 4, a turbulent flat plate flow is computed to validate the turbulence models used. The details of these computations are provided there; suffice it here to say that the Reynolds number based on distance from the leading edge for this flow reaches $O(10^6)$ and the grid is therefore very refined. If a typical value of $\kappa_4 = 0.02$ is used with the modified eigenvalue scalings presented in equations [3.14] and [3.16], and the flat plate flow is computed, a standard law-of-the-wall velocity profile similarity is not achieved. This is illustrated in Figure 3.5a, where converged boundary layer velocity profiles are plotted in inner variables, at a streamwise location where the local Reynolds number based on boundary layer thickness is approximately 80000 [to match Klebanoff's (1954) experiments; see Chapter 4]. Clearly, local velocity is seen to undershoot a standard log-law profile.

The artificial dissipation scale factor, κ_4, had to be reduced by a factor of 40 in order to bring the converged solution to within acceptable agreement of law-of-the-wall profiles. This is illustrated in Figure 3.5b, where κ_4 has been reduced to 0.0005.

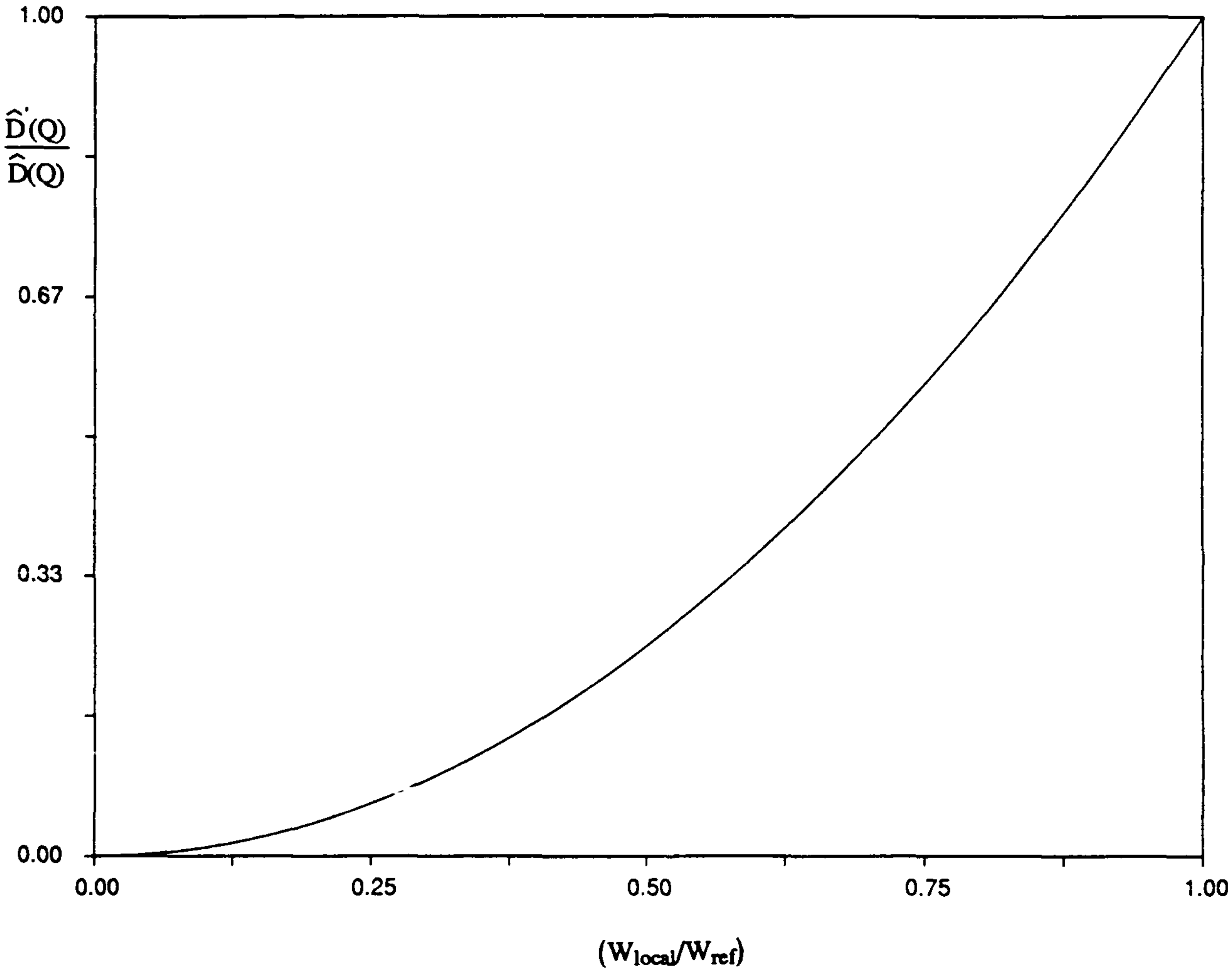

Figure 3.4 Artificial dissipation local velocity scaling function used in this thesis.

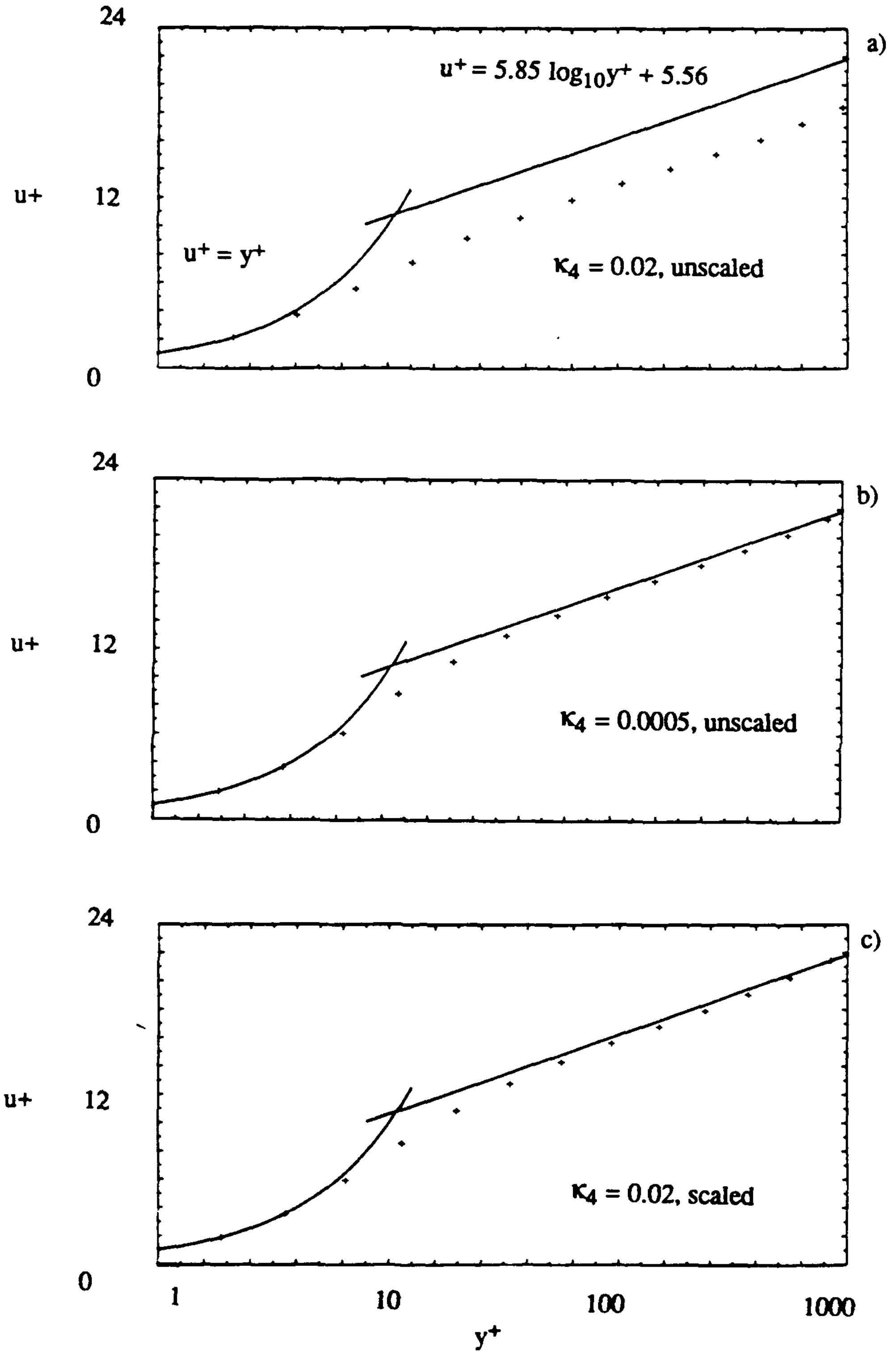

Figure 3.5 Effect of artificial dissipation velocity scaling on law-of-the-wall predictions for a turbulent flat plate flow computation. Standard law-of-the-wall relations (solid lines) and computed values (symbols). Refer to section 4.1 for details of configuration and computation.

If free stream velocity is used for W_{ref}, and equation [3.20] is used to provide additional scaling in near wall regions, the standard value of $\kappa_4 = 0.02$ can be used without corrupting the solution accuracy. This is illustrated in Figure 3.5c.

It is noted that although a stable solution could be obtained for the flat plate flow, using $\kappa_4 = 0.0005$, such a low value would bring about a rapidly unstable solution in typical engineering calculations, where the flow physics are not diffusion dominated. To illustrate the above scaling issue for such a typical high Reynolds number turbomachinery computation, the low subsonic cascade flow, described in detail in Chapter 4, was subject to a similar numerical experiment. Figure 3.6 shows the converged suction surface skin friction coefficient predictions for the same case run with and without the velocity scaling defined in equation [3.20]. This diagram again illustrates that significant errors can be introduced due to near wall artificial dissipation levels in viscous computations on highly stretched grids.

It is also worth noting that the dissipation scaling considerations addressed above are especially important when a multigrid acceleration scheme is used. Careful tuning of artificial dissipation levels is crucial when performing explicit multigrid calculations on highly stretched grids. This is because inadequate or excessive dissipation can diminish the high wave number damping properties of the driving scheme thereby rendering multigrid acceleration less effective Swanson (1990).

Lack of adequate grid resolution in the ξ direction just upstream and downstream of the blade edges, causes the wall damping function, f_μ, in equation [2.12] to be effective only over two to four grid points in this direction. This gives rise to very large streamwise gradients in k and ε at leading and trailing edges, which in turn leads to slowly growing oscillations in these variables. It has therefore been found necessary, in turbomachinery

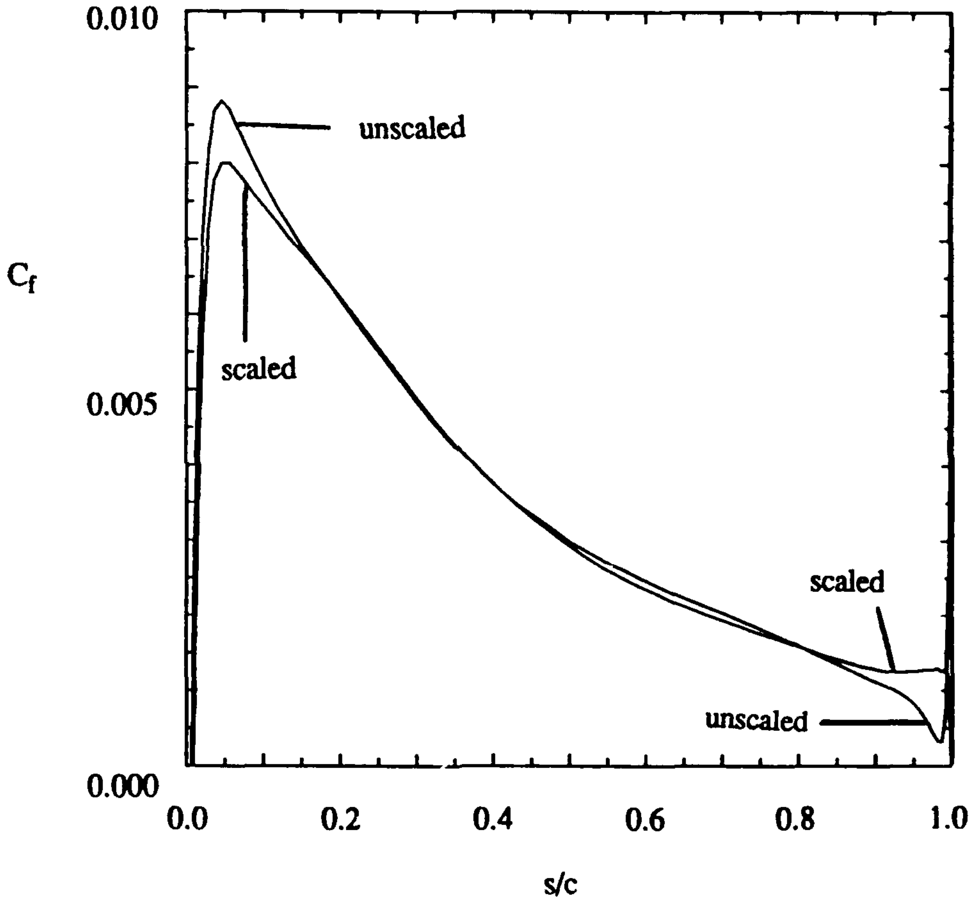

Figure 3.6 Comparison of predicted skin friction coefficient, along the suction surface of a subsonic double circular arc cascade, with and without velocity scaling of artificial dissipation.

blade row computations, to smooth these oscillations by incorporating small amounts of second order artificial dissipation in the k and ε equations, in the streamwise direction only, in a manner consistent with equation [3.14], with $S_{2\xi} \cong 0.01$, $S_{2\eta} = S_{2\zeta} = S_{4\xi} = S_{4\eta} = S_{4\zeta} = 0.0$.

Both the eigenvalue scaling (equation [3.14]) and local velocity scaling (equation [3.20]) were used in all computations that follow. The precise values of the reference relative velocity used in the scaling equation [3.20], are stated for each of the computations presented.

3.3 Stability and Order of Magnitude Analyses of Discretized Equations

In order to provide some verification of the conclusions of the analyses provided in this section, a number of parametric studies have been undertaken using the code applied to a series of numerical test cases. The effects of rotation and turbulence source terms, grid stretching and effective diffusivity and artificial dissipation are to be investigated, and therefore these test cases should embody some or all of these features. Also, the test cases should typify engineering calculations of complex internal flowfields such as occur in turbomachines. Accordingly, a three-dimensional subsonic compressor rotor and a two-dimensional cascade flow configuration are used. In Chapters 4 and 5, 180,225 and 11,739 point grids have been used to compute these flows, where the method is seen to capture much of the complex viscous flow physics, within the accuracy of the turbulence and tip clearance models used. The computational grids and configuration details for these cases are included there. The author feels that these grid sizes are typical of those used for viscous turbomachinery flow computations in industry. Additionally, for some of the parametric studies performed herein, it was necessary to run the code many times. Every fourth grid point was retained from the "production" 3D rotor grid for these cases. The resulting grid, is much too coarse to accurately resolve the near wall physics, but convergence properties are similar to those of the fine grid solution.

A standard four stage Runge-Kutta scheme was chosen for its familiarity in the numerical verification studies that follow, but the results obtained are valid for any Runge-Kutta scheme.

3.3.1 Treatment of Mean Flow and Turbulence Transport Systems

Researchers who have implemented two-equation turbulence models in time-marching Navier-Stokes procedures, have often adopted schemes where the turbulence transport equations are numerically decoupled from the mean flow equations (Grasso and Speziale (1989), Holmes and Connell (1989), Liu (1987), Sahu and Danberg (1986), Gerolymos (1990), Mavriplis and Martinelli (1991)). In the present context, numerical uncoupling implies that at each iteration the mean flow equations are integrated in time, using frozen values of k and ε from the previous iteration. The mean flowfield is then frozen and the turbulence equations are integrated. This type of procedure is referred to as "uncoupled" by Grasso and Speziale (1989), but elsewhere in the literature as "lagged" (Sahu and Danberg (1986)) or "split" (Lee and Dulikravich (1991)). In explicit multistage schemes, "coupling" simply means that fluxes are evaluated at each stage using values of transport variables obtained at the previous stage of the scheme rather than using some values from the previous iteration. This should not be confused with the standard coupling of systems of equations in many implicit schemes.

Simple linear stabilty analysis indicates that the stability characteristics of the "coupled" and decoupled approaches are identical. In earlier work by the present author (Kunz and Lakshminarayana (1990)) a decoupled approach was chosen to simplify code development, and was used for the two-dimensional results presented in Chapter 4. Others have cited code modularity (Gerolymos (1990)) and the ability to advance the equation sets at different local timesteps (Holmes and Connell (1989)) as advantages to an decoupled approach. More recently, a coupled approach has been adopted by the author; all three-dimensional results presented in Chapters 5 and 6 used this approach. It has been the experience of the author that this gives rise to a more compact and better organized code and has no affect at all on the stability, accuracy or CPU performance of the scheme.

3.3.2 Vector VonNeumann Procedure

In generalized curvilinear coordinates, the compressible three-dimensional continuity, momentum, energy, turbulent kinetic energy and turbulent kinetic energy dissipation rate equations can be written in conservation form as :

$$\frac{\partial \hat{Q}}{\partial t} = -\left(\frac{\partial \hat{E}_c}{\partial \xi} + \frac{\partial \hat{F}_c}{\partial \eta} + \frac{\partial \hat{G}_c}{\partial \zeta}\right) + \left(\frac{\partial \hat{E}_v}{\partial \xi} + \frac{\partial \hat{F}_v}{\partial \eta} + \frac{\partial \hat{G}_v}{\partial \zeta}\right) + \hat{S} \qquad [2.16]$$

where the transport variable, flux and source vectors are given in equations [2.17]. When an effective diffusivity formulation is adopted, we have $\hat{E}_v = \hat{E}_v(\mu_e, Q, Q_\xi, Q_\eta, Q_\zeta)$, $\hat{F}_v = \hat{F}_v(\mu_e, Q, Q_\xi, Q_\eta, Q_\zeta)$, $\hat{G}_v = \hat{G}_v(\mu_e, Q, Q_\xi, Q_\eta, Q_\zeta)$. To simplify the problem, viscous flux vectors are linearized as $\hat{E}_v = \hat{E}_v(Q_\xi, Q_\eta, Q_\zeta)$, $\hat{F}_v = \hat{F}_v(Q_\xi, Q_\eta, Q_\zeta)$, $\hat{G}_v = \hat{G}_v(Q_\xi, Q_\eta, Q_\zeta)$. So in the stability analysis, the diffusivities are taken as locally constant, and the influence of the components of the normal stress terms, $\frac{\partial}{\partial x_i}\left(-\delta_{ij}\rho k\right)$ are neglected, as is a heat transfer term proportional to $\frac{\nabla \rho}{\rho} \cdot \nabla T$. Such linearizations have also been incorporated in stability analyses performed by other authors (MacCormack and Baldwin (1975), Abarbanel and Gottlieb (1981)). These assumptions are not invoked in the Navier-Stokes procedure but provide simplification in the following analysis. Specifically, they allow us to write the nonconservative form of the governing equations, with $Q = (\rho, u, v, w, p, k, \varepsilon)^T$, as :

$$\frac{\partial Q}{\partial t} = -\left[\hat{A}_1\frac{\partial Q}{\partial \xi} + \hat{A}_2\frac{\partial Q}{\partial \eta} + \hat{A}_3\frac{\partial Q}{\partial \zeta}\right] + \hat{D}Q +$$

$$\left[\hat{S}_1\frac{\partial^2 Q}{\partial \xi^2} + \hat{S}_2\frac{\partial^2 Q}{\partial \eta^2} + \hat{S}_3\frac{\partial^2 Q}{\partial \zeta^2} + \hat{T}_1\frac{\partial^2 Q}{\partial \xi \partial \eta} + \hat{T}_2\frac{\partial^2 Q}{\partial \xi \partial \zeta} + \hat{T}_3\frac{\partial^2 Q}{\partial \eta \partial \zeta}\right] \qquad [3.21]$$

where

$$\hat{A}_1 = PJ\frac{\partial \hat{E}_c}{\partial Q}\ ,\ \hat{A}_2 = PJ\frac{\partial \hat{F}_c}{\partial Q}\ ,\ \hat{A}_3 = PJ\frac{\partial \hat{G}_c}{\partial Q}\ ,$$

$$\hat{S}_1 = PJ\frac{\partial \hat{E}_v}{\partial Q_\xi}\ ,\ \hat{S}_2 = PJ\frac{\partial \hat{F}_v}{\partial Q_\eta}\ ,\hat{S}_3 = PJ\frac{\partial \hat{G}_v}{\partial Q_\zeta}\ ,$$

$$\hat{T}_1 = PJ\left(\frac{\partial \hat{E}_v}{\partial Q_\eta} + \frac{\partial \hat{F}_v}{\partial Q_\xi}\right),\hat{T}_2 = PJ\left(\frac{\partial \hat{E}_v}{\partial Q_\zeta} + \frac{\partial \hat{G}_v}{\partial Q_\xi}\right),\ \ \hat{T}_3 = PJ\left(\frac{\partial \hat{F}_v}{\partial Q_\zeta} + \frac{\partial \hat{G}_v}{\partial Q_\eta}\right),\ \hat{D} = \frac{\partial(PJ\hat{S})}{\partial Q}$$

These flux and source Jacobians are provided. Matrix P, which scales the viscous and source terms consistent with the operations performed to convert to nonconservative form, also appears in Appendix A. In the linearization of source Jacobian $\hat{D}$,we take $\hat{S} = \hat{S}(Q)$. Such a linearization has been used in an uncoupled implicit scheme by Sahu and Danberg (1986) and in uncoupled explicit schemes which incorporate pointwise implicit treatment of the turbulence equation source terms by Liu (1987) and Gerolymos (1990). Additionally, the density is taken as locally constant in linearizing the near wall modelling terms $\mathcal{D}$ and $\mathcal{E}$. This is justified since these functions are very small except in the immediate vicinity of the wall where local Mach numbers are low. It is noted that viscous deformation work terms do not appear in the nonconservative form of the energy equation due to the choice of pressure as the dependent variable.

Fourth order difference artificial dissipation operators are incorporated in the stability analysis (inclusion of second order dissipative terms follows analogously and is not included for brevity), so we add the following to the RHS of equation [3.21] :

$$\text{(equation [3.21])} + \left[\sigma_\xi I \frac{\partial^4 Q}{\partial \xi^4} + \sigma_\eta I \frac{\partial^4 Q}{\partial \eta^4} + \sigma_\zeta I \frac{\partial^4 Q}{\partial \zeta^4} \right] \qquad \text{[3.22]}$$

where σ_ξ, σ_η, σ_ζ are any general locally varying dissipation scale factors. These factors are real and negative (so that the fourth difference operators be dissipative) and have dimension t^{-1}.

If second order accurate central differences are used to discretize the spatial derivatives, the corresponding Fourier symbols for the spatial derivatives in equations [3.21] and [3.22] become :

$$\begin{array}{llll} Q_\xi \rightarrow iS_\xi & Q_{2\xi} \rightarrow 2(C_\xi - 1) & Q_{\xi\eta} \rightarrow -S_\xi S_\eta & Q_{4\xi} \rightarrow 4(C_\xi - 1)^2 \\ Q_\eta \rightarrow iS_\eta & Q_{2\eta} \rightarrow 2(C_\eta - 1) & Q_{\xi\zeta} \rightarrow -S_\xi S_\zeta & Q_{4\eta} \rightarrow 4(C_\eta - 1)^2 \\ Q_\zeta \rightarrow iS_\zeta & Q_{2\zeta} \rightarrow 2(C_\zeta - 1) & Q_{\eta\zeta} \rightarrow -S_\eta S_\zeta & Q_{4\zeta} \rightarrow 4(C_\zeta - 1)^2 \end{array} \qquad \text{[3.23]}$$

where $S_\xi = \sin(\phi)$, $C_\xi = \cos(\phi)$, etc..., ϕ is the phase of the error mode, and $\Delta\xi = \Delta\eta = \Delta\zeta \equiv 1$. The Fourier symbols given above are consistent with the flux differencing in the code. This is an important consideration as factors of 2 and 4 can appear in the final stability expressions if viscous fluxes are discretized differently.

If a standard multi stage Runge-Kutta scheme is incorporated, then a vector VonNeuman stability analysis yields a polynomial expression for amplification matrix, $G = P(\Delta t Z)$, where P represents some matrix polynomial function, and Z is the Fourier matrix of the spatial discretization of the governing equations. A necessary condition for stability is $\rho(G) \leq 1$, for all ϕ. Analyzing the eigenvalues of G for each error mode is not practical computationally. Useful approximations are adopted here to simplify the problem. We split $Z = Z_I + Z_R$, such that $\lambda(Z_I)$ are all pure imaginary, and $\lambda(Z_R)$ are all pure real, and analyze the individual problems $G_I = P_I(\Delta t Z_I)$, $G_R = P_R(\Delta t Z_R)$ (where now P_I and P_R need not necessarily be the same polynomial function). Considering the Fourier matrix Z_I (given in Appendix A), we estimate :

$$\rho(G_I) = \rho(P_I(\Delta t Z_I)) \approx P_I(\rho(\Delta t Z_I)) \qquad [3.24a]$$

The second equality in equation [3.24a] is strictly true only if $\Delta t Z_I$ is hermetian, in which case [3.24a] would be a straightforward application of the spectral mapping theorem (Varga (1962), for example). In the present context of local linearized analysis, equation [3.24a] is submitted as an approximation which provides useful information as will be seen.

Matrix Z_R is pure real and there exists S such that $\overline{Z}_R = S^{-1} Z_R S$ is real and symmetric (Abarbanel and Gottlieb (1981)). That is, the spectral mapping theorem applies directly :

$$\rho(G_R) = \rho(S^{-1} G_R S) = \rho(P_R(\Delta t \overline{Z}_R)) = P_R(\rho(\Delta t \overline{Z}_R)) = P_R(\rho(\Delta t Z_R)) \qquad [3.24b]$$

So we have $\rho(G_R) = P_R(\rho(\Delta t Z_R))$, and estimate $\rho(G_I) \approx P_I(\rho(\Delta t Z_I))$. It remains then only to ensure that the locus of $\rho(\Delta t Z_I)$ and $\rho(\Delta t Z_R)$ remain simultaneously within the scalar stability bound for the chosen scheme. Accordingly, if we evaluate all elements of Z_I

and Z_R at the phase for which they are a maximum, conservative criteria to ensure stability become :

$$\Delta t\rho(Z_I) \leq i\ \mathrm{CFL}_{op} \text{ and } \Delta t\rho(Z_R) \leq \Omega_{op} \qquad [3.25]$$

where CFL_{op} and Ω_{op} are operational Courant and VonNeumann numbers chosen such that the rectangle formed by, $0 < \Omega < \Omega_{op}$, $0 < \mathrm{CFL} < \mathrm{CFL}_{op}$ lies within the scalar stability boundary of the chosen scheme (see Figure 3.2).

So it is assumed in equation [3.25] that all of the eigenvalues of

$$Z_I = iS_\xi\hat{A}_1+iS_\eta\hat{A}_2+iS_\zeta\hat{A}_3+i(-i\hat{D}_I) \qquad [3.26]$$

are imaginary, and that all of the eigenvalues of

$$Z_R=2(C_\xi-1)\hat{S}_1+2(C_\eta-1)\hat{S}_2+2(C_\zeta-1)\hat{S}_3-S_\xi S_\eta\hat{T}_1-S_\xi S_\zeta\hat{T}_2-S_\eta S_\zeta\hat{T}_3$$

$$+4(C_\xi-1)^2\sigma_\xi I+4(C_\eta-1)^2\sigma_\eta I+4(C_\zeta-1)^2\sigma_\zeta I+\hat{D}_R \qquad [3.27]$$

are real. This assumption will be verified below. Here, for convenience, $\hat{D}$ has been split $\hat{D} = \hat{D}_I + \hat{D}_R$, such that $\lambda(Z_R)$ are all pure real and $\lambda(Z_I)$ are all pure imaginary. $\hat{D}_I$ and $\hat{D}_R$ are given in Appendix A.

Commencing with the hyperbolic analysis, an expression for Z_I (also given in Appendix A) can be obtained from equation [3.26]. The seven eigenvalues of Z_I are :

$$\lambda(Z) = i\overline{U},$$

$$i\left[\overline{U} \pm \frac{1}{2}\sqrt{4\omega^2+4c\omega k_1+c^2\left(k_1^2+k_2^2+k_3^2\right)} \pm \frac{1}{2}\sqrt{4\omega^2-4c\omega k_1+c^2\left(k_1^2+k_2^2+k_3^2\right)}\right],$$

$$i\left[\overline{U} \pm \frac{\varepsilon}{k}\sqrt{\left(\frac{P}{\rho\varepsilon}+1\right)\left(C_1 f_1 \frac{P}{\rho\varepsilon}+C_2 f_2\right)}\right] \qquad [3.28]$$

where $\overline{U} \equiv US_\xi+VS_\eta+WS_\zeta$ and $k_1 \equiv \xi_x S_\xi+\eta_x S_\eta+\zeta_x S_\zeta$, $k_1 \equiv \xi_y S_\xi+\eta_y S_\eta+\zeta_y S_\zeta$, $k_3 \equiv \xi_z S_\xi+\eta_z S_\eta+\zeta_z S_\zeta$. These eigenvalues are indeed pure imaginary (as per our choice of $\widehat{D}_I$), since the groups of terms inside the square root signs are never negative (independent of the sign of ω). The coefficients of the first derivative Jacobians are maximum at $\phi = \pi/2$. A conservative estimate for the maximum value of $\rho(Z_I)$ is therefore obtained by evaluating the trigonometric terms at this phase, so the spectral radius of Z_I ,

$$\rho(Z_I) \leq i\,\mathrm{MAX}$$

$$\{ \left[\overline{U} + \frac{1}{2}\sqrt{4\omega^2+4c\omega k_1+c^2\left(k_1^2+k_2^2+k_3^2\right)} + \frac{1}{2}\sqrt{4\omega^2-4c\omega k_1+c^2\left(k_1^2+k_2^2+k_3^2\right)}\right],$$

$$\left[\overline{U} \pm \frac{\varepsilon}{k}\sqrt{\left(\frac{P}{\rho\varepsilon}+1\right)\left(C_1 f_1 \frac{P}{\rho\varepsilon}+C_2 f_2\right)}\right] \} \qquad [3.29]$$

where now $\overline{U} \equiv |U|+|V|+|W|$, $k_1 \equiv |\xi_x|+|\eta_x|+|\zeta_x|$, $k_2 \equiv |\xi_y|+|\eta_y|+|\zeta_y|$, $k_3 \equiv |\xi_z|+|\eta_z|+|\zeta_z|$.

Moving to the parabolic stability analysis, we have :

$$\rho(Z_R) = \rho(\; 2(C_\xi-1)\widehat{S}_1 + 2(C_\eta-1)\widehat{S}_2 + 2(C_\zeta-1)\widehat{S}_3$$

$$- S_\xi S_\eta \widehat{T}_1 - S_\xi S_\zeta \widehat{T}_2 - S_\eta S_\zeta \widehat{T}_3$$

$$+ 4(C_\xi-1)^2\sigma_\xi I + 4(C_\eta-1)^2\sigma_\eta I + 4(C_\zeta-1)^2\sigma_\zeta I + \hat{D}_R \;) \qquad [3.30]$$

The non-symmetric element of $\hat{S}_i$ does not affect the eigenvalues of $\hat{S}_i$, nor of Z_R, therefore this term can be dropped in the following analysis, so $\hat{S}_i$ is treated as symmetric and real hereafter. We can invoke the matrix inequality :

$$\rho(Z_R) \leq \;\|\; 2(C_\xi-1)\hat{S}_1 + 2(C_\eta-1)\hat{S}_2 + 2(C_\zeta-1)\hat{S}_3$$

$$- S_\xi S_\eta \hat{T}_1 - S_\xi S_\zeta \hat{T}_2 - S_\eta S_\zeta \hat{T}_3$$

$$+ 4(C_\xi-1)^2\sigma_\xi I + 4(C_\eta-1)^2\sigma_\eta I + 4(C_\zeta-1)^2\sigma_\zeta I + \hat{D}_R \;\| \qquad [3.31]$$

where $\|\cdot\|$ represents any consistent matrix norm (Stewart (1973), for example). The triangle inequality provides :

$$\rho(Z_R) \leq \|2(C_\xi-1)\hat{S}_1\| + \|2(C_\eta-1)\hat{S}_2\| + \|2(C_\zeta-1)\hat{S}_3\|$$

$$+ \|-S_\xi S_\eta \hat{T}_1\| + \|-S_\xi S_\zeta \hat{T}_2\| + \|-S_\eta S_\zeta \hat{T}_3\|$$

$$+ \|4(C_\xi-1)^2\sigma_\xi I\| + \|4(C_\eta-1)^2\sigma_\eta I\| + \|4(C_\zeta-1)^2\sigma_\zeta I\| + \|\hat{D}_R\| \qquad [3.32]$$

The coefficients of the second and fourth derivative Jacobians are maximum at $\phi = \pi$, and those of the cross derivative terms are maximum at $\phi = \pi/2$. A conservative estimate for the maximum value of $\rho(Z_R)$ is therefore obtained by evaluating all the trigonometric terms at the phase for which they are the largest :

$$\rho(Z_R) \le 4\|\hat{S}_1\| + 4\|\hat{S}_2\| + 4\|\hat{S}_3\| + \|\hat{T}_1\| + \|\hat{T}_2\| + \|\hat{T}_3\|$$

$$+ 16\|\sigma_\xi I\| + 16\|\sigma_\eta I\| + 16\|\sigma_\zeta I\| + \|\hat{D}_R\| \qquad [3.33]$$

Choosing a matrix 2 norm :

$$\rho(Z_R) \le 4\left[\rho(\hat{S}_1) + \rho(\hat{S}_2) + \rho(\hat{S}_3)\right] + \left[\rho(\hat{T}_1) + \rho(\hat{T}_2) + \rho(\hat{T}_3)\right]$$

$$+ 16\left[\rho(\sigma_\xi I) + \rho(\sigma_\eta I) + \rho(\sigma_\zeta I)\right] + \rho(\hat{D}_R) \qquad [3.34]$$

where we have used the matrix identity $\|W\|_2 = \left[\rho\left(W^T W\right)\right]^{1/2}$, and the fact that $\hat{S}_i$, $\hat{T}_i$, $\sigma_i I$ and $\hat{D}_R$ are symmetric and real.

The eigenvalues of $\hat{T}_i$ are complicated, but if it is assumed that the grid is close to orthogonal in regions where the viscous stability bound becomes important (see Martinelli (1987)), the eigenvalues of $\hat{T}_1$ are found to be:

$$\lambda_1(\hat{T}_1) = \lambda_2(\hat{T}_1) = \lambda_3(\hat{T}_1) = \lambda_4(\hat{T}_1) = \lambda_5(\hat{T}_1) = 0,$$

$$\lambda_6(\hat{T}_1) = -\lambda_7(\hat{T}_1) = \frac{\mu_e}{3\rho}\sqrt{(\nabla\xi\cdot\nabla\xi)(\nabla\eta\cdot\nabla\eta)} \qquad [3.35]$$

The spectral radius is therefore,

$$\left[\rho(\hat{T}_1) + \rho(\hat{T}_2) + \rho(\hat{T}_3)\right] = \frac{\mu_e}{3\rho}\Big[\sqrt{(\nabla\xi\cdot\nabla\xi)(\nabla\eta\cdot\nabla\eta)}$$

$$+\sqrt{(\nabla\xi\cdot\nabla\xi)(\nabla\zeta\cdot\nabla\zeta)} + \sqrt{(\nabla\eta\cdot\nabla\eta)(\nabla\zeta\cdot\nabla\zeta)}\Big] \qquad [3.36]$$

A simple form for the eigenvalues of $\widehat{S}_i$ can be obtained without invocation of a local grid orthogonality assumption, but for consistency with the development for $\widehat{T}_i$, such terms are also dropped in $\widehat{S}_i$, so :

$$\lambda_1(\widehat{S}_1) = 0,\ \lambda_2(\widehat{S}_1) = \frac{4\mu_e}{3\rho}(\nabla\xi\cdot\nabla\xi),$$

$$\lambda_3(\widehat{S}_1) = \lambda_4(\widehat{S}_1) = \frac{\mu_e}{\rho}(\nabla\xi\cdot\nabla\xi),\ \lambda_5(\widehat{S}_1) = \frac{\gamma}{\rho}\left(\frac{\mu_l}{Pr_l} + \frac{\mu_t}{Pr_t}\right)(\nabla\xi\cdot\nabla\xi),$$

$$\lambda_6(\widehat{S}_1) = \frac{1}{\rho}\left(\mu_l + \frac{\mu_t}{Pr_k}\right)(\nabla\xi\cdot\nabla\xi),\ \lambda_7(\widehat{S}_1) = \frac{1}{\rho}\left(\mu_l + \frac{\mu_t}{Pr_\varepsilon}\right)(\nabla\xi\cdot\nabla\xi) \qquad [3.37]$$

For $\gamma = 1.4$, $Pr_l = 0.72$, $Pr_t = 0.9$, $Pr_k = 1.0$, $Pr_\varepsilon=1.3$, the spectral radius is therefore,

$$4\left[\rho(\widehat{S}_1) + \rho(\widehat{S}_2) + \rho(\widehat{S}_3)\right] = \frac{4\gamma}{\rho}\left(\frac{\mu_l}{Pr_l} + \frac{\mu_t}{Pr_t}\right)(\nabla\xi\cdot\nabla\xi + \nabla\eta\cdot\nabla\eta + \nabla\zeta\cdot\nabla\zeta) \qquad [3.38]$$

On inspection :

$16\left[\rho(\sigma_\xi I)+ \rho(\sigma_\eta I)+\rho(\sigma_\zeta I)\right] = -16(\sigma_\xi + \sigma_\eta + \sigma_\zeta)$ (recall that the artificial dissipation scale factors are negative and real). Lastly,

$$\lambda\left(\widehat{D}_R\right) = 0,\ 0,\ 0,\ 0,\ 0,\ \frac{2P}{\rho k} - \frac{2\mu_l}{\rho l^2},\ \frac{-2C_2 f_2 \varepsilon}{k} - \frac{2\mu_l}{\rho l^2}e^{-y^+/2} \qquad [3.39]$$

So

$$\rho\left(\widehat{D}_R\right) = MAX\left(\left|\frac{2P}{\rho k} - \frac{2\mu_l}{\rho l^2}\right|, \left|\frac{2C_2 f_2 \varepsilon}{k} + \frac{2\mu_l}{\rho l^2}e^{-y^+/2}\right|\right) \qquad [3.40]$$

The spectral radius of Z_R :

$$\rho(Z_R) \leq \Big\{ \frac{4\gamma}{\rho}\left(\frac{\mu_l}{Pr_l} + \frac{\mu_t}{Pr_t}\right)\left(\nabla\xi\cdot\nabla\xi + \nabla\eta\cdot\nabla\eta + \nabla\zeta\cdot\nabla\zeta\right)$$

$$+ \frac{\mu_e}{3\rho}\left[\sqrt{(\nabla\xi\cdot\nabla\xi)(\nabla\eta\cdot\nabla\eta)} + \sqrt{(\nabla\xi\cdot\nabla\xi)(\nabla\zeta\cdot\nabla\zeta)} + \sqrt{(\nabla\eta\cdot\nabla\eta)(\nabla\zeta\cdot\nabla\zeta)}\right]$$

$$- 16(\sigma_\xi + \sigma_\eta + \sigma_\zeta)^{+ \mathrm{MAX}\left(\left|\frac{2P}{\rho k} - \frac{2\mu_l}{\rho l^2}\right|, \left|\frac{2C_2 f_2 \varepsilon}{k} + \frac{2\mu_l}{\rho l^2}e^{-y^+/2}\right|\right)} \Big\} \qquad [3.41]$$

In practice, a stable local timestep could be obtained from :

$$\Delta t = \mathrm{MIN}\left[\ \Delta t_c, \Delta t_v\ \right] \equiv \mathrm{MIN}\left[\ \frac{CFL_{op}}{\rho(Z_I)}, \frac{\Omega_{op}}{\rho(Z_R)}\ \right] \qquad [3.42]$$

where $\rho(Z_I)$ and $\rho(Z_R)$ are given in equations [3.29] and [3.41]. It is noted that in the absence of rotation source terms, turbulence model source terms, and artificial dissipation terms, expressions [3.29] and [3.41] represent a three-dimensional extension to a form presented by Martinelli (1987).

3.3.3 Order of Magnitude Analyses

In order to ascertain the relative importance of the various terms which appear in equations [3.29] and [3.41], an order of magnitude analysis is undertaken here. It is first observed, upon inspection of equations [3.29] and [3.41], that the direct influence of rotation and turbulence source terms can only reduce the maximum allowable hyperbolic and parabolic timesteps, for plausible values of ω, k , ε $(-\infty < \omega < \infty, k > 0, \varepsilon > 0)$. For the following arguments, we choose constant reference length scale, l_∞ = blade height and velocity scale, V_∞ = blade tip speed.

3.3.3.1 Rotation Source Terms

Upon nondimensionalization, the terms in the square root sign on the second line of equation [3.29] are of order

$$4R_o^2 \pm \frac{4R_o}{M}N_1 + \frac{1}{M^2}\left(N_1^2 + N_2^2 + N_3^2\right) \qquad [3.43]$$

where $R_o = \frac{\omega l_\infty}{V_\infty}$, $M = \frac{c}{V_\infty}$, $N_i = \frac{l_\infty}{\Delta \bar{x}_i}$ are rotation, Mach and grid clustering parameters. By prescription of the reference scales, V_∞ and l_∞, $O(10^{-1}) < R_o < O(10^0)$. For the compressible flows considered herein, $O(10^{-1}) < M < O(10^0)$. Notice that here, M does not represent a typical local Mach number, rather it is formed from a reference velocity and local speed of sound. For realistic grids, $O(10^1) < N_i < O(10^5)$. The rotation terms will be most significant when R_o is large, M is large and N_i is small, that is in the core flow region. So the third term in equation [3.43] is no less than one order of magnitude greater than the other two terms, which suggests that the rotation terms can be neglected in the specification of a local timestep.

To substantiate this conclusion, three fully turbulent coarse grid test rotor flow cases were run. The nondimensional stability parameters as defined above are $R_o = 0.5$, $M \cong 0.2$, $N_{i\,min} \cong 10$, for this case. In light of the above arguments, there should be very little influence of the rotation terms in equation [3.29] on the stability of the scheme. In Figure 3.7, convergence rates are compared for the cases where ω was set to the machine rotation rate of 113.2 s^{-1} in equation [3.29], and where ω was set to zero in this equation.

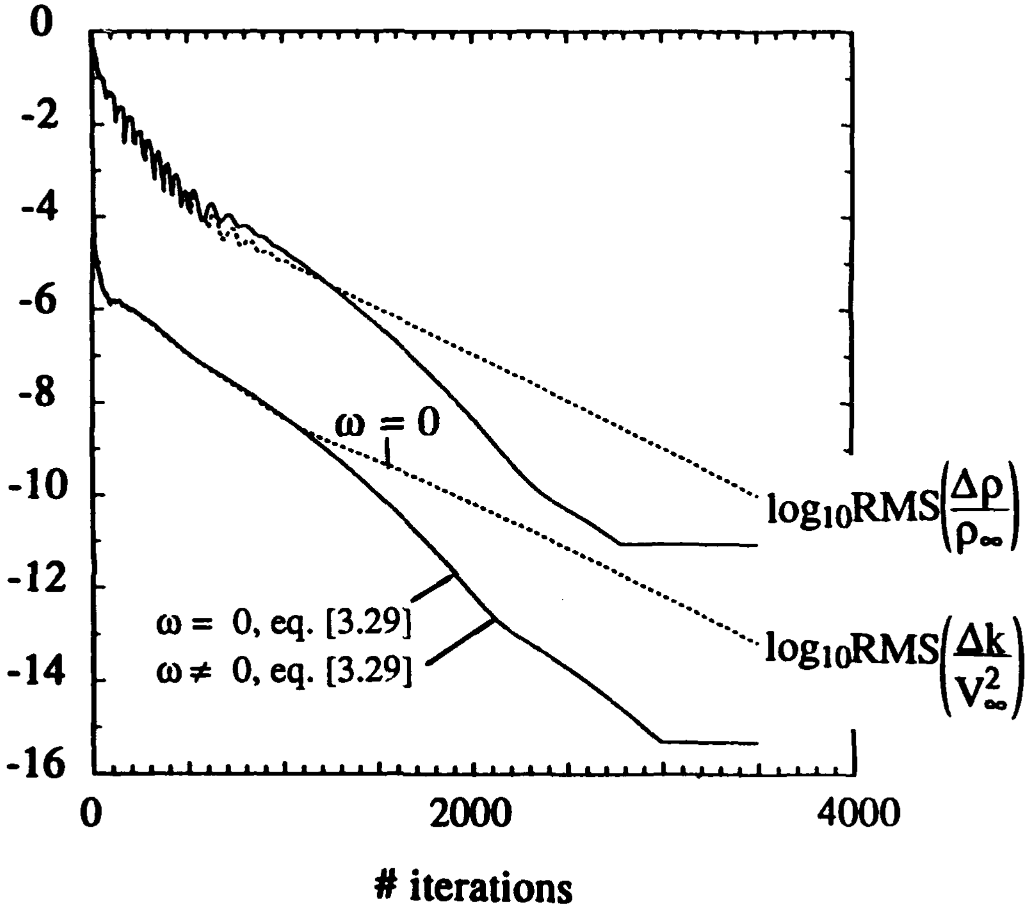

Figure 3.7 Comparison of convergence rates for rotating (solid) and stationary (dashed) rotor passage flow with and without inclusion of rotation terms in local timestep evaluations.

The plots are indistinguishable, indicating that local timesteps are indeed negligibly influenced by system rotation for this case. Accordingly, the first term in equation [3.29] may be replaced by the expression :

$$\overline{U} + c\sqrt{\nabla\xi\cdot\nabla\xi+\nabla\eta\cdot\nabla\eta+\nabla\zeta\cdot\nabla\zeta+2[\nabla\xi\cdot\nabla\eta+\nabla\xi\cdot\nabla\zeta+\nabla\eta\cdot\nabla\zeta]} \qquad [3.44]$$

The term $\overline{U}$ should be retained in equation [3.44] as it can be easily shown that this term may be of the same order of magnitude as the other term in equation [3.44] if $M_{local} = q/c \approx 1$. Also appearing in Figure 3.7 is the convergence history for the same case run with the machine rotation rate set to zero in the flow solution. The convergence rates compare closely to approximately a five decade drop in the mean density residual, after which the rotating case converges more quickly. This result is included to stress that the physics of the flowfield can, of course, influence the stability of the scheme, and that the above conclusions apply only to the determination of a stable local timestep. It is noted, that these conclusions should break down for very high tip speeds and very coarse grids, in which case, for stability, the rotation terms should be retained in equation [3.29], and the rotation source terms should be evaluated at every stage.

3.3.3.2 Turbulence Model Source Terms

The term $P/\rho\varepsilon$, the ratio of turbulent kinetic energy production to dissipation, appears in equations [3.29] and [3.41]. Assuming that the flow solver converges to a physically reasonable solution, it can be argued that at convergence this term is of order 1 or less. Specifically, the local equilibrium assumption, $P/\rho\varepsilon \cong 1$, is valid for the nearly homogeneous core flow turbulence, and for thin shear layers, whereas, near the boundary layer edge and in separated shear layers and wakes, $P/\rho\varepsilon < 1$ (see Hinze (1975), for example). Additionally, in the immediate vicinity of the wall $P/\rho\varepsilon_a$ goes to zero, where subscript "a" denotes the true dissipation rate. In Chien's model, the dissipation variable, ε, is the isotropic component of the dissipation rate. Though the isotropic component of the dissipation rate goes to zero at the wall, unlike the true dissipation which assumes a finite value there, $P/\rho\varepsilon$ still goes to zero. To see this, designate subscripts a and i to correspond to actual and isotropic components of the dissipation rate. Then :

$$\frac{P}{\rho\varepsilon_i} = \frac{P}{\rho\varepsilon_a + \mathcal{D}} \qquad [3.45]$$

where $\mathcal{D} \equiv -\frac{2\mu_l k}{l^2}$. Both numerator and denominator in equation [3.45] go to zero as the wall is approached. The denominator going to zero is simply a statement that dissipation and molecular diffusion of turbulence energy are in balance at the wall. Through the entire near wall region (say $y^+ < O(10^2)$), convection of turbulence energy is negligible by comparison to dissipation, diffusion and production (Hinze (1975)). Therefore, in order that the turbulence energy budget be in balance in the immediate vicinity of the wall, $\frac{P}{\rho\varepsilon_a + \mathcal{D}}$, must uniformly approach zero as $l \rightarrow 0$. So with $C_1 f_1 = 1.35$, $1.4 \le C_2 f_2 \le 1.8$ (for Chien's model), it can be assumed that at convergence, the terms

$$\sqrt{\left(\frac{P}{\rho\varepsilon} + 1\right)\left(C_1 f_1 \frac{P}{\rho\varepsilon} + C_2 f_2\right)} = O(1) \qquad [3.46]$$

in equation [3.29]. Turning to the factor ε/k, the magnitude of the hyperbolic terms in equation [3.29] are now compared. In the core flow and outer regions of the boundary layer

$$\frac{l_\infty}{V_\infty} \cdot c\sqrt{\nabla\xi\cdot\nabla\xi + \nabla\eta\cdot\nabla\eta + \nabla\zeta\cdot\nabla\zeta + 2[\nabla\xi\cdot\nabla\eta + \nabla\xi\cdot\nabla\zeta + \nabla\eta\cdot\nabla\zeta]} = O\left(\frac{1}{M} N_i\right) > 10^1 \qquad [3.47]$$

where the same constant reference length and velocity scales are chosen as before. If local turbulence intensity and turbulence length scales are defined :

$$T \equiv \frac{k^{1/2}}{V_\infty}, \; L \equiv \frac{C_\mu k^{3/2}}{\varepsilon} \qquad [3.48]$$

then $\left(\frac{l_\infty}{V_\infty}\right)\frac{\varepsilon}{k} = O\left(\frac{C_\mu T}{C}\right)$, where C is the ratio of integral turbulence length scale to blade height, $L = Cl_\infty$. Reasonable bounds are $O(10^{-3}) < T < O(10^{-2})$, $O(10^{-3}) < C < O(10^{-2})$. So $\left(\frac{l_\infty}{V_\infty}\right)\frac{\varepsilon}{k} < 10^0$, that is, comparing equation [3.47], away from the immediate vicinity of solid boundaries, the turbulence source terms should be no more than one order of magnitude less than the convective acceleration terms in equation [3.29], at convergence.

In the immediate vicinity of the blade and endwalls, an appropriate near wall length scale, ν/u^*, and velocity scale, u^*, are chosen. The ratio of convection to turbulence source terms is of order

$$\frac{c/\Delta y}{\varepsilon/k} = \frac{(c/u^*)\left([\nu/u^*]/\Delta y\right)}{(\varepsilon^+/k^+)} \qquad [3.49]$$

where y is chosen as the blade normal coordinate here for familiarity, $u^* = \sqrt{\tau_w/\rho}$ is the friction velocity, and $\varepsilon^+ \equiv \frac{\nu\varepsilon}{u^{*4}}$, $k^+ \equiv \frac{k}{u^{*2}}$. Again, in Chien's model, ε is the isotropic component of dissipation rate. For turbulence models which solve for the actual dissipation rate (Lam-Bremhorst (1981), Myong and Kasagi (1990) for instance), $\varepsilon^+/k^+ \rightarrow \infty$ as $y \rightarrow 0$, since ε is finite at a solid boundary. This may be why these models show unfavorable stability properties in time-marching Navier-Stokes computations, as noted by the present author and others (Choi and Knight (1989), Kirtley (1989)). In the opinion of the author, this near wall behavior is more likely the cause of numerical problems than the

Neumann or second derivative boundary conditions on the ε equation, to which these difficulties are often attributed, in models which solve for ε_a (Speziale et al. (1990), for example).

For Chien's model, we estimate from published near wall distributions of k^+ and ε^+ for simple shear layers (Patel et al. (1985)) the following :

$$O(10^{-2}) < \varepsilon^+/k^+ < O(10^{-1}) \qquad [3.50]$$

Also

$$O(10^{-1}) < \left([v/u^*]/\Delta y\right) \approx \left([y/\Delta y]/y^+\right) < O(10^0) \qquad [3.51]$$

depending on near wall grid resolution (at the wall $([y/\Delta y]/y^+) = 1/y^+ \cong O(10^0)$), and

$$(c/u^*) \approx (c/V_\infty)\left(\frac{V_\infty^2\rho}{\tau_w}\right)^{1/2} \approx \left(\frac{1}{M}\right)\left(\frac{1}{C_f^{1/2}}\right) > O(10^1) \qquad [3.52]$$

So near the wall, we also expect the turbulence source terms to be no more than one order of magnitude less than the convective acceleration terms in equation [3.29], at convergence.

Turning to the other turbulence source terms, we can invoke exactly the same arguments as above to neglect the terms $\frac{2P}{\rho\varepsilon}\left(\frac{\varepsilon}{k}\right)$ and $2C_2f_2\left(\frac{\varepsilon}{k}\right)$ which appear in equation [3.41], since they will be negligible by comparison to the convective acceleration terms in equation [3.29] everywhere in the flowfield. However, the near-wall modelling terms, $\frac{2\mu_l}{l^2}$ and $\frac{2\mu_l}{l^2}e^{-y^+/2}$ can be very large near solid boundaries and should be considered. Again choosing y as the blade normal coordinate, near solid surfaces the ratio of physical dissipation to wall correction terms in equation [3.41] is of order $\frac{\mu_l + \mu_t}{\Delta y^2} / \frac{\mu_l}{y^2}$. This expression will be very large except in the immediate vicinity of the wall (μ_t --> 0, y --> Δy), where it approaches unity. Therefore, very near a solid wall, where turbulent diffusivity damping effects dominate, the wall modelling functions give rise to parabolic stability restrictions approximately equal in magnitude to physical diffusion terms (This is not a surprising result since $\mathfrak{D}$ represents molecular diffusion of k at the wall). However, it is shown in the next section that convection dominates the overall stability of the scheme in such regions, so it is expected that the wall modelling terms in equation [3.41] may be neglected as well.

In summary, the foregoing arguments suggest all turbulence source terms have negligible influence on the numerical stability of the scheme, at convergence. To investigate this, the relative magnitudes of the terms above were examined for the fine grid rotor and cascade calculations in both early and late stages of iteration. Designating

A) $$\frac{\varepsilon}{k}\sqrt{\left(\frac{P}{\rho\varepsilon} + 1\right)\left(C_1 f_1 \frac{P}{\rho\varepsilon} + C_2 f_2\right)}$$

B) $$\frac{2P}{\rho\varepsilon}\frac{\varepsilon}{k}$$

C) $$2C_2 f_2 \frac{\varepsilon}{k}$$

D) $$\frac{2\mu_l}{\rho l^2}$$

E) $$\overline{U} + c\sqrt{\nabla\xi\cdot\nabla\xi + \nabla\eta\cdot\nabla\eta + \nabla\zeta\cdot\nabla\zeta + 2[\nabla\xi\cdot\nabla\eta + \nabla\xi\cdot\nabla\zeta + \nabla\eta\cdot\nabla\zeta]}$$

F) $$\frac{4\gamma}{\rho}\left(\frac{\mu_l}{Pr_l} + \frac{\mu_t}{Pr_t}\right)(\nabla\xi\cdot\nabla\xi + \nabla\eta\cdot\nabla\eta + \nabla\zeta\cdot\nabla\zeta) + \frac{\mu_e}{3\rho}\left[\sqrt{(\nabla\xi\cdot\nabla\xi)(\nabla\eta\cdot\nabla\eta)} + \sqrt{(\nabla\xi\cdot\nabla\xi)(\nabla\zeta\cdot\nabla\zeta)} + \sqrt{(\nabla\eta\cdot\nabla\eta)(\nabla\zeta\cdot\nabla\zeta)}\right]$$

For the fine grid rotor flow computation, at convergence, the magnitudes of terms A, B and C were less than 0.1 times the magnitude of term E, and the magnitude of term D was less than 0.1 times the magnitude of term F, at every point in the computational domain, thereby substantiating the arguments of the previous section for this case. Upon cold start "inviscid" initialization the same conditions were observed except for term B. Specifically, at iteration 1, the magnitude of term B was greater than one tenth the value of term E at approximately .15 of the grid points in the flowfield. This number decreased to .002 in 250 iterations. For the cascade computation, the ratio of these terms were all less than 0.1, both at iteration 1 and at convergence.

Some discussion is warranted here. The foregoing arguments suggest that the stiffness associated with large values of near wall turbulence transport source terms is negligible for Chien's model, except in early stages of iteration. The stiffness (local timestep restriction) associated with computing flows on very highly stretched grids using time marching algorithms supersedes difficulties brought about by these source terms. For this reason, the present author has been able to compute successfully a variety of high Reynolds number flowfields using this model (see following chapters), without taking account of the k-ε source terms in the determination of a local timestep and while evaluating source terms prior to the first stage only. Additionally, the convergence rates have been found to be nearly identical to calculations performed using an algebraic eddy viscosity model. This is illustrated in Figure 3.8, which has been adapted from Kunz and Lakshminarayana (1990). In this figure, a flat plate plate boundary layer computation was performed on a highly stretched grid (refer to validation studies, Chapter 4) using both the low Reynolds number k-ε model and an algebraic eddy viscosity model due to Baldwin and Lomax (1978). As seen in the figure, the convergence rates are very similar.

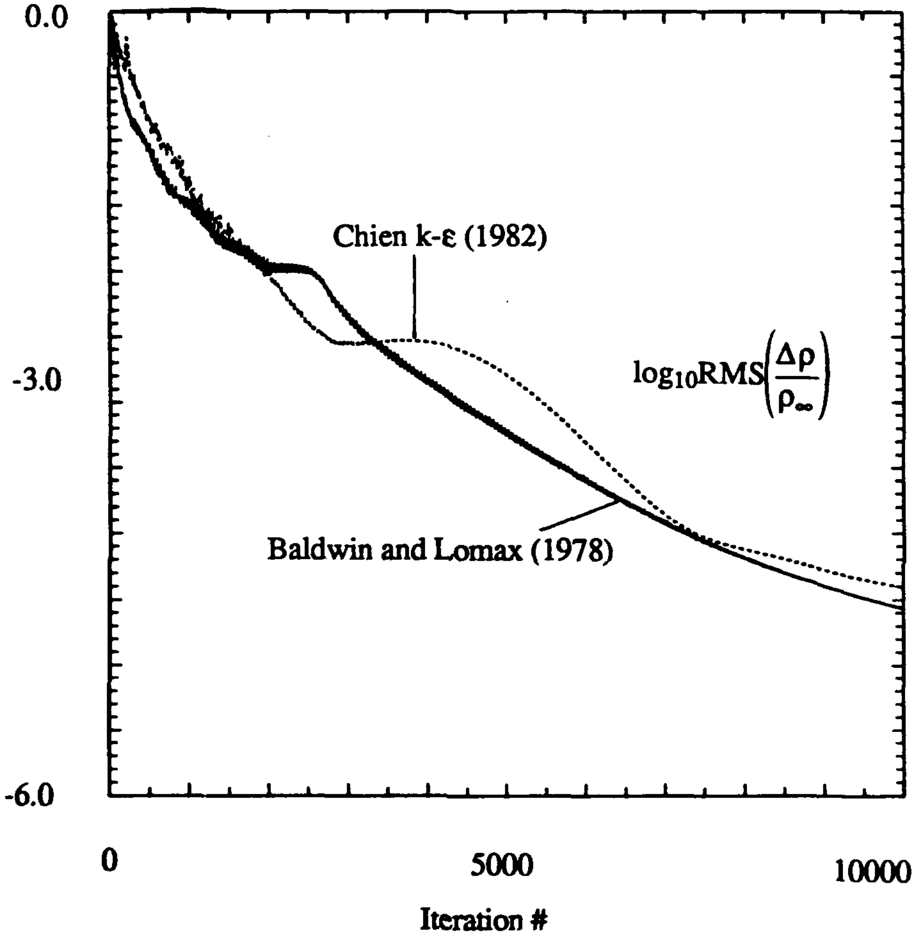

Figure 3.8 Convergence histories for turbulent flat plate flow computations. Baldwin and Lomax (1978) model (solid line) and present k-ε model (dashed line).

Since the source terms do not significantly influence the stability of the scheme, the use of locally implicit treatment of the source terms should not be necessary. This reconciles with recent results obtained by Martelli and Michelassi (1990) who used a factored implicit time marching scheme. They found that pointwise implicit treatment for the source terms in the near-wall q-ω model they used provided no difference in convergence rate over a purely explicit treatment.

To investigate this further, the fine grid cascade computation was run three times. First the standard approach was used, where all source and dissipative terms are evaluated prior to the first stage. Next, the code was run evaluating all source and dissipative terms at every stage. Lastly, the code was run using pointwise implicit treatment of the turbulence source terms. Specifically, for the k and ε equations, each stage in the standard RK4 procedure (equation [3.4]) is replaced by :

$$Q^{k+1} = Q^0 + \alpha_{k+1}\Delta t\left[I - \alpha_{k+1}\Delta t\hat{D}^k\right]^{-1} R(Q^k), \quad k = 0, N\text{-}1 \qquad [3.53]$$

where $\hat{D}$ is given in Appendix A (note : $\omega = 0$ for this case). For each of the three computations, CFL_{op} was chosen as 2.8, and Ω_{op} was adjusted to the maximum value for which a stable solution could be obtained. Specifically, $\Omega_{op1} = 0.95$, $\Omega_{op2} = 0.80$, $\Omega_{op3} = 0.30$. The convergence histories for these calculations appear in Figure 3.9a. In Figure 3.9b, the predicted boundary layer velocity and turbulent kinetic energy profiles at s/c = 0.2 on the suction surface are compared. The convergence histories are quite similar for all three approaches, and the converged solutions are indistinguishable. These findings further substantiate the claims made above.

Recently, Gerolymos (1990) obtained two dimensional supersonic duct flow results on very fine grids using an explicit multigrid scheme and a low Reynolds number

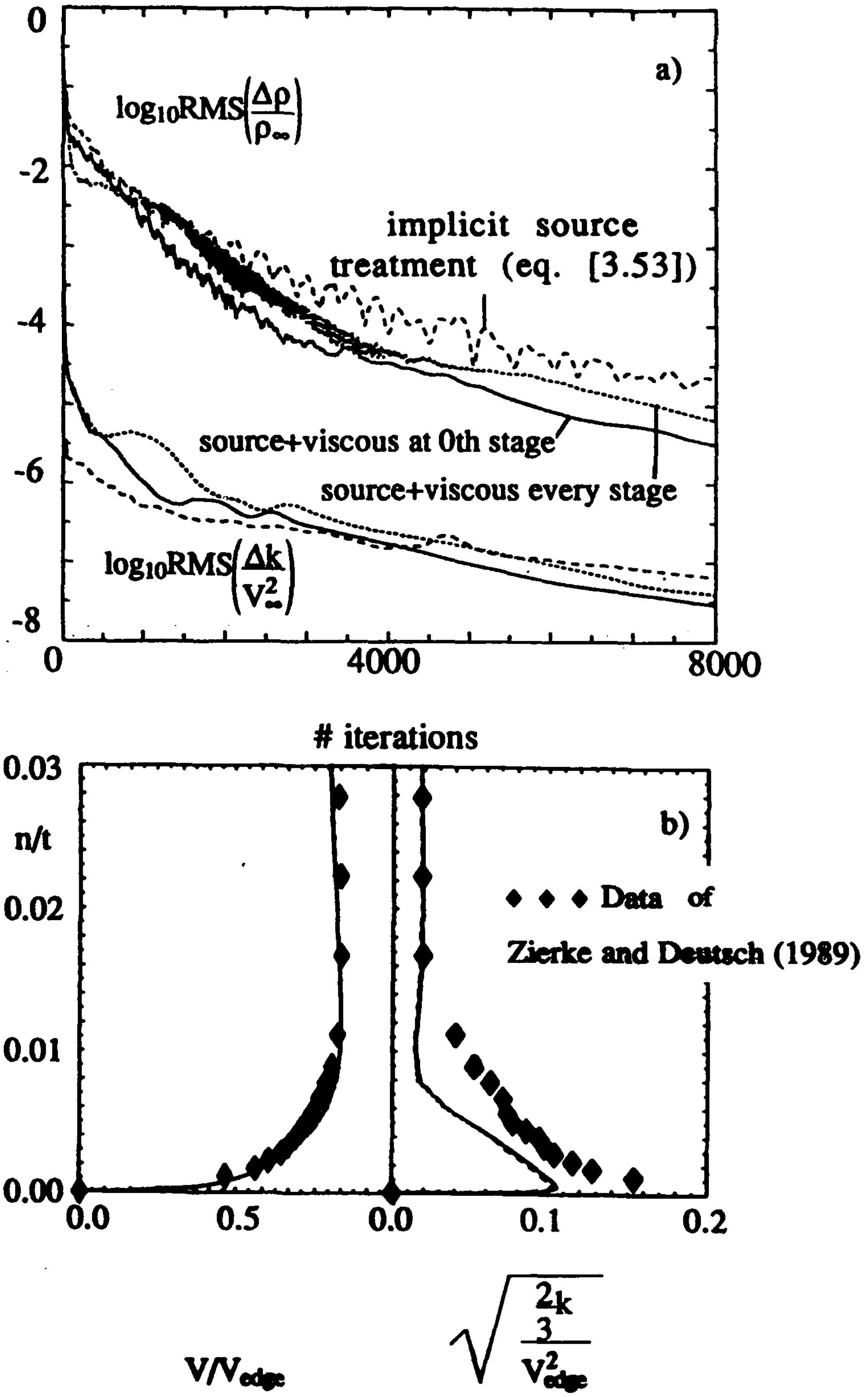

Figure 3.9 Comparison of a) convergence histories, b) converged boundary layer velocity and local turbulence intensity profiles at a location on the suction surface for fine grid cascade computations. Results for three different source and dissipation term treatments are compared.

model due to Launder and Sharma (1974). This model is similar to Chien's in that the isotropic component of dissipation is a transport variable. Gerolymos notes that "for both the driver scheme and the multiple-grid procedure, [pointwise implicit treatment] of the source terms is essential to the stability of the method." Since the source term linearization he chose is similar to that analyzed and used above, his statement for the driver scheme is in contradiction to the present findings. However, when a multigrid procedure is incorporated, the thesis conclusions reached above become less valid if the complete residuals, including source terms, are evaluated on successively coarser grids. Specifically, grid metric stability constraints associated with convection and diffusion operators are relaxed when going to coarser grids, whereas timestep constraints associated with the source terms are not. This is pointed out by Mavriplis and Martinelli (1991), who, like Gerolymos, chose a multigrid procedure where the turbulence source term residuals are retained on coarse grids. They justify using implicit source treatment so that these source terms will not limit the larger timesteps allowed by relaxing the convection and diffusion stability constraints on coarser grids. This exact same argument may be extended to consideration of the rotation source terms as well.

In practice the author has encountered several cases, including flat plate and supersonic cascade flow computations where large relative values of production, $P/\rho\varepsilon$, cause the turbulence model to become rapidly unstable in early stages of iteration, when standard inviscid initialization is used. These cases have in common that freestream turbulence levels are low and Reynolds numbers are very high. It has been found that incorporation of the turbulence source terms in equations [3.29] and [3.41] is ineffective in stabilizing these cases. However, several procedures are effective. Specifically, k and ε are required to remain positive :

$$\rho\varepsilon > K_\varepsilon \, \rho_\infty \varepsilon_\infty \qquad [3.54a]$$

$$\rho k > K_k \, \rho_\infty k_\infty \qquad [3.54b]$$

where $K_\varepsilon = 0.01 - 0.0001$ and $K_k = 0.0001$. These two procedures were recommended to the author by Connell (1989), and are used by Gerolymos (1990). Also the inflow turbulence intensity can be increased to an unrealistically high value for the first 20-50 iterations :

$$T_\infty = 5 \, T_{\infty \, \text{actual}} \qquad [3.54c]$$

This has the effect of significantly reducing $P/\rho\varepsilon$ in early stages of iteration, since upon initialization $\frac{P}{\rho\varepsilon} = O\left(\frac{\mu_t}{\varepsilon}\right) = O\left(\frac{L_\infty^2}{T_\infty^2}\right)$.

So in lieu of the above analyses and verification studies, rotation and turbulence source terms are not included in the specification of a local timestep, in any of the computations to follow.

3.3.3.3 Physical and Artificial Dissipation

Turning next to the physical diffusion terms in equation [3.41], both of order

$$\left(\frac{1}{R_{el}} + \frac{1}{R_{et}}\right) N_i^2 \text{, where } R_{el} \equiv \frac{\rho V_\infty l_\infty}{\mu_l} \text{, } R_{et} \equiv \frac{\rho V_\infty l_\infty}{\mu_t} \qquad [3.55]$$

In many internal and external flows including turbomachinery flows, we have $R_{el} \approx O\left(10^5 - 10^6\right)$ and $(10^1) < R_{et} < O(10^5)$, except in regions where wall damping is effective (where $R_{et} \to \infty$). So comparing the inviscid terms in equation [3.29], which are of order $\frac{1}{M}N_i$, we invoke the bounds on M and N_i provided in the previous sections, and conclude that the parabolic timestep may be smaller than the hyperbolic term, $\Delta t_v < \Delta t_c$, in regions of very high grid clustering ($N_i = O(10^5)$) and low R_{et} ($= O(10^1)$), ie. $\frac{1}{R_{et}}N_i^2 > \frac{1}{M}N_i$. In Figure 3.10, the $\Delta t_v / \Delta t_c = 1$ contour is plotted for the fully converged production and coarse grid rotor computations at an annular grid slice near midspan. In both cases, the parabolic stability considerations described above are seen to manifest themselves near the leading and trailing edges. This provides numerical verification of the necessity to include the effective diffusivity terms in equation [3.42] in calculations where large diffusivities occur in regions of large grid stretching. It has been the experience of the author that this is especially important during the course of iteration as illustrated in Figure 3.11. There it is shown that the parabolic stability bound dominates for more than half of the grid points in early stages of iteration for the coarse grid test flow configuration, and for approximately 7% of the grid points at convergence. The cascade computation yielded similar results. Specifically, at convergence $\Delta t_v < \Delta t_c$ for approximately 4 % of the grid points, all in the immediate vicinity of the blade leading and trailing edges. It is noted that algebraic eddy viscosity models do not typically give rise to the parabolic stability mechanism presented here, when applied to turbomachinery blade row computations. This is because eddy viscosity is assumed to be zero upstream of the blade row (as for say Baldwin and Lomax (1978) point transition model), so that, depending on wake treatment, there should be no regions of the flowfield where large eddy viscosity is coincident with high levels of grid clustering.

Artificial dissipation is added to the discrete equations by design to influence the stability of the scheme. If physical dissipation gives rise to a locally dominant parabolic stability constraint, any artificial dissipation will destabilize the calculation. Therefore, the artificial dissipation terms in equation [3.41] must be retained if maximum operational

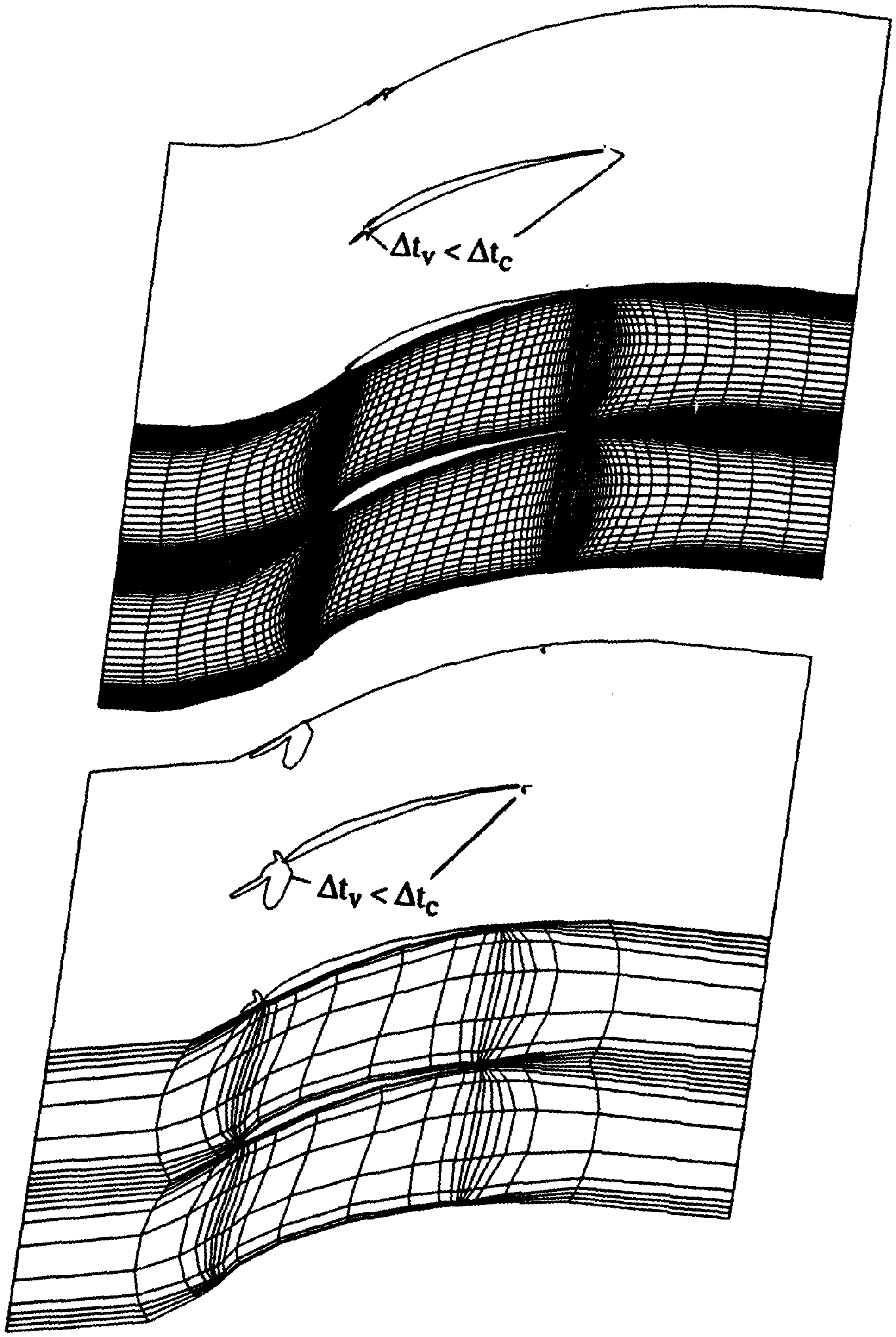
$\Delta t_v < \Delta t_c$
$\Delta t_v < \Delta t_c$

Figure 3.10 Regions of computational domain where $\Delta t_v < \Delta t_c$ for a) fine grid and b) coarse grid rotor flow calculations at convergence (annular grid slice near midspan).

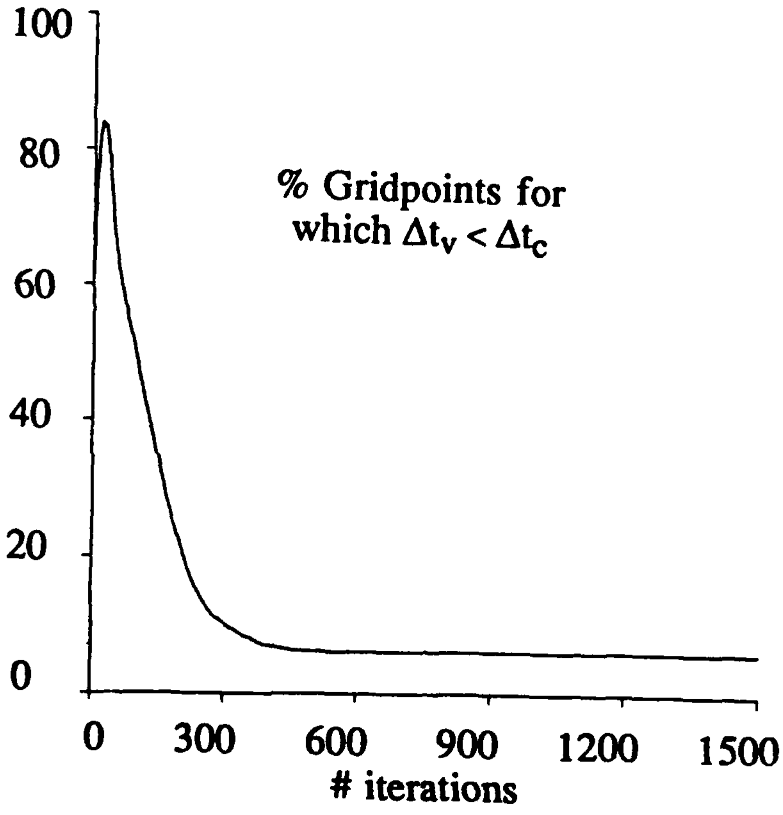

Figure 3.11 Percentage of grid points for which $\Delta t_v < \Delta t_c$ as a function of iteration number for coarse grid rotor flow computation.

VonNeumann numbers are to be used independent of levels of added dissipation. This is illustrated in Figure 3.12. The solid line in this figure is the convergence history for the coarse grid test rotor flow computation run with $\Omega_{op} = 1.75$, $CFL_{op} = 2.80$. Standard values of fourth difference dissipation (refer to section 3.2), were used for this calculation, the local timesteps being computed from equations [3.29] and [3.41]. Due to the parabolic stability constraints arising from physical dissipation, Ω_{op} had to be lowered substantially when artificial dissipation was not incorporated in equation [3.41]. The three dashed curves in Figure 3.12 illustrate this. A choice of $\Omega_{op} = .6$ yielded a divergent solution; $\Omega_{op} = .5$ showed some unstable behavior in early stages of iteration (compare Figure 3.11), but recovered and converged. $\Omega_{op} = .4$ provided a stable iterative process with a slightly diminished convergence rate. This demonstrates that it is useful to incorporate artificial dissipation in the parabolic timestep prescription in problems of this type, to avoid ad hoc specification of an optimum VonNeumann number which varies with amount of artificial dissipation used.

3.3.4 Stability Boundary

The investigations reported in the previous section, suggest that the rotation and turbulence source terms can be neglected in equations [3.29] and [3.41], but all other terms including artificial dissipation should be included, and the procedures summarized in equations [3.54a-c] should be adopted. This gives rise to a robust and convergent code for computation of internal flows, including turbomachinery flows, using the low Reynolds number k-ε model in an explicit solution procedure. In Figure 3.13, the location of CFL_{op} and Ω_{op} corresponding to maximum attainable convergence rates, for the fine grid cascade and rotor flow computations, are plotted with the stability boundary for the scheme. The locations of these operating points are very close to the scalar bound for the scheme (compare Figure 3.2). The corresponding convergence histories for these two

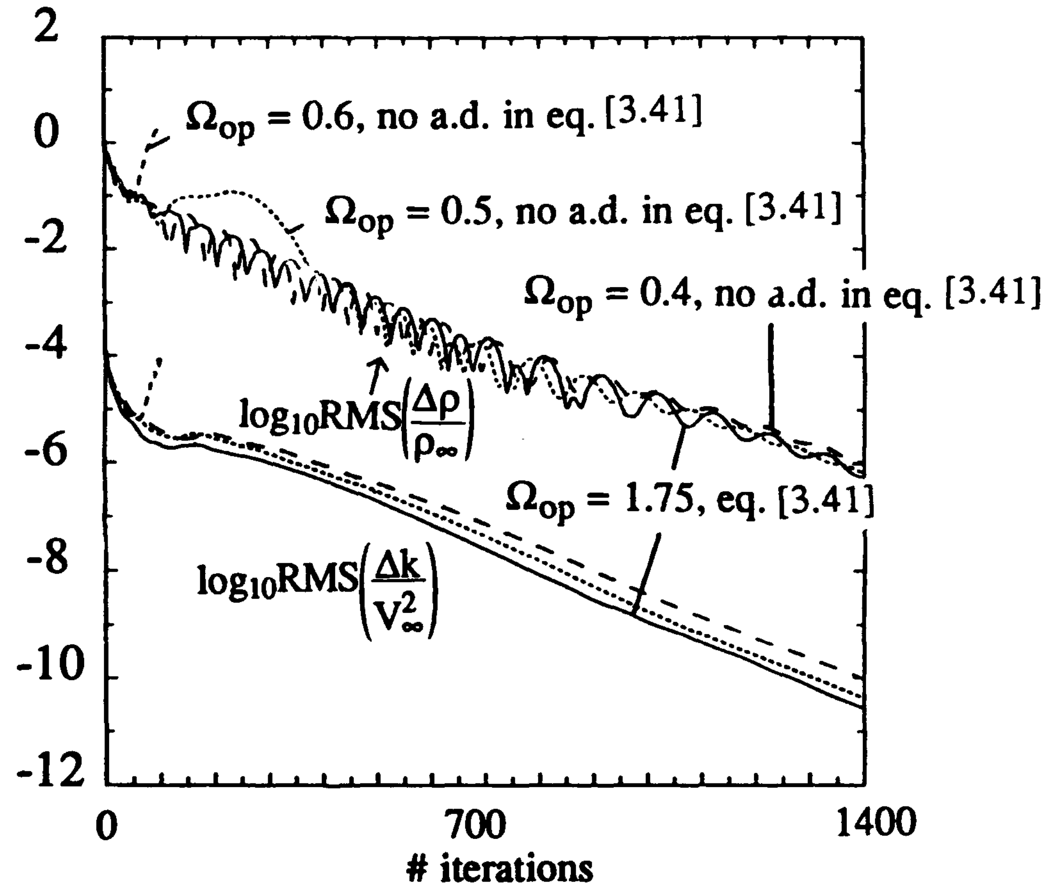

Figure 3.12 Comparison of convergence rates for several operating Von Neumann numbers with (solid) and without (dashed) inclusion of artificial dissipation terms in timestep computations.

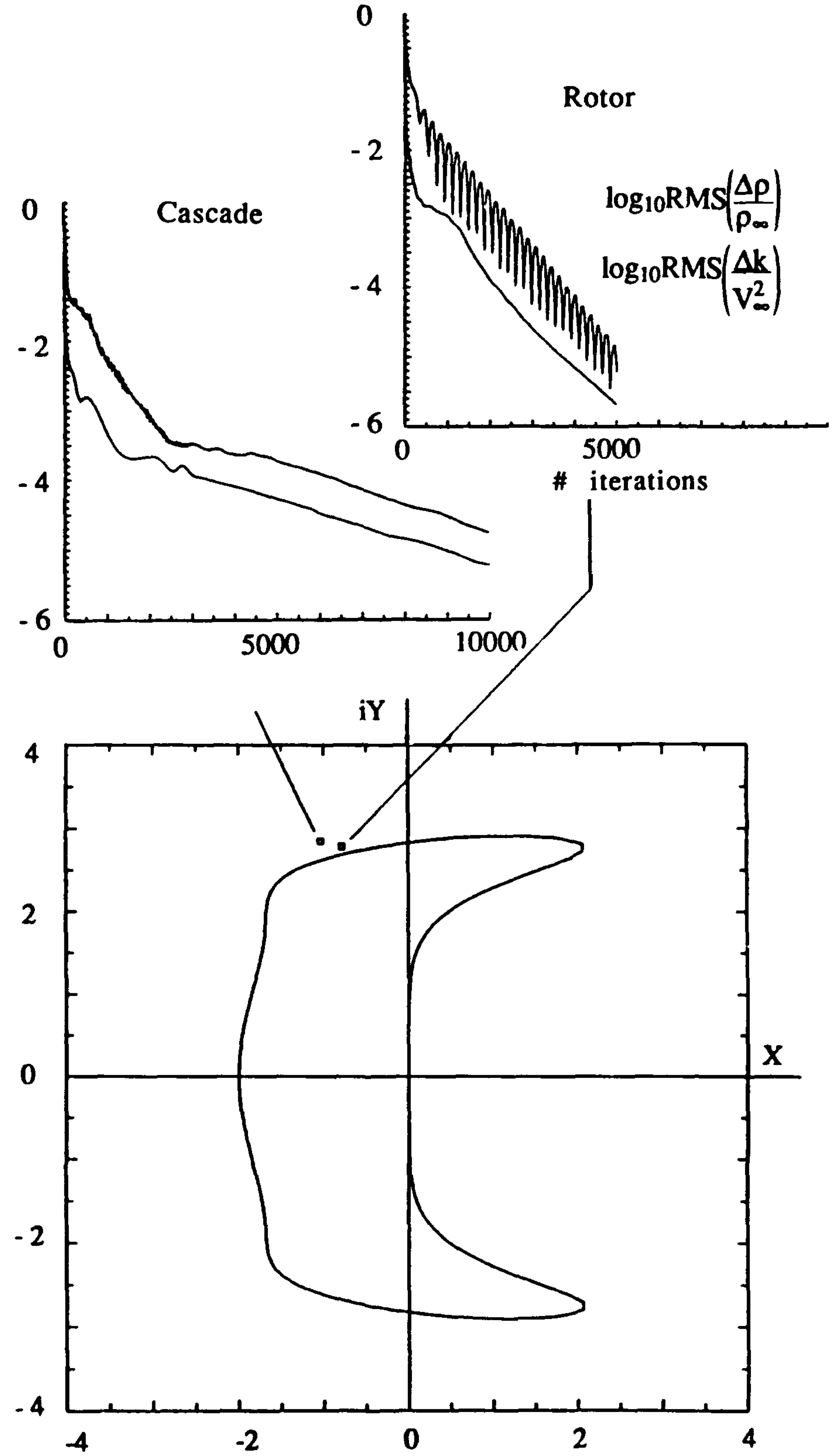

Figure 3.13 Location of numerical operating point, (CFL_{op}, Ω_{op}), for full scale cascade and rotor flow computations, plotted in the complex Z plane with the stability boundary for the RK4 scheme used. Corresponding convergence histories for these two calculations are also included.

"production" runs also appear there. This figure provides additional support to the validity of the foregoing analyses in application to full scale engineering computations.

3.4 Numerical Implementation and Stability of Algebraic Reynolds Stress Model

In Chapter 2, a hybrid algebraic Reynolds stress model was introduced. Equations [2.14] are implemented directly in the flow solver as follows. The nonlinear coupled algebraic system defined by equation [2.14] can be implemented by lagging the turbulence energy production term, P, by one iteration or by using the production of turbulence kinetic energy obtained from the 2-equation model. The latter approach is adopted here. If the machine axis is chosen to be coincident with the x-axis (no loss of generality), the cartesian components of the rotation production tensor (equation [2.14]) are simplified. The resulting 6 x 6 algebraic linear system of equations become $A\ R = B$ where :

A = [3.56]

$$\begin{bmatrix}
1+L[k_2(\frac{4}{3}u_x)] & L[k_2(-\frac{2}{3}v_y)] & L[k_2(-\frac{2}{3}w_z)] & L[k_2(\frac{4}{3}u_y-\frac{2}{3}v_x)] & L[k_2(\frac{4}{3}u_z-\frac{2}{3}w_x)] & L[k_2(-\frac{4}{3}v_z-\frac{2}{3}w_y)] \\
L[k_2(-\frac{2}{3}u_x)] & 1+L[k_2(\frac{4}{3}v_y)] & L[k_2(-\frac{2}{3}w_z)] & L[k_2(\frac{4}{3}v_x-\frac{2}{3}u_y)] & L[k_2(-\frac{2}{3}u_z-\frac{2}{3}w_x)] & \begin{array}{c} L[k_1(-4\Omega)+ \\ k_2(\frac{4}{3}v_z-\frac{2}{3}w_y)] \end{array} \\
L[k_2(-\frac{2}{3}u_x)] & L[k_2(-\frac{2}{3}v_y)] & 1+L[k_2(\frac{4}{3}w_z)] & L[k_2(-\frac{2}{3}u_y-\frac{2}{3}v_x)] & L[k_2(\frac{4}{3}w_x-\frac{2}{3}u_z)] & \begin{array}{c} L[k_1(4\Omega)+ \\ k_2(\frac{4}{3}w_y-\frac{2}{3}v_z)] \end{array} \\
L[k_2(v_x)] & L[k_2(u_y)] & 0 & 1+L[k_2(v_y+u_x)] & \begin{array}{c} L[k_1(-2\Omega)+ \\ k_2(v_z)] \end{array} & L[k_2(u_z)] \\
L[k_2(w_x)] & 0 & L[k_2(u_z)] & \begin{array}{c} L[k_1(2\Omega)+ \\ k_2(w_y)] \end{array} & 1+L[k_2(w_z+u_x)] & L[k_2(u_y)] \\
0 & \begin{array}{c} L[k_1(2\Omega)+ \\ k_2(w_y)] \end{array} & \begin{array}{c} L[k_1(-2\Omega)+ \\ k_2(v_z)] \end{array} & L[k_2(w_x)] & L[k_2(v_x)] & 1+L[k_2(w_z+v_y)]
\end{bmatrix}$$

$$R = [\overline{-\rho u_1'' u_1''},\ \overline{-\rho u_2'' u_2''},\ \overline{-\rho u_3'' u_3''},\ \overline{-\rho u_1'' u_2''},\ \overline{-\rho u_1'' u_3''},\ \overline{-\rho u_2'' u_3''}]^T,$$

$$B = [\frac{2}{3}\rho k,\ \frac{2}{3}\rho k,\ \frac{2}{3}\rho k,\ 0,\ 0,\ 0]^T$$

and $L = \frac{\rho k}{P + \rho\varepsilon k_3}$, $k_1 = \frac{2-C_2}{2}$, $k_2 = 1-C_2$, $k_2 = C_1 - 1$, with $C_1 = 1.5$, $C_2 = 0.6$ as empirically obtained (Launder et al. (1975)) FRS modelling constants.

System [3.56] is solved at every grid point directly by Gaussian elimination [subroutine provided by Rao (1982)].

The direct inversion of a linear 6 x 6 system of equations at every grid point, at every iteration would be prohibitive computationally. Numerical experimentation has shown that evaluating the Reynolds stresses every 20 iterations (while reevaluating viscous fluxes every iteration for stability) gives rise to a convergent procedure.

Recalling the effective stress tensor for the ARS model :

$$\tau_{ij} = \mu_l \left[\left(\frac{\partial u_i}{\partial x_j} + \frac{\partial u_j}{\partial x_i} \right) - \frac{2}{3} \delta_{ij} \frac{\partial u_k}{\partial x_k} \right] \qquad - \rho k T_{ij} \qquad - \frac{2}{3} \delta_{ij} \rho k \qquad [2.15]$$

By comparison, the effective stress tensor for the two-equation model used can be written :

$$\tau_{ij} = \mu_l \left[\left(\frac{\partial u_i}{\partial x_j} + \frac{\partial u_j}{\partial x_i} \right) - \frac{2}{3} \delta_{ij} \frac{\partial u_k}{\partial x_k} \right] + \mu_t \left[\left(\frac{\partial u_i}{\partial x_j} + \frac{\partial u_j}{\partial x_i} \right) - \frac{2}{3} \delta_{ij} \frac{\partial u_k}{\partial x_k} \right] - \frac{2}{3} \delta_{ij} \rho k \qquad [3.57]$$

So for the ARSM, an "anisotropic eddy viscosity" can be identified :

$$\mu_{tij} = \frac{-\rho k T_{ij}}{\left[\left(\frac{\partial u_i}{\partial x_j} + \frac{\partial u_j}{\partial x_i} \right) - \frac{2}{3} \delta_{ij} \frac{\partial u_k}{\partial x_k} \right]} \qquad [3.58]$$

It has been found that this identification is useful in evaluating the numerical stability of the turbulence model. Specifically, if the individual components of μ_{tij}, as defined by equation [3.58], are all of the same order of magnitude as μ_t provided by the k-ε model, then the effective diffusivity arguments provided in the stability analysis of Section 3.3.3.3 remain valid. That is, the eddy viscosity computed in the k-ε solution can still be used to provide a local stable timestep, and the convergence rate of the numerical scheme should not be significantly affected, when the ARSM is used.

To illustrate this, a flat plate turbulent flow computation was performed using

1) the low Reynolds number k-ε model, 2) the pure high Reynolds number ARSM, 3) the hybrid model, with $y^+_{match} = 200$. The convergence history for the computation using the hybrid model showed some "peaking" behavior during the course of iteration. This phenomena was traced to grid points whose local y^+ values were very close to y^+_{match} during iteration. If this local value crosses y^+_{match}, the other turbulence model is suddenly used locally, and this gives rise to a very large local residual which in turn strongly affects the RMS residual. To alleviate this problem, a weighting function approach was devised, which blends the two models near y^+_{match}. Specifically the viscous residuals are weighted as follows :

$$\hat{R}_{viscous} = W_{ARSM}\hat{R}_{ARSM} + W_{k\text{-}\varepsilon}\hat{R}_{k\text{-}\varepsilon}$$

where $$W_{ARSM} = \frac{1}{2}\left(\frac{\tanh\left(\beta\left[\frac{y^+}{y^+_{match}} - 1\right]\right)}{\tanh(\beta)} + 1 \right), \quad W_{k\text{-}\varepsilon} = 1. - W_{ARSM} \qquad [3.59]$$

These weighting functions are plotted in Figure 3.14, for a clustering parameter $\beta = 10.0$, which is the value used in the calculations presented using the hybrid model in this thesis. In Figure 3.15, the convergence history for the blended hybrid model is seen to closely compare to those of the two component models, thereby substantiating the stability argument presented above for this case.

In the first section of the next chapter, the results of these flat plate computations are presented.

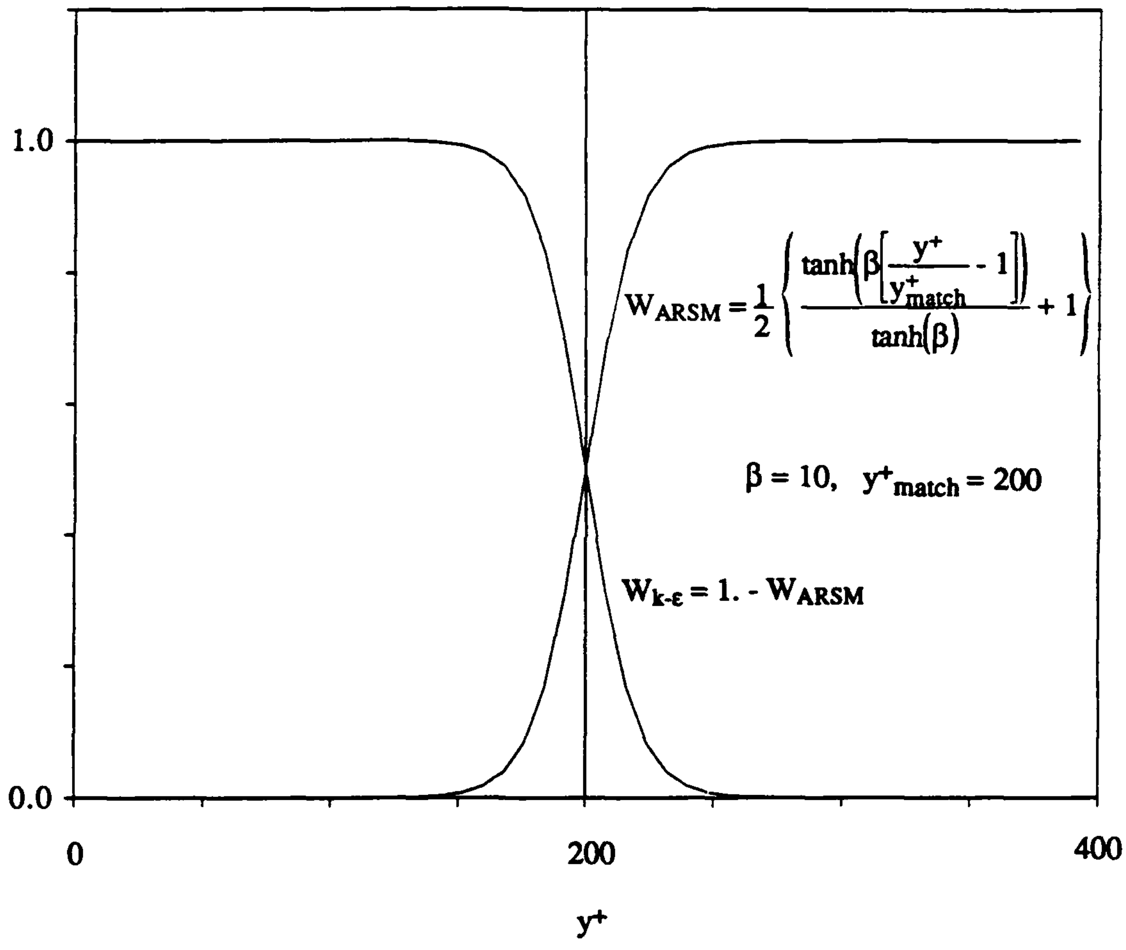

Figure 3.14 Blending function for hybrid turbulence model.

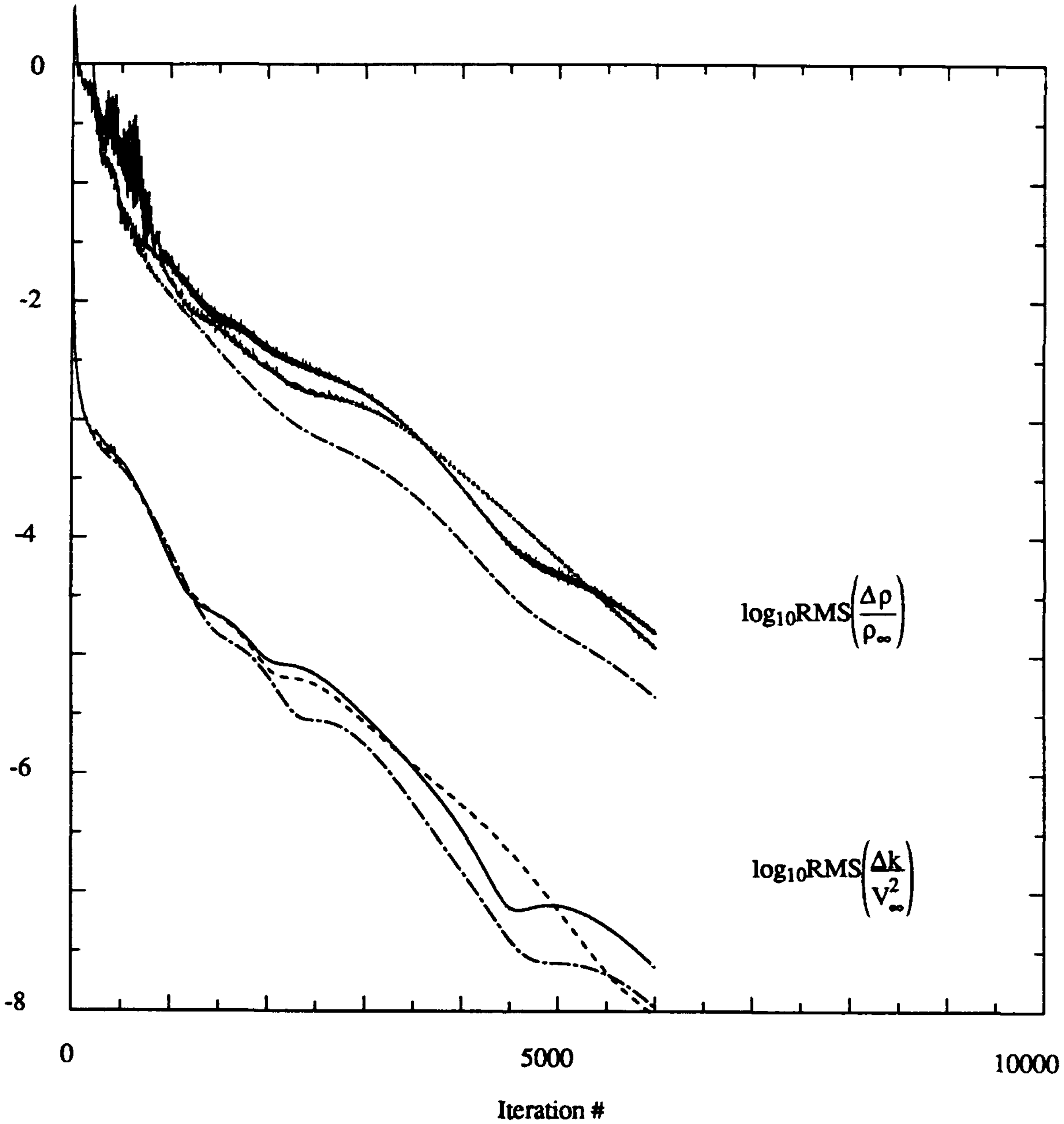

Figure 3.15 Convergence histories for turbulent flat plate flow computations. Low Reynolds number k-ε model (alternating long dash-short dash), high Reynolds number ARSM model (solid), hybrid model, blending function, equation [3.63] used (short dash).

3.5 Computational Considerations

At the time of the writing of this thesis, the vectorized code executed at 4.2×10^{-5} CPU seconds / (gridpoint * iteration) on the NAS Cray Y-MP at NASA Ames Research Center, when the low Reynolds number k-ε model is used. As discussed above, the convergence penalty for implementing a two-equation model in a purely explicit procedure is small. The two additional transport equations, which require only partially vectorizable source term and eddy viscosity computations give rise to an overall factor of 1.5 in execution rate over laminar flow computations on a Cray 2. The current overhead associated with computations using the hybrid k-ε/ARS model is an additional 40 % for three-dimensional calculations on the Y-MP. This overhead is due to computation of both k-ε and ARSM viscous flux residuals at every iteration, and re-evaluation of the Reynolds stress components every 20 iterations.

CHAPTER 4

PREDICTION OF TWO-DIMENSIONAL INTERNAL AND CASCADE FLOWS

In this chapter, results and interpretation of two-dimensional flow computations are presented.

Two complex cascade flows are computed, for supersonic and low subsonic freestream conditions. For the supersonic cascade, isentropic blade Mach number, shock-boundary layer structure and wake loss profiles are compared with experimentally measured values. Pressure distribution and boundary layer profiles of velocity and turbulent kinetic energy are compared with data for the subsonic cascade.

4.1 Turbulent Flat Plate Boundary Layer Flow - Turbulence Model Validation

In Chapters 2 and 3, the formulation and numerical implementation of the turbulence models incorporated in this thesis were presented. Stability analysis and numerical verification results, including convergence histories for simple shear layer computations, using a compressible extension of Chien's (1982) low Reynolds number k-ε model and a hybrid k-ε/ARS model, were presented. It remains to present accuracy validation for these computations. These results are provided in this section.

A 33 x 33 computational grid was used for the flat plate computations. The grid and freestream conditions were chosen to provide a Reynolds number based on boundary layer thickness, $R_{e\delta} = 80000$, near the exit of the computational domain. This corresponds to the flat plate measurements of Klebanoff (1954), against which the computational results provided here are compared.

For both turbulence models used, a low Reynolds number k-ε model is used in the very near wall region. Accordingly, it is appropriate, where practically feasible, to provide near wall grid clustering such that $y^+ \cong 1$ at the first grid point off of solid boundaries. This reconciles with the observations of many authors (see Avva et al. (1990), for example), that grid independent solutions using such models require such near wall grid spacing.

To ensure that the first grid point off of solid boundaries, will be near a prespecified value of y^+, a standard empirical momentum integral relation for skin friction on a turbulent developing flat plate flow is used (see Fox and McDonald (1985), for example) :

$$\tau_{\text{wall}} = \frac{\frac{1}{2}\rho_\infty V_\infty^2 (0.0577)}{(\text{Re}_x)^{1/5}} \qquad [4.1]$$

Using the definition of y^+, $y^+_{\text{specified}} = \dfrac{\Delta y_{\text{wall}}\sqrt{\dfrac{\tau_{\text{wall}}}{\rho}}}{\nu}$, an expression for Δy_{wall} can be obtained :

$$\Delta y_{\text{wall}} = \nu y^+_{\text{specified}} \left(\frac{(\text{Re}_L)^{1/5}}{\frac{1}{2} V_\infty^2 (0.0577)} \right)^{1/2} \qquad [4.2]$$

where $\text{Re}_L = \dfrac{V_\infty L}{\nu}$, and L is taken as the plate length (or chord length, as it were). Because Δy_{wall} is a weak function of Reynolds number (proportional to $\text{Re}_L{}^{1/10}$), equation [4.2] provides an appropriate value of Δy_{wall} along the length of the plate.

The grid spacing at the wall for the flat plate computation was 3.1 x 10^{-6} times the plate length. The aspect ratio of near wall grid elements in this extremely highly stretched grid reached 30000 at the aft end of the plate. Uniform total pressure and temperature profiles were specified, and the back pressure was set such that the free stream Mach number was approximately 0.5 to accommodate the compressible formulation of the flow solver. Three calculations were performed, using the low Reynolds number form of the k-ε model, the high Reynolds number form of the ARSM with no near wall treatment, and the hybrid model, with $y^+_{match} = 200$. As shown in Chapter 3, the artificial dissipation levels were scaled by the square of the ratio of local velocity to free stream velocity.

In Figure 4.1, the predicted velocity profiles are plotted in inner variables at $Re_\delta = 80000$, and compared against standard law-of-the-wall correlations. The k-ε and hybrid models match the correlations, whereas the high Reynolds number ARSM shows poor agreement as expected. Klebanoff (1954) measured the turbulent kinetic energy profile in the boundary layer, and his data are used for comparison with predictions of this parameter in Figure 4.2. Again agreement is excellent for the k-ε and hybrid models.

In Figure 4.3, the distribution of turbulence intensities, predicted using the hybrid model are shown, and compared to Klebanoff's measurements. Comparison is good, with the notable exception that the hybrid model does not predict the distribution of energy between $-\overline{\rho u_2'' u_2''}$, $-\overline{\rho u_3'' u_3''}$. This is a direct consequence of not explicitly modelling the pressure strain term, $\phi_{ij,w}$, presented in Chapter 2. Despite this modelling shortcoming, the difference between the streamwise and wall normal intensities, is reasonably well predicted, a prerequisite for predicting the influence of rotation on the turbulence structure in a rotating boundary layer. Specifically, Reynolds shear stress source terms in the full Reynolds stress and algebraic Reynolds stress equations are directly proportional to both the difference between these intensities, and the rotation rate. The location of y^+_{match} is

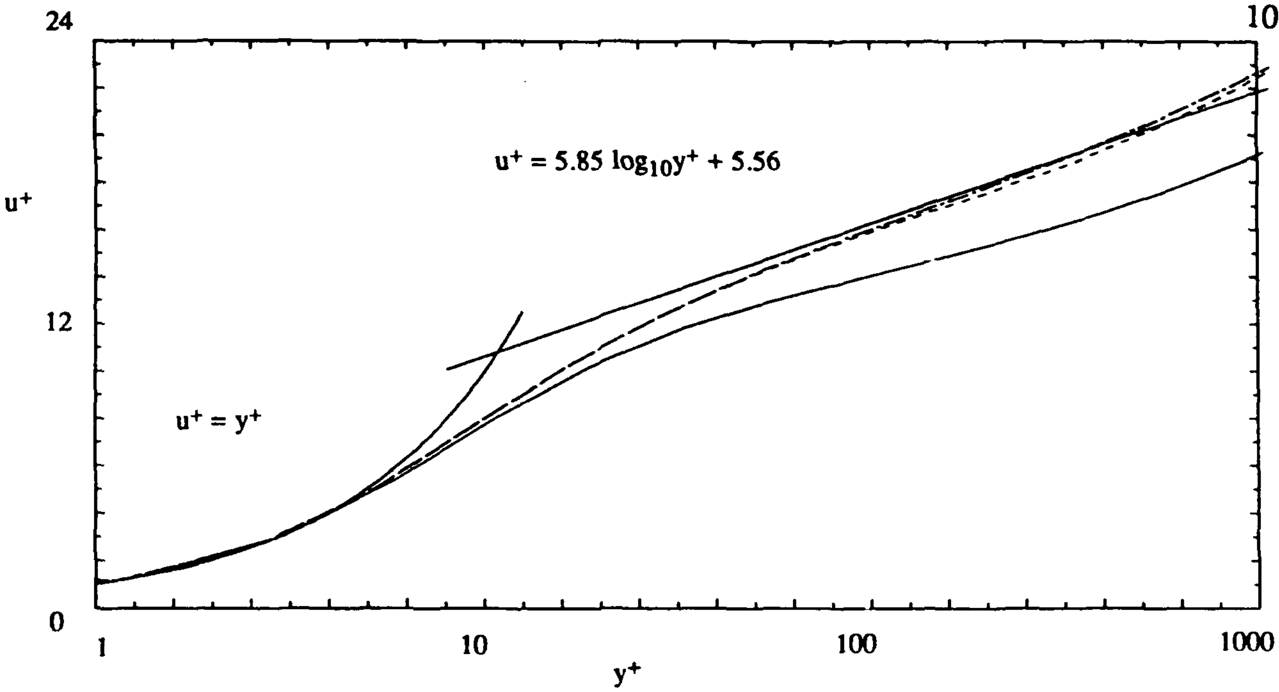

Figure 4.1 Law-of-the-wall predictions for a turbulent flat plate flow computation. Crossing curves represent standard law-of-the-wall relations. Low Reynolds number k-ε model (alternating long dash-short dash), high Reynolds number ARSM model (solid), hybrid model (short dash).

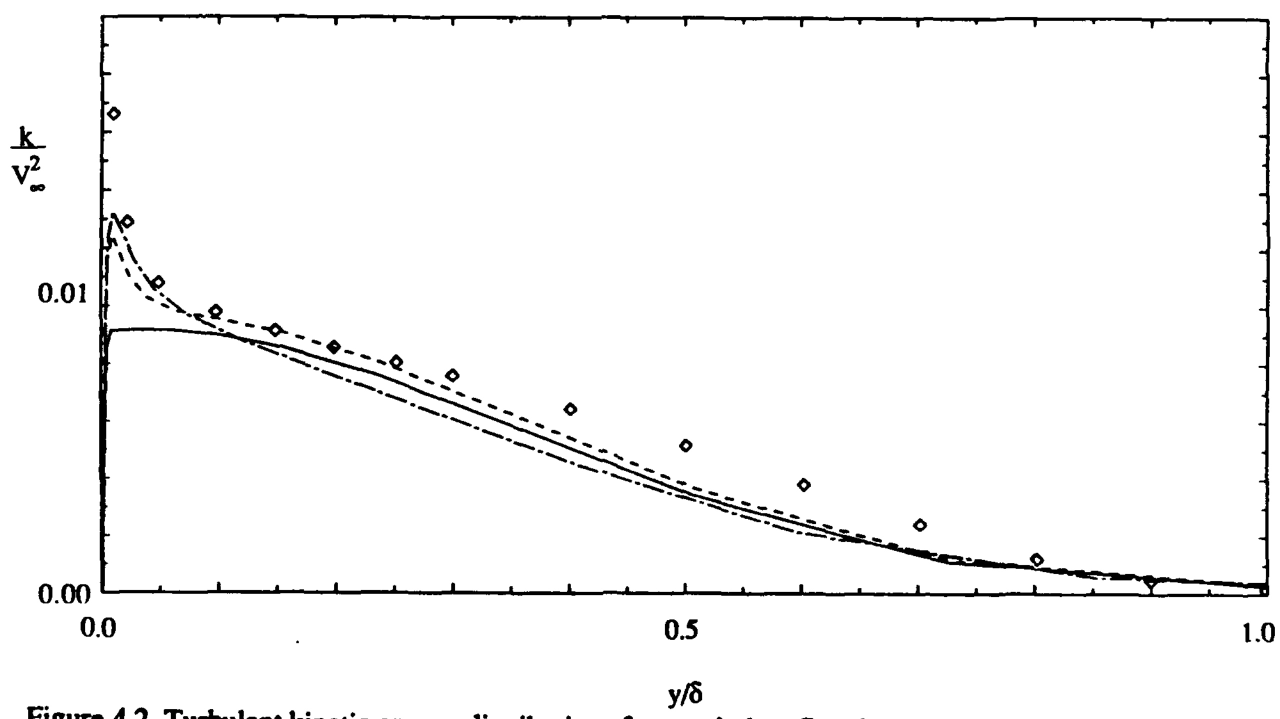

Figure 4.2 Turbulent kinetic energy distributions for a turbulent flat plate flow. Experimental data due to Klebanoff (1954) (symbols). Computations using : low Reynolds number k-ε model (alternating long dash-short dash), high Reynolds number ARSM model (solid), hybrid model (short dash).

indicated in Figure 4.3. Preliminary efforts to validate the hybrid model for an isolated rotational strain case were undertaken. Specifically, a rotating fully developed channel flow, tested experimentally by Johnston et al. (1972), was computed. An appropriate deflection of the mean flow was observed, as was the characteristic redistribution of Reynolds intensities near the leading and trailing sides of the channel. Unfortunately a converged solution for this flow was not attainable due to the compressible formulation of the flow solver, and the fully developed nature of the measured channel flow. It is anticipated that appropriate validation against a developing boundary layer subject to spanwise rotation will provide more precise validation in regards to isolated rotational strain.

The following cascade computations were performed with an earlier version of the code , where the k and ε equations were numerically decoupled (as defined in Chapter 3) from the mean flow equations. Additionally, the cases were run in laminar mode for several hundred iterations before the k-ε model was turned on (see convergence histories below). This strategy was used by the author in earlier versions of the code, to help reduce the size of production terms in the turbulence transport equations upon "cold-start" initialization.

4.2 Turbulent Flow Through a Supersonic Compressor Cascade Operating at Unique Incidence Condition

The first cascade to be investigated is the PAV-1.5 supersonic compressor cascade tested at DFVLR by Schreiber (1988). This pre-compression blade was designed especially to investigate shock-boundary layer interaction with separation. At the test freestream Mach number, a standoff leading edge shock forms, which gives rise to a separated shock-boundary layer interaction aft of mid chord on the suction surface of the

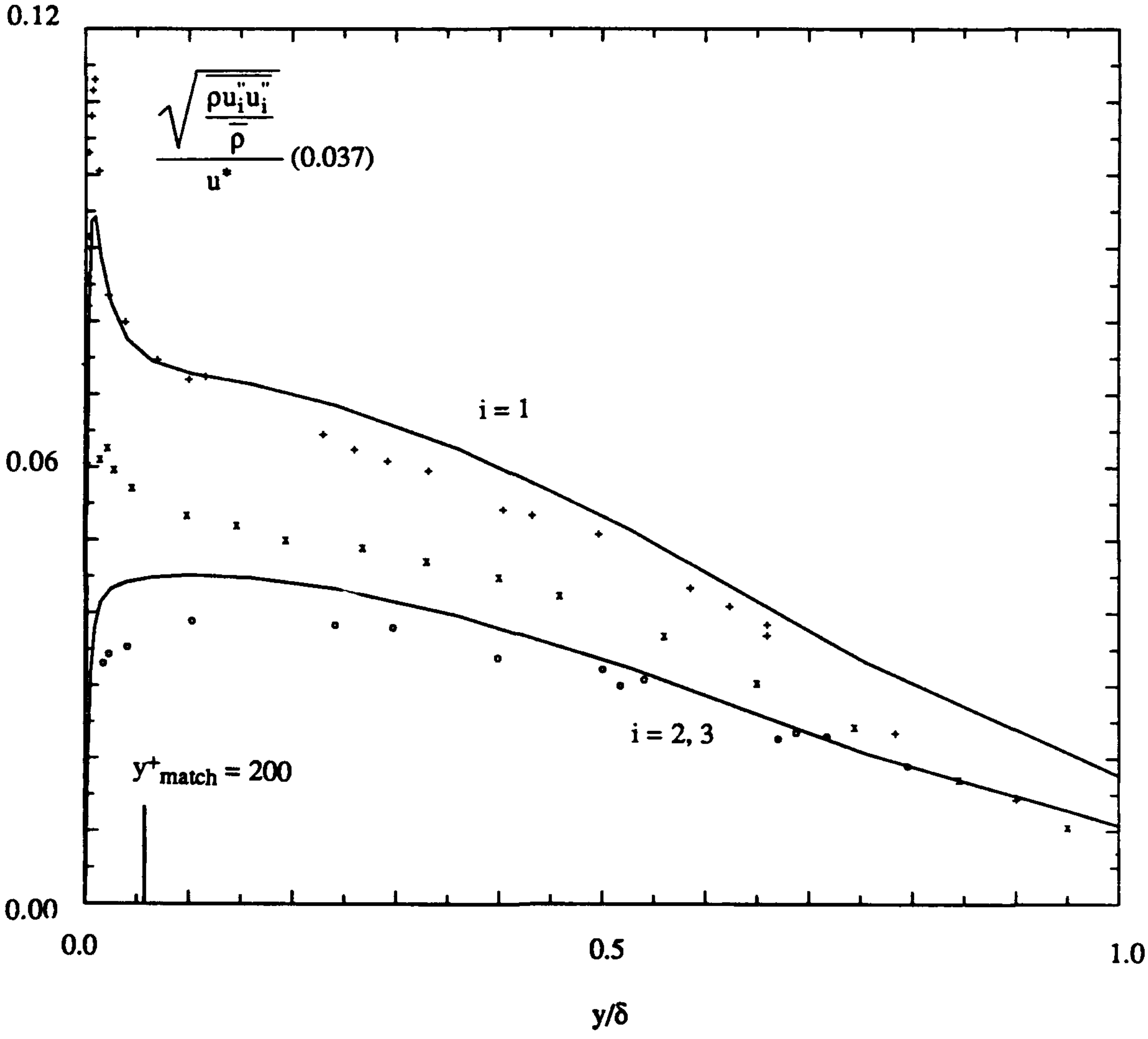

Figure 4.3 Boundary layer Reynolds normal stress distributions for a turbulent flat plate flow. Experimental data due to Klebanoff (1954) : streamwise intensity (++++ symbols), plate normal intensity (oooo symbols), crossflow intensity (xxxx symbols). Computations using hybrid model (solid line).

adjacent passage. Though the measured absolute inlet Mach number was supersonic, the blade row stagger angle was high so the axial component of the inlet velocity was subsonic. This gives rise to the "unique incidence" condition wherein there exists a fixed relationship between inlet Mach number and inlet flow angle. This phenomena as well as the complex wave interaction field within the passage and shock-boundary-layer interaction provide a challenging test case for both numerical scheme and turbulence model. Prediction of the unique incidence angle requires reasonably good resolution of both the leading edge geometry and the leading edge shock structure.

The computed case was experimentally tested in air at an inlet Mach number of 1.53 and a maximum attainable static pressure ratio of 2.13. The measured axial velocity density ratio (AVDR) of 1.02 indicated that the flow was close to two-dimensional. The Reynolds number based on chord was 2.7 x 10^6. The inlet turbulence intensity was measured using a Laser-two-focus (L2F) velocimeter to be no more than 1 %, which is the value used in the computations. As mentioned above, the inlet Mach number is supersonic, but axial velocity at the inlet to the computational domain is subsonic allowing left running characteristics to propagate out of the inlet plane. For this reason, subsonic inlet boundary conditions were specified : $p_o = 101325$ N/m^2, $T_o = 300$ K, $V_{\theta\infty} = 379.5$ m/s. At the subsonic exit plane the back pressure, $p_e = 56500$ N/m^2, was specified corresponding to the experimentally measured pressure ratio of the cascade, $p_2/p_1 = 2.13$.

The 129 x 100 computational grid used was generated using Sorenson's (1980) GRAPE code, modified by Gorski (1983) to generate H-grids, and is shown in Figure 4.4, where only every other grid line in the ξ and η directions are plotted, for clarity. The blade normal grid spacing at the wall was prescribed as .000011 chord. This yielded values of $y^+ \equiv 1$ at grid points adjacent to the walls. Except in the immediate vicinity of the leading

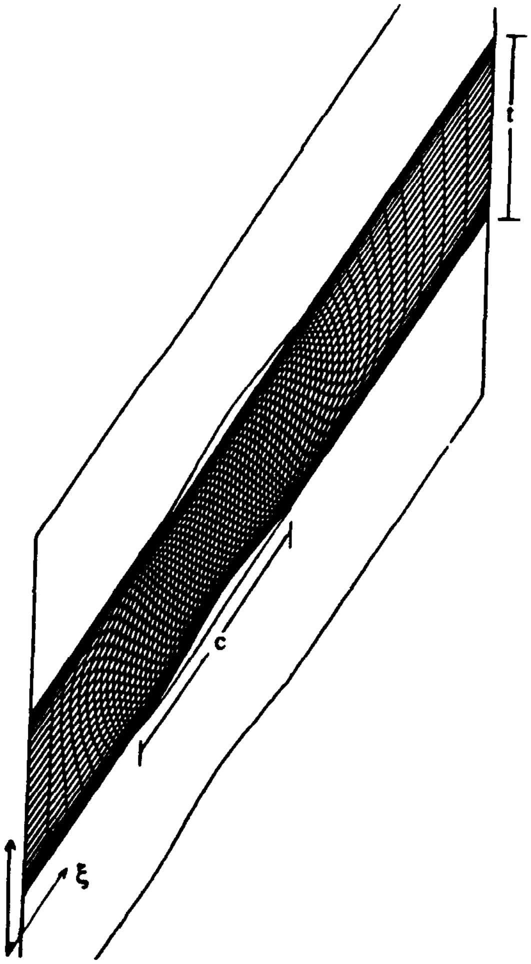

Figure 4.4 129 x 100 computational grid for the PAV-1.5 cascade.

For clarity, only every other grid line is shown in both ξ and η directions.

and trailing edges, the suction and pressure surface boundary layers had at least 9 grid points with values of $y^+ \leq 20$.

The convergence history for this computation is shown in Figure 4.5. It took approximately 6500 iterations for this calculation to converge as measured by the invariance of total number of supersonic gridpoints in the field. It was not possible to "cold start" the initialized flowfield at the specified pressure ratio, because the code became rapidly unstable when this was attempted. Rather, the back pressure had to be increased in a stepwise fashion with iteration (notice "jumps" in convergence at iteration 500, 1000, 2000), until the experimentally imposed pressure ratio could be specified at iteration 2000. The "unhealthy" convergence history is due in part to the highly clustered grid and also to the nearly choked operating condition.

At the time it was run, the solution using the two-dimensional version of the code required approximately 40 minutes of CPU time on a Y-MP. For this cascade computation, $\Delta t_v < \Delta t_c$ for 40.0% of the grid points in the domain at convergence. The artificial dissipation was scaled as in equation [3.20], where the reference velocity, $V_{ref} = a_\infty M_\infty$, was used. With this scaling, a significant recirculation zone exists aft of a shock boundary layer interaction region aft of mid-chord on the suction surface. This region, extends well out into the passage ($nj \cong 25$), and reattaches a short distance downstream. When the velocity scaling was used exactly as presented in Chapter 3, significant local oscillations in flowfield properties were seen to develop in this region, immediately prior to the code blowing up. This is not surprising since though local velocities are small in the recirculation zone, physical diffusion terms in the momentum equations are also small. Therefore, significant artificial dissipation is required to stabilize the solution in this region. The solution was stabilized in an "ad-hoc" fashion for this calculation, by implementing the

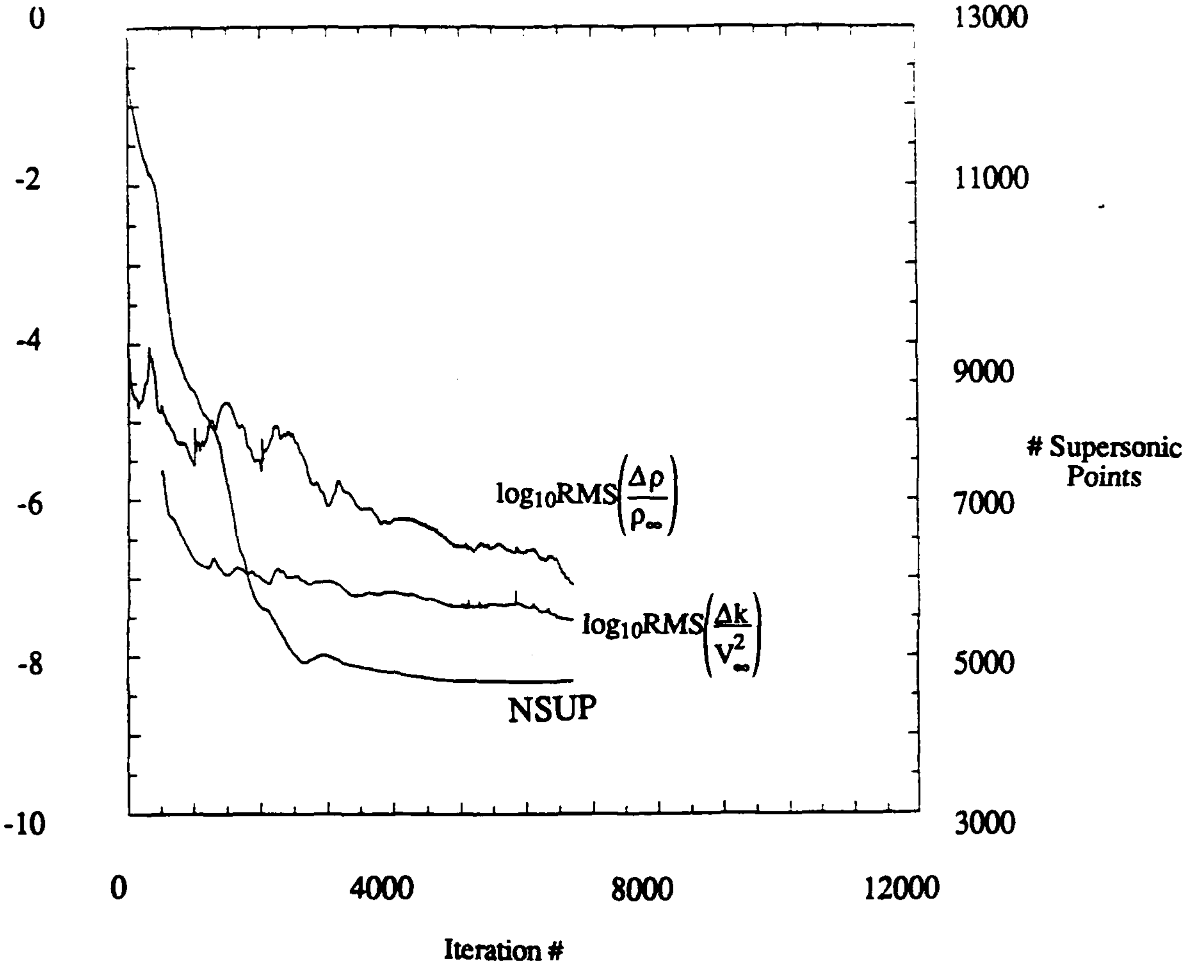

Figure 4.5 Convergence history for PAV-1.5 cascade computation.

velocity scaling given in equation [3.20], only in the immediate vicinity of the blade surfaces ($j < j_{specified}$).

In Figure 4.6, a hand rendering of the shock wave pattern deduced from Schlieren visualization has been reproduced from Schreiber (1988), alongside the computed shock wave pattern presented as divergence of velocity contours. The key features of the flowfield are evident in this diagram, including the bow, lamda and passage shocks. In both experiment and computation, the bow shock is seen to impinge on the suction surface boundary layer of the adjacent passage. This gives rise to a lambda shock structure, a rapid thickening and separation of the boundary layer, and a Mach reflection which impinges on the pressure surface of the same passage. The high pressure ratio operating condition of this test case gives rise to a normal passage shock which impinges upstream of midchord on the pressure surface. This feature is also evident in both experiment and computation. The computation also shows some evidence of an oblique trailing edge shock, typical of supersonic compressor cascades at high operating pressure ratios.

In Figure 4.7, the predicted isentropic blade surface Mach number is plotted against the experimental values. The calculation and experiment show fairly good agreement. The features labelled A, B and C in Figure 4.7 correspond to local compression regions where the bow shock impinges on the suction surface, the Mach reflection impinges on the pressure surface and the passage shock impinges on the pressure surface.

In Figure 4.8, the computed total pressure ratio is compared with traverse probe measurements at an axial location 0.09 chord downstream of the cascade exit plane. The wake profile and loss distribution is reasonably well predicted, with the losses associated with the lambda shock system underpredicted. The wake centerline total pressure ratio is

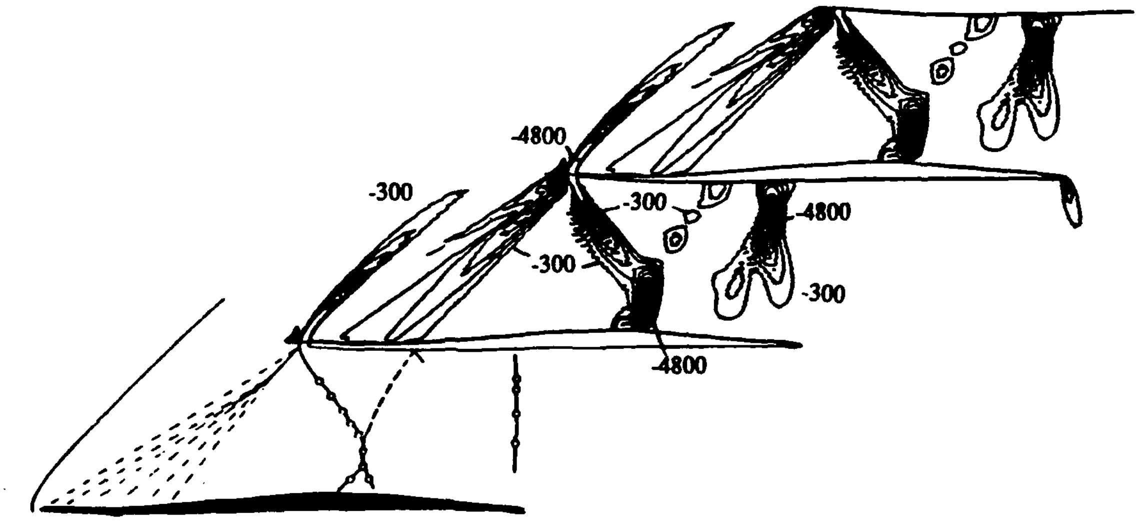

Figure 4.6 Shock wave pattern for PAV - 1.5 cascade. Divergence of velocity contours (-300 to -4800 by -500 [s^{-1}]). In this diagram, the top two passages show computed contours. The bottom passage is the shock wave pattern deduced from flow visualization and L2F measurements, adapted from Schreiber (1988).

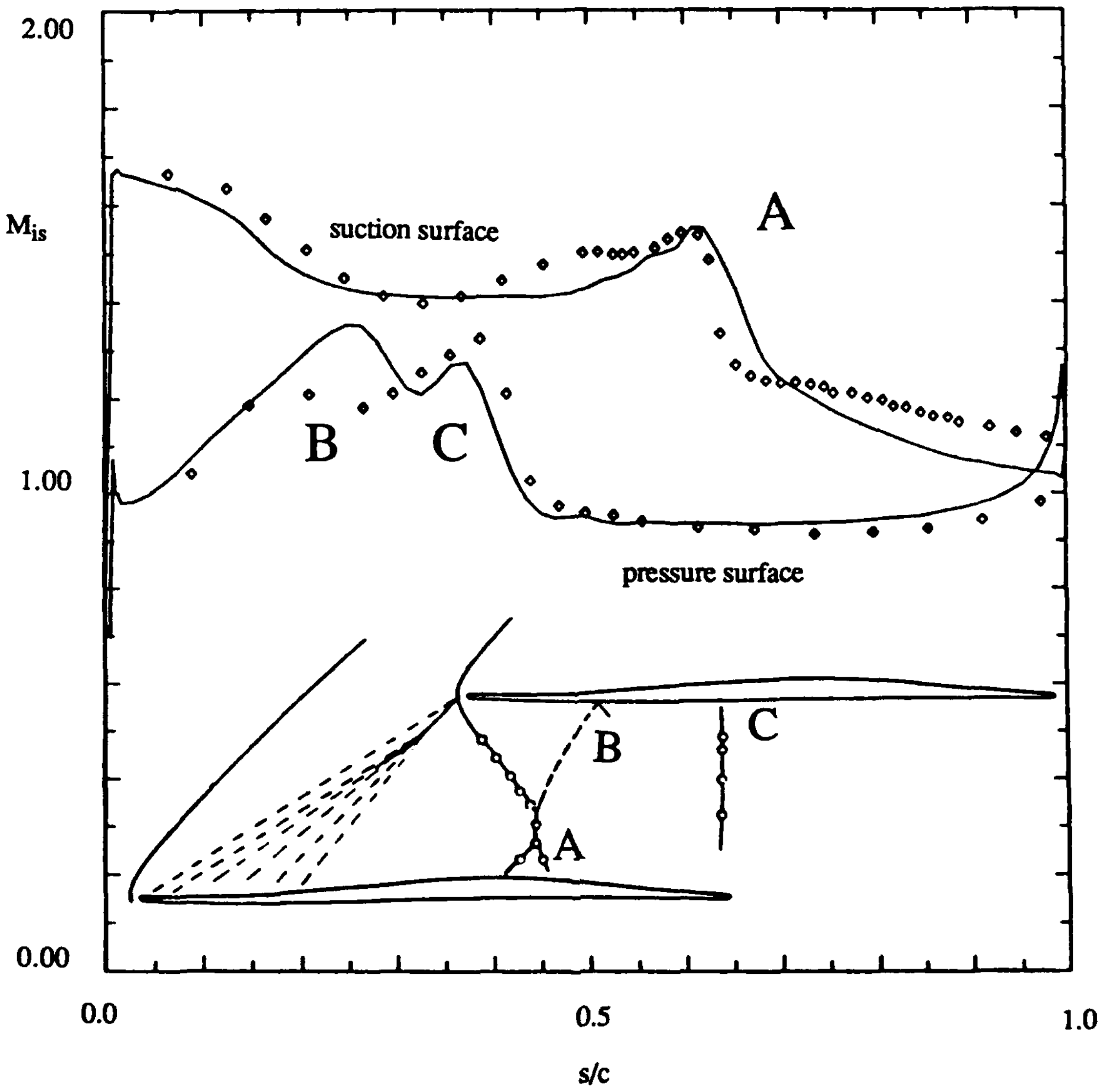

Figure 4.7 Isentropic blade surface Mach numbers and shock structure identification for PAV-1.5 cascade computation. Calculated (solid line) and experimental values (symbols). The bottom half of the plot shows the shock wave pattern deduced from flow visualization and L2F measurements, adapted from Schreiber (1988).

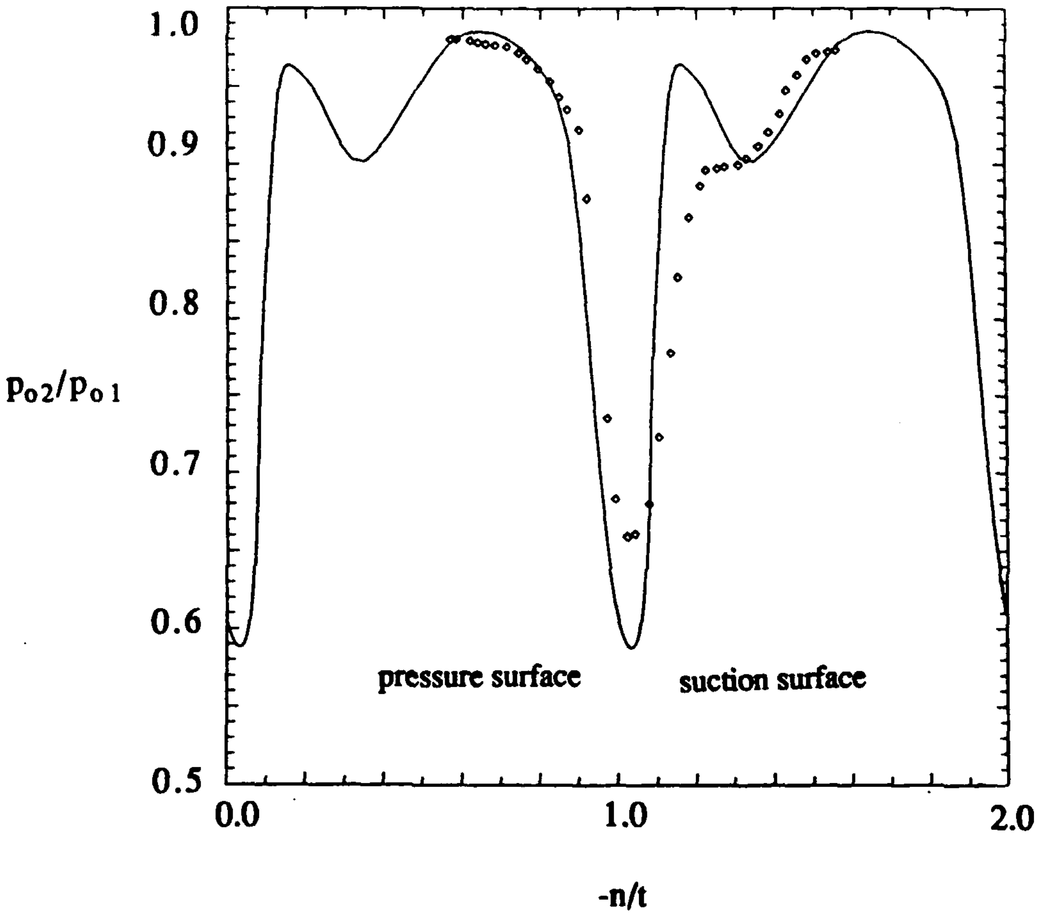

Figure 4.8 Total pressure ratio profile 0.09 chord downstream of trailing edge for PAV-1.5 cascade computation. Calculated (solid line) and experimental values (symbols).

predicted reasonably well considering the difficulty in L2F measurement at this location. It is noted that the results presented are not fully grid independent. Small changes in the pitchwise grid clustering near midpassage gave rise to as much as a 2% chord difference in the impingement location of the bow shock on the suction surface and a 5% chord difference in the location of the passage shock. The loss distribution aft of the blade was hardly affected, but the blade surface Mach number distributions varied noticeably.

In Figure 4.9, computed velocity and turbulence intensity profiles at four locations on the suction and pressure surfaces are presented. Along the suction surface, the predicted boundary layer is seen to remain quite thin for this high Reynolds number flow, thickening to about .01 chord at midchord. At .75 chord the boundary layer has separated due to the bow shock impinging at .67 chord, and the boundary layer thickness is seen to have rapidly increased to approximately .03 chord. At .90 chord, the separated boundary layer has grown to .05 chord. The turbulence intensity profile behaves in a manner consistent with a boundary layer separation. Namely, aft of the onset of separation the turbulent kinetic energy boundary layer thickens rapidly and the peak in intensity appears well away from the blade surface. Careful examination of Figure 4.9 also shows that the turbulence intensity has been amplified well outside of the boundary layer. This amplification is presumably due to the influence of the shock on the normal stress components of the production term in the turbulent kinetic energy equation.

The predicted boundary layers along the pressure surface are seen to remain quite thin along the entire blade. The influence of the passage shock at .40 chord separates the boundary layer at .50 chord, but the flow reattaches and the boundary layer thickness remains approximately .02 chord from .75 to .90 chord. Similar trends are noticed in the local turbulence intensity profiles, with the typical peak away from the blade just aft of separation, returning very close to the wall some distance after reattachment.

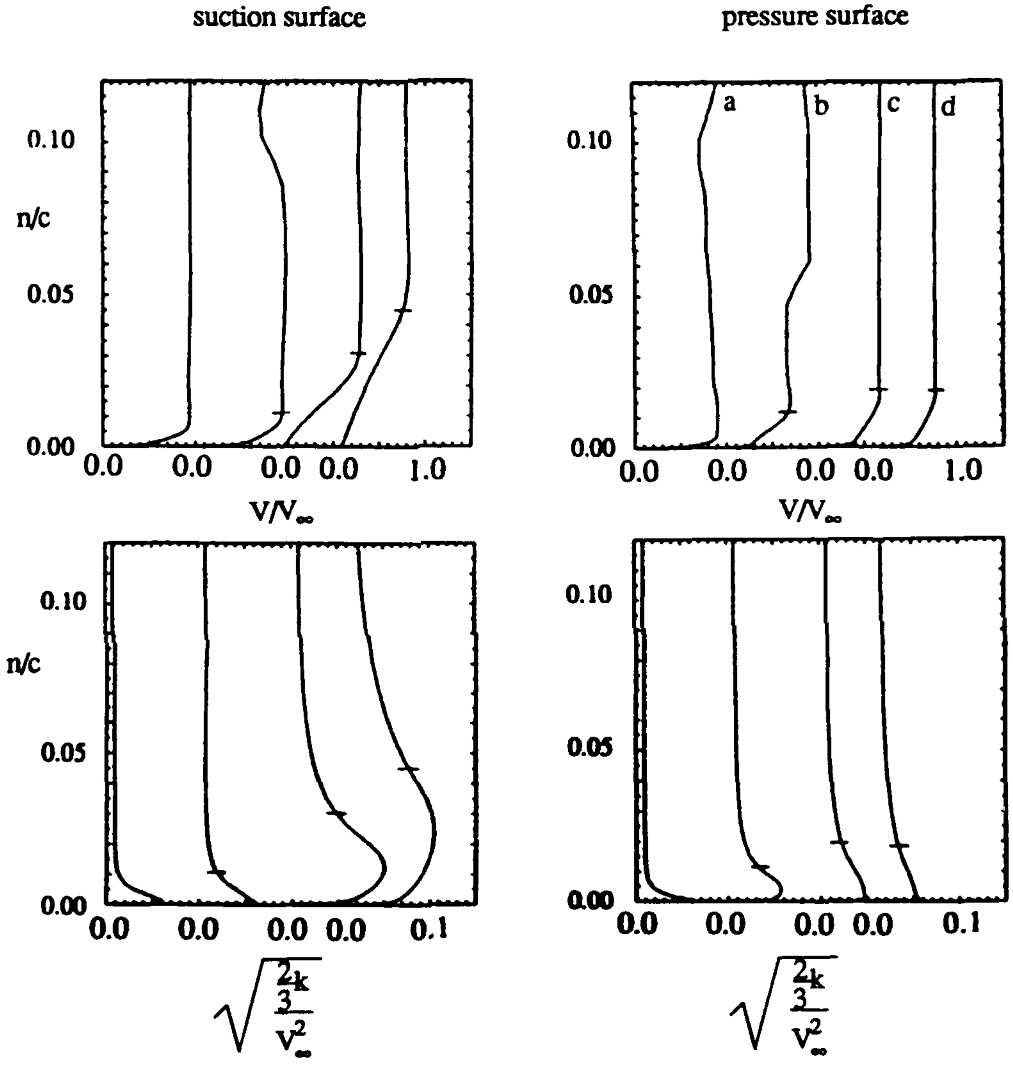

Figure 4.9 Local boundary layer velocity and turbulence intensity profiles at four chord locations along the suction and pressure surfaces for the PAV-1.5 cascade computation. Locations a, b, c, d correspond to .25, .50, .75, .90 chord respectively. The hash marks correspond to the estimated boundary layer thicknesses reported by Schreiber (1988).

Schreiber (1988) provided measured loss coefficients at maximum attainable cascade pressure ratio for a number of operating inlet Mach numbers. For comparison, the code was run at two additional operating points within the envelope of the experimental tests ($p_2/p_1 = 2.01$, $M_{inlet} = 1.45$ and $p_2/p_1 = 2.28$, $M_{inlet} = 1.58$). Figure 4.10 shows computed total pressure loss coefficients at all three operating points computed along with the envelope of experimental loss coefficients. Computed values lie within the envelope of experimental values. It is noted that Schreiber attributes the scatter in measured loss coefficient to variations in experimental axial velocity density ratio.

Predicted and measured performance parameters for this cascade, operating at the design condition ($p_2/p_1 = 2.13$, $M_{inlet} = 1.53$) are presented in Table 4.1.

Table 4.1. Comparison of Performance Parameters for PAV-1.5 Cascade

Flowfield Parameter	Measured	Computed	Difference
C_L[a]	≅ 0.43	0.38	≅ 12 %
ω[b]	0.144	.149	3.4 %
β_1	-1.8°	-1.3°	0.5°
β_2	2.7°	3.1°	0.4°
$s/c_{sep_{ss}}$	.63	.67	6.3 %
$s/c_{sep_{ps}}$	≅ 0.40	.40	≅ 0.0
AVDR	1.02	1	NA

[a] lift coefficient computed from $C_L = \dfrac{(\text{Lift per unit span})_{\perp V_m}}{.5\rho_m V^2_m}$.

[b] pressure loss coefficients computed from $\omega = \dfrac{p_{o\infty} - p_o}{p_{o\infty} - p_\infty}$.

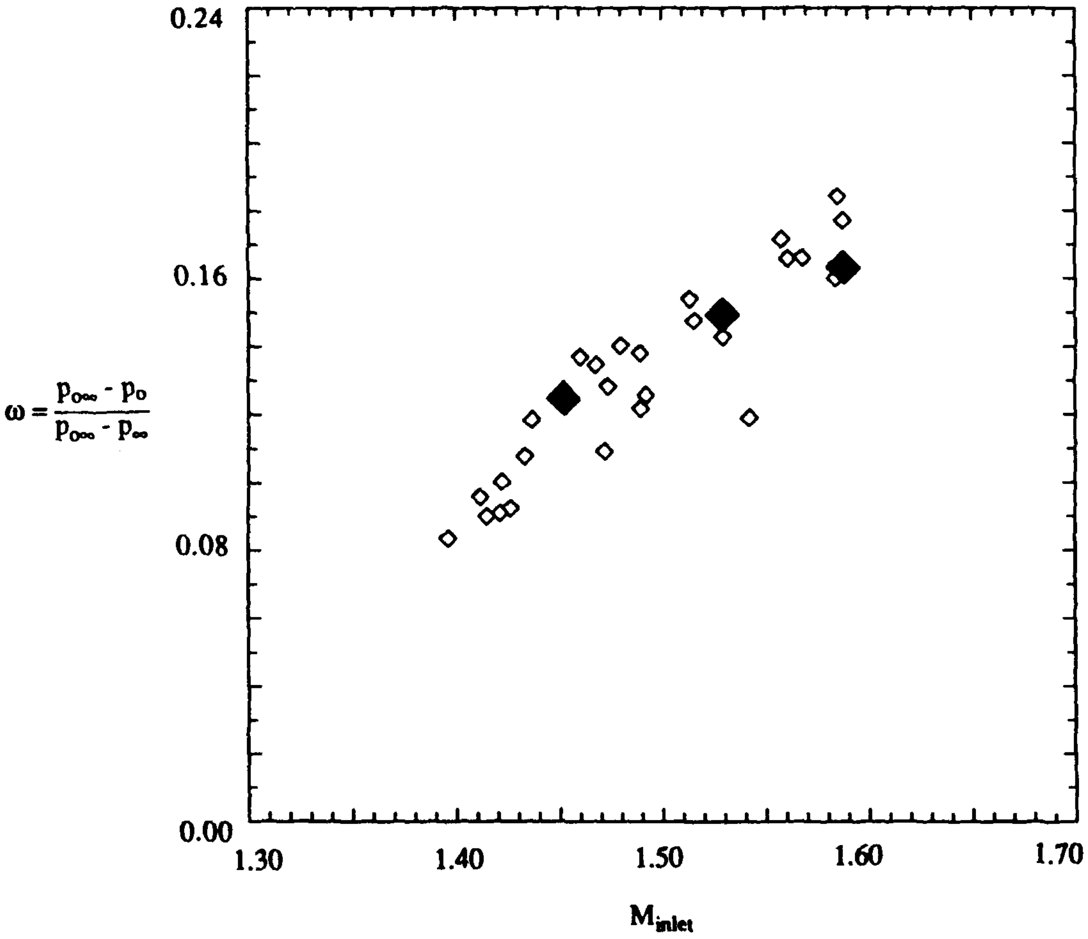

Figure 4.10 Total pressure loss coefficients at several cascade operating points. Calculated (solid symbols) and experimental values (open symbols).

4.3 Turbulent Flow Through a Subsonic Cascade of Double Circular Arc Profiles with Flow Reversal

The second cascade flow to be computed is the Applied Research Laboratory (ARL) double circular arc cascade tested at Penn State by Zierke and Deutch (1989). The computed case was tested at a negative incidence of 1.5 degrees. The working fluid was air at standard atmosphere with an inlet velocity of 32.9 m/s (inlet Mach number = 0.1). The Reynolds number based on chord was 5.0×10^5. Freestream turbulence intensity was measured at 1.8 % at 20 % chord along the suction surface, which is the value used in the computation. The axial velocity ratio was measured to be between 0.97 and 1.03, indicating that the flow was close to two-dimensional.

The 129 x 91 computational grid used was generated using the GRAPE code, and is shown in Figure 4.11. Grid spacing in the blade normal direction was set to .000023 chord on the blade surfaces. This yielded values of $y^+ \cong 1$ at grid points adjacent to the walls. Except in the immediate vicinity of the leading and trailing edges, the suction and pressure surface boundary layers had at least 11 grid points with values of $y^+ \leq 20$.

It was only possible to obtain a steady solution when a coarse "preliminary" grid was used for this case. These coarse grid calculations overpredicted skin friction along the entire length of the suction surface, so the flow remain attached and a steady state solution was achieved. The more refined grid, shown in Figure 4.11, adequately resolved both inner layer and core flow regions yielding more accurate skin friction and boundary layer profiles. However, because both calculation and experiment show regions of mean flow reversal near the trailing edge, it was not possible to obtain a steady solution.

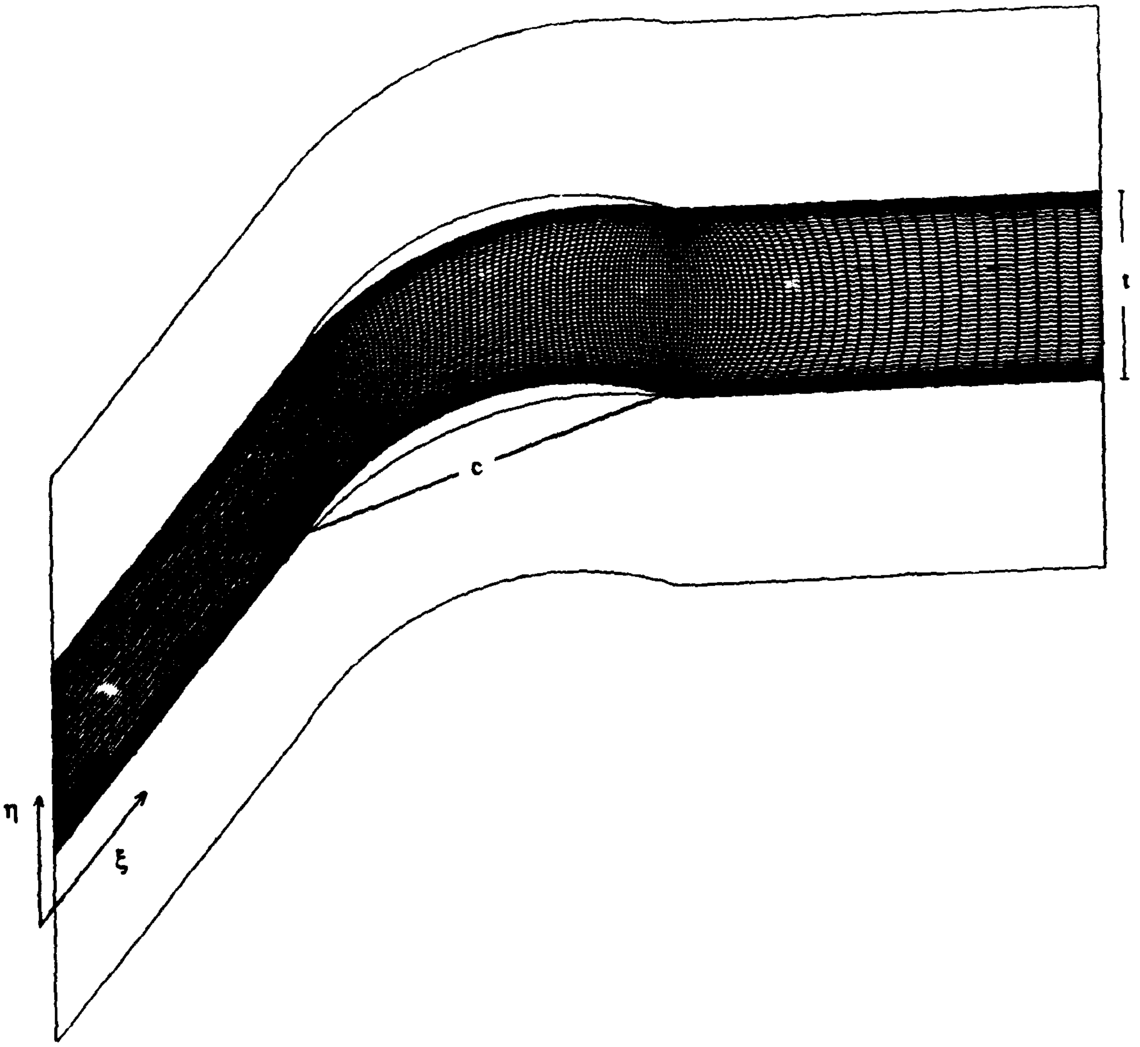

Figure 4.11 129 x 85 Computational grid for the ARL DCA cascade.

The convergence history for this computation is shown in Figure 4.12. It took approximately 7000 iterations for this calculation to acquire a 4.5 order of magnitude drop in the RMS density residual. At the time this computation was performed, this corresponded to approximately 36 minutes of CPU time on the Y-MP. However as shown in Figure 4.12, after 7000 iterations, the residual changes begin to increase and then level off. This is attributed to periodic shedding of vorticity from the aft portion of the suction surface. For this cascade computation, $\Delta t_v < \Delta t_c$ for 7.5 % of the grid points in the domain when the calculation was stopped at 14000 iterations.

Despite the lack of a steady state solution, the flow along the blade remained relatively unchanged after 7000 iterations except for quasi-periodic shifts in the boundary layer velocity and turbulence intensity profiles near the aft end of the suction surface. The measured flow also showed a small region of mean backflow near the trailing edge of the blade (Zierke and Deutsch, 1989), and for that reason was also probably unsteady. In Figure 4.13, comparison is made between computed blade surface pressure coefficient and measured values. Agreement is good along both blade surfaces. The oscillations in the pressure distributions near the leading and trailing edges in Figure 4.13 are caused by the velocity scaling of the artificial dissipation. The artificial dissipation was scaled as in equation [3.20], where the reference velocity, $V_{ref} = a_\infty M_\infty$. The H-grid used gives rise to highly skewed regions near the relatively blunt leading and trailing edges of this configuration, causing the velocity scaling presented "as is" to give rise to these oscillations.

In Figure 4.14, the predicted boundary layer profiles at three chordwise locations on the suction surface are plotted with those measured by laser Doppler velocimeter. Agreement is excellent at 20 % chord and 50% chord and reasonable at 90 % chord. Local turbulence intensity profiles are presented for three chordwise locations on the suction

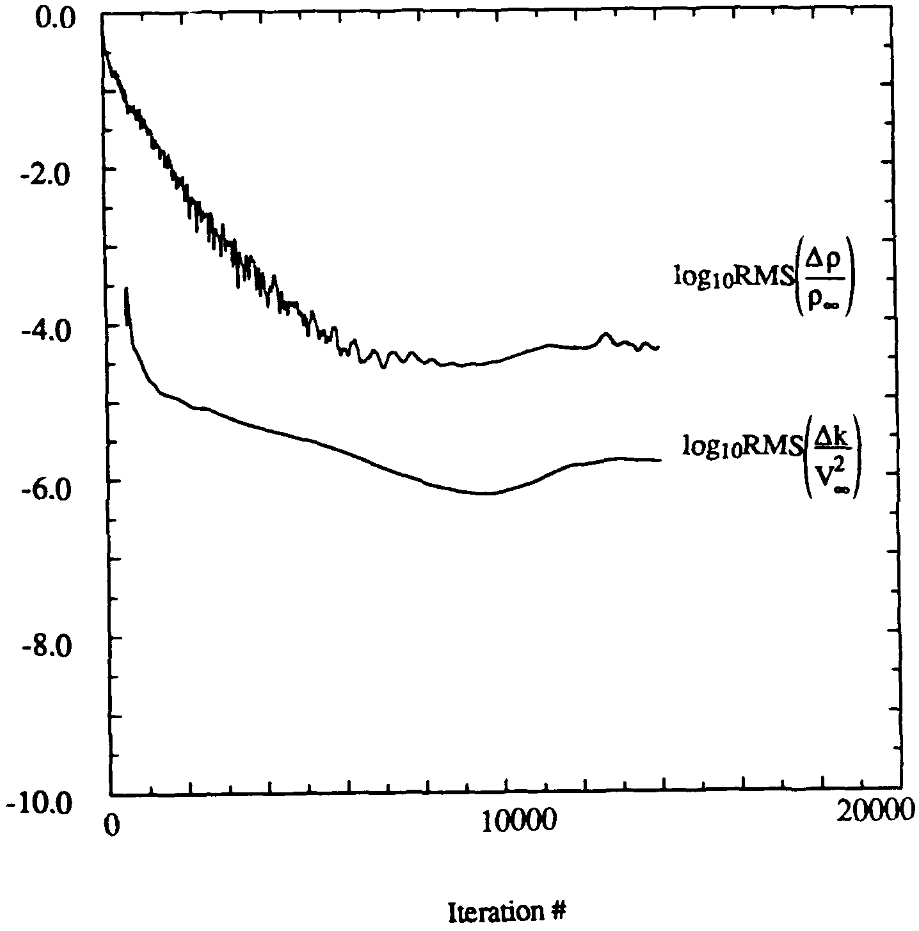

Figure 4.12 Convergence history for ARL DCA cascade computation.

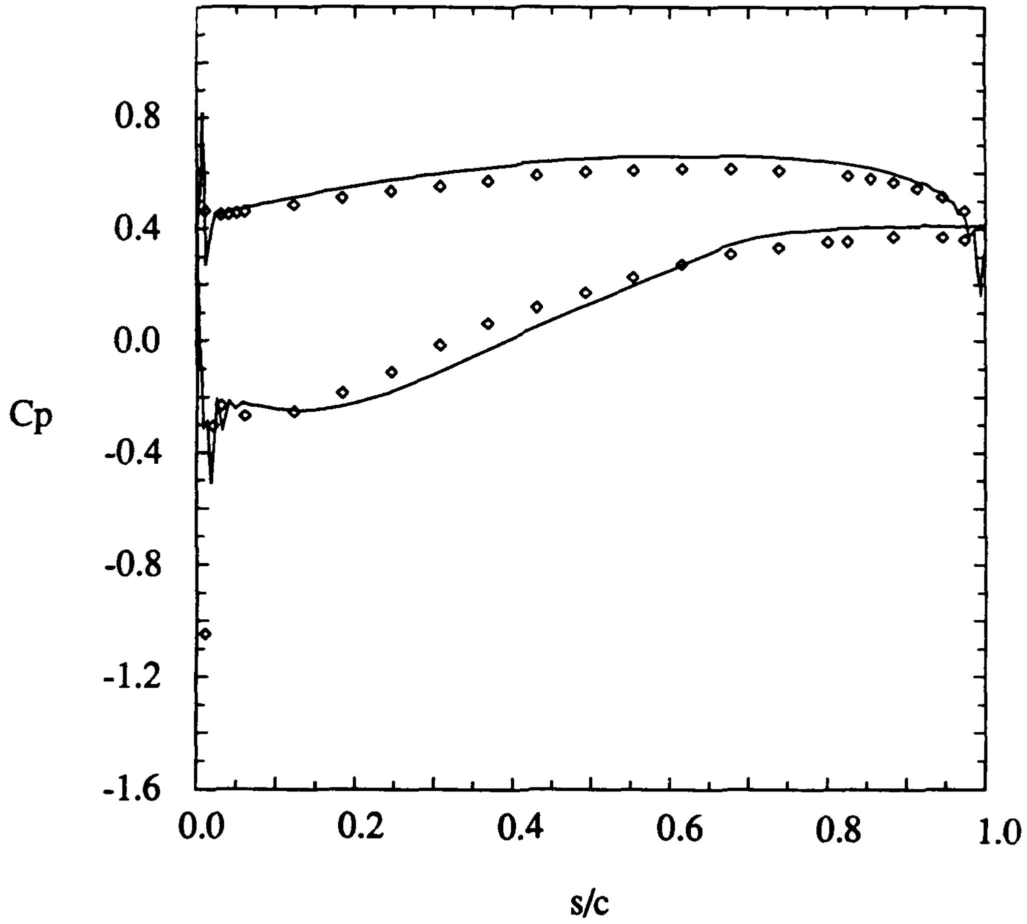

Figure 4.13 Pressure coefficient for ARL DCA cascade computation.

Calculated (solid line) and experimental values (symbols).

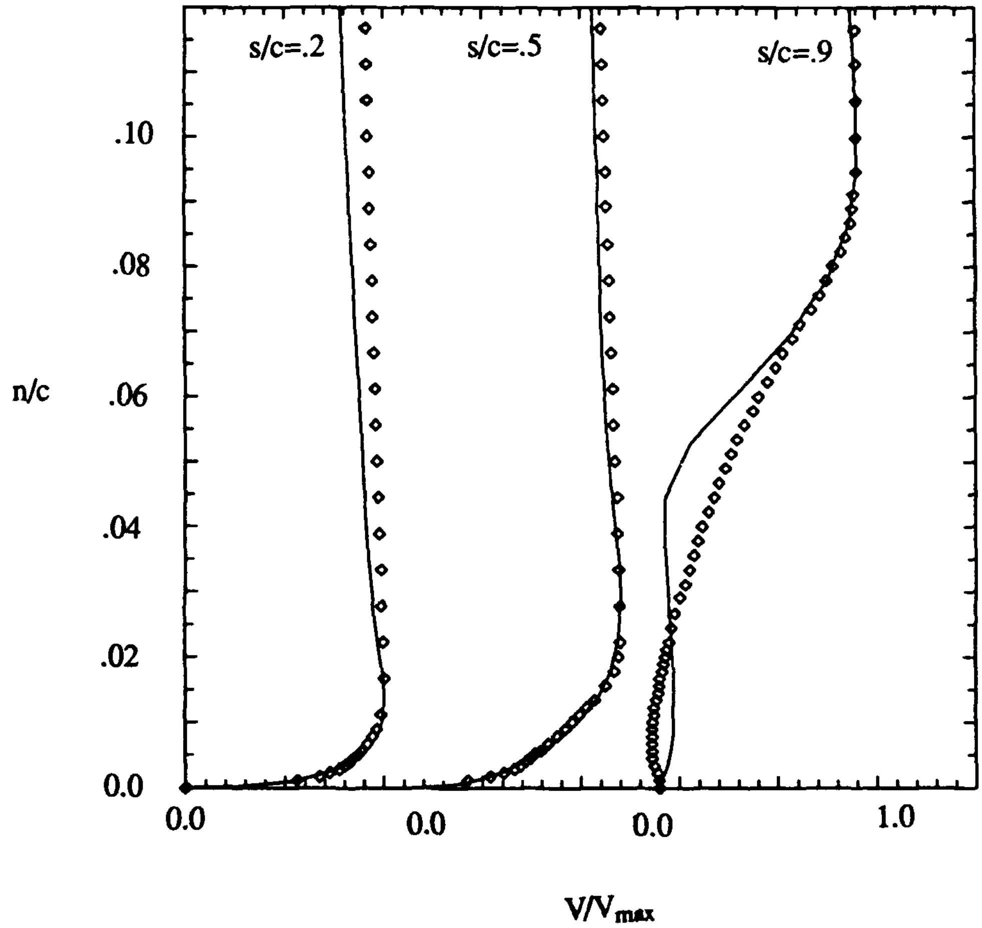

Figure 4.14 Boundary layer profiles at three chord locations along the suction surface for the ARL DCA cascade computation. Calculated (solid line) and experimental values (symbols).

surface in Figure 4.15. As above, agreement between calculation and experiment is good at the first two stations, and reasonable in the aft portion of the blade.

Predicted and measured performance parameters for this cascade are presented in Table 4.2.

Table 4.2. Comparison of Performance Parameters for ARL-DCA Cascade

Flowfield Parameter	Measured	Computed	Difference
C_L[a]	0.82	0.88	7 %
ω[b]	0.094	0.111	18 %
β_1	-1.5°	prescribed	NA
β_2	14.1°	13.0°	1.1°
$s/c_{sep_{ss}}$	.45	fluctuates near 0.90	NA
$s/c_{sep_{ps}}$	none	none	NA
AVDR	0.97-1.03	1	NA

[a] lift coefficient computed from $C_L = \frac{(\text{Lift per unit span})_{\perp V_m}}{.5\rho_m V^2_m}$.

[b] pressure loss coefficients computed from $\omega = \frac{p_{o\infty} - p_o}{.5\rho_\infty V^2_\infty}$.

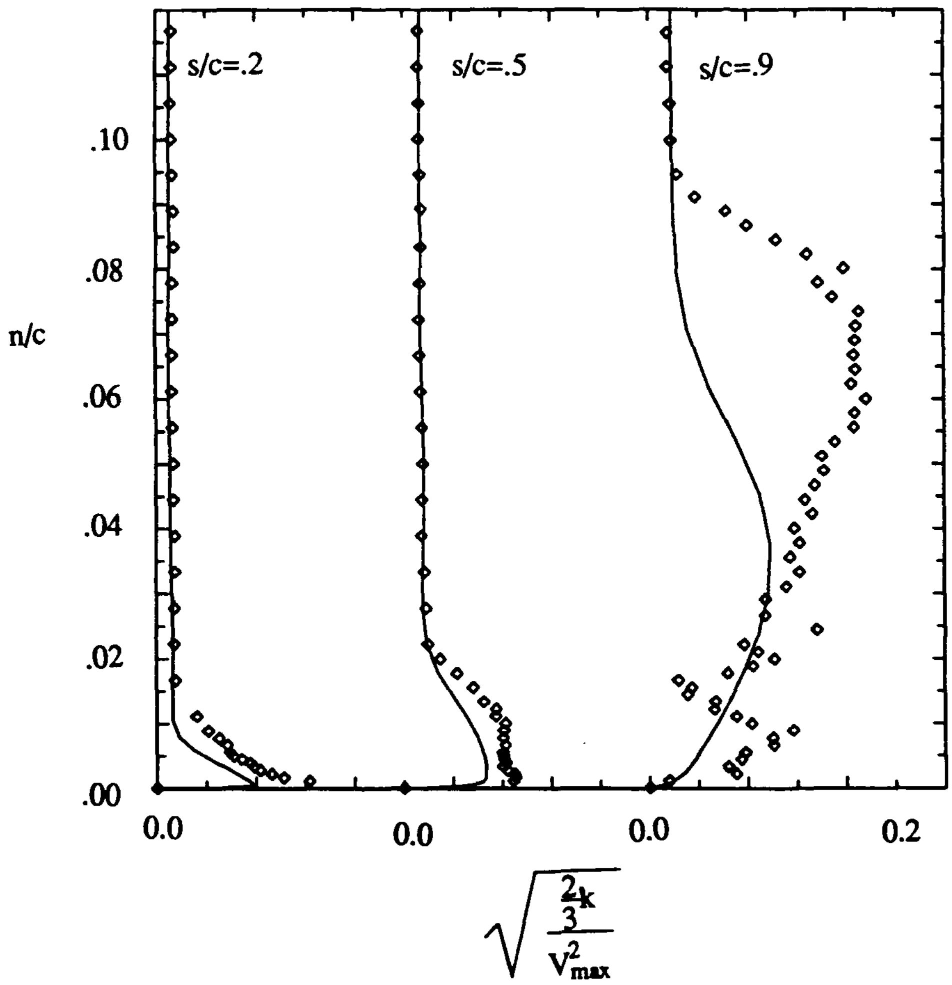

Figure 4.15 Local turbulence intensity profiles at three chord locations along the suction surface for the ARL DCA cascade computation. Calculated (solid line) and experimental values (symbols).

CHAPTER 5

PREDICTION OF THREE-DIMENSIONAL INTERNAL AND TURBOMACHINERY FLOWS

In order to provide three-dimensional validation of the turbulence modelling and numerical methodologies, the code was used to predict the pressure distribution, primary velocity and secondary flows in an incompressible, turbulent curved duct flow for which CFD validation quality data is available. Also, a subsonic compressor rotor passage, for which detailed laser, rotating hot-wire and five-hole pressure probe measurements have been made is computed. Detailed comparisons between predicted and measured core flow and near wall velocity profiles, wake profiles, and spanwise mixing effects downstream of the rotor passage are presented for this case.

5.1 Turbulent Flow in a 90° Bending Duct of Square Cross-Section

The ability of the present approach to predict three-dimensional turbulent flows was tested by computing an incompressible duct flow investigated experimentally by Taylor et al. (1981). The bulk velocity of water through the 90° bending duct of square cross-section was 1.00 m/s. This corresponds to a Reynolds number based on hydraulic diameter of approximately 40000 and a Dean number of approximately 18700. A short inlet extension to the duct was designed by the experimenters to provide thin inlet boundary layers at the bend entrance. In earlier work by Humphrey et al. (1981), the same facility was fitted with a longer inlet section so as to provide fully developed turbulent velocity profiles near the bend entrance. The thinner inlet velocity profiles of the present case give rise to weaker, but significant, secondary motions in the bending portion of the duct, and therefore this case provides an appropriate three-dimensional test case for the numerical scheme and the turbulence model.

An interesting difficulty in computing this flow arises from the fact that the velocity profiles near the bend inlet are significantly influenced by the development of secondary motions of the second kind in the the straight duct section upstream of the bend. Accurate computation of secondary flows within the duct relies primarily on rotational inviscid transport of accurately prescribed near wall inlet transverse vorticity profiles [see Lakshminarayana and Horlock (1973) for example]. However, isotropic eddy viscosity models are incapable of predicting the Reynolds stress anisotropies which give rise to secondary motions of the second kind and therefore to the "bowed" inlet velocity profiles these motions give rise to. This difficulty seems to discount the use of a computational grid with an inlet extension corresponding to the experimental apparatus, if the present two-equation turbulence model is used. In the present work, this difficulty is overcome by setting the inlet boundary very close to the bend inlet. Measured velocity and pressure distributions are used to provide inlet boundary conditions which are physically plausible enough to allow a convergent Navier-Stokes solution despite the proximity of the inlet boundary to regions where significant flowfield gradients exist.

In Figure 5.1, the 81 x 41 x 21 computational grid used for this calculation is shown. The half duct was computed here to exploit the symmetry of the problem. Grid spacing at the wall was 0.00033 times the duct height which gave rise to wall adjacent grid point values of $y^+ \cong 1.5$ along the entire length of the duct. The inlet extension was 1/4 hydraulic diameter upstream of the bend entrance. Measured primary velocity magnitudes and the radial static pressure distribution at this location were interpolated onto the inlet grid plane. A composite law-of-the-wall due to Spalding [see White (1974) for instance] was used to approximate the primary velocities between the wall and the first measurement

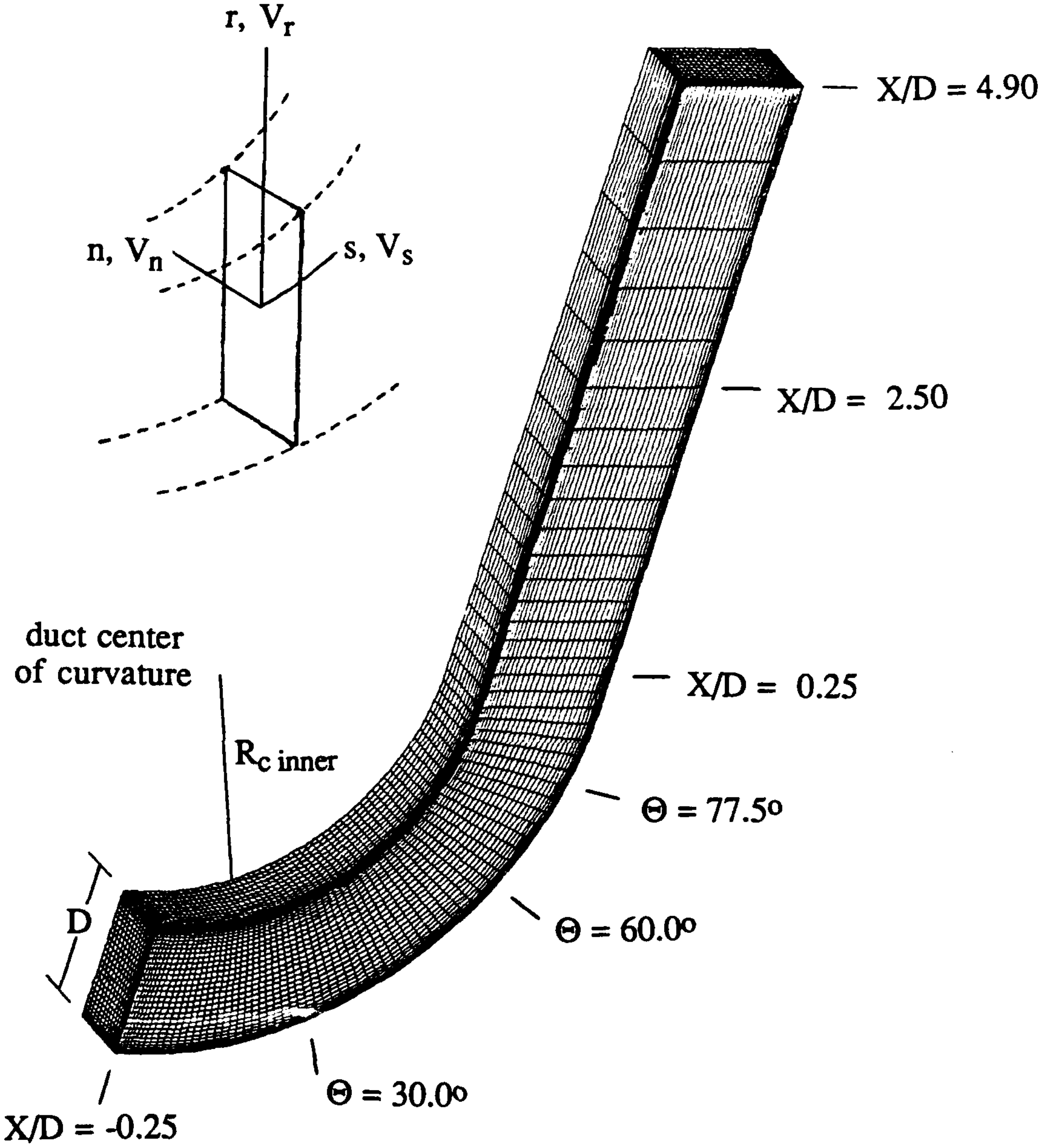
r, V_r
n, V_n
s, V_s
X/D = 4.90
X/D = 2.50
duct center
of curvature
X/D = 0.25
R_c inner
Θ = 77.5°
D
Θ = 60.0°
Θ = 30.0°
X/D = -0.25

Figure 5.1 81 x 21 x 41 Computational grid and notation for incompressible duct flow computation.

location away from the wall (0.1 times the duct height). The simulation was run with an average inlet Mach number close to 0.2, and the subsonic Riemann extrapolation boundary condition described in Chapter 3 was used, to accommodate the compressible formulation of the flow solver. Inlet total pressure and temperature profiles were specified from the above prescriptions and the assumption of constant inlet static temperature. Additionally, zero inlet flow angles and a back pressure adjusted to pass the mass flow necessary to achieve Reynolds number similarity were specified. Inlet turbulence intensity was set to 3% corresponding to approximate measured inlet average intensity. The artificial dissipation was scaled by $(V_{local}/V_{ref})^2$, as in equation [3.20],where the mean inlet velocity was used as the reference velocity, V_{ref}.

The code was run for 3000 iterations, at which point the RMS density and turbulent kinetic energy residuals had dropped 3 orders of magnitude. The computation was then stopped, since the pressure and primary and secondary velocity fields remained unchanged after about 2500 iterations. The convergence history for this computation is shown in Figure 5.2. This computation required approximately 7 hours on an IBM 3090-600S. At convergence, the parabolic stability constraint was less restrictive than the hyperbolic constraint for all of the grid points in the domain, that is $\Delta t_v > \Delta t_c$ everywhere. This is due to the fact that since the duct walls (and hence the near wall damping effects in the low-Reynolds number turbulence model) extend from inlet to exit, there is no region in the computed flow where both large effective diffusivities and large grid metrics occur. Therefore, the first term in equation [3.46] is less than the second at every grid point.

In Figure 5.3, the predicted streamwise distribution of pressure coefficient along the symmetry plane is presented. Agreement between the experiment and the computation at all five radial locations is very good. The high wave number pressure oscillations near

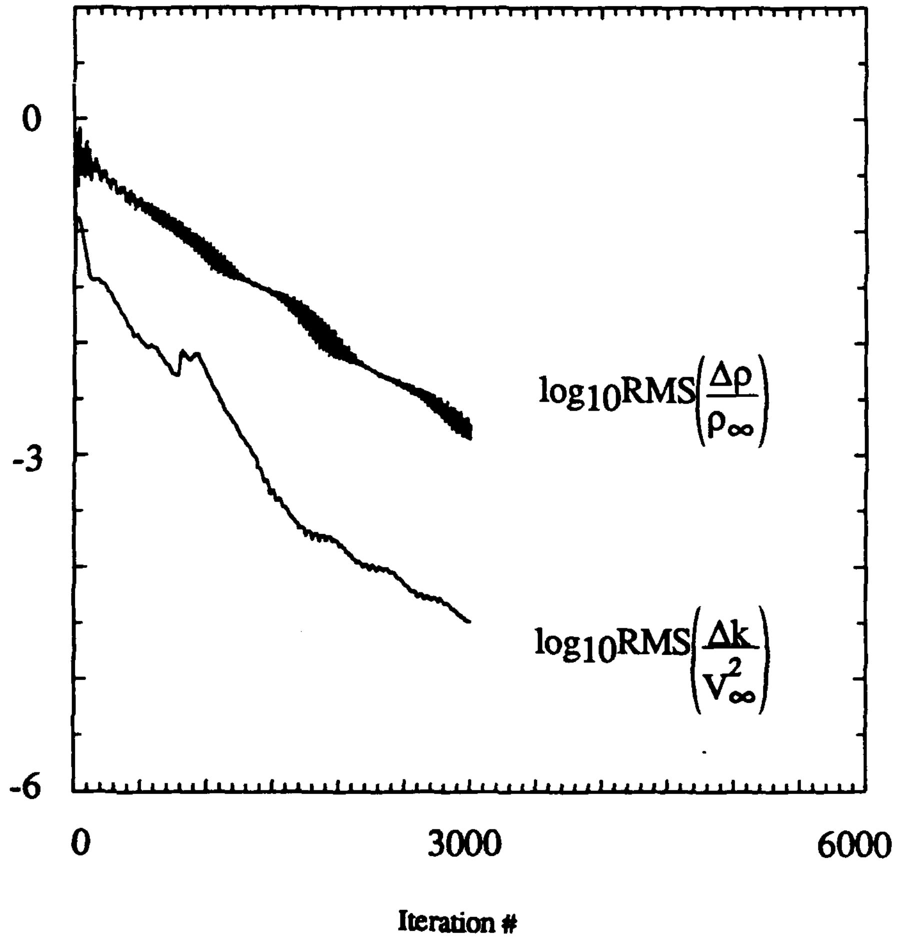

Figure 5.2 Convergence history for incompressible duct flow computation.

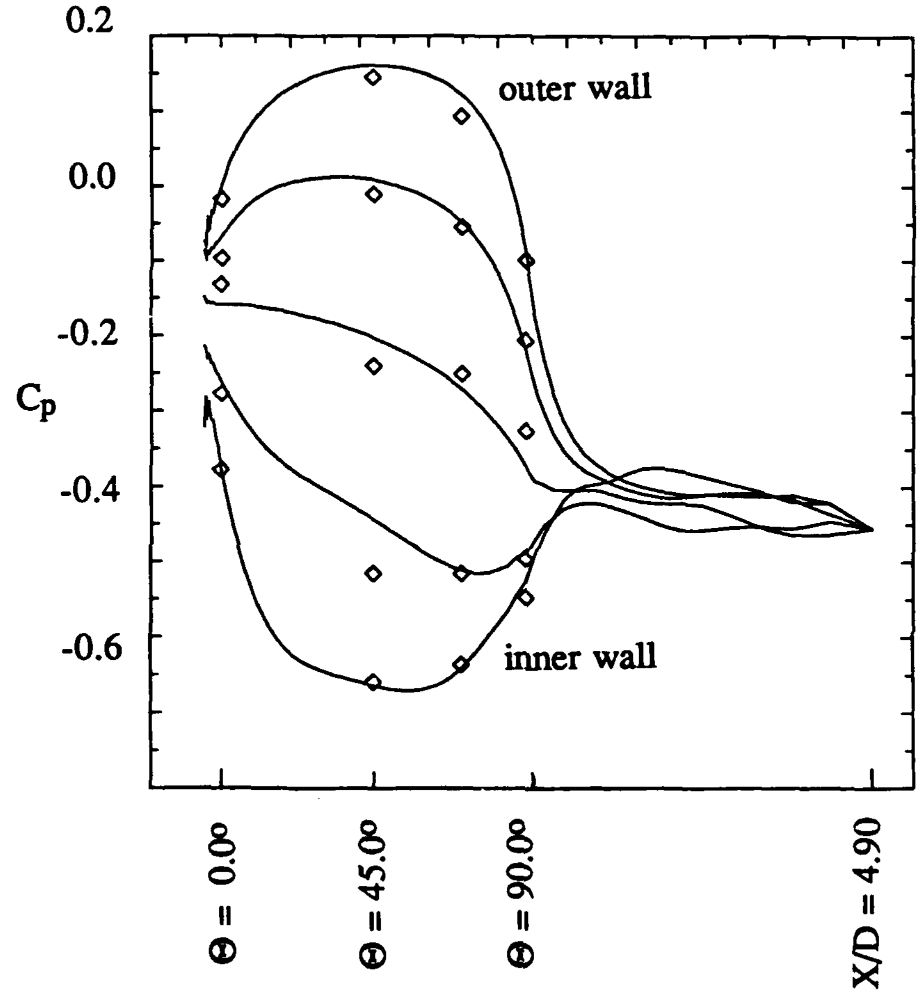

Figure 5.3 Streamwise static pressure coefficient distribution at several locations along symmetry plane for incompressible duct flow computation. Calculated (solid line) and experimental values (symbols).

the inlet section are attributed to the proximity of the imposed inlet boundary conditions to the bend.

Streamwise velocity contours are plotted at six streamwise locations in Figure 5.4, and show reasonably good agreement with the experimental data. The nearly exact correspondence at the inlet (X/D = -0.25) is due to boundary condition specification from the data. The development of the secondary vortex at the inner wall and its effect on velocity defect in the mainstream is captured accurately. Both the size of this vortex and the magnitude of the streamwise velocities in this secondary flow region are well predicted. The secondary velocities are shown in Figure 5.5. Here again, agreement is good. The ability of the code to capture the far downstream flow, where considerable redistribution of the flowfield has occurred is evident from both Figures 5.4 and 5.5.

The good agreement between experiment and computation achieved in this validation study provides evidence that the numerical and modelling strategies used can yield acceptable solutions of complex three-dimensional internal flows.

5.2 Subsonic Compressor Rotor Operating at Peak Pressure Rise Coefficient

As stated in Chapter 1, the ultimate goal of this thesis work is to provide accurate, detailed predictions of viscous flows in complex three-dimensional turbomachinery configurations. Accordingly, the code has been utilized to predict the flow field in a subsonic rotor operating at peak pressure rise coefficient. The so called "Penn State Compressor Rotor" has a hub to tip ratio of 0.5 with an outer annulus wall diameter of 0.936 m. The rotor has 21 blades. The chord length increases from 0.124 m. at the hub to 0.154 m. at the tip. The blade stagger angle increases from 22.5° at the hub to 45.0° at the

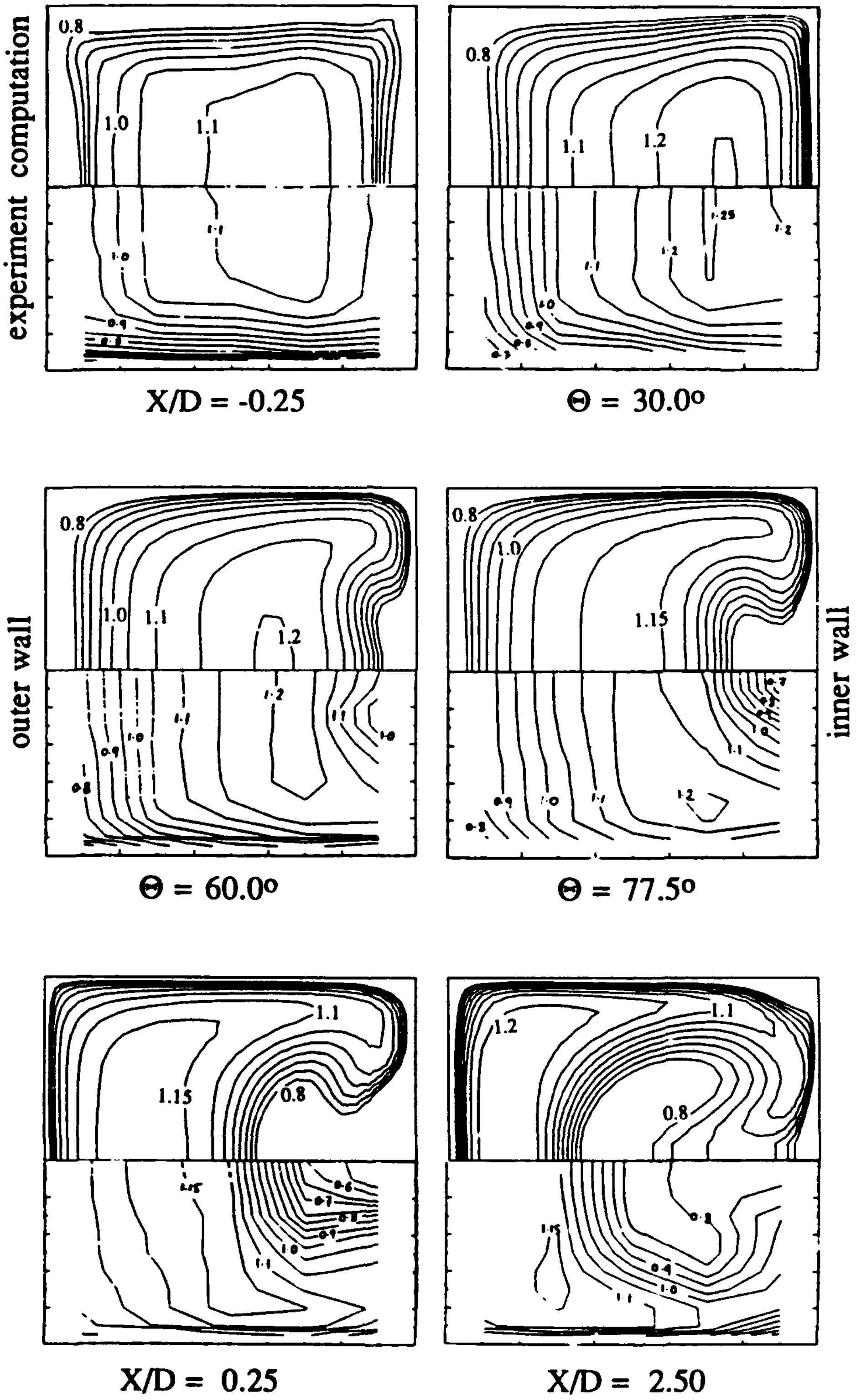

X/D = -0.25

Θ = 30.0°

Θ = 60.0°

Θ = 77.5°

X/D = 0.25

X/D = 2.50

Figure 5.4 Contours of normalized streamwise velocity, V_s/V_b, for incompressible duct flow computation. Experimental contours, reproduced from Taylor et al. (1981), appear on bottom side of each cross section. Computed contours appear on top. See Figure 5.1 for notation.

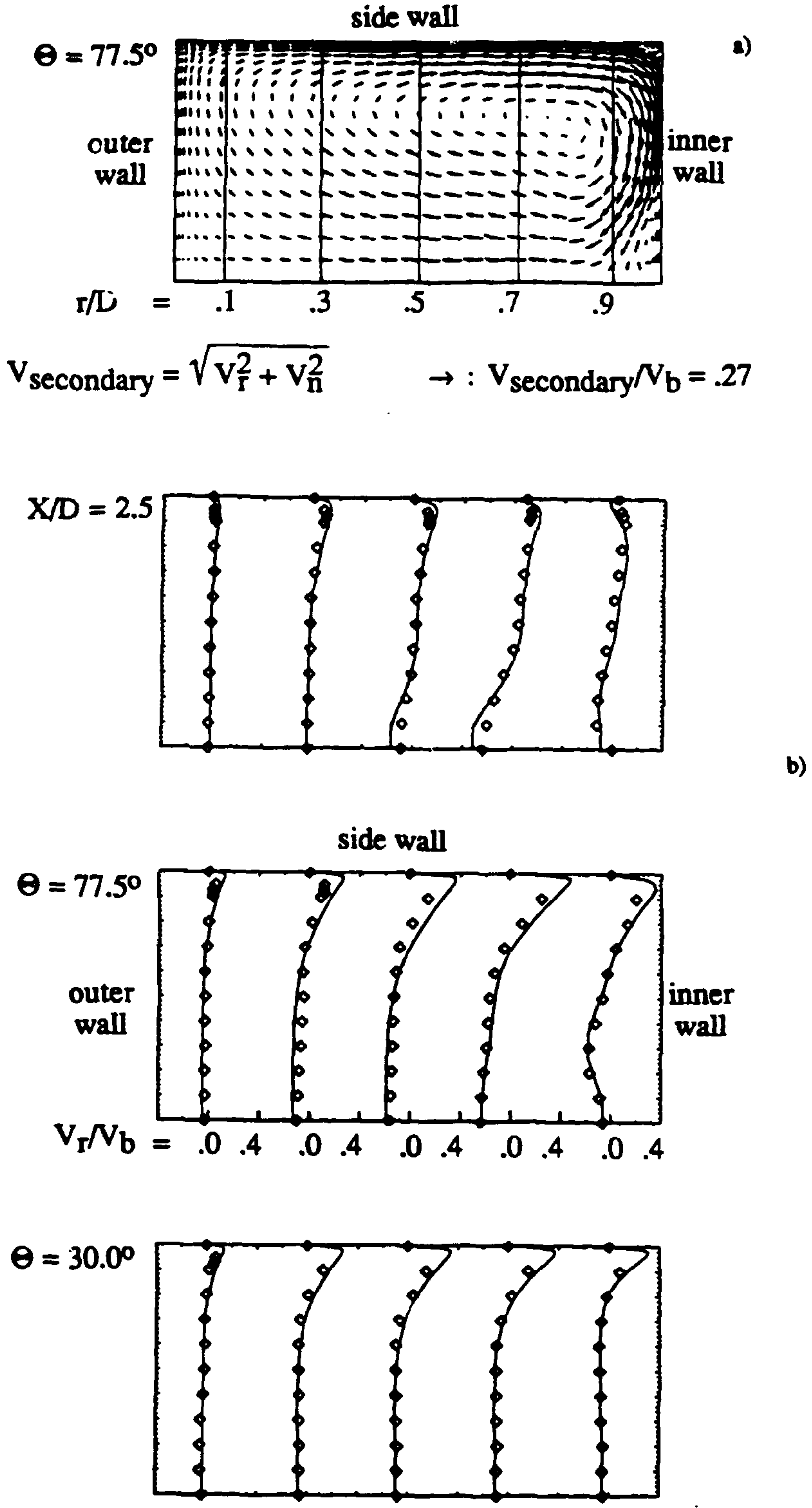

Figure 5.5 Secondary velocities at various streamwise stations for incompressible duct flow computation. a) Computed secondary velocity vectors [solid lines indicate location of traverses in b)]. b) Scaled radial velocities, V_r/V_b, at five radial locations. Calculated (solid line) and experimental values (symbols). See Figure 5.1 for notation.

tip. The tip clearance was either 2 mm or 3.3 mm for the various experimental tests as specified below.

The operating conditions for the computed case are as follows : flow coefficient, $\Phi = 0.50$, pressure rise coefficient (peak), $\overline{\Psi} = 0.55$, rotor shaft angular velocity, $\omega = 113$ s^{-1}, tip velocity, $U = 53$ m/s. The Reynolds number of the flow based on chord length at midspan and rotor tip speed was 480,000.

A large amount of laser Doppler velocimeter, hotwire and five hole pressure probe data is available for this rotor. The axial and tangential components of relative velocity were measured from blade to blade at various chordwise locations inside the passage, using an ensemble averaging technique (Popovski and Lakshminarayana (1986)). The flowfield near the blade surfaces was measured using a two sensor miniature hotwire probe, rotating with the rotor (Lakshminarayana and Popovski (1987)). Additionally, the wakes downstream were measured recently by Prato (1990) using a five hole pressure probe. For the passage flow measurements, the tip clearance was 2 mm. The blade tips were shaved to provide a 3.3 mm tip clearance prior to the wake measurements.

In Figure 5.6a, the 89 x 45 x 45 (180225 points) computational grid used for this calculation is shown. This H-grid was generated using a interactive program developed by Beach (1990), which is described in detail there. The normal grid spacing on the blade surfaces was 4.7×10^{-4} span. The normal grid spacing at the hub and shroud was 1.9×10^{-3} span. This yielded values of $y^+ \cong 6$ at grid points adjacent to the blade surfaces and $y^+ \cong 30$ along the endwalls. It is noted, that for accurate implementation of nearwall two-equation turbulence models, values of y^+ should be closer to 1 at the first gridpoint off the wall. Resource limitations allowed only 45 blade to blade and hub to casing grid points. For this high Reynolds number rotor flow, the resulting grid generation compromised

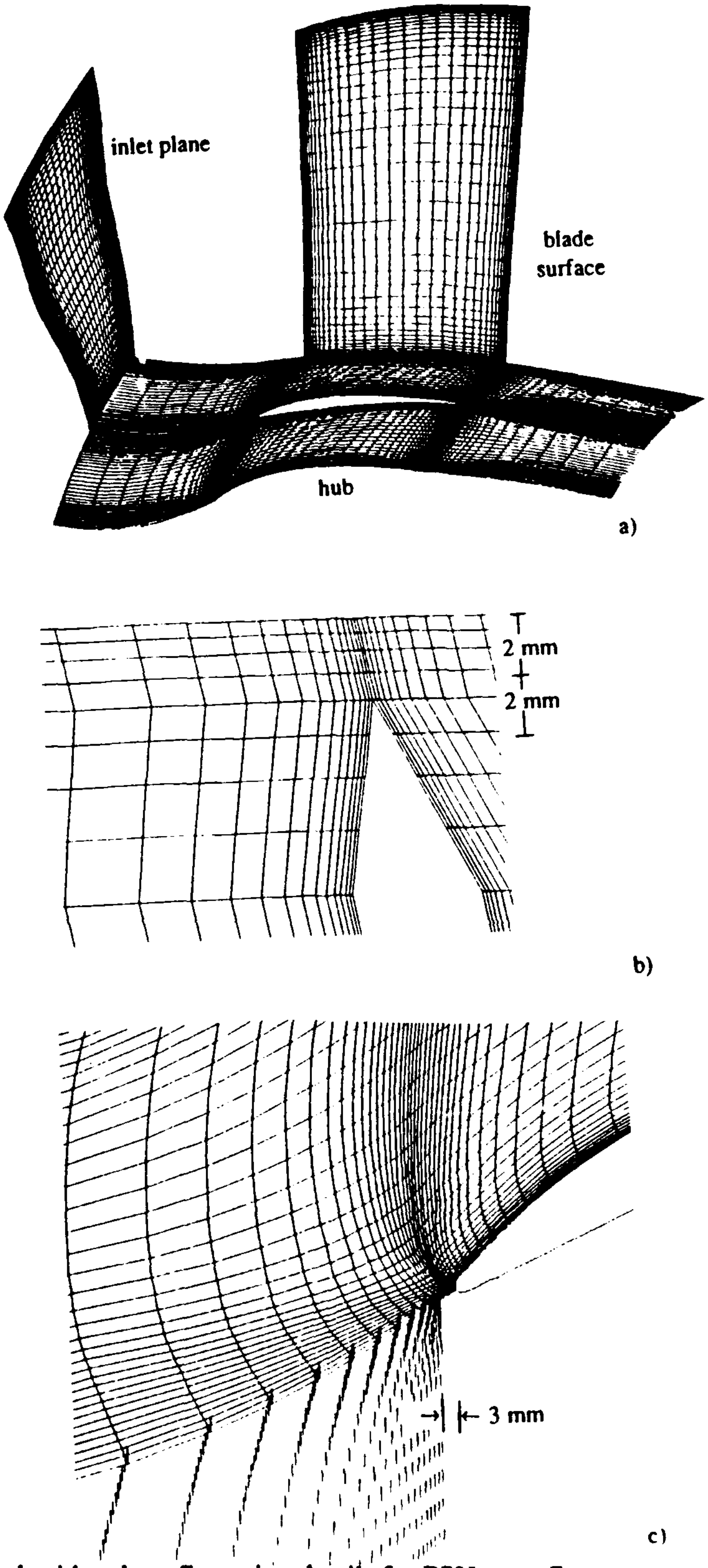
inlet plane
blade surface
hub
a)
2 mm
2 mm
b)
3 mm
c)

Figure 5.6 Computational grid and configuration details for PSU rotor flow computation. a) 89 x 45 x 45 computational grid. b) detail of "thin blade" tip clearance gap at midchord. c) hub-leading edge detail showing relative flow velocities at stationary-rotating hub interface in relative frame.

between refined nearwall and core region grid resolution in order to provide reasonable grid clustering everywhere.

In order to account for tip clearance flow, the grid was modified in the immediate vicinity of the shroud, as shown in Figure 5.6b. This allows for three periodic flow through grid points in the gap region. Such a "thin blade" tip clearance approach has been undertaken by several researchers [see Bansod and Rhie (1990) for example]. In the compressor facility, the location of the interface between rotating and stationary segments of the hub is 3 mm upstream of the leading edge at the root. To accommodate this in the flow computation, a no-slip relative velocity of $-\omega r_{hub}$ is enforced at all grid points on the hub for which $x < x_{ile} - 3$ mm. This is illustrated in Figure 5.6c. Measured inlet axial and tangential velocities, provided in Popovski and Lakshminarayana (1986), were interpolated onto the inlet plane to provide the rotor flow inlet boundary conditions discussed previously. A composite law-of-the-wall due to Spalding [see White (1974) for instance] was used to approximate the total velocities between the endwalls and the first measurement location away from these walls. The inlet turbulence intensity was specified as .02, and the inlet turbulence length scale as .01 times the blade spacing at midspan.

The code was run for 5200 iterations, at which point the RMS density and turbulent kinetic energy residuals had dropped 5.0 orders of magnitude. The computation was then stopped, since the streamwise and radial near-wall velocity profiles remained unchanged after about 4500 iterations. The convergence history for this computation is shown in Figure 5.7. This computation required approximately 25 hours on a Cray 2. At convergence, the parabolic stability constraint was more restrictive than the hyperbolic constraint, that is $\Delta t_v < \Delta t_c$, for 6.5 % of the grid points in the domain. The artificial dissipation was scaled according to equation [3.20], where the rotor tip speed, U, was used as the reference velocity.

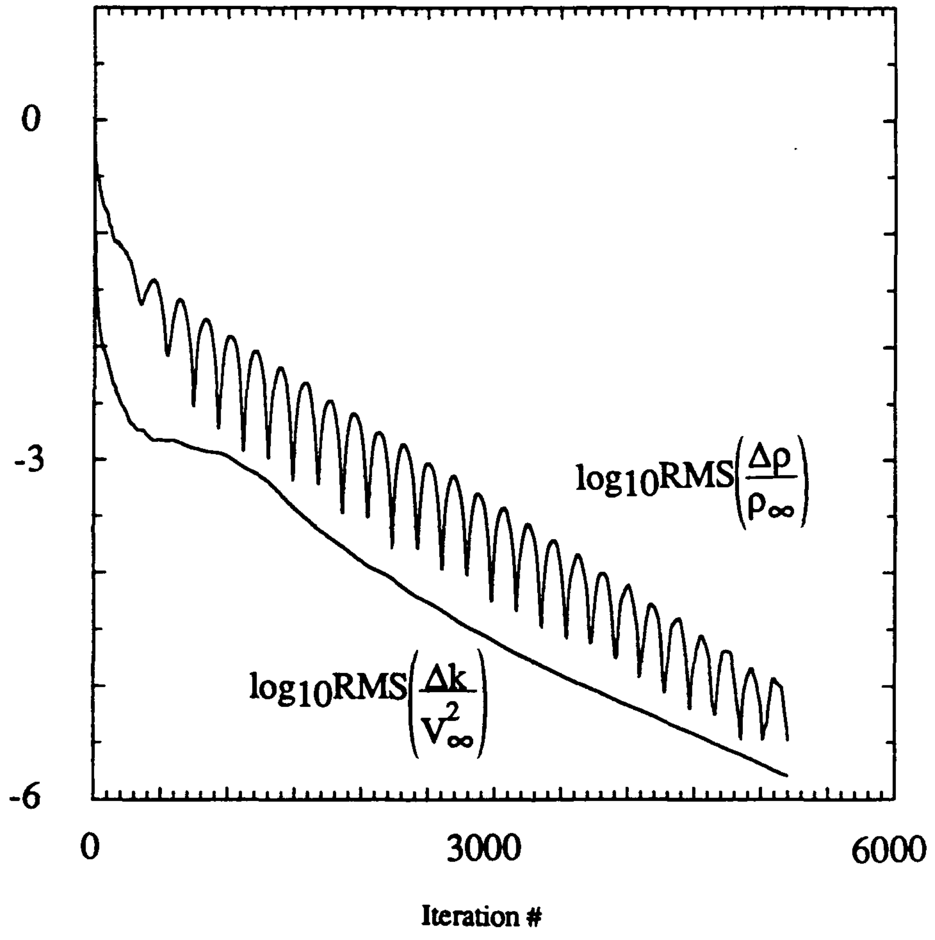

Figure 5.7 Convergence history for PSU rotor flow computation.

Passage Flowfield

In Figure 5.8, the blade to blade axial velocity distributions, obtained at several spanwise locations by Popovski and Lakshminarayana (1986), using LDV measurements, is presented with the Navier-Stokes predictions. The rotational inviscid flow features are seen to be well captured by the simulation, including immediately upstream of the leading edge where the presence of the blade gives rise to small velocity magnitudes due to the proximity of the stagnation point (inviscid effect). The effect of tip clearance flow, which interacts with the core flow near the tip ($r/r_{tip} = 0.96$) to produce a velocity defect near the midpassage is captured qualitatively by the code.

Detailed blade boundary layer measurements were made for this operating condition, using a rotating hot wire, by Lakshminarayana and Popovski (1987). In Figures 5.9 and 5.10, the predicted streamwise and radial velocity profiles are compared with measured values. The streamwise boundary layer velocity profile near the hub and midspan regions is captured with reasonable accuracy. The region $r/r_{tip} = 0.92 - 0.96$ shows significant discrepancy, in the near wall region. The measured profiles in the near wall region of the tip sections, $r/r_{tip} = 0.92 - 0.96$, show a tendency to separate, and this is not captured well by the simulation. This is a region of large radial boundary layer transport interaction with the leakage and secondary flow. Considering these complexities, the predictions are reasonably good.

The radial velocity profiles are shown in Figure 5.10. The agreement between experiment and computation is good up to $r/r_{tip} = 0.92$, but deteriorates as the casing is approached. Some of the discrepancy is attributed to poor resolution of tip clearance flow and the resulting blade unloading in this region. The radial velocities are strongly

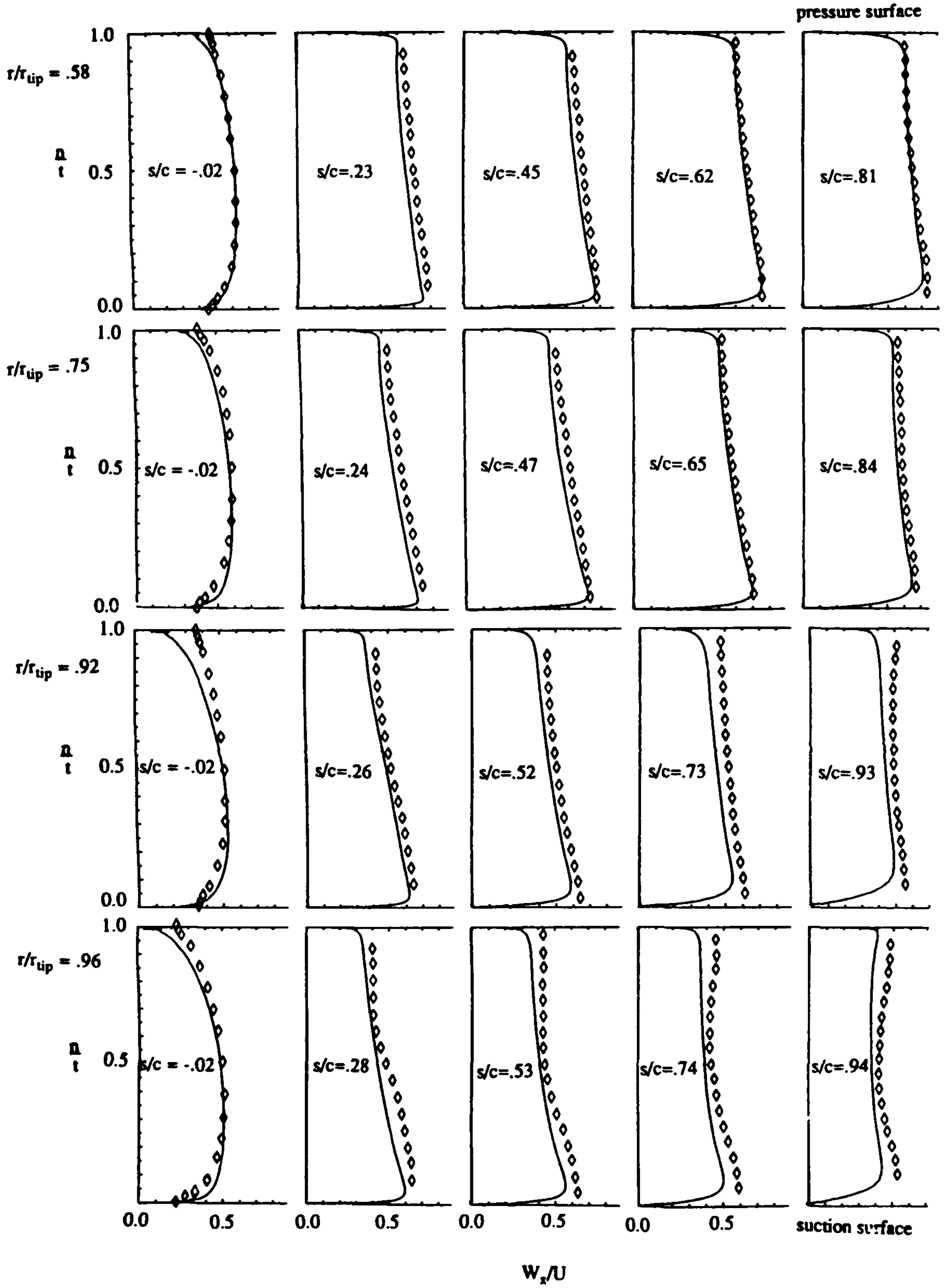

Figure 5.8 Blade to blade axial velocity distribution (W_x/U) for PSU rotor flow, at four spanwise locations. Laser velocimeter measurements due to Popovski and Lakshminarayana (1986) (symbols) and computed distributions (solid lines).

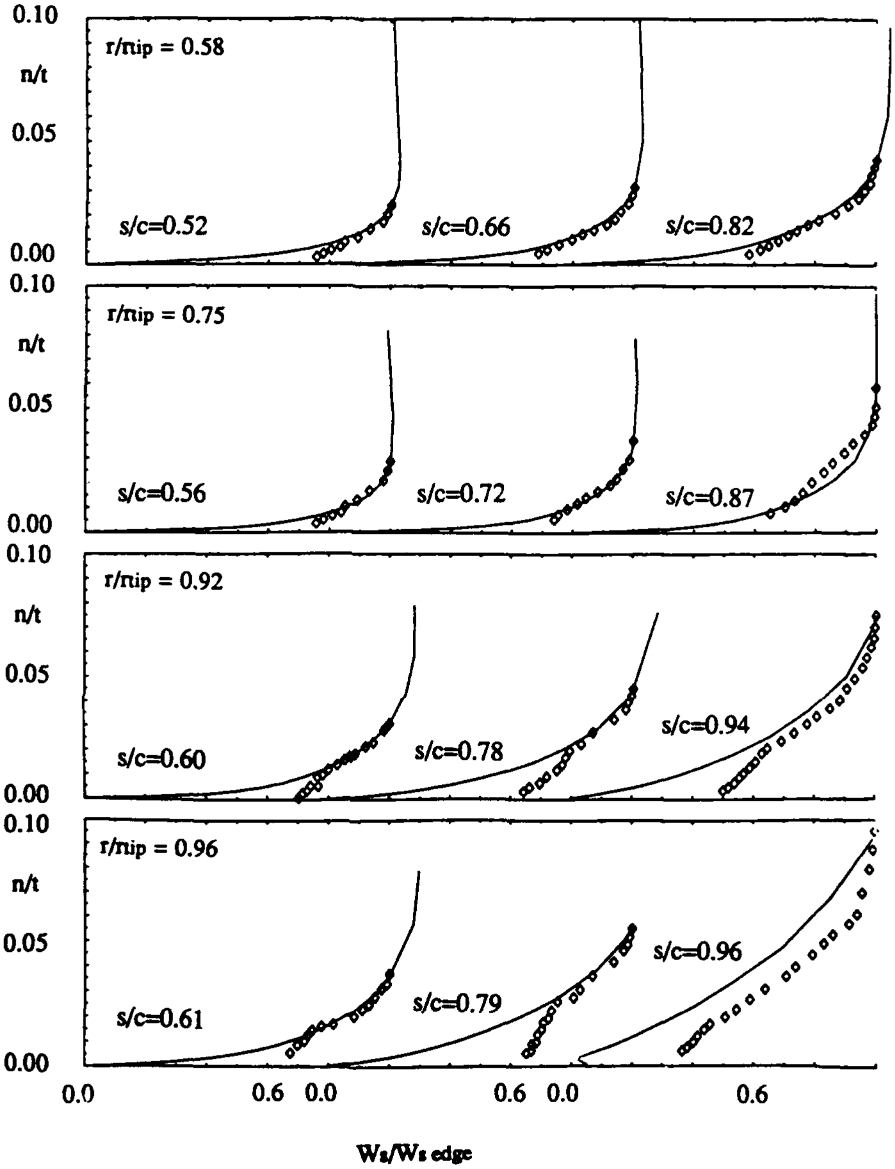

Figure 5.9 Suction surface streamwise boundary layer velocity distribution ($W_s/W_{s\ edge}$) for PSU rotor flow, at four spanwise locations. Rotating hot wire measurements due to Lakshminarayana and Popovski (1987) (symbols) and computed distributions (solid lines).

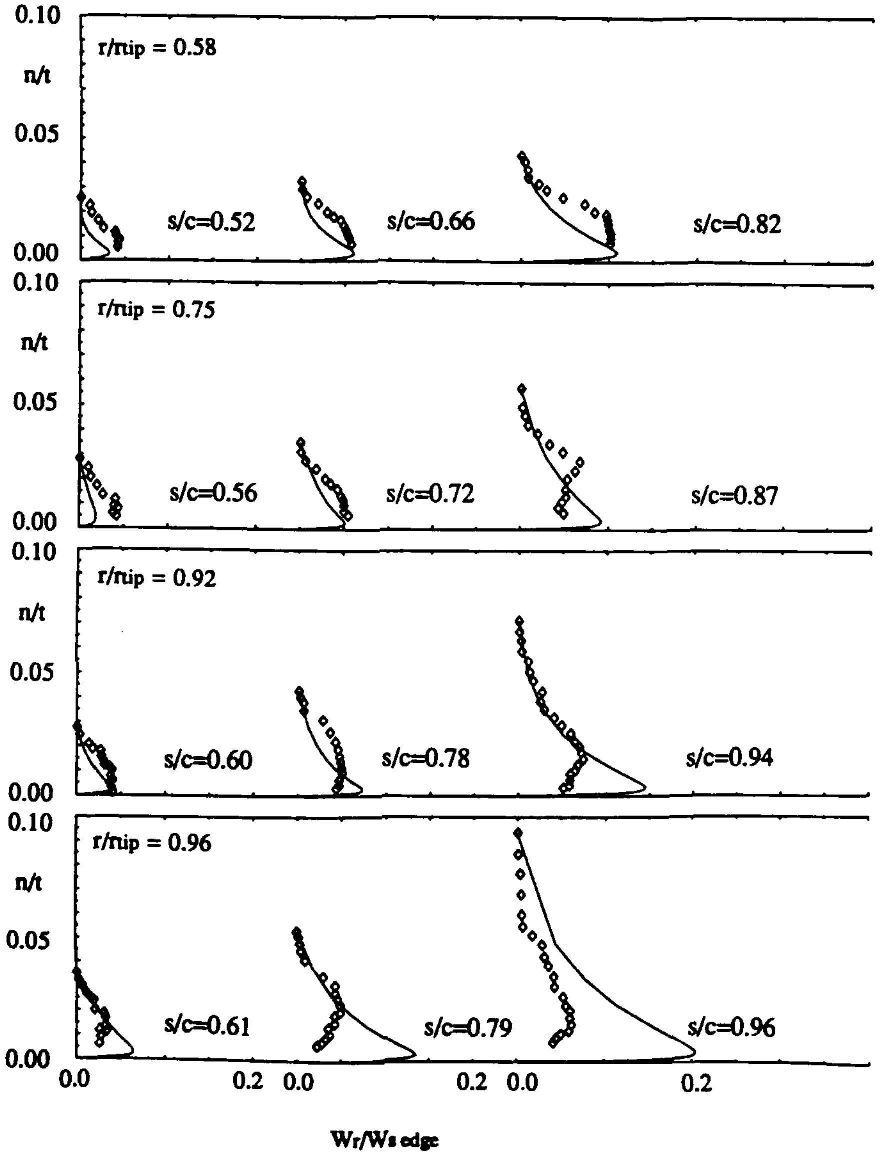

Figure 5.10 Suction surface radial boundary layer velocity distribution ($W_r/W_{s\ edge}$) for PSU rotor flow, at four spanwise locations. Rotating hot wire measurements due to Lakshminarayana and Popovski (1987) (symbols) and computed distributions (solid lines).

dependent on both the streamwise velocity defect near the blade surface, and the local radial pressure gradient. Good prediction of radial velocities at $r/r_{tip} = 0.58$ and 0.75 is due to good prediction of streamwise velocity profiles in this region (compare Figure 5.9). The discrepancy between radial velocity data and prediction from $r/r_{tip} = 0.92$ to 0.96 is due to poor prediction of streamwise velocity. The predicted nearwall gradients, $\frac{\partial W_s}{\partial n}$ (Figure 5.9), in these regions are smaller than their measured values. This gives rise to large discrepancies between measured and predicted radial velocities in the tip regions (Figure 5.10).

Rotor Wakes

Recently, Prato (1990) obtained extensive wake flow measurements for this rotor flow. In Figures 5.11 to 5.13, measured axial, relative tangential and radial velocity profiles in the near and far wake are compared with computed profiles. Agreement between calculated and measured profiles is very good. Comparisons are included only for three radius ratios, $r/r_{tip} = 0.57$, 0.73 and 0.86. Agreement in the near casing region, $r/r_{tip} = 0.96$, was not good, due to the dominant tip vortex physics in this region and the relatively crude gap modelling undertaken herein. The simulated wake thicknesses and spreading rates are good. Wake centerline velocities are all well predicted, as is wake spreading rate. The fairly accurate prediction of wake radial velocity profiles, as seen in Figure 5.13, is encouraging, considering the low relative magnitude of these spanwise flows. The wake data at $r/r_{tip} = 0.57$ shows the influence of secondary flow, with both inward and outward radial velocities. Blade rotation gives rise to radially outward components along both the suction and pressure surface boundary layers, while near the hub, spanwise secondary flow components are radially outward on the suction side and inward on the pressure side. Thus the two effects are additive on the suction side and

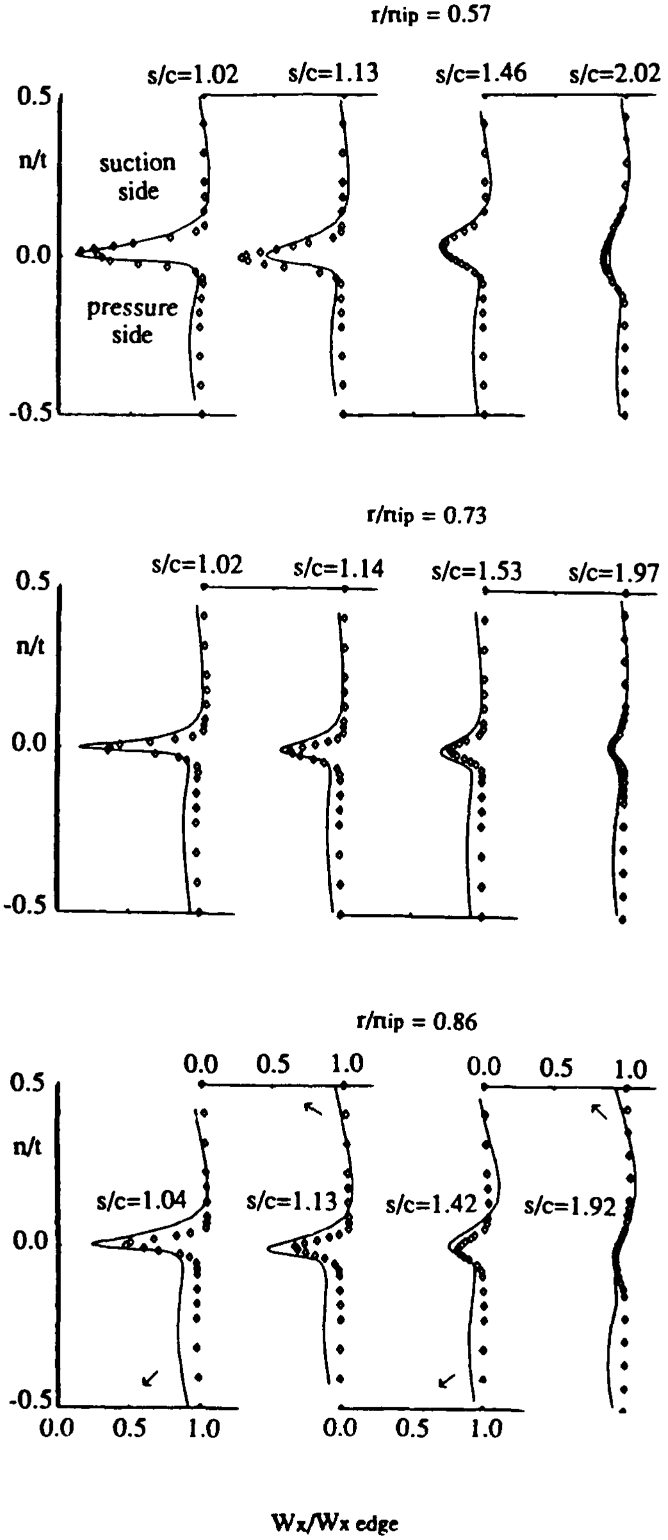

Figure 5.11 Wake axial velocity distribution ($W_x/W_{x\ edge}$) for PSU rotor flow, at three spanwise locations. Five hole probe measurements due to Prato (1990) (symbols) and computed distributions (solid lines).

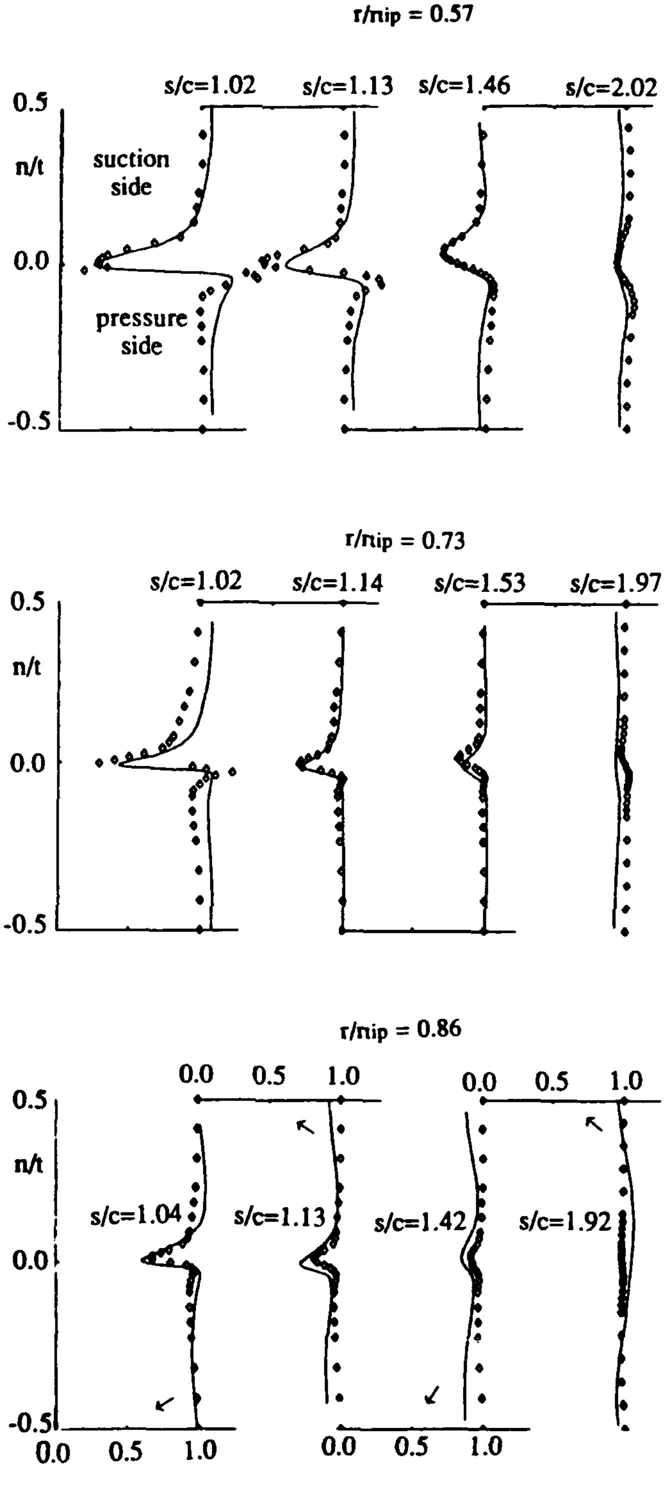

Figure 5.12 Wake tangential velocity distribution ($W_\theta/W_{\theta\ edge}$) for PSU rotor flow, at three spanwise locations. Five hole probe measurements due to Prato (1990) (symbols) and computed distributions (solid lines).

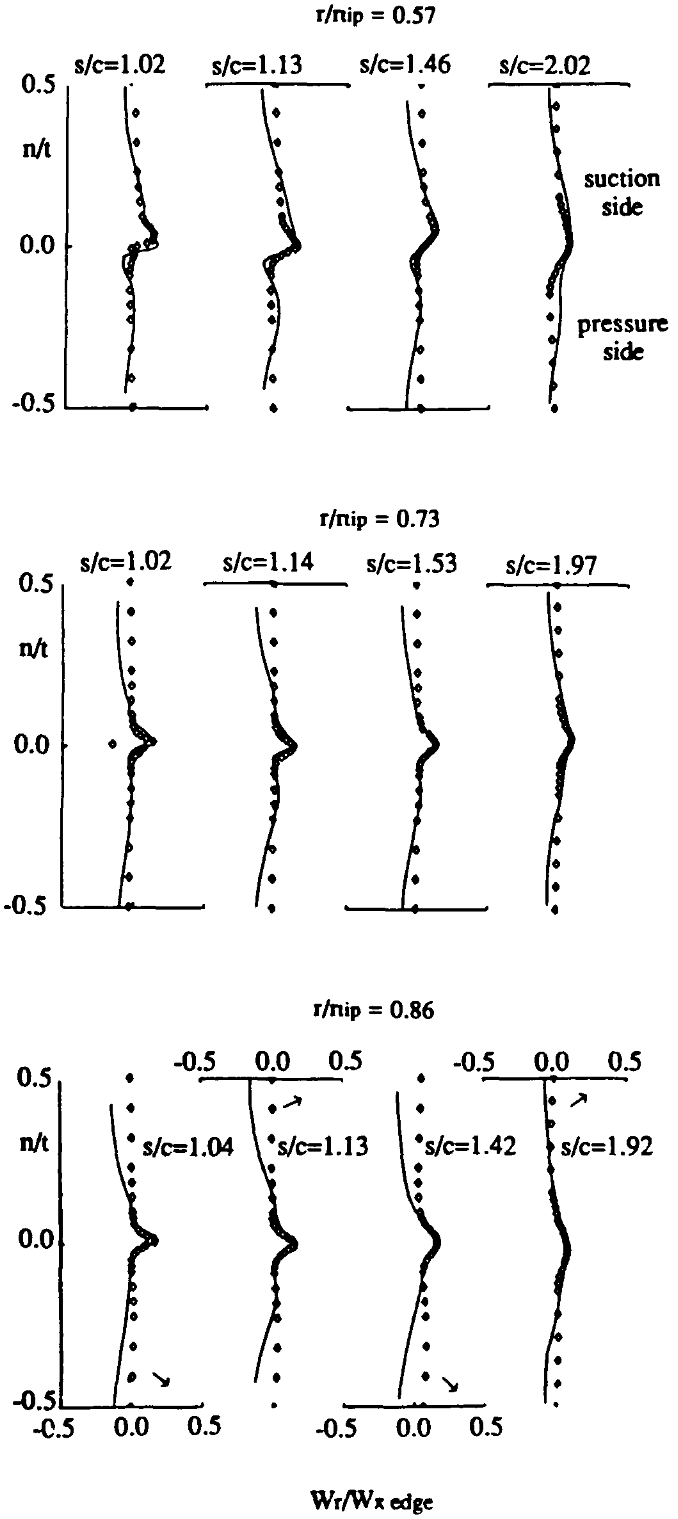

Figure 5.13 Wake radial velocity distribution ($W_r/W_{x\,edge}$) for PSU rotor flow, at three spanwise locations. Five hole probe measurements due to Prato (1990) (symbols) and computed distributions (solid lines).

opposing on the pressure side. This effect has been measured as well as predicted as seen in the wake profiles presented in Figure 5.13 ($r/r_{tip} = 0.57$, s/c=1.02).

Spanwise Mixing Effects and Losses

In Figure 5.14, spanwise distributions of circumferentially averaged axial velocity and absolute flow angle are presented at five downstream locations, ranging from the very near wake to the far wake regions. Agreement between experiment and computation is excellent except near the tip. The simulation captures well the radial distribution of these quantities through the extent of the wake. Also, the streamwise increase in V_x and decrease in absolute flow angle near both endwalls is captured.

In Figure 5.15, the computed contours of relative stagnation pressure loss coefficient are presented for grid planes coincident with the blade trailing edge and the exit of the computational domain in the far wake. A number of sensible and interesting flow features are apparent in these plots. The loss contours at the trailing edge plane (Figure 5.15a) reveal the presence of boundary layers near the blade surfaces where peak loss coefficients as high as 0.50 are predicted. The presence of secondary flow in the hub wall region and the resulting migration of low momentum fluid toward the suction side is indicated by the presence of a large loss region near the intersection of the suction surface and hub wall. The presence of high losses near the outer wall reveal the qualitative effect of leakage flow. The scraping vortex (of small radius) at the intersection of the pressure surface and the annulus wall is also captured qualitatively by the computation.

The loss contours far downstream (Figure 5.15b) reveal an interesting phenomena related to spanwise and lateral mixing downstream of the blade row. The wake spreading (compare Figures 5.11 to 5.13), decreases losses near the wake centerline and increases

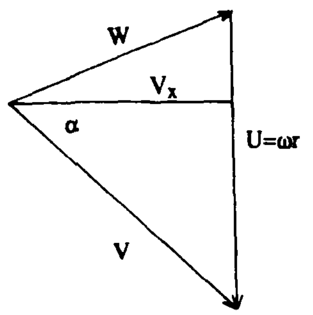

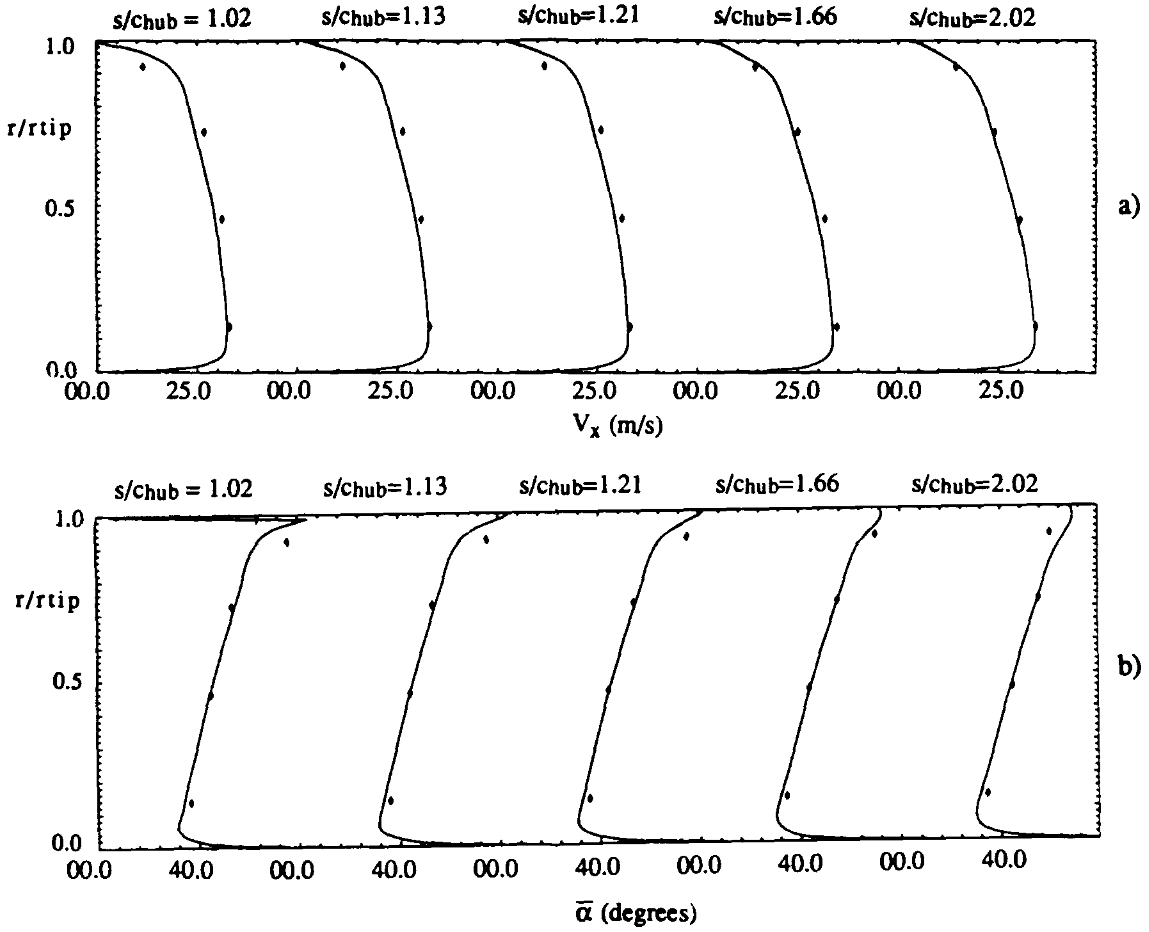

Figure 5.14 Passage averaged (mass weighted) values of a) axial velocity and b) flow angle downstream of PSU rotor passage. Averaged five hole probe measurements due to Prato (1990) (symbols) and computed distributions (solid lines).

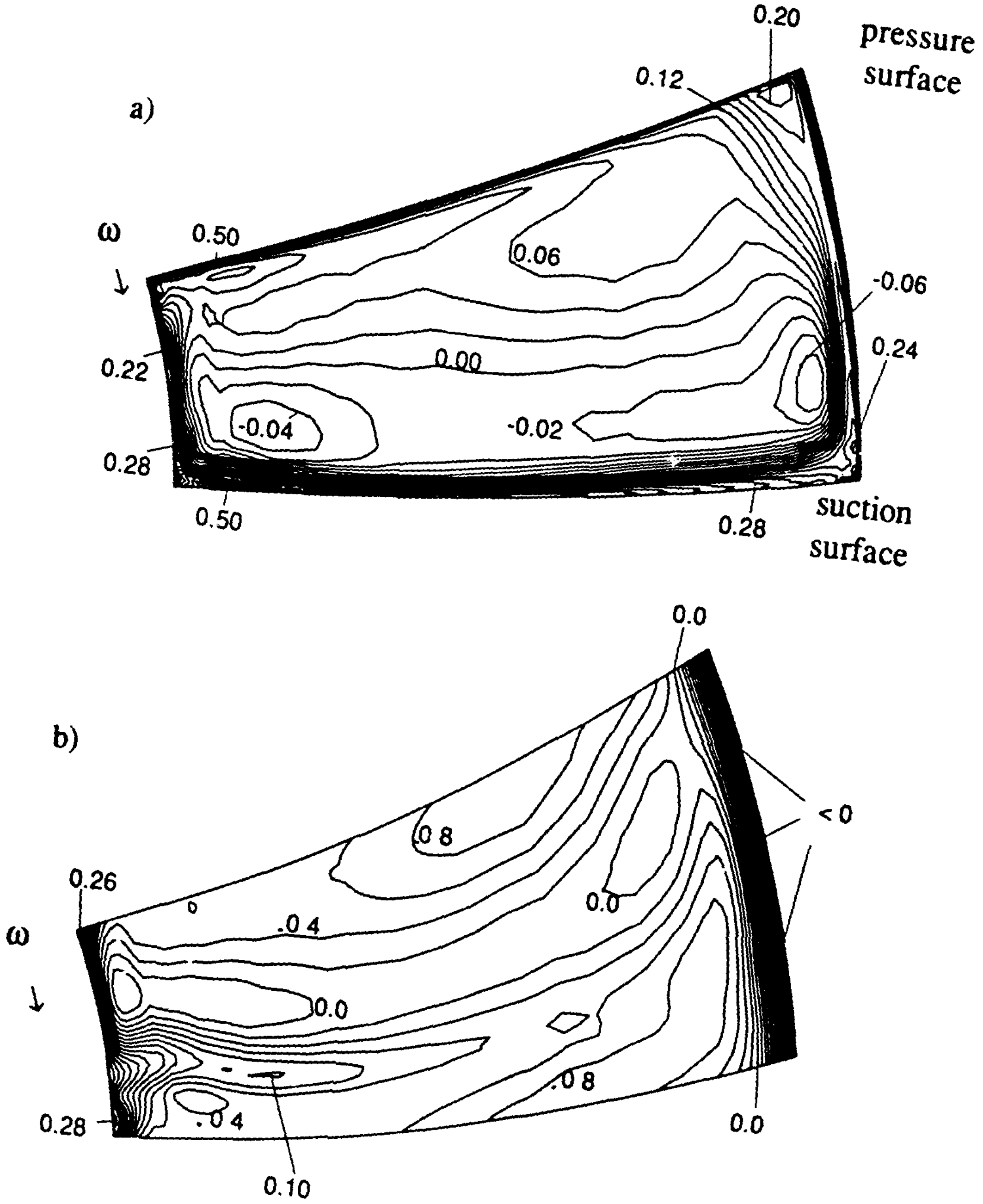

Figure 5.15 Computed contours of relative stagnation pressure loss coefficient, $C_{p\ loss}$, at a) trailing edge, and b) exit plane of computational domain.

losses away from it. The effect of transverse mixing increases losses substantially everywhere except in the inviscid core region. The inviscid core region is located approximately in the middle third of the passage, where the losses are nearly zero. The corner flow loss region (at the intersection of suction surface and hub wall) has grown both in the blade to blade and spanwise direction. The radial velocities in the wake on the suction side have transported and elongated this loss region to higher radius.

An interesting phenomenon is identified in the tip region of Figure 5.15b. Here the losses have not only decreased, but very close to the wall negative loss coefficients are predicted. This is caused by spanwise and lateral mixing due to wakes, leakage vortices and secondary flows. This is consistent with the spanwise mixing analysis carried out by Adkins and Smith (1982), whose results have been reproduced in Figure 5.16. Their input loss distribution was based on empirical correlations. The computation was based on a spanwise mixing analysis. The measured values indicate negative loss coefficient near the outer wall, consistent with the present computational results. Additionally, the PSU rotor computation predicts that the loss core in the annulus wall region is washed out by mixing. This is clear evidence that the high loss region observed at the trailing edge in the annulus wall region is "peeled off" by secondary flows and the entire loss core region is convected and diffused to inner radii. The spanwise mixing effects are thus simulated by this Navier-Stokes code, supporting the physical phenomena postulated by Adkins and Smith.

The passage averaged (mass weighted) losses just downstream of the trailing edge, both measured by Prato (1990) and predicted by the present authors, are shown in Figure 5.17a. The profile losses, away from the endwalls are captured with reasonable accuracy. Underprediction of losses at hub and midspan regions are consistent with the underprediction of wall shear stresses along the blade surfaces, evident upon close examination of Figure 5.9. The data includes one point in the tip region and the prediction

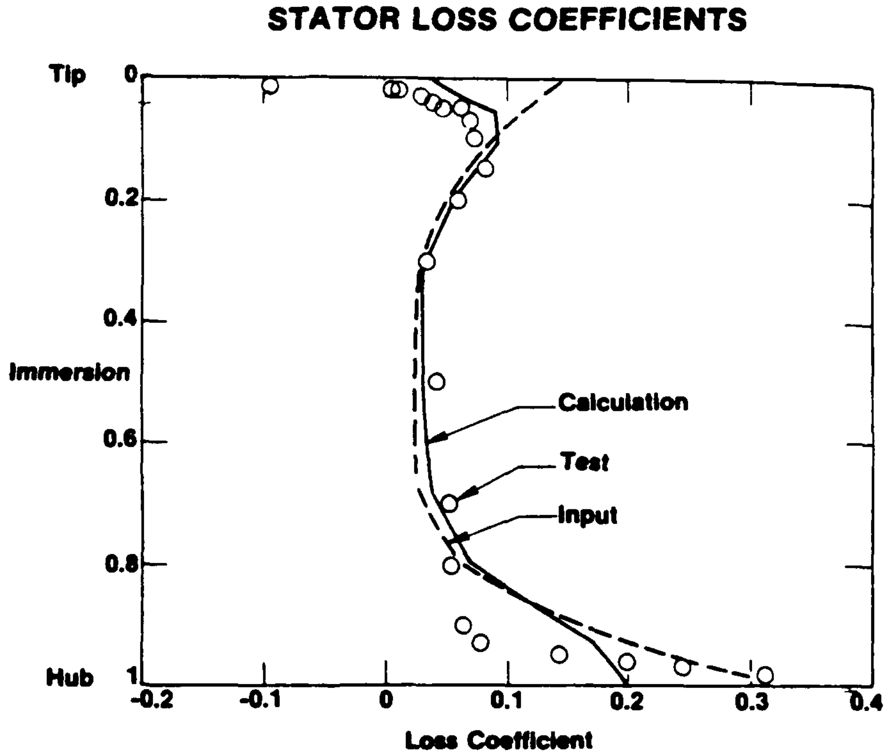

Figure 5.16 Loss coefficient distributions for General Electric Low Speed Research Compressor. This figure is reproduced from Adkins and Smith (1982).

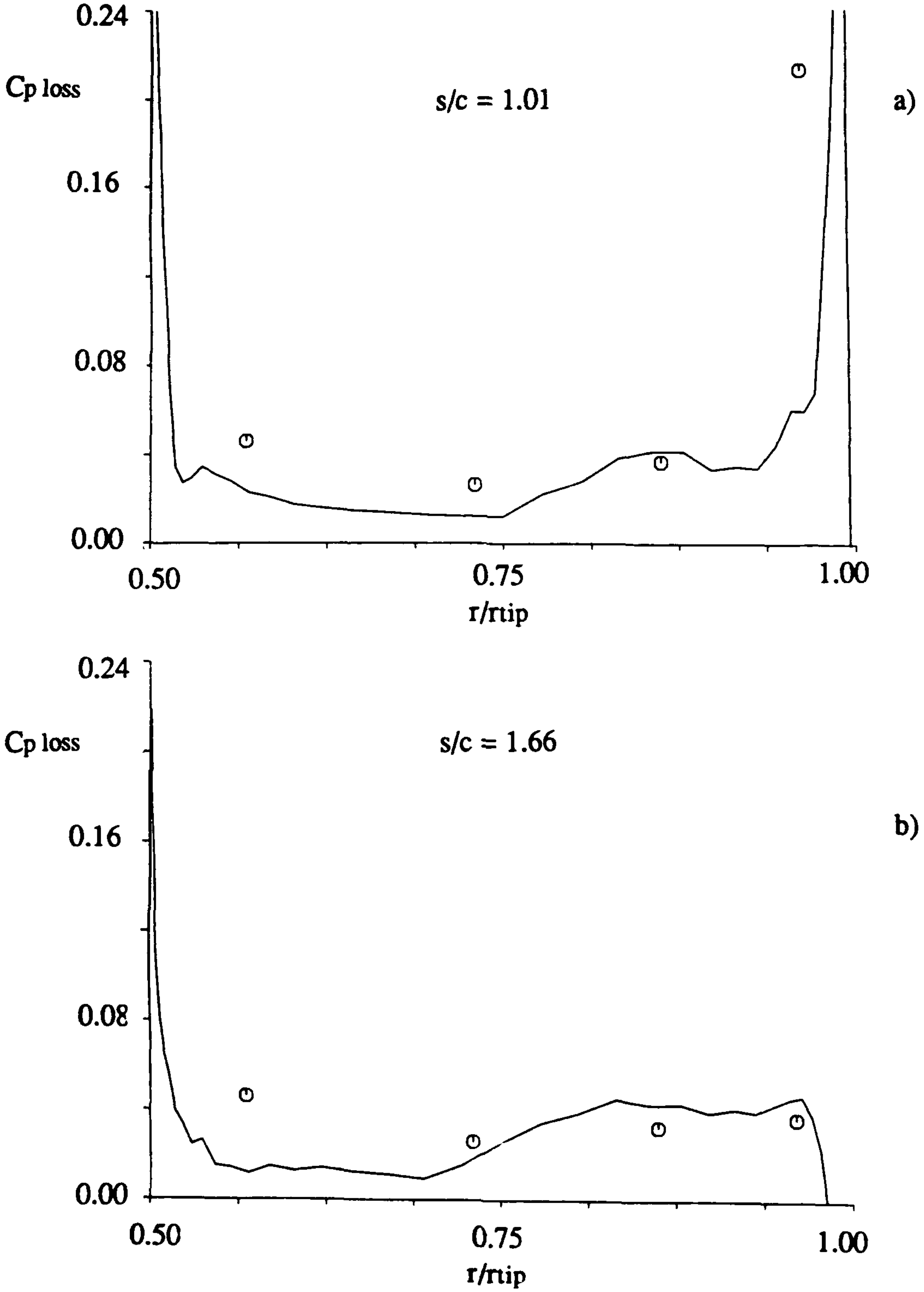

Figure 5.17 Passage averaged (mass weighted) relative stagnation pressure loss coefficient, $C_{p\ loss}$, a) in the near wake and b) .66 chord downstream of hub trailing edge. Averaged five hole probe measurements due to Prato (1990) (symbols) and computed distributions (solid lines).

is poor there. The losses predicted approximately one chordlength downstream are shown in Figure 5.17b. The spanwise mixing phenomena, referred to above, decrease losses in the tip region, and this feature is captured by the code. Major redistribution of losses occur only in the tip region, where intense spanwise and lateral mixing due to leakage flow, secondary flow and wake radial velocities occur. This is consistent with the results of Adkins and Smith (1982).

Overall Performance

Computed and measured flow coefficients and pressure rise coefficients are presented in Table 5.1.

Table 5.1. Comparison of Performance Parameters for Penn State Compressor Rotor

Flowfield Parameter[a]	Measured[b]	Computed	% Difference
Flow Coefficient, $\bar{\phi}$	0.50	0.495	1.0[c]
Pressure Rise Coefficient, $\bar{\psi}$	0.55	0.563	2.4

a $$\bar{\phi} \equiv \int_1 \frac{v_{x1}}{U} \, dA/A, \qquad \bar{\psi} \equiv \frac{\overline{p_{o2}} - \overline{p_{o1}}}{\frac{1}{2}\rho_\infty U^2}, \quad \overline{p_o} \equiv \frac{\int \rho v_x p_o \, dA}{\int \rho v_x \, dA}$$

b Values from Lakshminarayana and Popovski (1987)

c Note that close agreement for $\bar{\phi}$ is due to choice of inlet boundary condition (see discussion above).

It it evident that the overall pressure rise coefficient (Table 5.1) as well as overall losses (Figure 5.17) are reasonably well predicted.

CHAPTER 6

TRANSONIC CENTRIFUGAL COMPRESSOR COMPUTATIONS

In this chapter, results of computations of the flowfield within a modern transonic centrifugal compressor stage are presented and interpreted. These results are compared with available L2F meridional velocity measurements within the impeller passage, shroud static pressure measurements and overall performance measurements. First, solutions using the low Reynolds number k-ε model are provided. The hybrid k-ε / ARS model was also used to compute this flow, both with and without incorporation of the production by system rotation terms (R_{ij} in equation [2.14]) included in the model, and results of these computations are also included.

6.1 Background

The centrifugal compressor chosen for detailed computational study was designed and tested by Krain et al. (1988, 1989). The low specific speed impeller ($N_s = 80$) has 24 straight blade surfaces (hub to tip) to allow flank milling manufacture, and a 30° backsweep. In Figure 6.1, a photograph of the impeller is reproduced from Krain (1988). In Figure 6.2, the periphery of the computational grid used in the simulations is provided. Except for the modern impeller wheel, the experimental facility used by Krain was the same as that used by Eckardt (1975, 1976), with a constant area vaneless diffuser to allow a wide operating range. As seen in Figure 6.2, the diffuser flowfield was also computed. In Figure 6.3, experimentally obtained performance maps for the stage have been reproduced from Krain (1988), and the operating point computed is indicated. The design point was chosen for the present calculations. The flow parameters corresponding to this operating condition were : mass flow rate = 4.0 kg/s (.167 kg/s each passage), maximum inlet

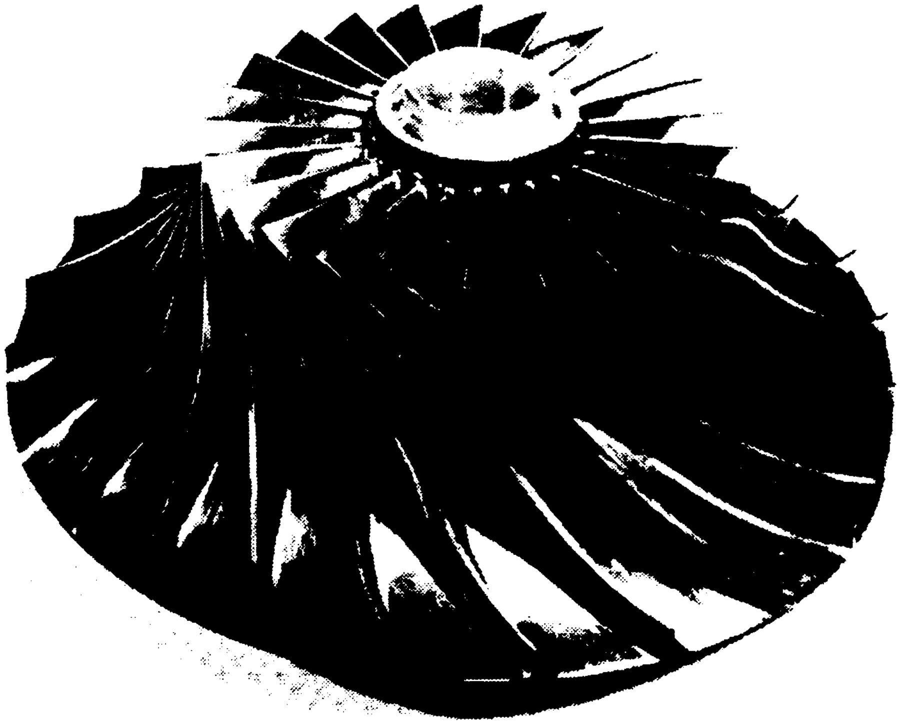

Figure 6.1 Impeller wheel tested experimentally by Krain (1988), and investigated computationally in this chapter. This figure was reproduced from Krain (1988).

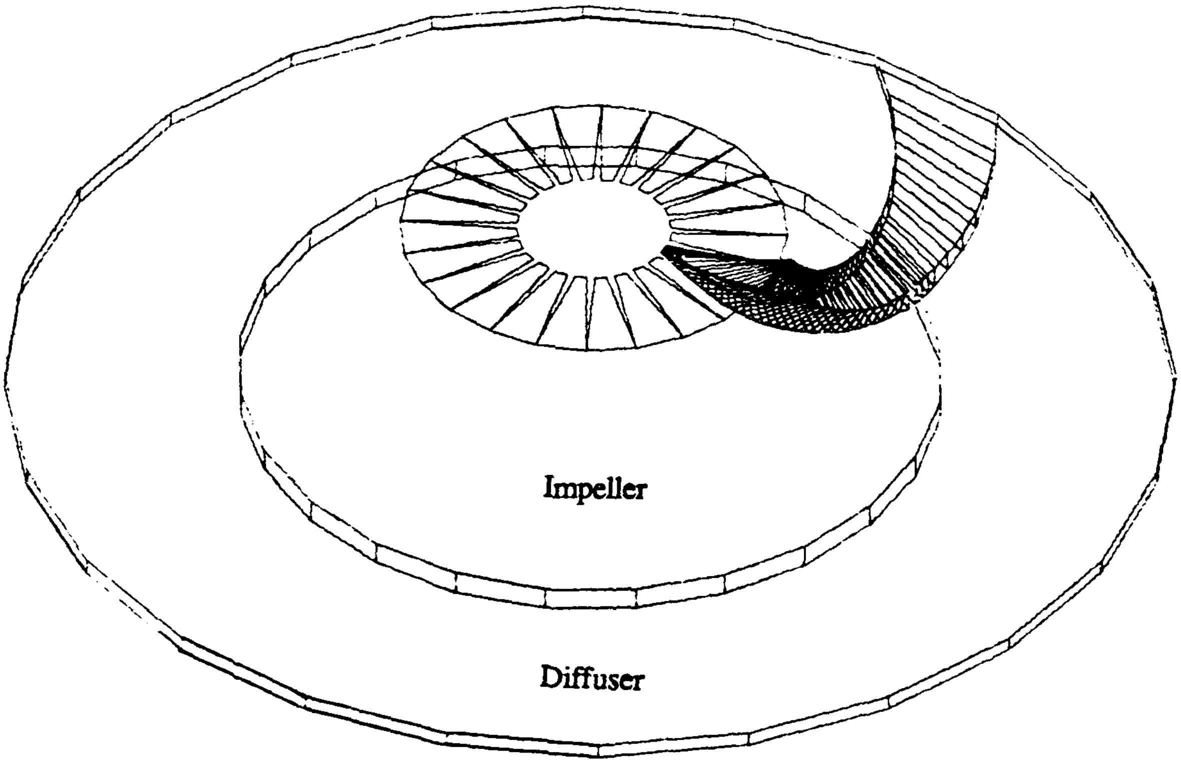
Impeller
Diffuser

Figure 6.2 Periphery of computational grid used in numerical simulation studies, showing impeller and diffuser sections of centrifugal compressor stage.

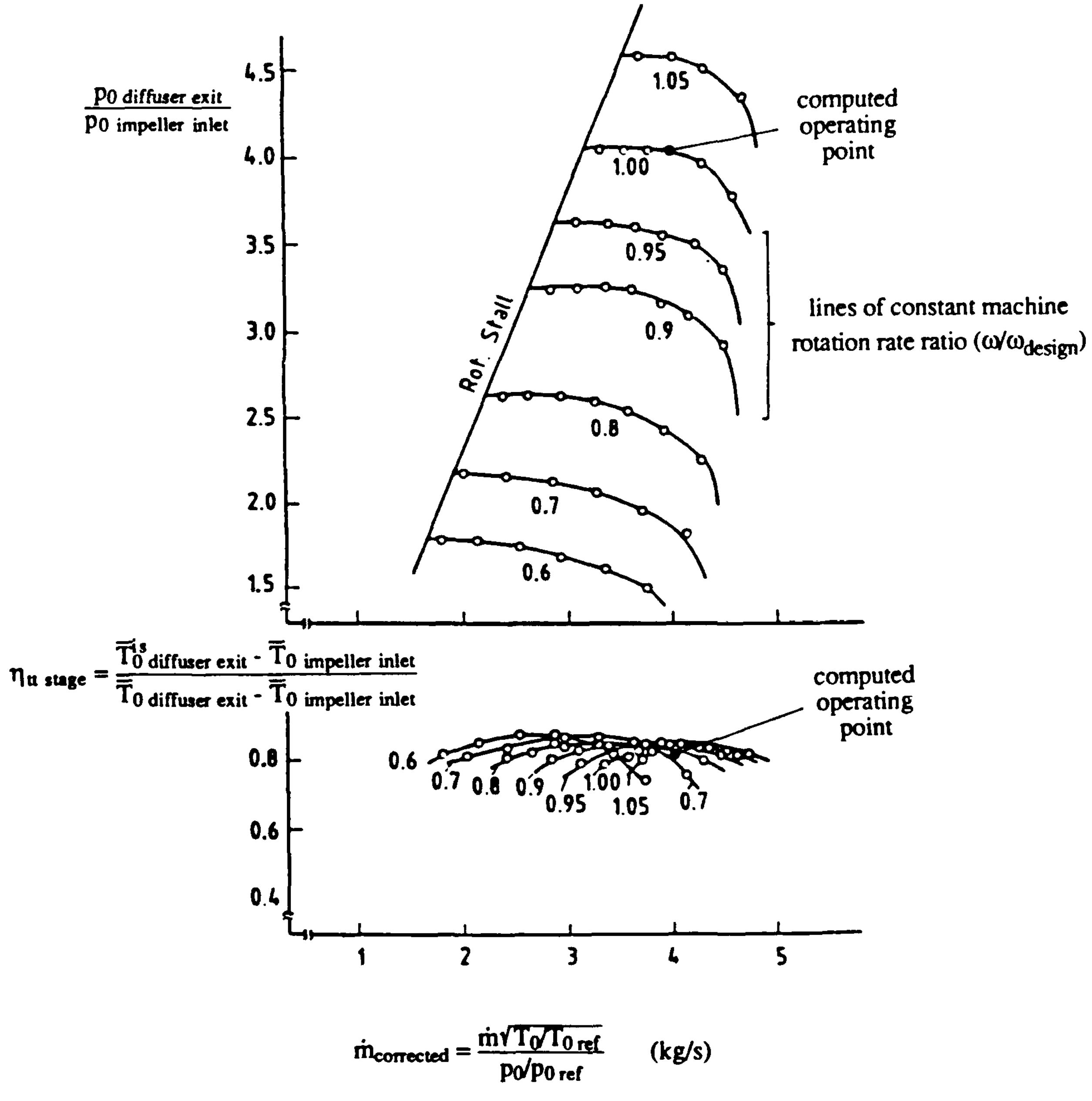

Figure 6.3 Performance maps for Krain impeller, indicating computed operating point. This figure was adapted from Krain (1988).

relative Mach number $\cong 0.8$ (at shroud), machine rotation rate = 22,363 rpm, $p_{0,\text{diffuser exit}}/p_{0,\text{impeller inlet}} \cong 4.0:1$.

In Figures 6.4 and 6.5, meridional and streamwise views of the 59 x 27 x 27 computational grid (43011 grid points) used for this calculation are shown. Also appearing in Figure 6.4 are the locations of the experimental laser planes used by Krain and referred to in the results to follow. The experimentally measured impeller wheel was fitted with a spherical nose cone. For the computations, a cusped spinner cone was implemented, as shown in Figure 6.4, to accommodate the H-grid topology of the code. One of the few practicalities in computing centrifugal compressor flowfields arises from the fact that the impeller flowfield is dominated by shear layers which encompass the entire passage. For this reason, nearly grid independent solutions were obtained in the present study, by using 27 grid points in the blade to blade and hub to tip directions. This phenomenon has also been noted by Hah and Krain (1989) (28704 grid points), and is apparently the reason for the relatively coarse cross stream grids used in centrifugal compressor calculations by Rhie et al. (1985) (14250 grid points), Dawes (1988) (17051 grid points) and Choi and Knight (1989) (81600 grid points).

The grid was generated algebraically using the impeller geometry provided by Krain and Hoffmann (1989, 1990), and a grid clustering routine provided by Basson (1991). Krain (1990) measured the impeller inlet and exit tip clearance at design operating speed to be 0.5 mm and 0.2 mm, respectively. The tip gap was varied linearly along the shroud from inlet to exit in the grid generation procedure. As with the rotor flow computation presented in Chapter 5, a "thin blade" tip gap approximation is used in the present calculations. As shown in Figure 6.5, eight grid points were used to resolve the gap region. Additionally, the leading and trailing edges were cusped over two streamwise grid points. Wall normal grid spacing was 4.4×10^{-4} times the inlet span along the hub

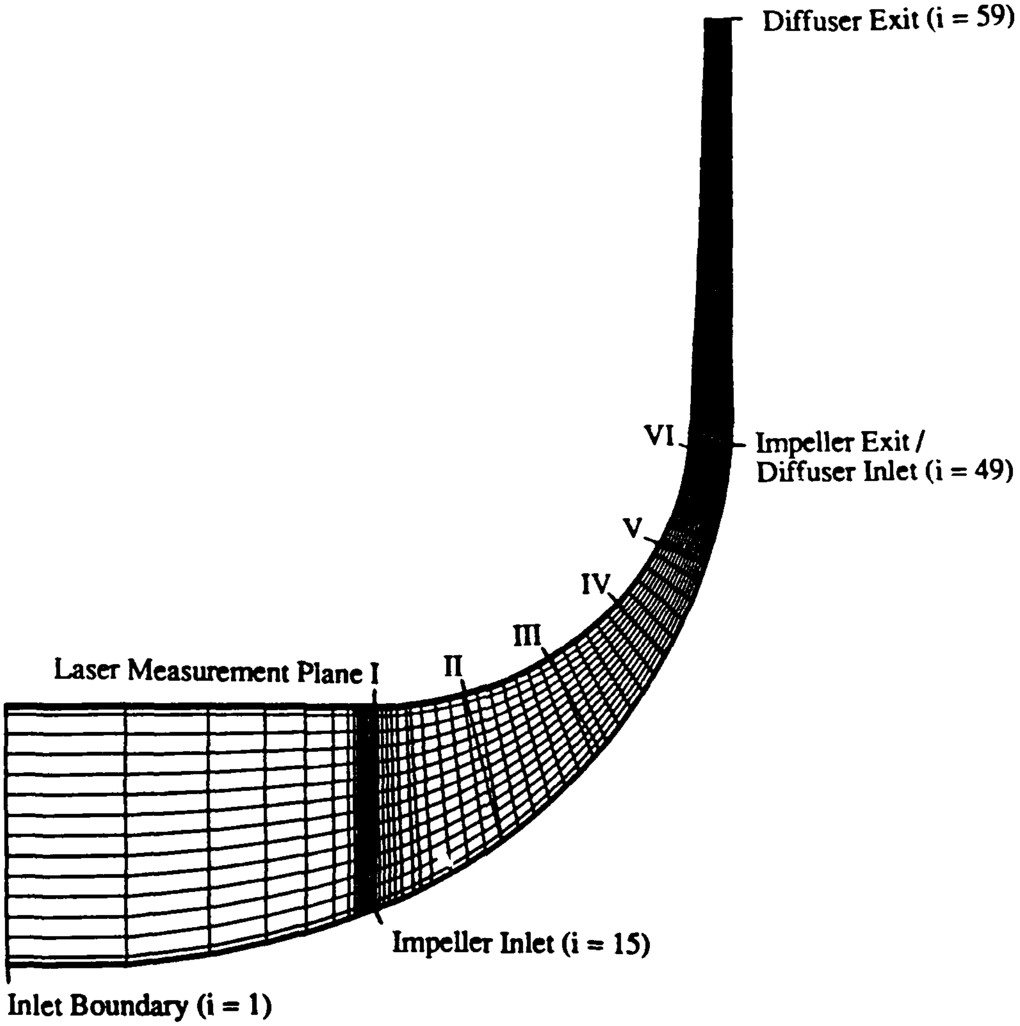
Diffuser Exit (i = 59)
VI
Impeller Exit / Diffuser Inlet (i = 49)
V
IV
III
II
Laser Measurement Plane I
Impeller Inlet (i = 15)
Inlet Boundary (i = 1)

Figure 6.4 Meridional view of 59 x 27 x 27 computational grid for Krain impeller computation. Streamwise grid indexing and location of experimental laser planes are indicated for reference.

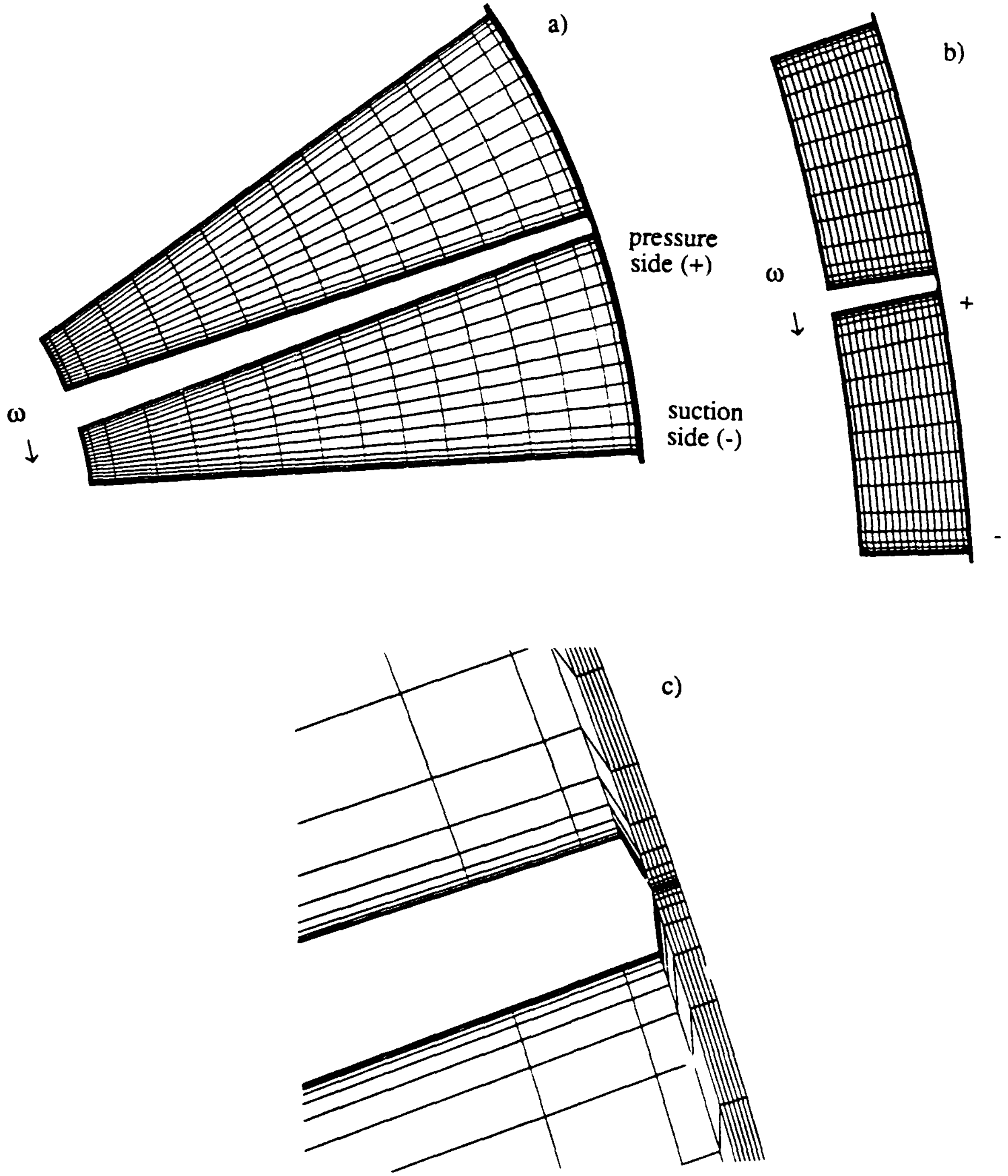
a)
pressure
side (+)
ω
↓
suction
side (-)
b)
ω
↓
+
-
c)

Figure 6.5 Cross stream views of 59 x 27 x 27 computational grid for Krain impeller computation. a) Impeller inlet grid slice, b) grid slice near impeller exit and c) tip gap detail at inlet grid plane.

and 2.2×10^{-4} times the inlet span on the blade surfaces. This clustering yielded converged values of y^+ ranging from 2 to 7 along the hub endwall and both blade surfaces at midchord, for the k-ε solution provided below.

As discussed previously, curvature, rotation and viscous physical phenomena strongly influence the impeller flowfield, especially in the aft portions of the passage. Specifically, strong secondary motions, caused by turning of blade and endwall boundary layers, and coriolis forces, influence the flow development as illustrated schematically in Figure 6.6a. In this figure, the secondary flow effects labelled A through D correspond to :

A) Secondary flows arising from axial to radial turning of blade boundary layers.

B) Secondary flows arising from axial to tangential turning of endwall boundary layers. No direction convention is provided for this effect, since endwall boundary layers are convected towards the suction side due to tangential to axial turning in the inducer, but axial to tangential turning due to backsweep of the impeller under consideration gives rise to the opposite effect in aft portions of the passage.

Figure 6.6b is a sketch which illustrates the nature of these curvature induced secondary motions. Specifically, the three dimensional cross flow associated with axial to radial turning of the pressure side blade boundary layer (A above) is illustrated.

C) Coriolis "pipe" force or "eddy" arising from $-2\vec{\omega} \times \overrightarrow{W_\theta}$ component of coriolis acceleration (gives rise to slip velocity; see performance discussion below).

D) Coriolis "spin" force arising from $-2\vec{\omega} \times \overrightarrow{W_r}$ component of coriolis acceleration.

The dominant flow feature in centrifugal compressors is the so called "jet-wake" structure which forms near the shroud in all impeller flows. Cross flows which are

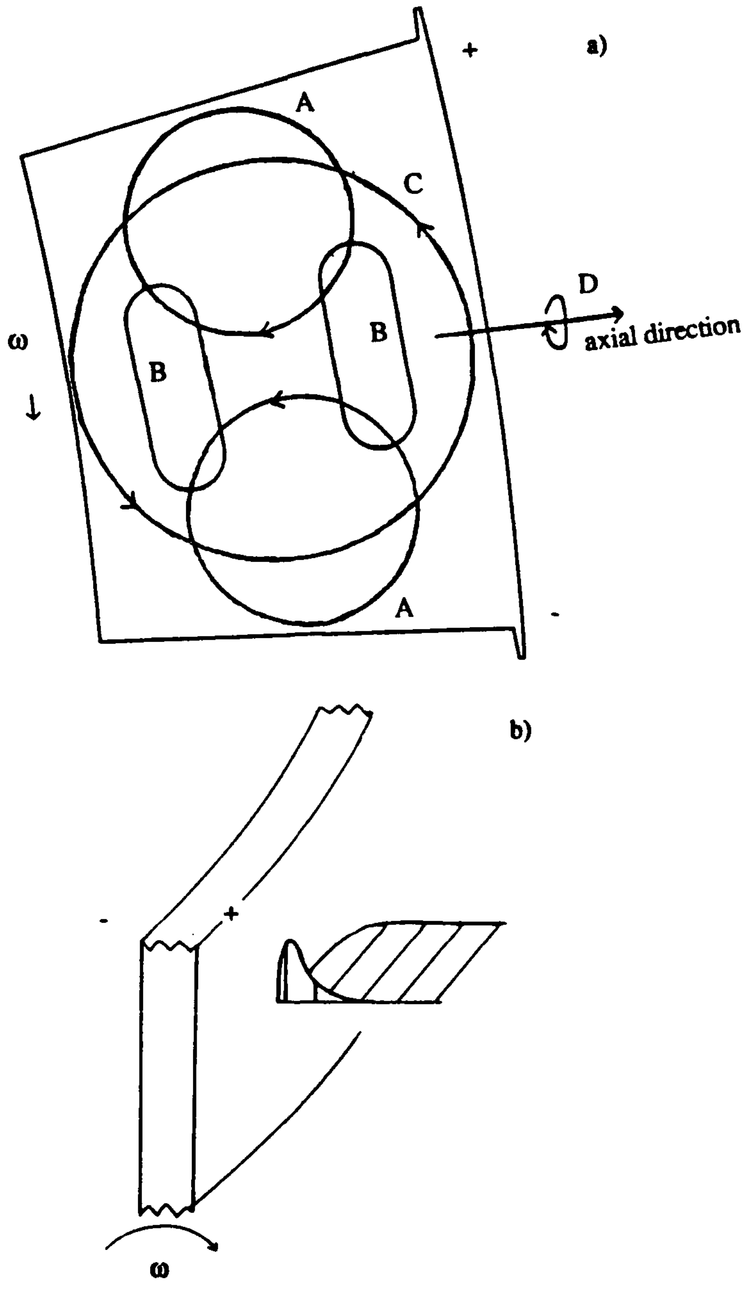

Figure 6.6 Qualitative representation of secondary motions present in a centrifugal compressor impeller.

a) Sense of curvature and rotation induced motions :

A) Secondary flows arising from axial to radial turning of blade boundary layers.

B) Secondary flows arising from axial to tangential turning of endwall boundary layers.

C) Coriolis "pipe" force.

D) Coriolis "spin" force.

b) qualitative sketch of pressure surface crossflow arising from axial to radial turning of the meridional flow.

induced by axial to radial turning of the blade boundary layers (effect A above), accumulate low momentum boundary layer fluid into the shroud region near mid-passage. Typically, the pressure side vortex is stronger than the suction side counterpart, of this vortex pair, labelled A in Figure 6.6a. For this reason, the location of this region of low energy fluid is typically closer to the suction surface. As discussed by Eckardt (1976) and others, this pocket of low momentum fluid forms approximately halfway through the impeller channel. It typically grows to fill a significant portion of the midpassage region, though accounts for a significantly smaller percentage of total mass flow. This "wake" flow introduces significant blockage and thereby acceleration of the surrounding high momentum fluid, termed the "jet" flow. In the impeller investigated experimentally by Eckardt, this jet-wake structure persisted through to the exit of the impeller.

Additionally, tip clearance flow can significantly alter the flow pattern in centrifugal compressor impellers. Specifically, some 10 % of the total mass flow passes through the tip gap, driven by the pressure gradient between suction and pressure surfaces. Typically this leakage flow gives rise to a strong vortex, whose sense is opposite the main flow direction, and which strays into the adjacent passage and interacts with the wake flow.

Lastly, the direct influence of streamline curvature and system rotation on the structure of local turbulence has been attributed to the formation and persistence of the wake. Specifically, concave curvature along the shroud tends to stabilize the turbulence locally, which should in turn lessen the resistance of the developing shroud boundary layer fluid from being transported away from the shroud towards the hub (transverse flow separation). Additionally, the relatively distinct boundary often observed between wake and jet flow, may be attributable to locally reduced turbulence mixing. This reduction could arise from damping near the shroud due to concave curvature and/or damping near the suction surface due to rotation in the radial portion of the impeller.

In short, the variety of physics which begin to manifest themselves in the aft sections of an impeller are very complex. Since the performance of the machine is critically dependent on these phenomena, especially the nature of exit flow, full Navier-Stokes and turbulence modelling methods, which can provide more accurate prediction and understanding of these phenomena, are useful to the engineer.

Often in unswept impeller computations, relative velocity vectors are used to illustrate the development of secondary motions. In machines with blade sweep, the choice of an appropriate viewing projection can be difficult, and will not in general align with a local grid slice. Accordingly, velocity vector plots are not very useful in interpreting the secondary motions in the impeller under consideration here. Normalized helicity density is used in this chapter to help interrogate the cross stream physics.

Normalized relative helicity, $H = \frac{\vec{W} \cdot \vec{\zeta}}{|\vec{W}|\,|\vec{\zeta}|}$, is a useful parameter in three-dimensional postprocessing of vortical flow solutions. Levy et al. (1990) recently itemized the advantages of normalized helicity as :

1) Vortices can be distinguished from boundary layers (which have large vorticity but $\vec{W} \cdot \vec{\zeta}$ is small).

2) Helicity is a scalar, and as such does not introduce the ambiguities mentioned above that velocity and vorticity vectors give rise to.

3) The sign of the helicity indicates the rotational sense of a vortex.

4) Maxima in normalized helicity correspond to vortex cores, and as such provide a convenient means for tracking developing vortices.

6.2 Flowfield Calculation Using the k-ε Model

The first set of results to be presented are for a solution obtained using the low Reynolds number k-ε model. The standard quasi-one-dimensional flow initialization procedure is a very poor initial guess for this flowfield, since centrifugal pressure rise dominates the rotational inviscid physics in this machine, but is not accounted for in such an initialization. Only by running the half grid problem (30 x 14 x 14) and enforcing inlet mass flow rate, through the course of iteration, was it possible to obtain a converged solution from the quasi-one-dimensional flow initialization. The converged coarse grid solution was then interpolated onto the more refined grid, thereby providing a good initialization.

The convergence history for the full scale computation is shown in Figure 6.7. The code was run for 5000 iterations, at which point the RMS density and turbulent kinetic energy residuals had dropped nearly four orders of magnitude. (Note that the total number of supersonic points ($M_{rel} > 0$) in the computational domain remained nearly unchanged in early iteration due to the coarse grid solution initialization). The solution required approximately 2.5 CPU hours on a Cray Y-MP. The turbulence intensity was arbitrarily set to 3 % , since no experimental value was available, and the artificial dissipation was scaled by the reference velocity $a_{\infty}M_{rel\,\infty}$ for these computations.

In Figure 6.8, circumferentially averaged shroud static pressure is plotted against time averaged static tap measurements made by Krain (1988). The agreement is very good except in the immediate vicinity of the impeller inlet, due most likely to the cusped leading edge, which is relatively thick compared to the blade spacing there (refer to Figure 6.5).

In Figures 6.9 and 6.10, predicted meridional velocities ($W_{merid} = \sqrt{W_x^2 + W_r^2}$)

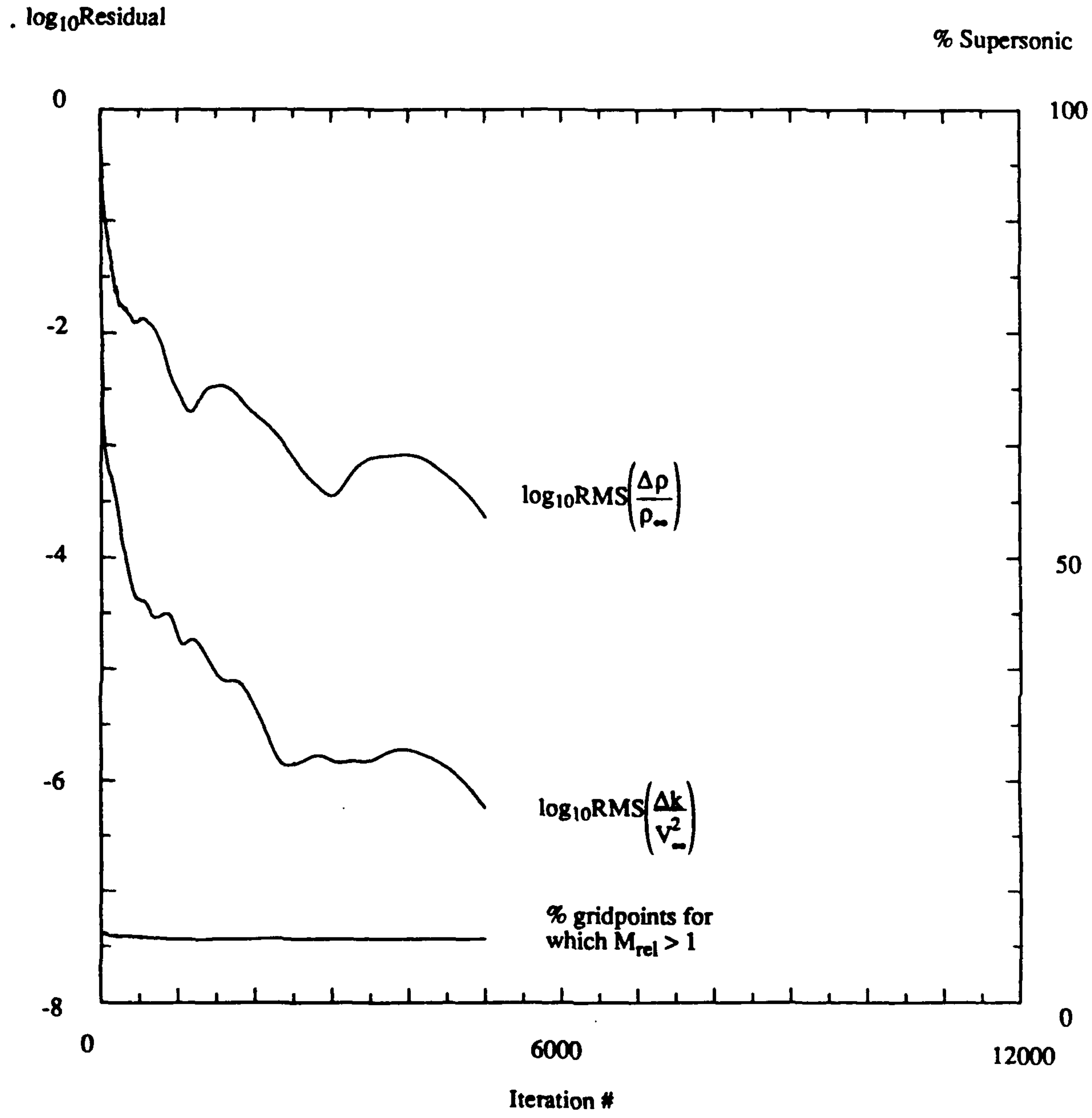

Figure 6.7 Convergence history for Krain impeller flow computation.

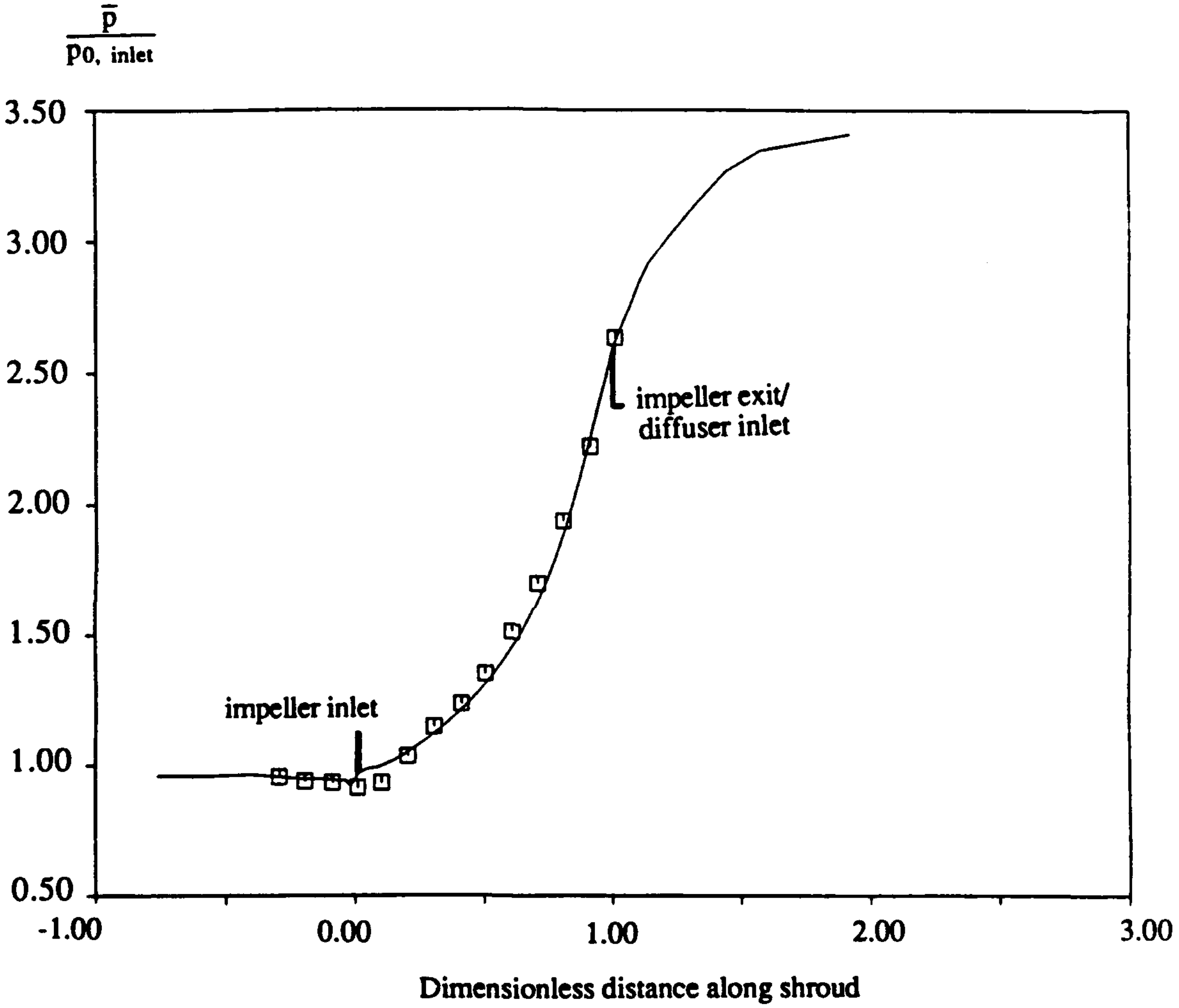

Figure 6.8 Shroud static pressure distribution. Experimentally obtained time averaged static pressure tap measurements (symbols), circumferentially averaged computed values (solid line).

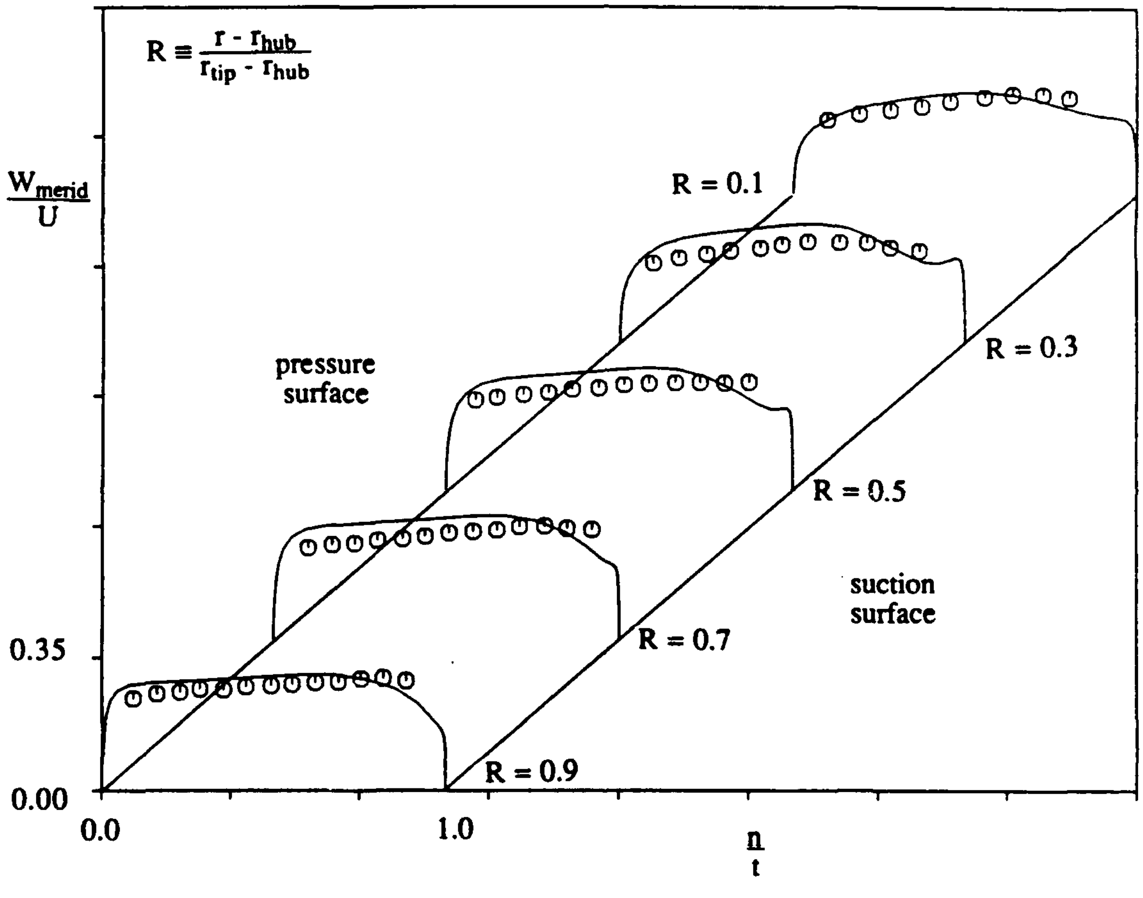

Figure 6.9 Meridional velocity profiles at L2F data acquisition Plane I. Experimental measurements (symbols), computed values (solid line).

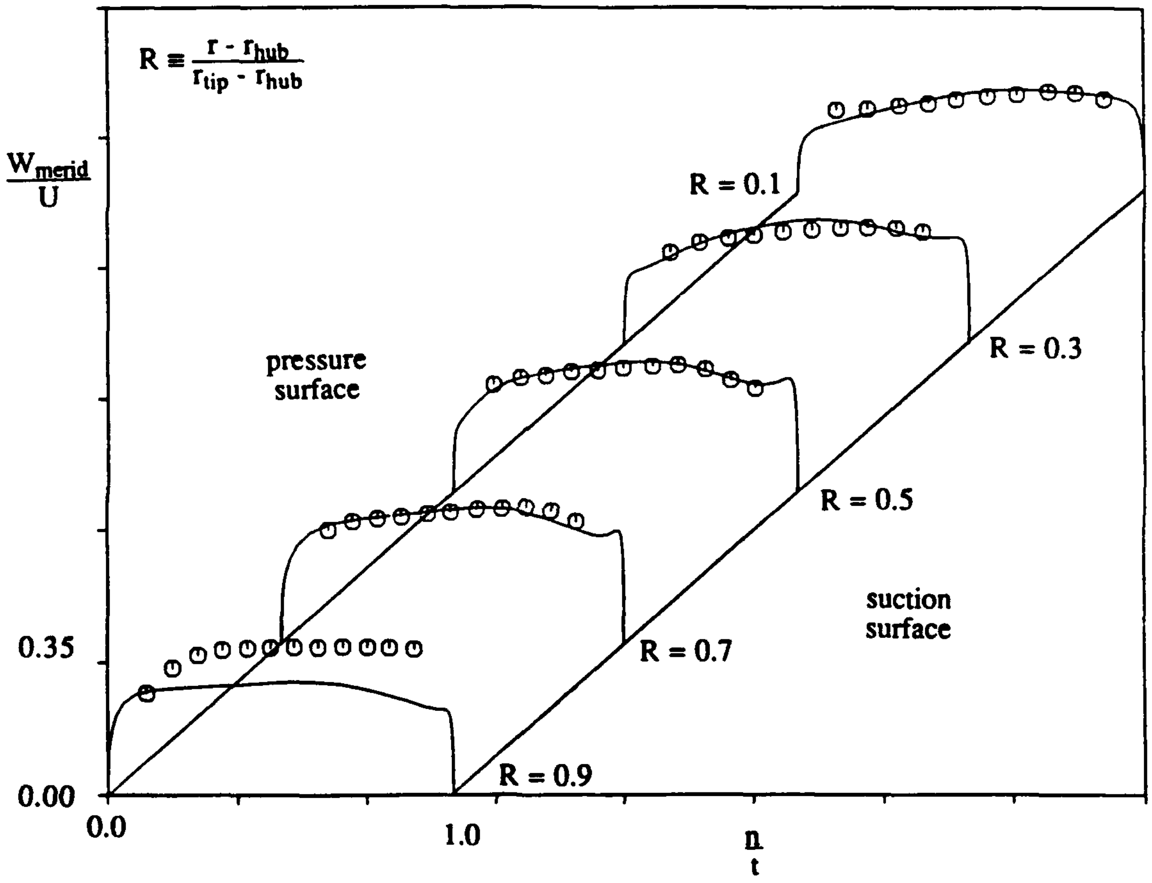

Figure 6.10 Meridional velocity profiles at L2F data acquisition Plane II. Experimental measurements (symbols), computed values (solid line).

are compared with laser measurements at planes I and II, which correspond to 0 % and 30 % chord as measured along the shroud (refer to Figure 6.4). Pitchwise flow turning is significant at the impeller inlet, since the blades are quite thick there (elliptic effect, as for a turbine blade). The resulting blade-to-blade pressure gradient gives rise to larger meridional velocities near the blade suction side, along the span. This is captured by the simulation, as seen in Figures 6.9 and 6.10. Rapid axial to radial turning near the impeller inlet gives rise to a positive gradient in meridional velocity in the hub to shroud direction as seen in both the experimental and computational results in Figure 6.10 (most notable if contrasted with inlet profiles in Figure 6.9).

In Figure 6.11, solution contours of normalized relative helicity are plotted at a grid slice corresponding to Plane III (48 % chord). In this figure, high positive values of normalized helicity (dark shading) correspond to a streamwise vortex (into page), whereas high negative values correspond to negative streamwise vorticity. The secondary motions arising from axial to radial turning of the blade boundary layers (effect A, Figure 6.6a) are clearly evident. Also, the tip clearance vortex is seen to have migrated well into the midpitch region near the shroud.

Figure 6.12 shows the meridional velocities at 50 % chord. Both experiment and computation clearly show a region of significant momentum deficit near the shroud. This is due primarily to the accumulation of low momentum boundary layer fluid arising from the dominant secondary motions discussed previously. Tip clearance fluid is also accumulated in this "wake" region. It was found that the level of agreement between experiment and computation in this region was only achieved when the number of grid points in the tip gap was increased from four to eight, and the grid was not clustered in the spanwise direction there (refer to Figure 6.5c). This reinforces that both axial to radial turning induced secondary motions and tip clearance flow play an important role in the

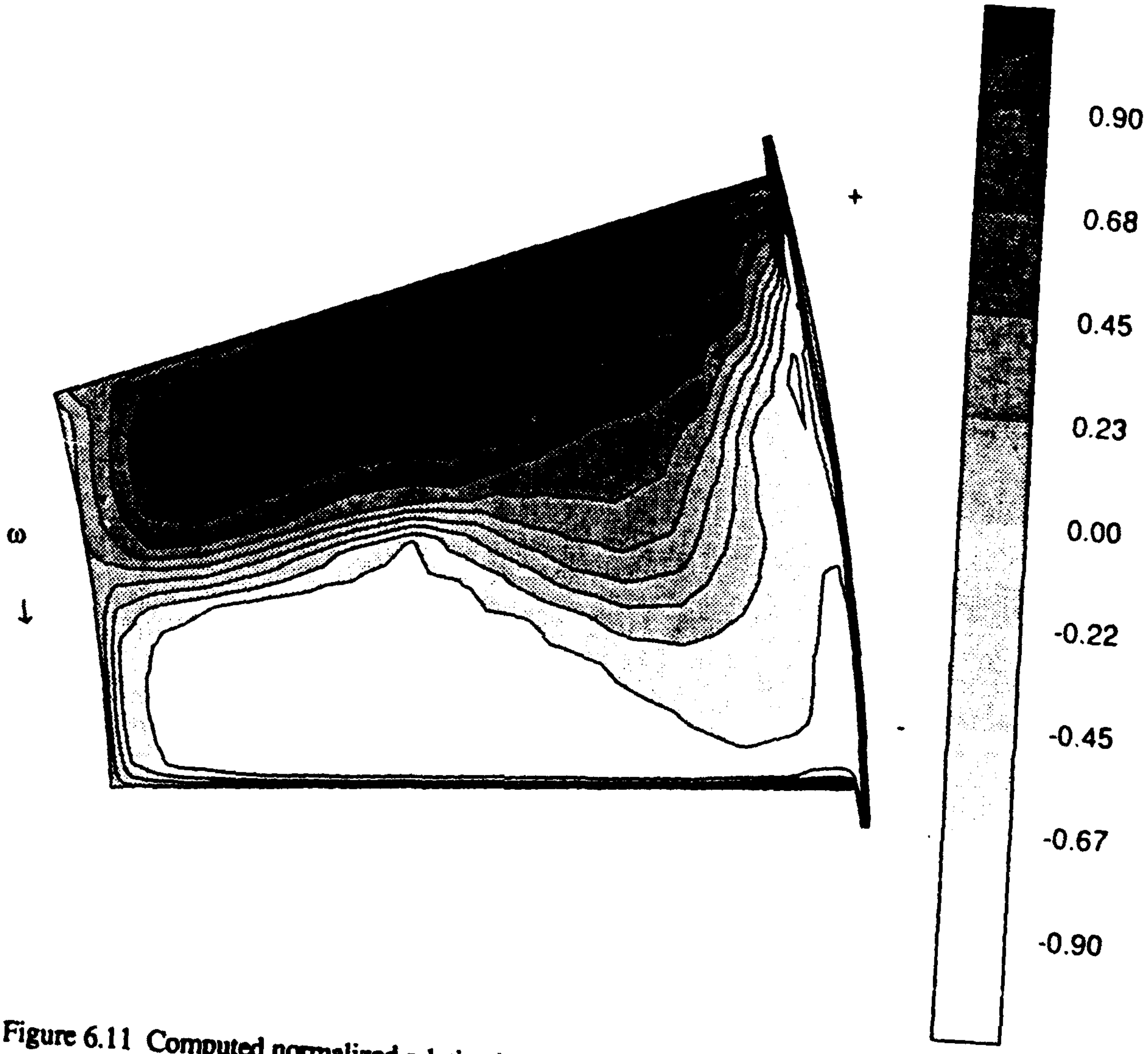

Figure 6.11 Computed normalized relative helicity contours at solution grid slice corresponding to L2F data acquisition Plane III.

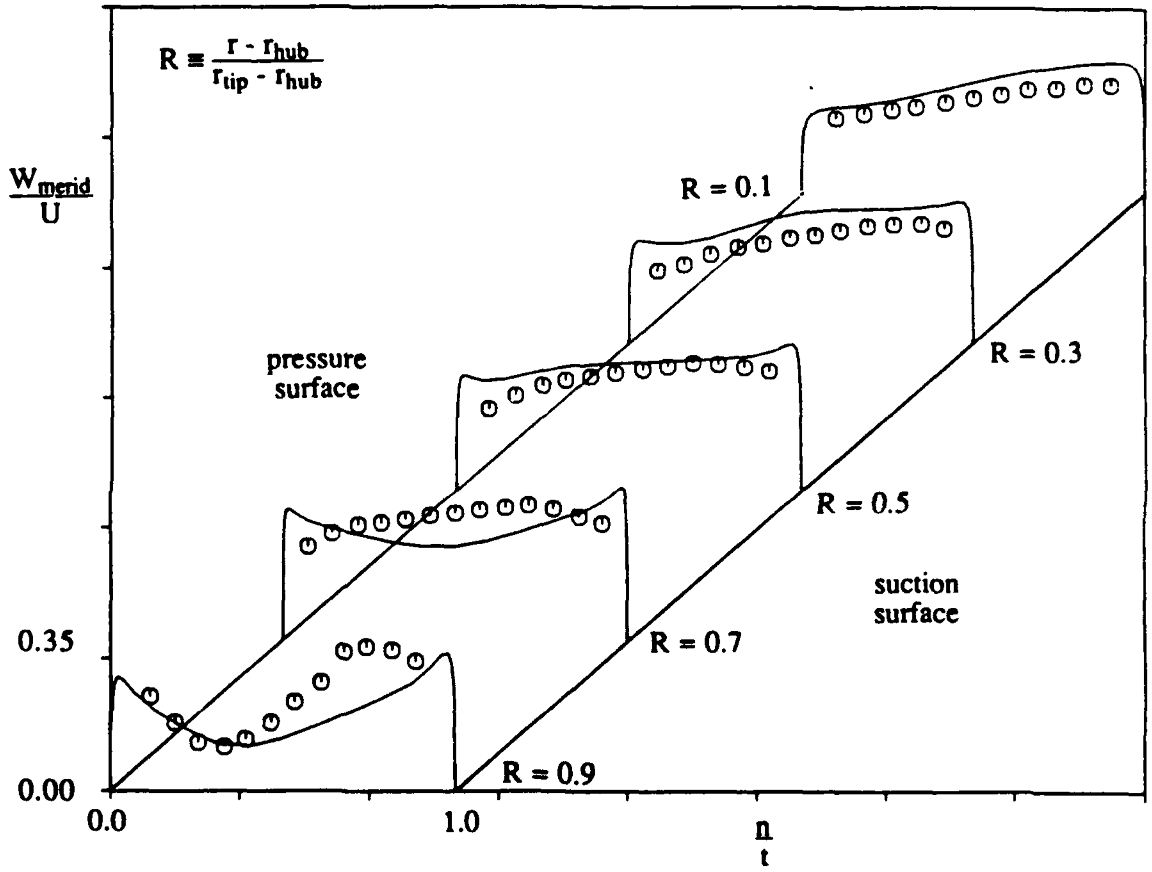

Figure 6.12 Meridional velocity profiles at L2F data acquisition Plane III. Experimental measurements (symbols), computed values (solid line).

formation of this low momentum fluid region. The Navier-Stokes solution overpredicts the extent of the wake region, in both the blade to blade and shroud to hub directions. In Figure 6.13, meridional velocity contours are plotted. Agreement between computation and experiment is good, although it appears that the predicted wake flow has displaced the high momentum inviscid core, or "jet," fluid towards the suction surface prematurely.

Figure 6.14 shows the normalized relative helicity contours at 65 % chord (Plane IV). The jet-wake structure is fully formed at this location. Still evident are the counter rotating secondary vortices. The tip clearance vortex is clearly distinguishable, and appears to have entrained some of the fluid from the pressure side half of the passage, "dragging" some high streamwise vorticity fluid towards the suction side. Meridional velocities compare quite well at Plane IV, as shown in Figure 6.15. Most notable is that the experimental and computed wake flow has extended to midspan. The blockage that this fluid provides is seen to accelerate the higher momentum jet fluid towards the two blade and hub surfaces. Peak values of meridional velocity occur near the suction side-hub corner. These features are evident in the meridional velocity contours provided in Figure 6.16, where it is also seen that the location of low meridional velocity near the shroud has migrated towards the suction surface.

The results at 65 % chord, presented in the previous paragraph, illustrate that the wake flow has fully manifested itself at this location. It is interesting to compare a highly referenced qualitative sketch provided by Eckardt (1976), with normalized relative helicity solution contours. In Figure 6.17a, Eckardt's sketch, which serves to illustrate the variety of phenomena which contribute to the formation of the jet-wake flow, has been adapted. A solution grid slice at 68 % chord was chosen for comparison in Figure 6.17b, since the salient features of the wake flow correspond well with Eckardt's sketch at this location. This comparison clearly serves to illustrate the appropriateness of the present Navier-

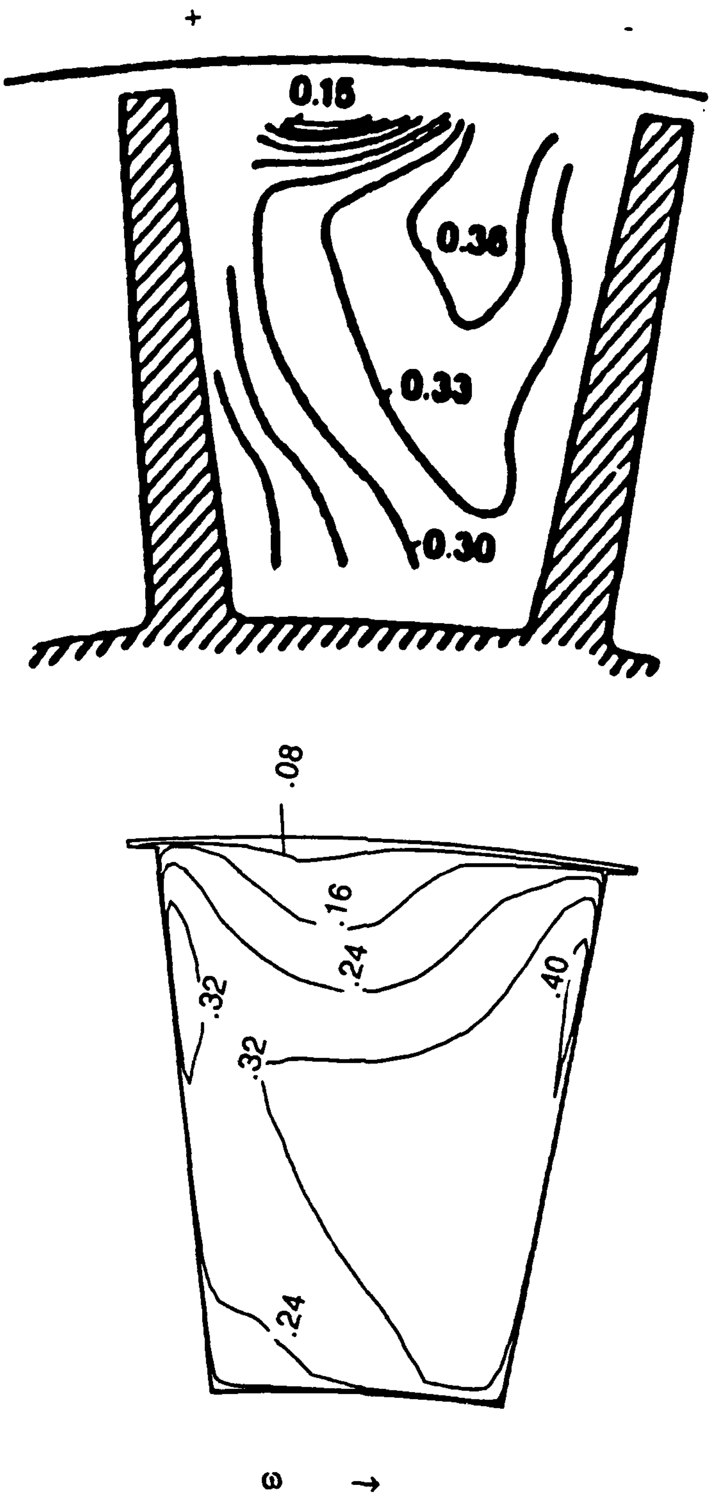

Figure 6.13 Meridional velocity contours at L2F data acquisition Plane III. Experimental contours (top), computed contours (bottom).

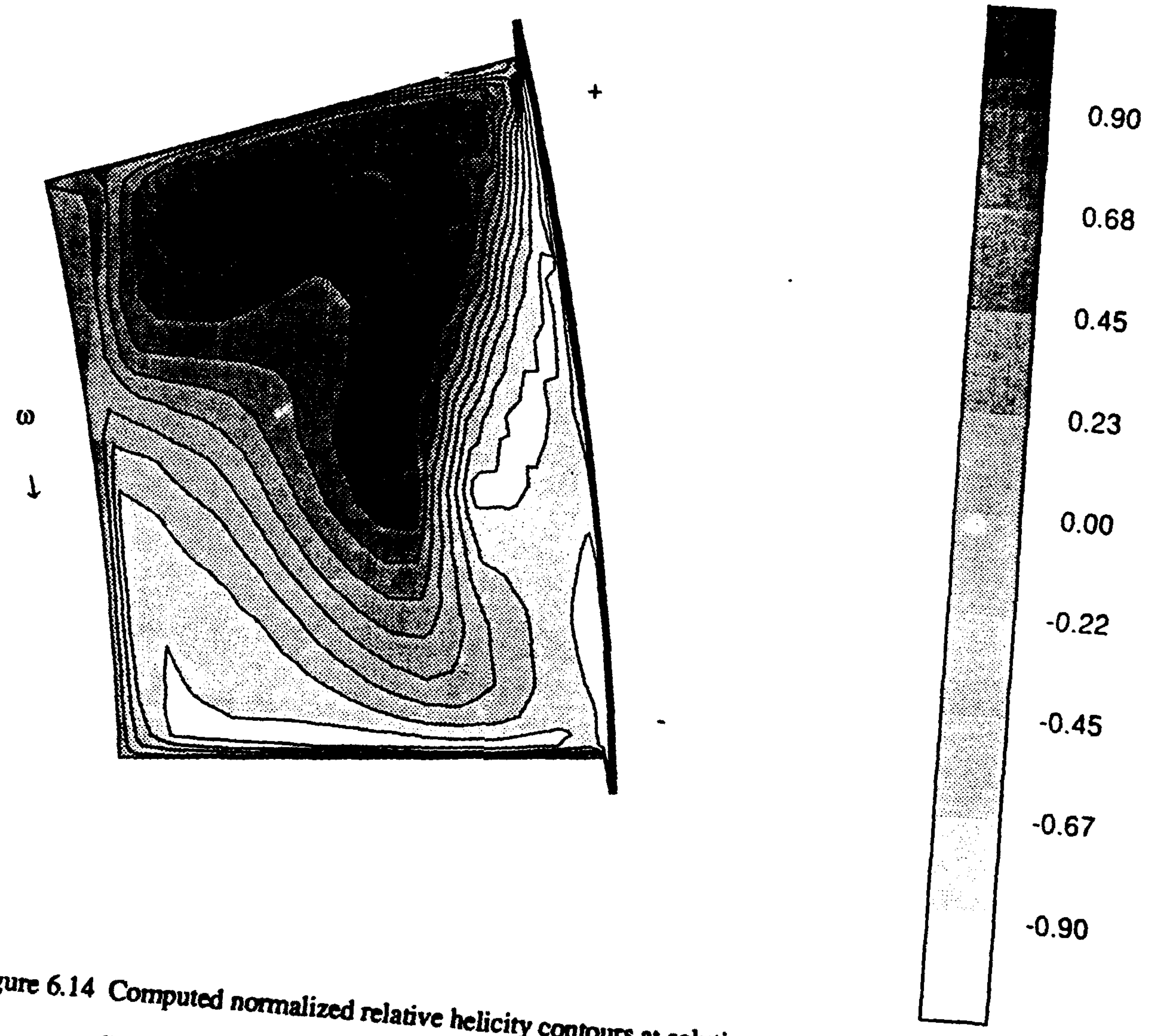

Figure 6.14 Computed normalized relative helicity contours at solution grid slice corresponding to L2F data acquisition Plane IV.

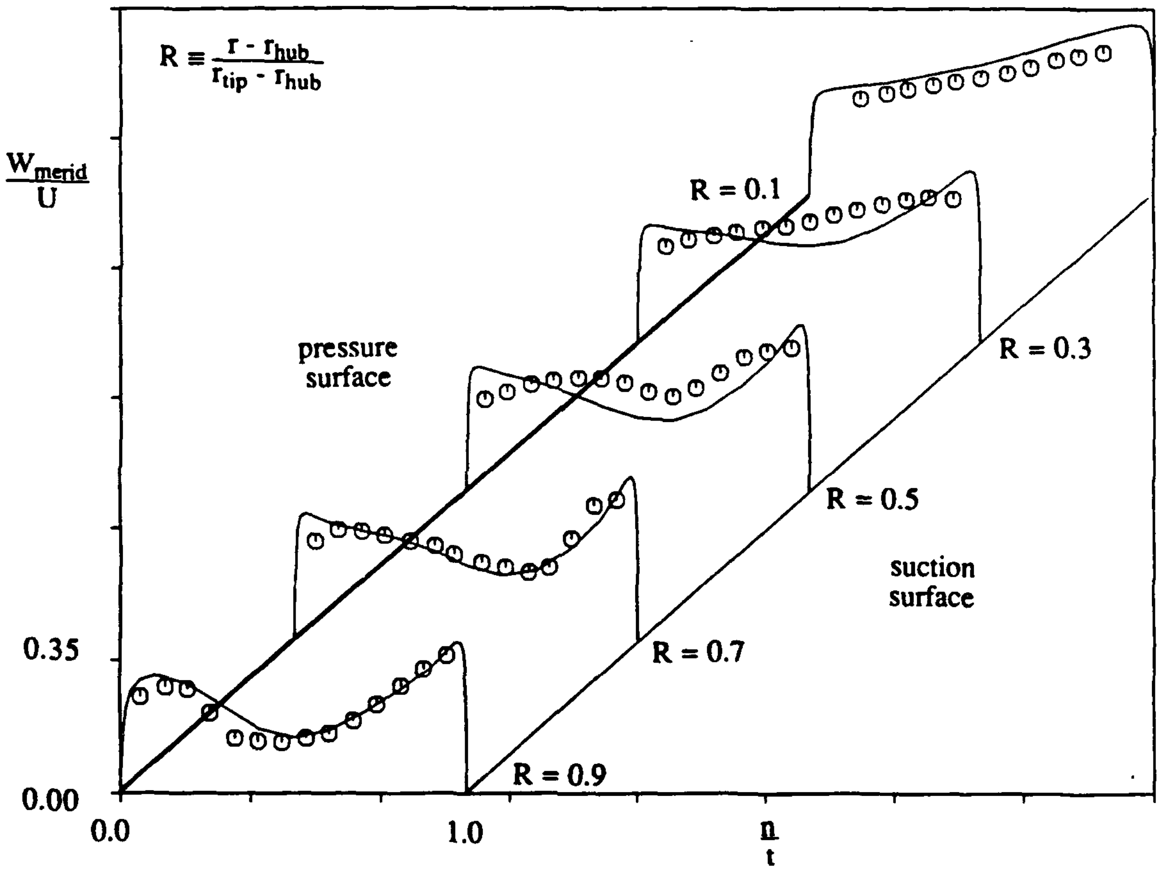

Figure 6.15 Meridional velocity profiles at L2F data acquisition Plane IV. Experimental measurements (symbols), computed values (solid line).

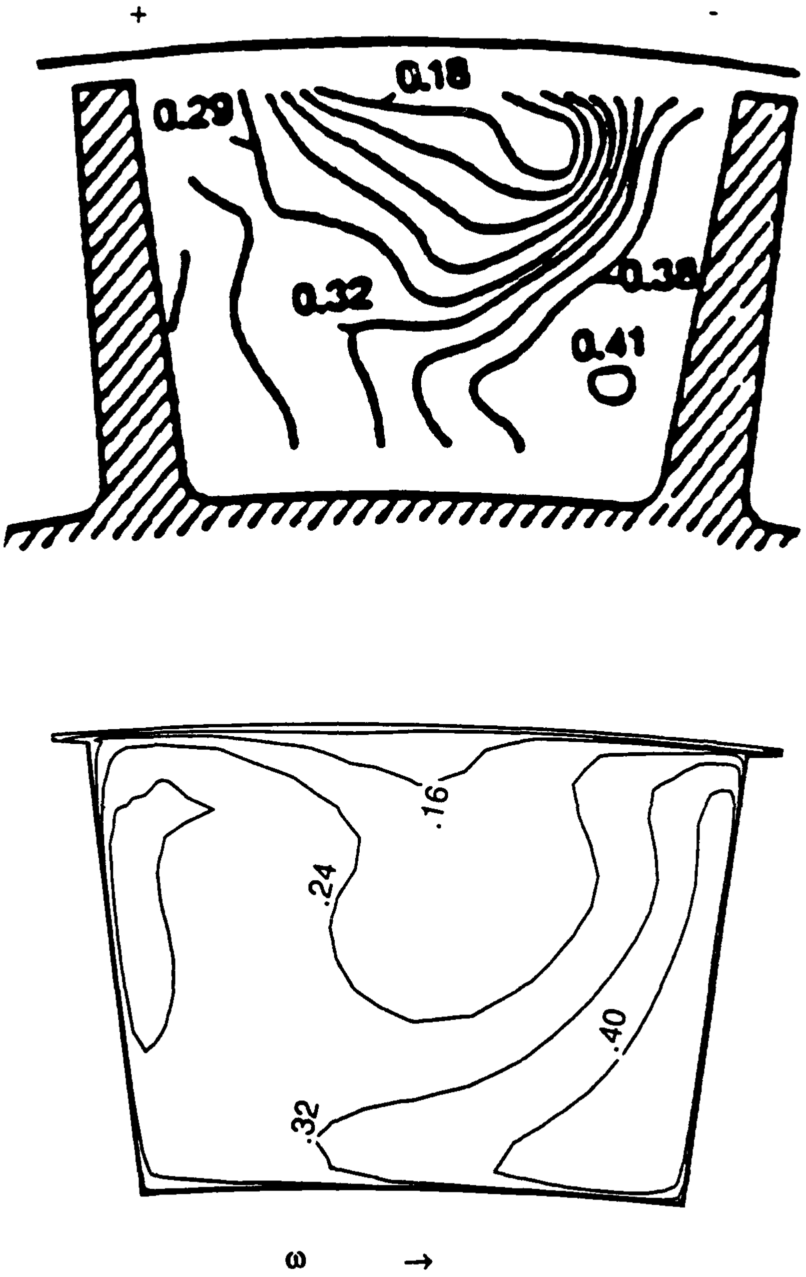

Figure 6.16 Meridional velocity contours at L2F data acquisition Plane IV. Experimental contours (top), computed contours (bottom).

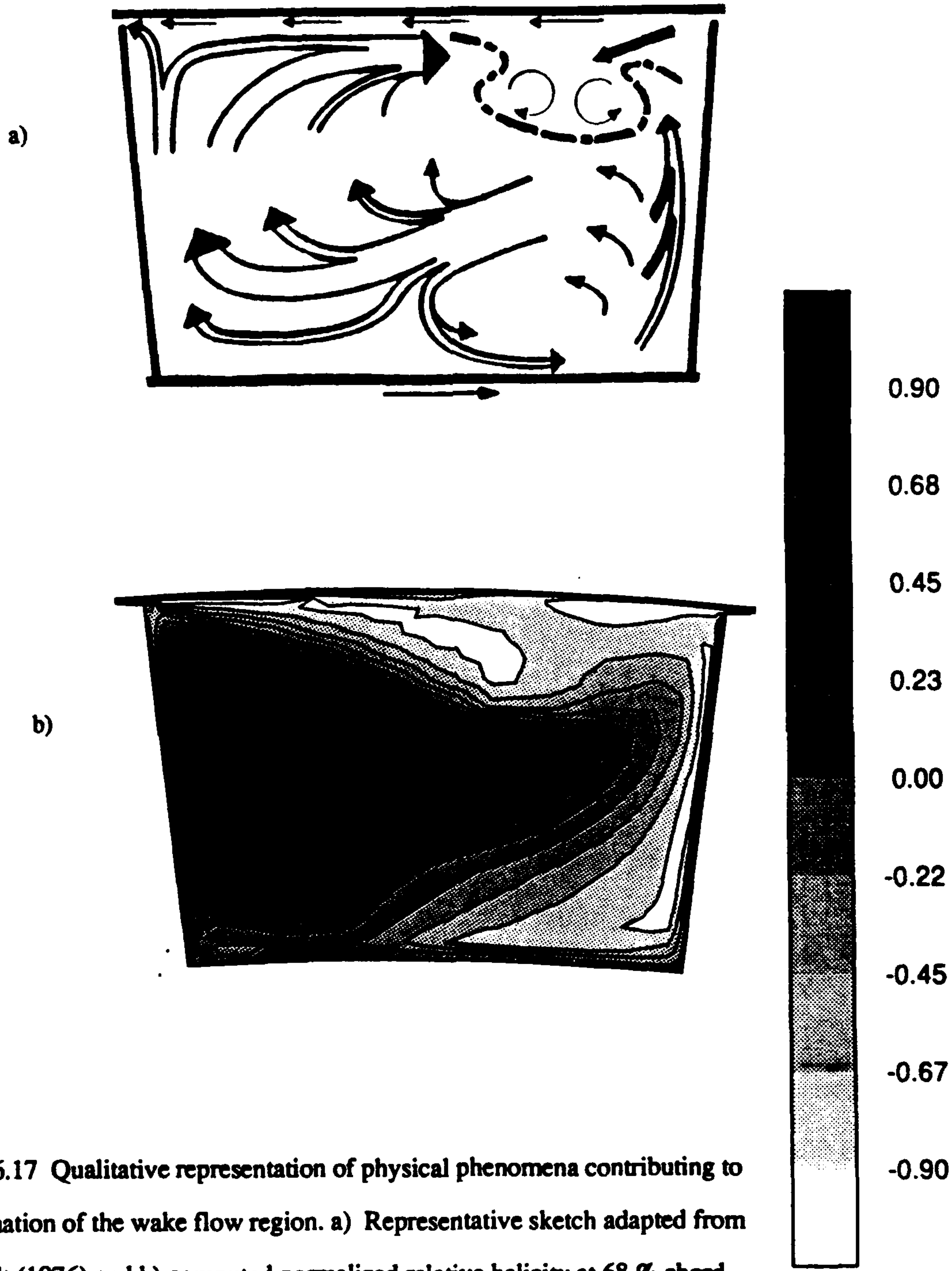
a)
b)
0.90
0.68
0.45
0.23
0.00
-0.22
-0.45
-0.67
-0.90

Figure 6.17 Qualitative representation of physical phenomena contributing to the formation of the wake flow region. a) Representative sketch adapted from Eckardt (1976) and b) computed normalized relative helicity at 68 % chord.

Stokes procedure in reconciling these flow physics.

At 80 % chord (Plane V), several channel vortices are clearly distinguishable as seen in Figure 6.18. One of these, of positive streamwise vorticity, has migrated from the pressure side half of the channel (refer to Figures 6.11 and 6.14). The tip clearance vortex has continued to migrate closer to the suction surface. The meridional velocity profiles in Figure 6.19 illustrate that only the near hub region shows inviscid flow features, the rest of the passage flow being highly distorted by the variety of interacting secondary motions. This is captured well by the numerical simulation, as seen by comparison of the experimental and computational results in Figures 6.19 and 6.20.

Near the impeller discharge plane (Plane VI, 98 % chord), the entire passage flow is encompassed by a very complex shear layer. Figure 6.21 shows normalized relative helicity contours in this plane. A variety of nearly indistinguishable secondary flow structures are present. Experimentally measured exit velocities are rather smooth, though clearly distorted across the discharge area. This is illustrated in Figure 6.22. Computational results at this measurement plane are poor, due to the "pinched" trailing edge. Meridional velocity profiles for the discharge plane are provided in Figure 6.23.

Computed and measured performance parameters are presented in Table 6.1.

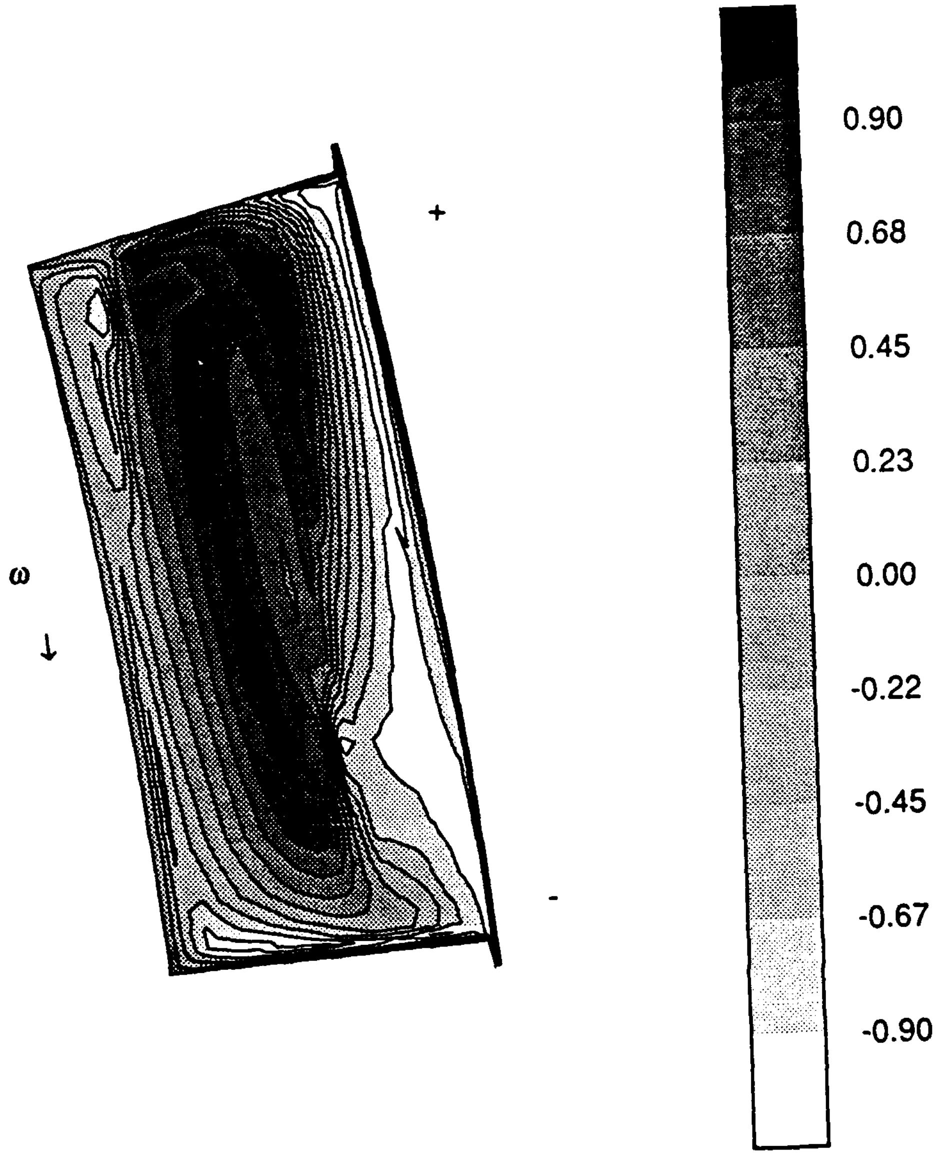

Figure 6.18 Computed normalized relative helicity contours at solution grid slice corresponding to L2F data acquisition Plane V.

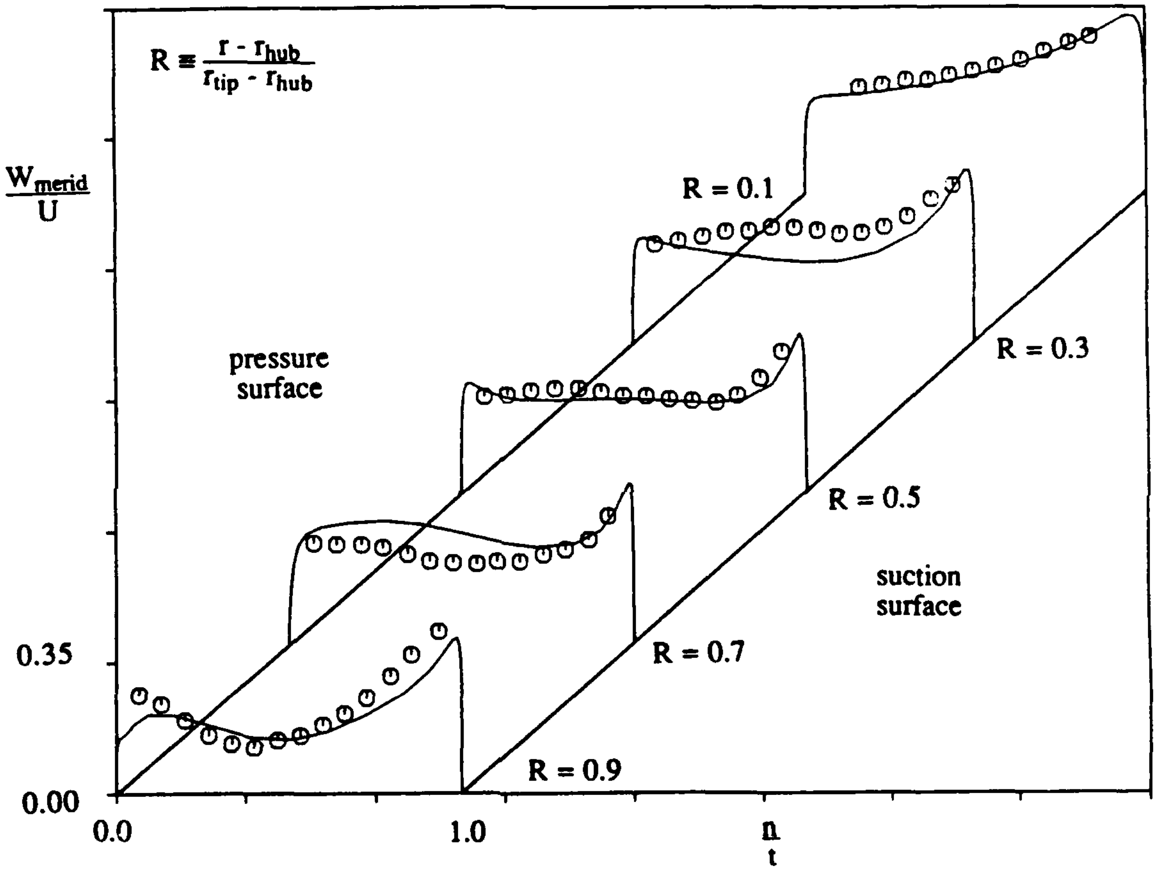

Figure 6.19 Meridional velocity profiles at L2F data acquisition Plane V. Experimental measurements (symbols), computed values (solid line).

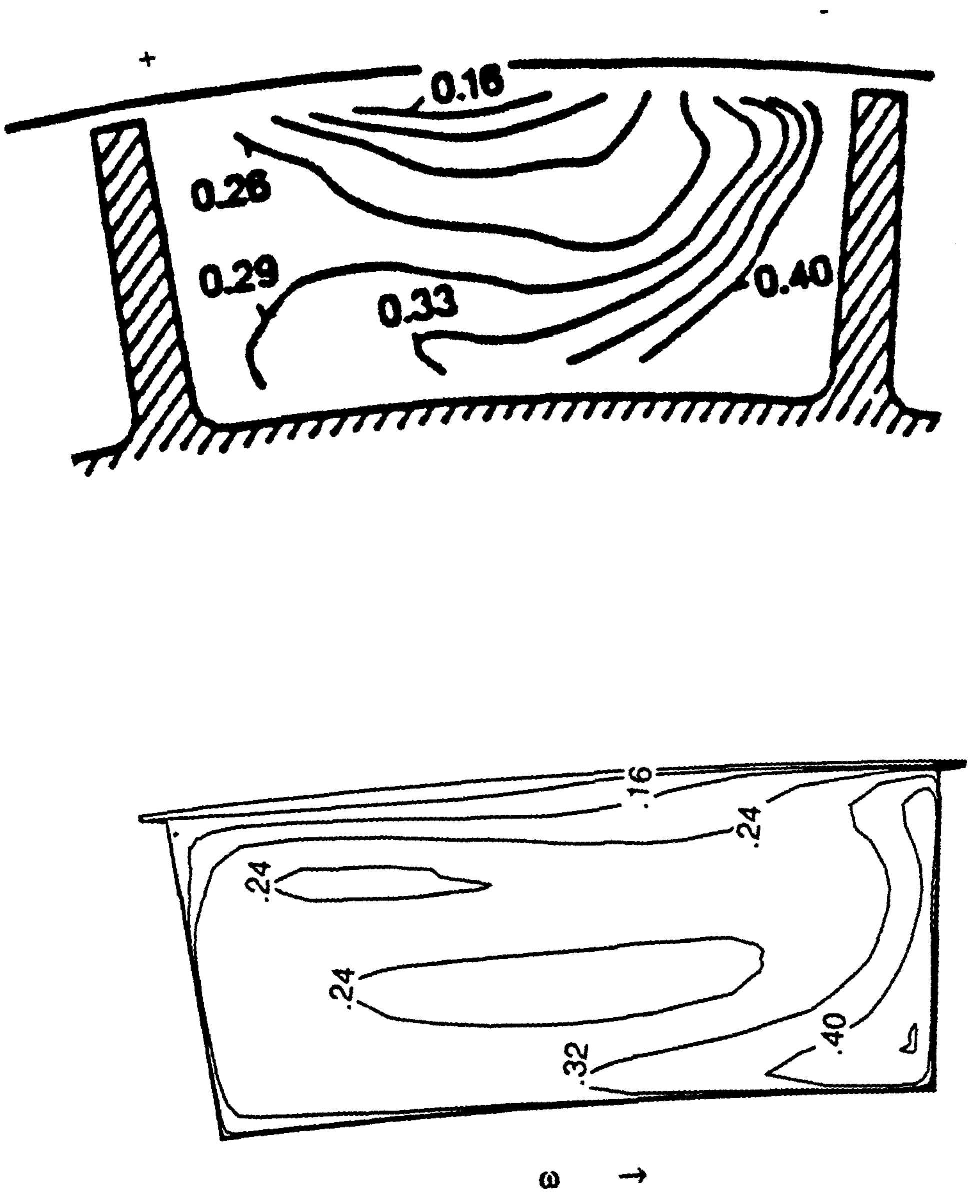

Figure 6.20 Meridional velocity contours at L2F data acquisition Plane V. Experimental contours (top), computed contours (bottom).

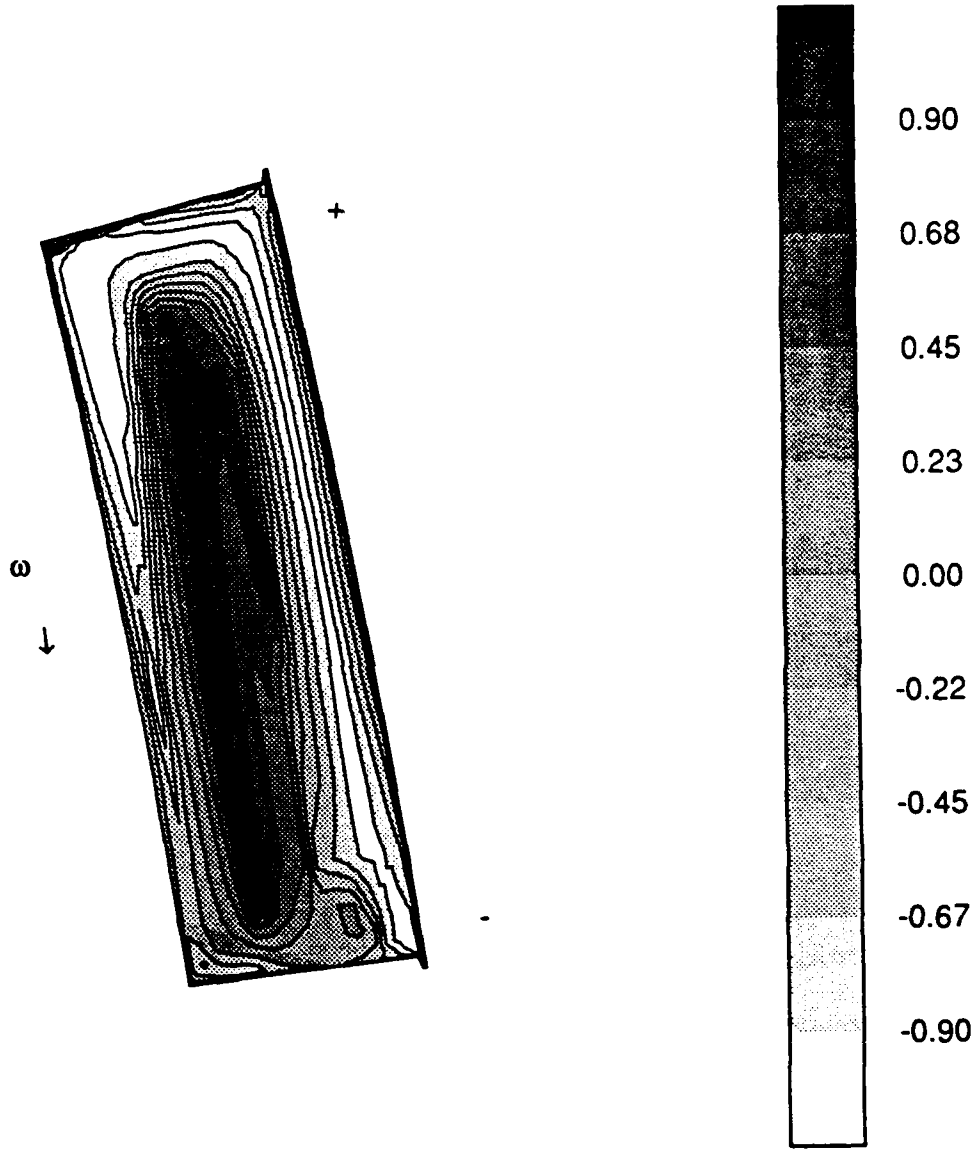

Figure 6.21 Computed normalized relative helicity contours at solution grid slice corresponding to L2F data acquisition Plane V.

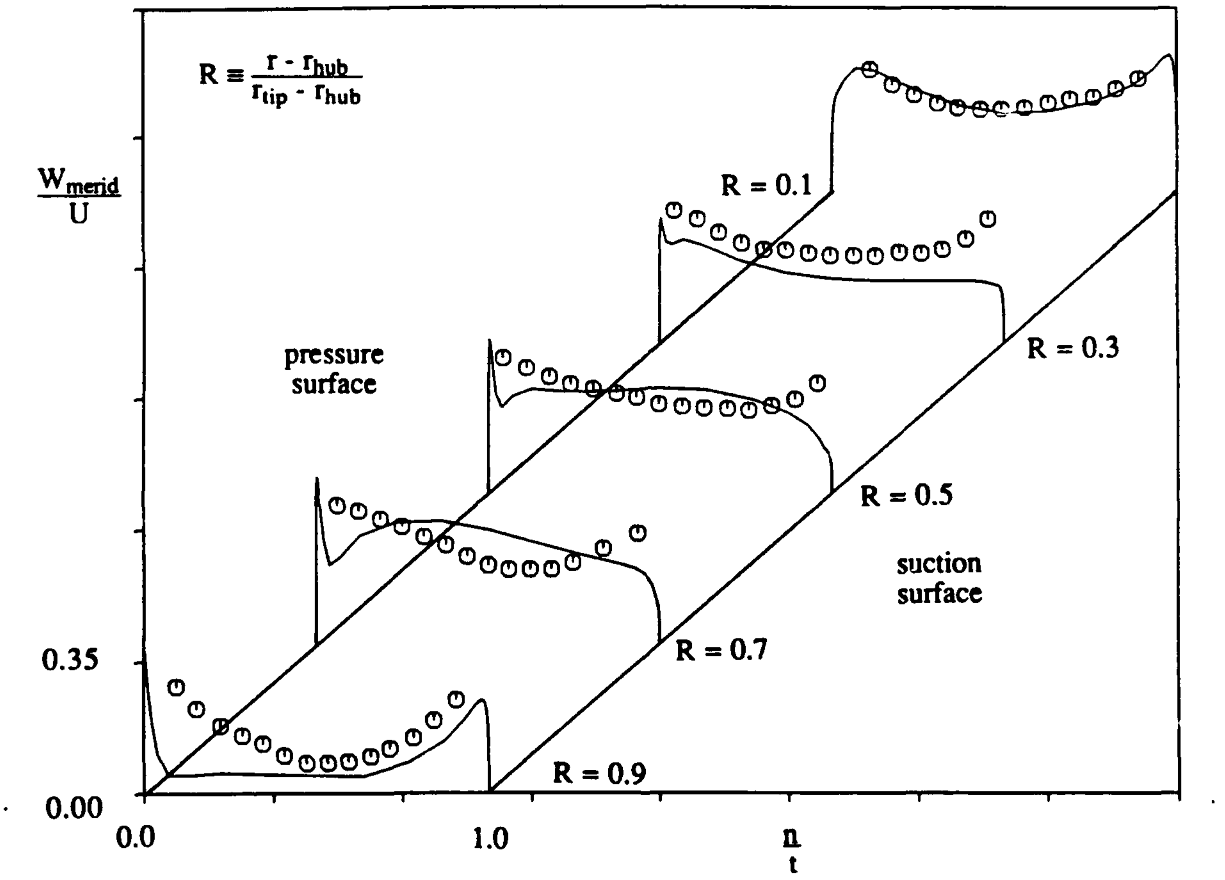

Figure 6.22 Meridional velocity profiles at L2F data acquisition Plane VI. Experimental measurements (symbols), computed values (solid line).

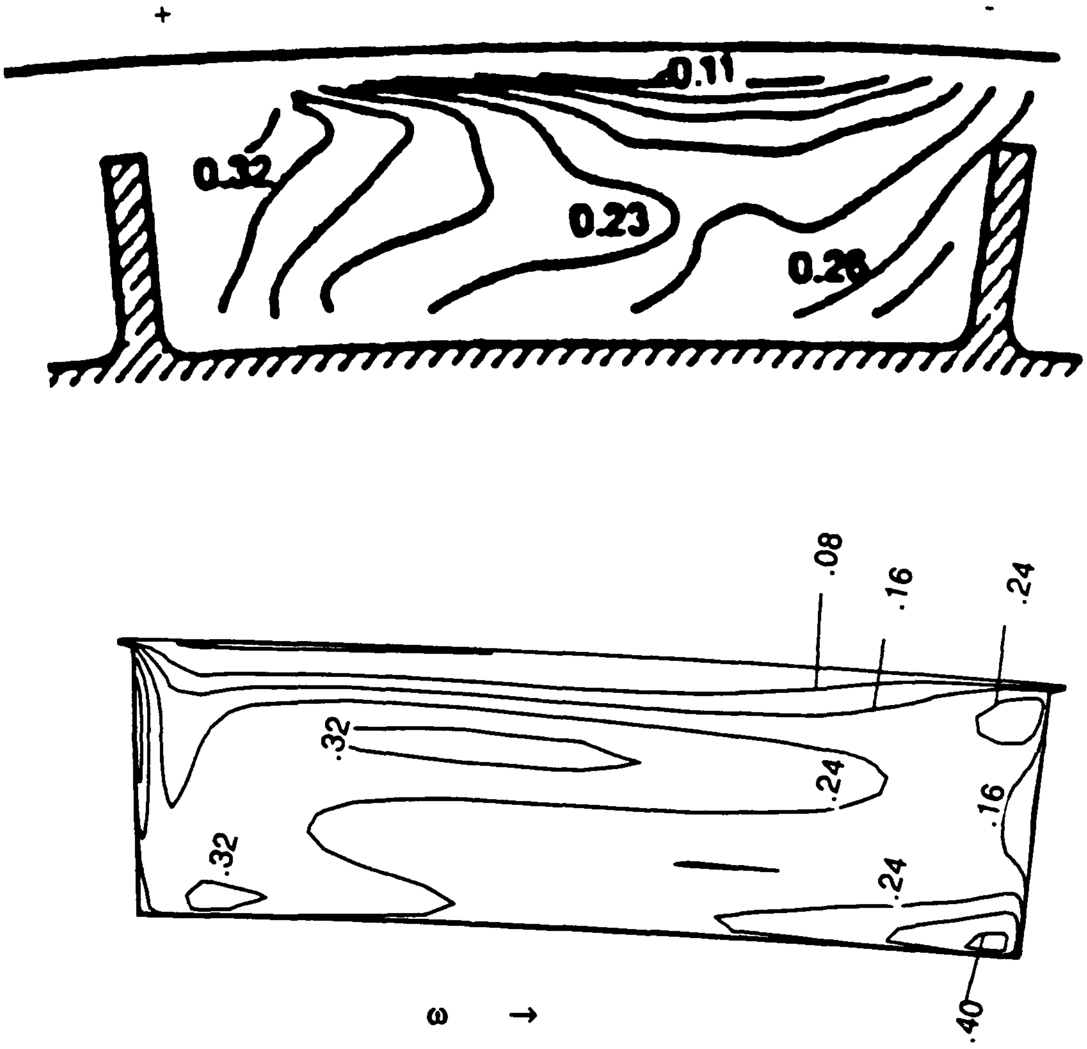

Figure 6.23 Meridional velocity contours at L2F data acquisition Plane VI. Experimental contours (top), computed contours (bottom).

Table 6.1. Comparison of Performance Parameters for Transonic Centrifugal Compressor Stage

Mass Averaged Flowfield Parameter[a]	Measured[b]	Computed (k-ε model)	% Difference
Pressure Rise, $\frac{\bar{p}_{0,\text{ diffuser exit}}}{\bar{p}_{0,\text{ impeller inlet}}}$	4.00	3.80	5.0
Slip Factor, $\frac{\bar{V}_{\theta,\text{ impeller exit}}}{U_{\text{impeller exit}}}$	–	0.85	–

[a]

$$\bar{\phi} \equiv \frac{\int \phi \rho \vec{W} \cdot d\vec{A}}{\int \rho \vec{W} \cdot d\vec{A}}$$

[b] Krain (1988)

6.3 Flowfield Calculation Using the Hybrid k-ε/ARS Model

In order to obtain some qualitative measure of the importance of Reynolds stress anisotropy on the flowfield structure for this case, and to examine the numerical robustness of the hybrid model in flows where significant extra strain rates are present, the model was used to compute the present impeller flowfield. In Figure 6.24, a convergence history for these calculations is presented. The 5000 iteration k-ε solution discussed above was used to initialize the ARSM run (compare Figure 6.7). The jump in residuals at iteration 5000 corresponds to a solution restart with the new model. Specifically, the hybrid model was run for 2880 iterations, with the production by rotation tensor, R_{ij} in equation [2.14], set to zero ($\Omega = 0$ in equation [3.60]). This solution was run until the RMS density residual

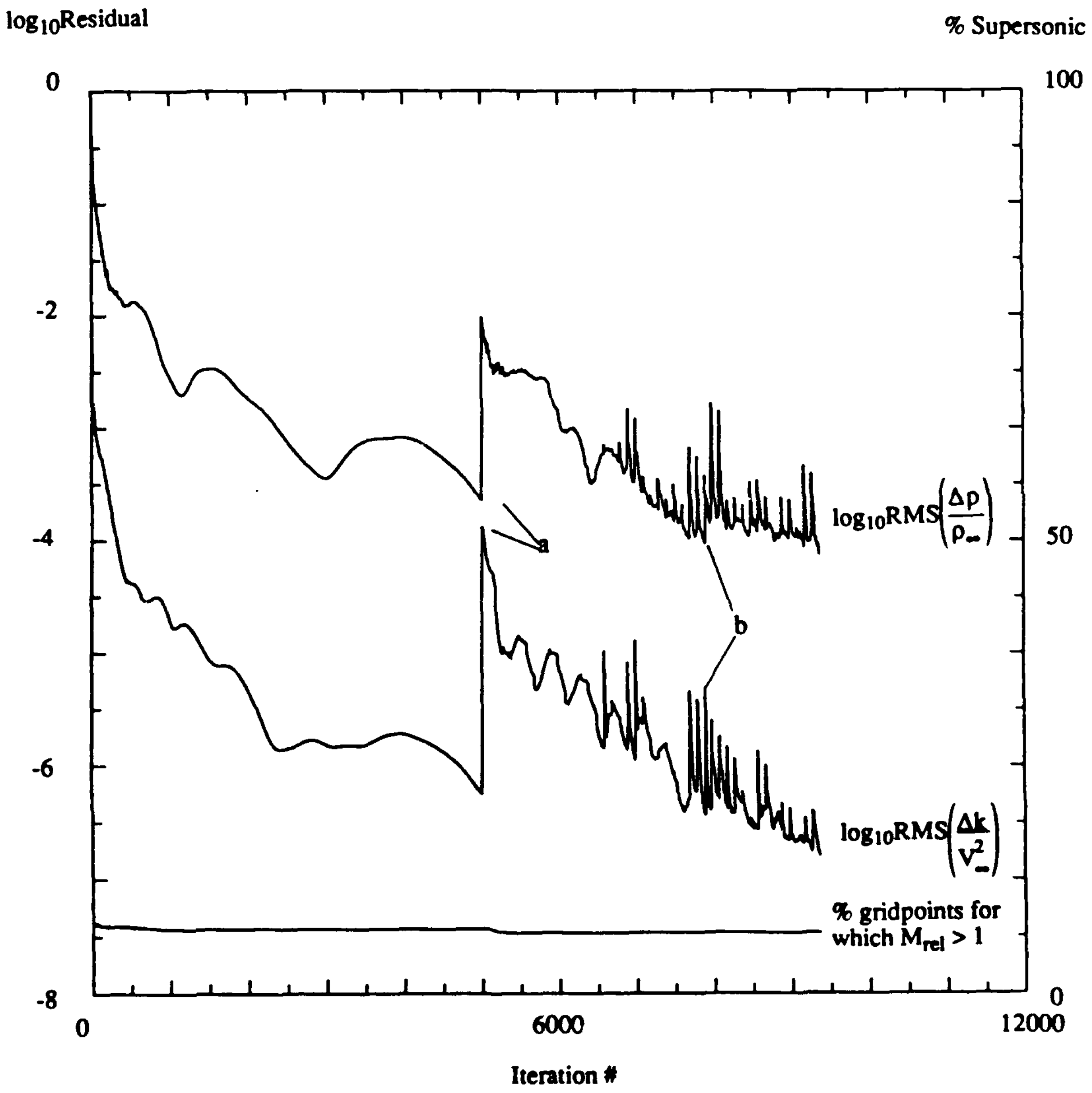

Figure 6.24 Convergence history for the three computations presented. Features labelled a and b correspond to solution restarts using alternate turbulence models.

recovered to a four decade drop. The production by rotation terms were then implemented and the code was run for another 1480 iterations where again the log of the density residual had dropped to -4. All three solutions are compared below. It is noted that the "peaks" in density and turbulent kinetic energy residual which develop with increased iteration count occur at 100 iteration intervals, corresponding to solution restart frequency, not the frequency with which Reynolds stresses are recomputed. The overall convergence rate of the ARSM solutions are not significantly deteriorated, and it is hoped that the mechanism which causes these features can be identified and fixed.

In Figure 6.25, the contour of $y^+_{match} = 200$ for the hybrid model is presented for a grid slice at 75 % chord, to illustrate the proximity of the hybrid model matching location to the passage surfaces.

Figure 6.26 shows converged meridional velocity profiles at laser Plane V for the 1) k-ε (solid line), 2) hybrid, $R_{ij} = 0$ (long dash), 3) hybrid, $R_{ij} \neq 0$ (short dash) solutions. The meridional velocity profiles are seen to be very similar. However, the near wall cross flow velocities and wall shear stress distributions were seen to vary substantially for the various models.

Figures 6.27 shows near wall cross flow velocity profiles near the exit of the impeller (90 % chord). Figures 6.27a and 6.27b are profiles taken at midspan on the suction and pressure surfaces respectively, whereas Figure 6.27c is taken at mid-hub. In these plots, the square, circular and triangular symbols correspond respectively to the k-ε, hybrid, $R_{ij} = 0$ and hybrid, $R_{ij} \neq 0$ solutions. Qualitatively, these spanwise flows seem to have been notably influenced by turbulence amplification effects on the developing passage flow boundary layers, as seen by the differences in the cross flow velocity profiles in these figures.

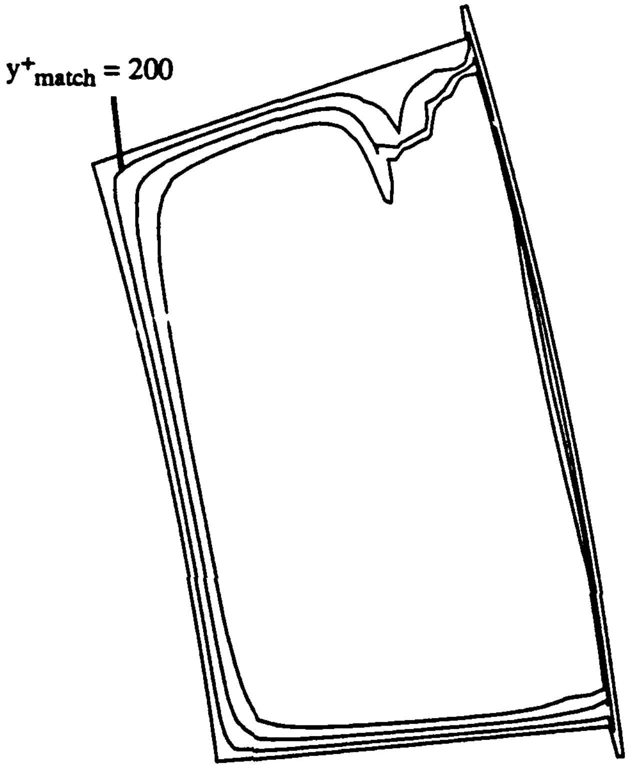

Figure 6.25 Converged hybrid model solution contours of y^+ on a grid slice at 75 % chord. The precise location of $y^+_{match} = 200$, the value used in the hybrid solutions, is indicated.

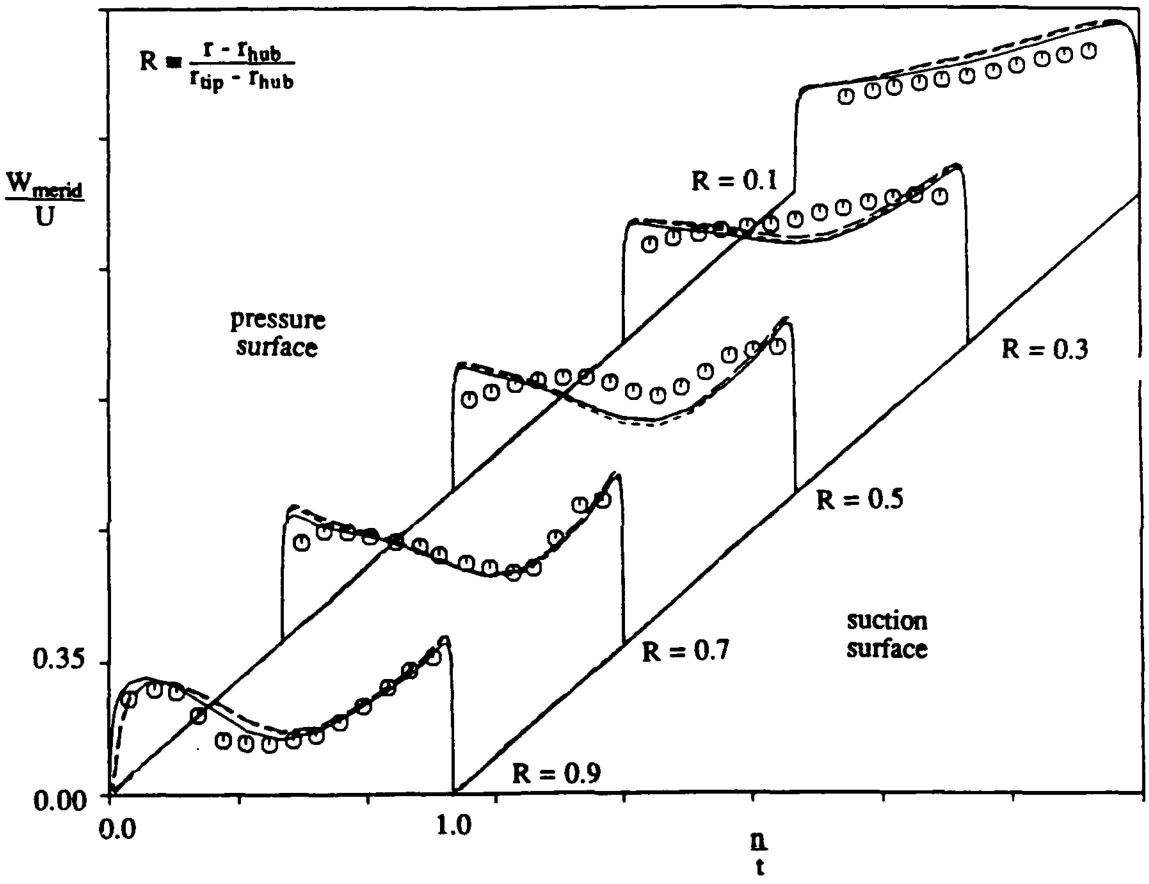

Figure 6.26 Meridional velocity profiles at L2F data acquisition Plane IV. Comparison of solutions using three turbulence models : low Reynolds number k-ε model (solid), hybrid model, $R_{ij} = 0$ (long dash), hybrid model, $R_{ij} \neq 0$ (short dash).

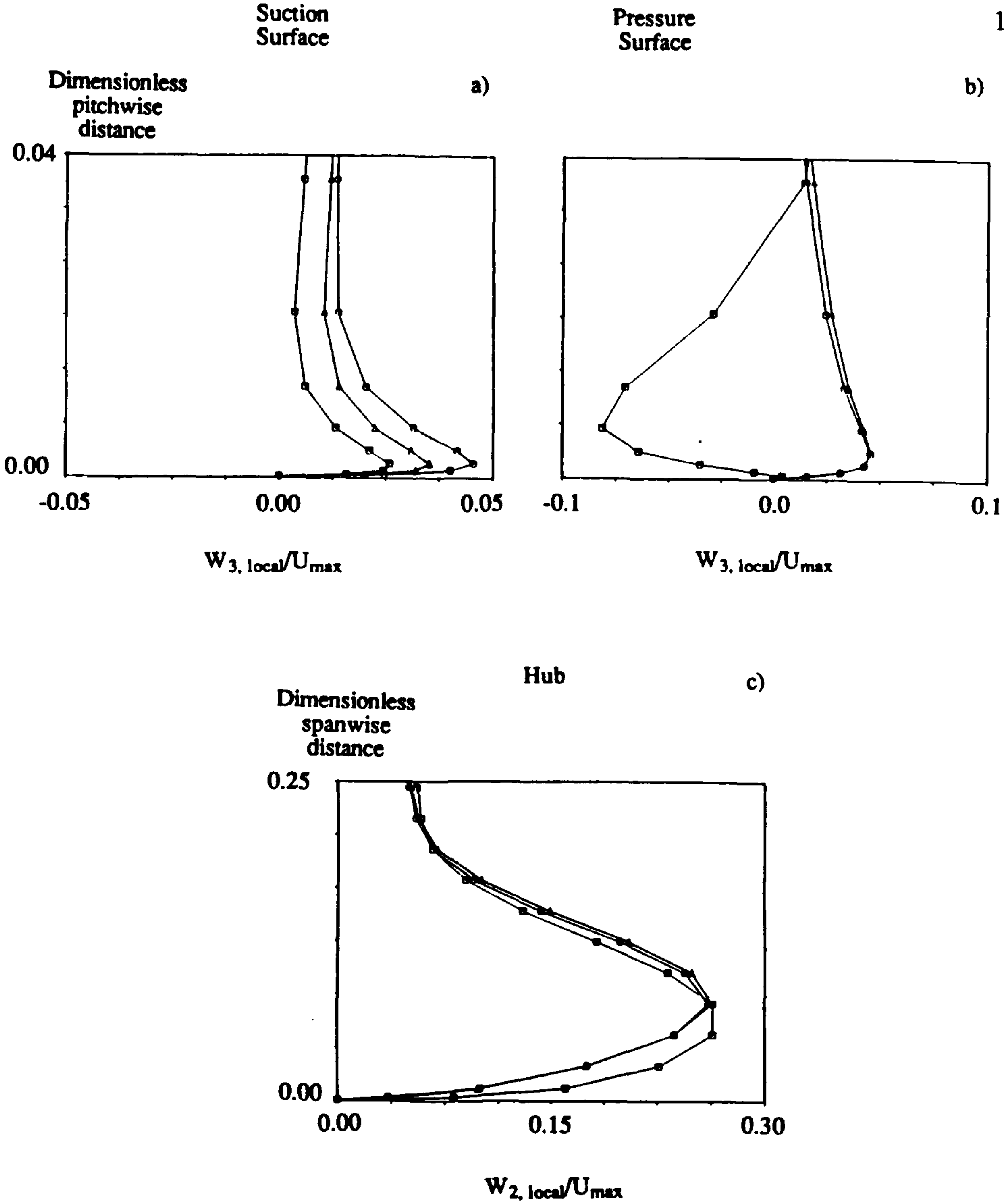

Figure 6.27 Near wall relative crossflow velocity profiles at 90 % chord. a) midspan on suction surface, b) midspan on pressure surface, c) mid passage on hub. Comparison of solutions using three turbulence models : low Reynolds number k-ε model (square), hybrid model, $R_{ij} = 0$ (circle), hybrid model, $R_{ij} \neq 0$ (triangle).

In Figure 6.28, predicted skin friction versus chord is plotted for the three solutions at midspan on the suction surface, mid span on the pressure surface, and at mid-hub locations. In this figure, the solid line corresponds to the k-ε model, the long dash to the hybrid model without rotation terms, and the short dash to the hybrid model with rotation terms. Choice of model seems to have little effect on suction surface shear stress. The effect of extra strain rates on the hybrid model do seem to significantly influence developing boundary layers along the hub and pressure surfaces.

In Figure 6.29, normalized relative helicity contours, at 68 % chord, are compared between the k-ε solution and the hybrid model solution, with rotation terms included. Secondary motions are qualitatively very similar in this region, where the jet-wake flow is fully realized. Quantitative differences are certainly noticeable. These results do not indicate that the influence of curvature and/or rotation on turbulence damping in the shroud-suction surface region significantly influence the structure of the wake.

Table 6.2 compares predicted performance parameters between the three modelling approaches.

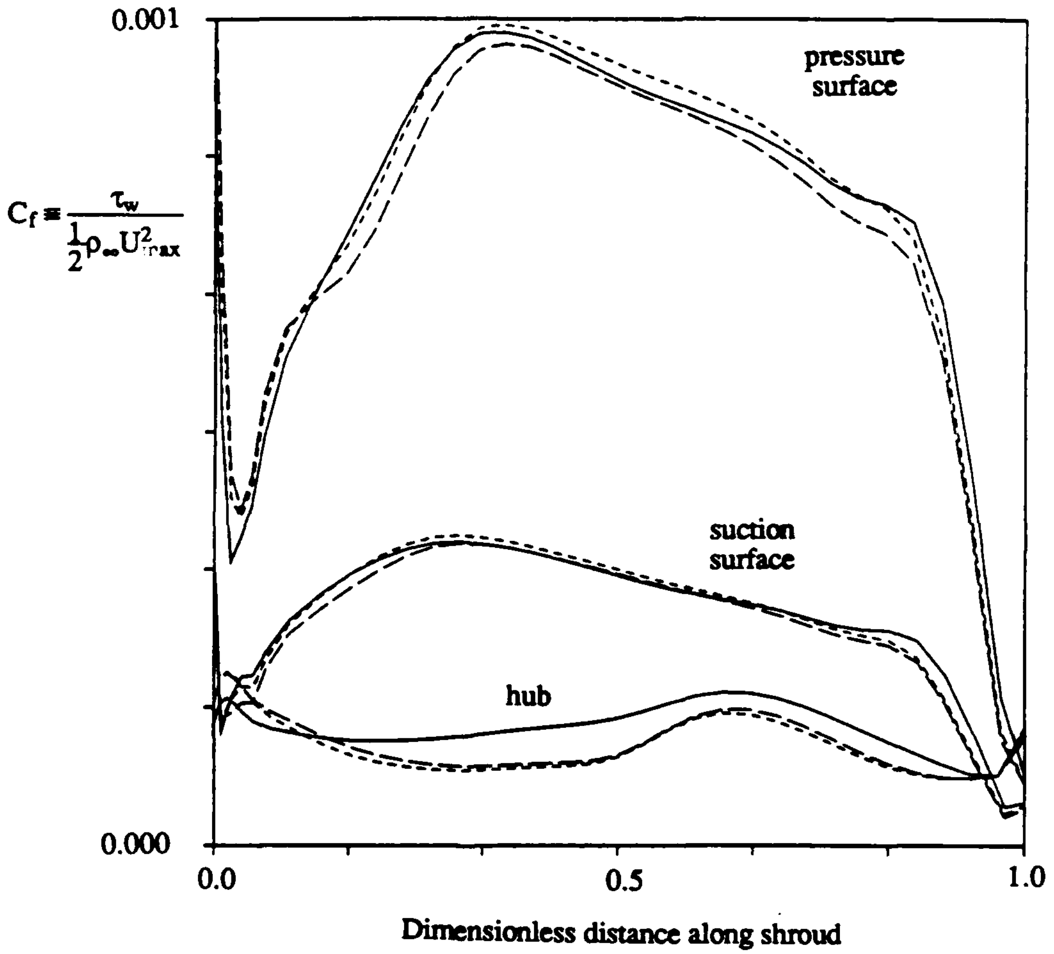

Figure 6.28 Predicted skin friction coefficient vs. dimensionless streamwise distance along shroud. Comparison of solutions using three turbulence models : low Reynolds number k-ε model (solid), hybrid model, $R_{ij} = 0$ (long dash), hybrid model, $R_{ij} \neq 0$ (short dash).

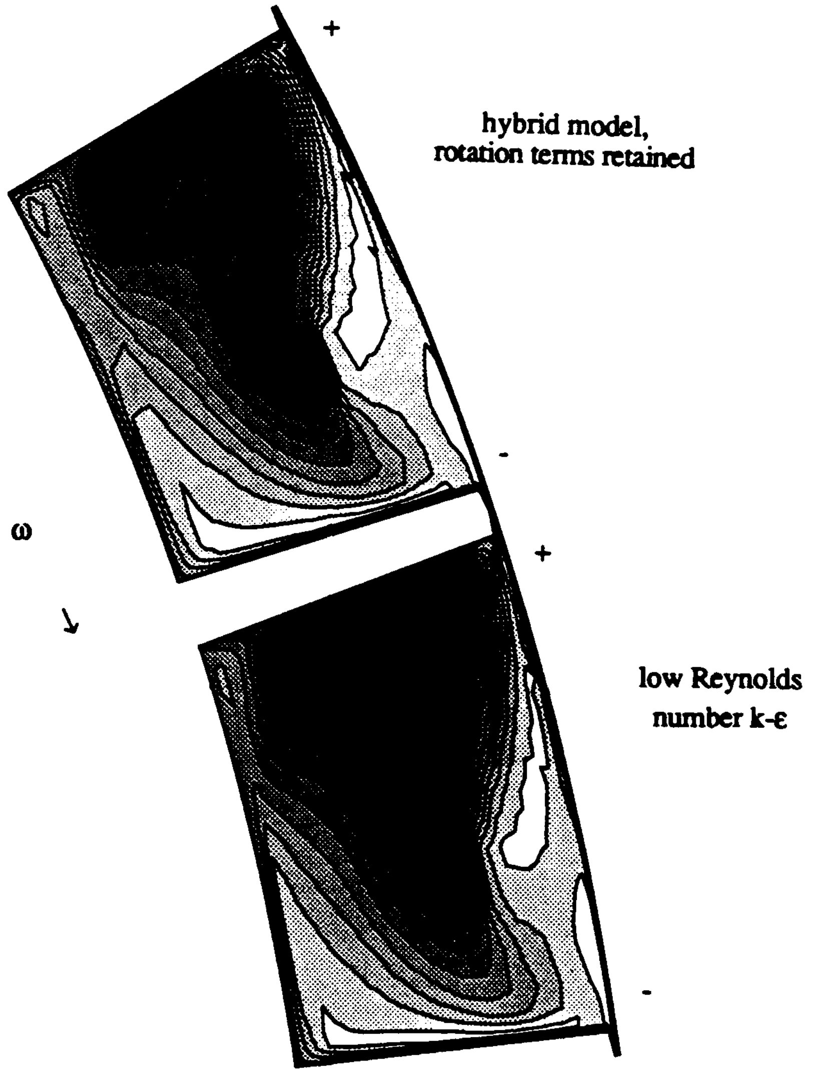

Figure 6.29 Computed normalized relative helicity contours on a solution grid slice at 68 % chord. Comparison of solutions using two turbulence models : low Reynolds number k-ε model (bottom), hybrid model, $R_{ij} \neq 0$ (top).

Table 6.2. Comparison of Predicted Performance Parameters for Transonic Centrifugal Compressor Stage, Using Different Turbulence Models

Mass Averaged Flowfield Parameter[a]	Computed (k-ε model)	Computed (hybrid,$R_{ij} = 0$)	Computed (hybrid,$R_{ij} \neq 0$)
Pressure Rise, $\frac{\overline{p}_{0,\text{ diffuser exit}}}{\overline{p}_{0,\text{ impeller inlet}}}$	3.80	4.01	3.92
Slip Factor, $\frac{\overline{V}_{\theta,\text{ impeller exit}}}{U_{\text{impeller exit}}}$	0.85	0.86	0.86

The slip factor, which arises due to coriolis "eddy"acceleration even in the absence of shear is seen to be negligibly affected by turbulence model choice. Predicted stage total pressure rise varies by as much as 5 % with different turbulence modelling.

As is clear from the foregoing results, the flow in this machine is very complex. As such, it is difficult in this case to make quantitative arguments as to the direct influence of the turbulence model on boundary layer structure. Specifically, it would be too bold to conclude that local extra strains in the algebraic model influence local boundary layers directly based on the results presented here. This is because local boundary layer physics, especially near the exit, are strongly dependent on the history of the entire developing passage flow.

What can be concluded from the results of this section are that extra strain rates are seen to influence the meridional flow physics only slightly, through local turbulence structure modification. Secondary motions, wall shear stress and total pressure rise performance show increased sensitivity to modelling choice. In the opinion of the author, the proposed hybrid k-ε/ARS model is a sensible engineering approach to computing complex flows where strong extra strains are present. This approach is computationally efficient, reconciles the low Reynolds number k-ε form with the algebraic stress modelling, and seems to be numerically stable. However, further validation work is still needed, specifically the treatment of flows with isolated extra strain rates.

CHAPTER 7

CONCLUSIONS AND RECOMMENDATIONS

A new three-dimensional explicit Navier-Stokes procedure, which incorporates two-equation turbulence modelling has been developed and presented in this thesis. Several analyses and techniques which have enabled convergent and accurate simulation of high Reynolds number turbomachinery flows on highly stretched grids have been developed and presented. These include extensive stability, order of magnitude and numerical verification studies applied to the discrete system of seven governing equations, with emphasis on turbulence modelling. A compact finite difference flux evaluation procedure was presented. Local velocity and flux Jacobian scalings of artificial dissipation operators were devised and applied. A hybrid low Reynolds number k-ε/high Reynolds number algebraic Reynolds stress model was developed. The procedure has been applied to a variety of turbomachinery flowfields, across a wide range of Mach numbers. The results of these computations were presented and interpreted, and indicated that the method provides accurate and convergent simulation of turbomachinery flowfields.

A study of the stability of the coupled system of seven transport equations, including a low Reynolds number form two-equation turbulence model, was presented. The linear analysis procedures, order of magnitude analyses and subsequent numerical verification studies presented, provided several conclusions. Most notable are three items which directly relate to the turbulence transport modelling. Specifically, it was shown through stability and order of magnitude analysis, and numerical verification , that the turbulence model source terms themselves do not adversely affect the stability of the explicit numerical procedure, anywhere in the flowfield, except in early stages of iteration.

This is a result contrary to that generally perceived. Secondly, it was shown that turbulence transport models, which provide large values of effective diffusion in regions where grid clustering may be high, give rise to dominant parabolic stability limitations, which must be incorporated in the numerical procedure. This is unlike the solely hyperbolic constraints often sufficient when algebraic eddy viscosity models are used in time marching Navier-Stokes procedures (point transition specification in these models preclude large values of eddy viscosity upstream of the blade row). This second item was clearly demonstrated as a mechanism in turbomachinery blade row computations. In the opinion of the author, this effect must manifest itself also in unstructured grid implementations where high local clustering appears well away from wall damping effects, as for, say, shock capturing. Thirdly, specific near wall modelling terms which appear in the stability analysis were identified, which upon inspection, reveal the adverse stability implications of incorporating a dissipation rate model which transports a total dissipation rate variable. This analysis substantiates claims to this effect which appear in the literature and have been the personal experience of several researchers, including the author.

Two other results, related to the numerical implementation of the turbulence model, were investigated and presented. Specifically, implicit treatment of the turbulence source terms did not improve the convergence rate of the explicit scheme, consistent with the first conclusion in the previous paragraph. Additionally, terms which account for unstable, early iteration turbulence model behavior, arising from inviscid initialization procedures, were identified, and several stabilization procedures that the author has found to be effective were presented.

The implementation of algebraic and full Reynolds stress closures in complex aerodynamic flow simulations should increase in the short term. This will be due to the desire to move to improved modelling, increased digital computer speed and memory, and the onset of radically different designs for which Navier-Stokes methods will be more critical in analysis. The turbulence model numerical considerations presented in Chapter 3, and summarized above, should be useful in the move to second order closures for two reasons. Firstly, the modelled FRS and dissipation rate equation system is similar to the k-ε system in that they are both convection-diffusion transport equations with large non-linear source terms. Accordingly, some of the procedures and conclusions presented in this thesis will be applicable. Secondly, in ARS closures, an "anisotropic eddy viscosity" can be identified, to which the parabolic stability conclusions recalled above are directly applicable. This conclusion was demonstrated analytically, and numerically verified, in Chapter 3.

In addition to turbulence model issues, analyses were presented which focused on the influence of numerical coupling of the mean flow and turbulence transport equations, system rotation source terms and artificial dissipation on the numerical stability of the Runge-Kutta procedure. Linear analysis and numerical verification provided that there is no advantage to numerically coupling the two-equation model system to the mean flow equation system in regard to convergence, accuracy or performance of the scheme. The appearance of rotation source terms in the discrete governing equations was found to have negligible influence on the stability of the scheme for rotation numbers and grids typical of high Reynolds number turbomachinery rotor computations. It was found useful to include artificial dissipation operators in the specification of a local timestep in problems where parabolic stability bounds dominate locally (as in the blade row computations considered) to avoid ad hoc specification of an operational VonNeumann number which varies with level of artificial dissipation used.

Some of the limitations of the foregoing stability results were also presented. In multigrid procedures, the turbulence model and rotation source terms give rise to stability limitations which may not be negligible on coarser grids, if complete residuals, including source terms, are evaluated on these successively coarser grids. Also, the flow physics are significantly altered by system rotation . Accordingly, system rotation does affect convergence rates since stationary and rotating flows, through the same geometry, will be very different (especially in centrifugal machines). The related conclusions presented thereby only apply to the specification of a local timestep. Lastly, the analyses presented are local and linearized. As such, the conclusions of these analyses are approximate, and their usefulness had to be verified, like any engineering approximation, through numerical application.

Two artificial dissipation issues of importance in high Reynolds number flowfield computations were presented and discussed. Two scaling functions which accommodate these considerations were presented. Specifically, an alternative flux Jacobian eigenvalue scaling was introduced and extended to three dimensions. This scaling reduces dissipation levels in the directions normal to grid stretching without increasing dissipation levels in the same direction as the grid stretching (nominally, the wall normal direction). It was found to be crucial to incorporate this anisotropic eigenvalue scaling in order that a converged three-dimensional rotor flow solution be obtained on a highly stretched grid. The role of artificial dissipation in corrupting solution accuracy in near wall regions, where physical diffusion is important, was illustrated. A local velocity squared scaling which tapers levels of artificial dissipation to zero near solid boundaries was introduced. It was demonstrated through numerical experimentation that it is crucial to incorporate this scaling in order that near wall physics be accurately resolved.

The flux evaluation scheme presented eliminates the metric ambiguity, at the interface between solid and periodic boundaries, associated with standard finite difference approaches. This scheme allows for straightforward inviscid and viscous flux evaluation, at complex rotor passage boundaries, including periodic cascade and tip gap boundaries, and the interface between rotating and stationary sections of the hub.

A hybrid low Reynolds number k-ε/high Reynolds number algebraic Reynolds stress model was developed. This model reconciles the near wall damping of the k-ε model, with the ability of the ARS model to provide Reynolds stress anisotropies which arise due to extra strain rates. The formulation of this model and its numerical implementation and stability topics were presented, and preliminary model validation was provided . The model was found to predict near wall turbulence behavior correctly, including normal stress anisotropy, and was shown to be stable when implemented numerically with a local blending function. This model is computationally efficient in full scale three-dimensional applications because the influence of near wall pressure strain terms, which are very complicated in three-dimensions, are implicitly accommodated in the modelled two-equation near wall damping terms. In the opinion of the author, this is a sensible engineering approach to employing a second order closure in a time-marching full Navier-Stokes procedure. Specifically, the influence of curvature and rotation on Reynolds stress anisotropy, which can significantly influence mean flow structure in turbomachines is incorporated, but wall functions are not used. Therefore, complex near wall three-dimensional boundary layer physics, which are important in many turbomachines can be explicitly resolved as well. Though preliminary validation has been provided and application to full scale turbomachinery computations demonstrated in this thesis, some further study may be useful. Specifically, the application of the model to configurations where isolated strains give rise to Reynolds stress and mean flow redistributions should be further investigated. The computation of a simple shear layer subject to spanwise rotation is under way, and the prediction of secondary motion of the second kind could be demonstrated for a square duct calculation.

Two-dimensional results were presented. Validation of the turbulence models was provided, and the results of one supersonic and one low subsonic compressor cascade computations were presented. Flowfield predictions were found to be acceptable for both cascades except in the aft potion of the subsonic cascade suction surface, due to mean flow reversal there. Overall cascade performance parameters were well predicted for the supersonic cascade but not well predicted for the low subsonic cascade, due again to flowfield unsteadiness as well as turbulence model shortcomings.

The three-dimensional procedure was used to predict the flow in a compressor rotor. The viscous incompressible flow through a curved duct was predicted accurately, as verified by comparison of CFD validation-quality pressure and primary and secondary velocity measurements with computed values. A number of conclusions apply to the rotor flow computation. Specifically, the viscous flow through a rotor was predicted, including inviscid regions, the stagnation region near the leading edge, blade boundary layers and wakes, and spanwise mixing region downstream. Flow losses and loading coefficient were predicted reasonably well. The flow in the tip region was resolved qualitatively, with the exception of nearwall streamwise and radial velocity profiles. The effects of rotation and endwall secondary flow on the radial velocity profiles in the near wake close to the hub was captured reasonably well. The ability of the code to predict spanwise and lateral mixing downstream of the rotor was demonstrated. Specifically, the redistribution of velocities and flow angles was predicted accurately. Additionally, the spanwise redistribution of losses between the trailing edge and the far wake region was captured well.

The flowfield in a transonic centrifugal compressor stage (impeller + diffuser) was computed. The numerical and modelling methodologies provided in this thesis give rise to a reasonably accurate simulation of this complex flowfield. Specifically, stage pressure rise distribution was captured accurately. Also, the secondary motions arising from coriolis and centrifugal effects and tip clearance flow were resolved with reasonable accuracy. Normalized relative helicity was helpful in qualifying and tracking some of these motions. The accumulation of low momentum fluid near the shroud, in the aft portion of the impeller was captured. This fluid includes that convected from blade boundary layers by curvature induced secondary motion and tip clearance flow, and accumulates in the mid-passage region. Near the impeller exit, this fluid extends well into the impeller passage towards the hub, causing blockage (and hence acceleration) of the high momentum fluid near the suction surface-hub corner. These physics are evident in experimental L2F meridional velocity measurements and in the numerical simulation.

The hybrid k-ε/ARS model was applied to this flowfield in order to obtain qualitative measure of the influence of Reynolds stress anisotropy on the developing flowfield structure in the centrifugal impeller, and to examine the numerical robustness of the model in flows where significant extra strain rates are present. This is the highest level of turbulence modelling ever attempted, to the knowledge of the author, in this type of machine. It was found that extra strain rates influence meridional flow physics and impeller slip factor only slightly, through local turbulence structure modification. Cross flows, wall shear stress and total pressure rise performance showed slightly increased sensitivity to modelling choice. The model was found to be stable for this computation, though solution restart anomalies remain to be resolved.

In light of the relatively small difference in predicted meridional physics arising due to modelling choice, when compared to the differences in computed and measured meridional flow, geometric modelling considerations are a priority, in order to provide improved prediction of these types of flows. Specifically, inclusion of the actual spinner geometry, though difficult from a grid topology standpoint, should provide more accurate inlet hub boundary layer resolution (and thereby the influence of the developing secondary motions which arise due to the turning and rotation of this shear layer.) More important, though, is the accurate resolution of the leading edge, trailing edge and tip gap regions. The "pinched" H-grid approach at these boundaries is most likely the dominant source of error in these computations, since blades are thick compared to passage dimensions, and the tip clearance flow is so important in centrifugal impellers. Lastly, as mentioned above, further validation is required for the turbulence models used, before stronger conclusions can be drawn in regard to application of the model to a flow as complex as that in a centrifugal compressor.

REFERENCES

ABARBANEL, S., GOTTLIEB, D. (1981), "Optimal Time Splitting for Two- and Three-Dimensional Navier-Stokes Equations with Mixed Derivatives," Journal of Computational Physics, Vol. 41.

ADKINS, G. G., SMITH, L. H. (1982), "Spanwise Mixing in Axial-Flow Turbomachines," Journal of Engineering for Power, Vol. 104, p.97.

ANDERSSON, H. I., NILSEN, P. J. (1989), "Generalized Algebraic Reynolds Stress Model for Rotating Turbulent Flow," The Norwegian Institue of Technology, Div. of Applied Mechanics, Report 89:01.

AVVA, R. K., SMITH, C. E., SINGHAL, A. K. (1990), "Comparative Study of High and Low Reynolds Number Versions of k-ε Models," AIAA Paper 90-0246.

BALDWIN, B. S., LOMAX, H. (1978), "Thin Layer Approximation and Algebraic Model for Separated Turbulent Flows," AIAA Paper 78-257.

BANSOD, P., RHIE, C. M. (1990), "Computation of Flow Through a Centrifugal Impeller with Tip Leakage," AIAA Paper 90-2021.

BASSON, A. H. (1991), personal communication.

BEACH, T. A. (1990), "An Interactive Grid Generation Procedure for Axial and Radial Flow Turbomachinery," AIAA Paper 90-0344.

BOUSSINESQ, J. (1877), "Theorie de L'ecoulement Tourbillant," Memoires Presente par Divers Savants Sciences Mathematique at Physiques, Academie des Sciences, Paris, France, Vol. 23, p.46.

CAUGHEY, D. A., TURKEL, E. (1988), "Effects of Numerical Dissipation on Finite Volume Solutions of Compressible Flow Problems," AIAA Paper 88-0621.

CEBICI, T. (1970), "Calculation of Compressible Turbulent Boundary Layers with Heat and Mass Transfer," AIAA Paper 70-741.

CHIEN, K. (1982), "Predictions of Channel and Boundary-Layer Flows with a Low-Reynolds-Number Turbulence Model," AIAA Journal, Vol. 20, No.1, p.33.

CHIMA, R. V., YOKOTA, J. W. (1988), "Numerical Analysis of Three-Dimensional Viscous Internal Flows," NASA TM-100878.

CHIMA, R. V. (1991), "Viscous Three-Dimensional Calculations of Transonic Fan Performance," to be presented at the AGARD Propulsion and Energetics Symposium on Computational Fluid Mechanics for Propulsion.

CHOI, D., KNIGHT, C. J. (1989), "Computations of 3D Viscous Flows in Rotating Turbomachinery Blades," AIAA Paper 89-0323.

COAKLEY, T. J. (1983), "Turbulence Modelling Methods for the Compressible Navier-Stokes Equations," AIAA Paper 83-1693.

COURANT, R., FRIEDRICHS, K. O., LEWY, H. (1928), "Uber die Partiellen Differenz-gleichungen der Mathematischen Physik," Mathematische Annalen, Vol. 100, p.32. English translation in IBM Journal, (1967), p.215.

CONNELL, S. D. (1989-1990), personal communications.

DAVIS, R. L., NI, R., CARTER, J. E. (1986), "Cascade Viscous Flow Analysis Using the Navier-Stokes Equations," AIAA Paper 86-0033.

DAVIS, R. L (1991), personal communication.

DAWES, W. N. (1988), "Development of a 3D Navier-Stokes Solver for Application to all Types of Turbomachinery," ASME Paper 88-GT-70.

DEGREZ, G., VANDROMME, D. (1985), "Implicit Navier-Stokes Calculations of Transonic Shock/Turbulent Boundary-Layer Interactions," from Turbulent Shear-Layer/Shock-Wave Interactions, edited by J. Delery, IUTAM Symposium, Palaiseau, France, Springer-Verlag).

DORNEY, D. J., DAVIS, R. L. (1990), "Centrifugal Compressor Impeller Aerodynamics (A Numerical Investigation)," ASME Paper 90-GT-213.

ECKARDT, D. (1975), "Instantaneous Measurements in the Jet-Wake Discharge Flow of a Centrifugal Compressor Impeller," ASME Journal of Engineering for Power, July, p.337.

ECKARDT, D. (1976), "Detailed Flow Investigations Within a High-Speed Centrifugal Compressor Impeller," ASME Journal of Fluids Engineering, September, p.390.

ELIASSON, P. (1988), "Solutions to the Navier-Stokes Equations Using a k-ε Turbulence Model," Flygtekniska Forsoksanstalten TN 1988-19, Stockholm.

FAVRE, A. (1965), "Equations des Gaz Turbulents Compressibles: 1. Formes Generales," Journal de Mechanique, Vol. 4.

FOX, R. W., MCDONALD, A. T. (1985), Introduction to Fluid Mechanics, Wiley.

GALMES, J. M., LAKSHMINARAYANA, B. (1984), "Turbulence Modelling for Three-Dimensional Shear Flows over Curved Rotating Bodies," AIAA Journal, Vol. 22, p.1420.

GEROLYMOS, G. A. (1990), "Implicit Multiple-Grid Solution of the Compressible Navier-Stokes Equations Using k-ε Closure," AIAA Journal, Vol. 28, pp. 1707-1717.

GIBSON, M. M., RODI, W. (1978), "A Reynolds-Stress Closure Model of Turbulence Applied to the Calculation of a Highly Curved Mixing Layer," Journal of Fluid Mechanics, Vol. 103, p.161.

GORSKI, J. (1983), "Generation of H-Type Grids Using the GRAPE Code," Internal Memo, Department of Aerospace Engineering, Penn State University.

GOTO, A., (1990) "Study of Internal Flows in a Mixed-Flow Pump Impeller at Various Tip Clearances Using 3D Viscous Flow Computations," ASME Paper 90-GT-36.

GRASSO, F., SPEZIALE, C. G. (1989), "Supersonic Flow Computations by Two-Equation Turbulence Modelling," AIAA Paper 89-1951.

HAH, C., KRAIN, H. (1989), "Secondary Flows and Vortex Motion in a High-Efficiency Backswep Impeller at Design and Off-Design Conditions," ASME Paper 89-GT-181.

HAH, C., WENNERSTROM, A. J. (1990), "Three-Dimensional Flowfields Inside a Transonic Compressor with Swept Blades," ASME Paper 90-GT-359.

HINZE, J. O. (1975), Turbulence, McGraw-Hill.

HOBSON, G. V., LAKSHMINARAYANA, B. (1990) "Computation of Turbine Flowfields with a Navier-Stokes Code," AIAA 90-2122.

HOLMES, D. G., CONNELL, S. D. (1989), "Solution of the 2D Navier-Stokes Equations on Unstructured Adaptive Grids," AIAA Paper 89-1932.

HUMPHREY, J. A. C., WHITELAW, J. H., YEE, G. (1981), "Turbulent Flow in a Square Duct With Strong Curvature," Journal of Fluid Mechanics, Vol. 103, p.443.

JAMESON, A., SCHMIDT, W., TURKEL, E. (1981), "Numerical Solutions of the Euler equations by Finite Volume Methods Using Runge-Kutta Time-Stepping Schemes," AIAA Paper 81-1259.

JOHNSTON, J.P., HALLEEN, R.M., LEZIUS, D.K. (1972), "Effects of Spanwise Rotation on the Structure of Two-dimensional Filly Developed Turbulent Channel Flow," Journal of Fluid Mechanics, Vol. 56, part 3, p.533.

JONES, W. P. (1971), Ph.D. Thesis, Imperial College, London University.

JONES, W. P., LAUNDER, B. E. (1972), "The Prediction of Laminarization With a Two-Equation Model of Turbulence," International Journal of Heat and Mass Transfer, Vol. 15.

JONES, W. P. (1980), "Models for Turbulent Flows with Variable Density and Combustion," from Prediction Methods for Turbulent Flows, edited by W. Kollmann, Hemisphere.

KING, L. S. (1987), "A Comparison of Turbulence Closure Models for Transonic Flows About Airfoils," AIAA Paper 87-0418.

KIRTLEY, K., LAKSHMINARAYANA, B. (1985), "Computation of Internal Incompressible Separated Flows Using a Space Marching Technique," AIAA Paper 85-1624.

KIRTLEY, K. R. (1989, 1990), personal communication.

KIRTLEY, K. R., BEACH, T. A., ADAMCZYK, J. J. (1990), "Numerical Analysis of Secondary Flow in a Two-Stage Turbine," AIAA Paper 90-2356.

KLEBANOFF, P. S. (1954), "Characteristics of Turbulence in a Boundary Layer With Zero Pressure Gradient," NACA TN-3178.

KRAIN, H. (1988), "Swirling Impeller Flow," ASME Journal of Turbomachinery, Vol. 110, p.122.

KRAIN, H., HOFFMANN, W. (1989), "Verification of an Impeller Design by Laser Measurements and 3D-Viscous Flow Calculations," ASME Paper 89-GT-159.

KRAIN, H. (1990), unpublished configuration details provided.

KUNZ, R. F., LAKSHMINARAYANA, B. (1990), "Computation of Supersonic and Low Subsonic Cascade Flows Using an Explicit Navier-Stokes Technique and the k-ε Turbulence Model," NASA CP-10045, [also to appear AIAA Journal, July 1991].

LAKSHMINARAYANA, B., HORLOCK, J. H. (1973), "Generalized Expressions for Secondary Vorticity Using Intrinsic Coordinates," Journal of Fluid Mechanics, Vol. 59, p.97.

LAKSHMINARAYANA, B. (1986)., "Turbulence Modelling for Complex Flows," AIAA Journal, Vol. 24, p. 1900.

LAKSHMINARAYANA, B., POPOVSKI, P. (1987), "Three-Dimensional Boundary Layer on a Compressor Rotor Blade at Peak Pressure Rise Coefficient," Journal of Turbomachinery, Vol. 109, p. 91.

LAM, C. K. G., BREMHORST, K. A. (1981), "Modified Form of k-ε Model for Predicting Wall Turbulence," Journal of Fluids Engineering, Vol. 103, p.460.

LAUNDER, B. E., SPALDING, D. B. (1974), "The Numerical Computation of Turbulent Flows," Computer Methods in Applied Mechanics and Engineering, Vol. 3, p.269.

LAUNDER, B. E., SHARMA, B. I. (1974), "Application of the Energy Dissipation Model of Turbulence to the Calculation of Flows near a Spinning Disk," Letters in Heat and Mass Transfer, Vol. 1, pp. 131-138.

LAUNDER, B. E., REESE, G. J., RODI, W. (1975), Progress in the Development of a Reynolds Stress Closure," Journal of Fluid Mechanics, Vol. 68, p.537.

LAUNDER, B. E., TSELEPIDAKIS, D. P., YOUNIS, B. A. (1987) "A Second Moment Closure Study of Rotating Channel Flow," Journal of Fluid Mechanics, Vol. 183, p.63.

LAX, P. D., WENDROFF, B. (1960), "Systems of Conservation Laws," Communications in Pure and Applied Mathematics, Vol. 13, p.217.

LEE, S., DULIKRAVICH, G. (1991), "Magnetohydrodynamic Flow Computations in Three Dimensions," AIAA Paper 91-0388.

LEVY, Y., DEGANI, D., SEGINER, A. (1990), "Graphical Visualization of Vortical Flows by Means of Helicity," AIAA Journal, Vol. 28, No. 8., p.1347.

LEYLEK, J. H., WISLER, D. C. (1990), "Mixing in Axial-Flow Compressors: Conclusions Drawn from 3-D Navier-Stokes Analyses and Experiments," ASME Paper 90-GT-352.

LIU, J. S. (1987), "Navier-Stokes Cascade Analysis With the k-ε Turbulence Model," Ph.D. Thesis, MAE, Case Western Reserve University.

MACCORMACK, R. W., BALDWIN, B. S. (1975), "A Numerical Method for Solving the Navier-Stokes Equations with Application to Shock-Boundary Layer Interactions," AIAA Paper 75-4.

MARTELLI, F., MICHELASSI, V. (1990), "3-D Implicit Navier-Stokes Solver for Internal Turbulent Compressible Flows." from Recent Advances and Applications in Computational Fluid Dynamics, ASME Publication, Edited by Oktay Baysal.

MARTINELLI, L. (1987), "Calculation of Viscous Flows with Multigrid Methods," Ph.D. Thesis, MAE Department, Princeton University.

MAVRIPLIS, D. J., MARTINELLI, L. (1991), "Multigrid Solution of Compressible Turbulent Flow on Unstructured Meshes Using a Two-Equation Model," AIAA Paper 91-0237.

MERKLE, C. (1988), Class Notes for ME-527, Department of Mechanical Engineering, Penn State University.

MOORE J., MOORE, J. G. (1990), "A Prediction of 3-D Viscous Flow and Performance of the NASA Low-Speed Centrifugal Compressor," ASME Paper 90-GT-234.

MYONG, H. K., KASAGI, N. (1990), "A New Approach to the Improvement of k-ε Turbulence Model for Wall-Bounded Shear Flows," JSME International Journal, Vol. 33, No. 1, p. 63.

NARAYAN, J. R., (1991) "A Two-Equation Turbulence Model for Compressible Reacting Flows," AIAA Paper 91-0755.

NI, R. H., (1982) "A Multiple Grid Scheme for Solving the Euler Equations," AIAA Journal, Vol. 20, No. 11.

PATEL, V. C., RODI, W., SCHEUERER, G. (1985), "Turbulence Models for Near-Wall and Low Reynolds Number Flows: A Review," AIAA Journal, Vol. 23, p.1308.

POPOVSKI, P., LAKSHMINARAYANA, B. (1986), "Laser Anemometer Measurements in a Compressor Rotor Flowfield at Off-Design Conditions," AIAA Journal, Vol. 24, No. 8, p.1337.

PRANDTL, L. (1925), "Uber die Ausgebildete Turbulenz," Zeitschrift fur Angewandte Mathematik un Mechanik, Vol. 5, p.136.

PRATO, J (1990), "Effects of Loading on the Wake Characteristics of a Compressor Rotor Blade," MS Thesis, Department of Aerospace Engineering, Pennsylvania State University.

PULLIAM, T. H. (1986), "Artificial Dissipation Models for the Euler Equations," AIAA Journal, Vol. 24, No. 12, December.

RADESPIEL, R., ROSSOW, C., SWANSON, R. (1990), "Efficient Cell-Vertex Multigrid Scheme for the Three-Dimensional Navier-Stokes Equations," AIAA Journal, Vol. 28, No.8, p.1464.

RAO, S. S. (1982), The Finite Element Method in Engineering, Pergamon,p.42.

RHIE, C., DELANEY, R. A., MCCAIN, T. F. (1985), Three-Dimensional Viscous Flow Analysis for Centrifugal Impellers," AIAA Journal of Propulsion, Vol. 4, p.257.

RODI, W. (1976), "A New Algebraic Relation for Calculating the Reynolds Stresses," Zeitschrift fur Angewandte Mathematik un Mechanik, Vol. 56, pT219.

SAHU, J., DANBERG J. (1986), "Navier-Stokes Computations of Transonic Flows with a Two-Equation Turbulence Model," AIAA Journal, Vol. 24, p.1744.

SCHREIBER, H. A. (1988), "Experimental Investigations on Shock Losses of Transonic and Supersonic Compressor Cascades," AGARD CP-401, Paper No. 11.

SHIH, T. H., LUMLEY, J. L. (1986), "Second Order Modelling of Near-Wall Turbulence,"Physics of Fluids, Vol. 4, p.971.

SORENSON, R. L. (1980), "A Computer Program to Generate Two-Dimensional Grids About Airfoils and Other Shapes by the Use of Poisson's Equation," NASA TM-81198.

SPEZIALE, C. G. (1989), "Discussion of Turbulence Modelling: Past and Future," ICASE Report 89-58.

SPEZIALE, C. G., Abid, R., Anderson, E. C. (1990), "A Critical Evaluation of Two-Equation Models for Near Wall Turbulence," AIAA Paper 90-1481.

STEGER, J. L., WARMING, R. F. (1981), "Flux Vector Splitting of the Inviscid Gas Dynamic Equations with Applications to Finite Difference Methods," Journal of Computational Physics, Vol. 40, p.263.

STEWART, G. W. (1973), Introduction to Matrix Computations, Academic Press.

SUBRAMANIAN, S. V. (1989), "Three-Dimensional Multigrid Navier-Stokes Computations for Turbomachinery Applications," AIAA Paper 89-2453.

SWANSON, R., TURKEL, E. (1987), "Artificial Dissipation and Central Difference Schemes for the Euler and Navier-Stokes Equations," NASA CR-178296.

SWANSON, R. (1990), personal communication.

TAYLOR, A. M. K. P., WHITELAW, J. H., YIANNESKIS, M. (1981), "Measurements of Laminar and Turbulent Flow in a Curved Duct With Thin Inlet Boundary Layers," NASA CP-3367.

VAN DRIEST, E. R. (1956), "On Turbulent Flow Near a Wall," Journal of Aeronautical Sciences, Vol. 23, p.1007.

VARGA, R. S. (1962), Matrix Iterative Analysis, Prentice-Hall.

VANDROMME, D. (1983), Ph.D. Thesis, University of Lille, France.

WAKE, B. E., EGOLF, T. A. (1991), "Implementatin of a Rotary-Wing Navier-Stokes Solver on a Massively Parallel Computer," AIAA Journal, Vol. 29, No.1, p.58.

WALKER, P. J., DAWES, W. N. (1989) "The Extension and Application of Three-Dimensional Time Marching Analyses to Incompressible Turbomachinery Flows," ASME Paper 89-GT-212.

WARFIELD, M. J., LAKSHMINARAYANA, B. (1989), "Calculation of Three-Dimensional Turbomachinery Rotor Flow Using Pseudocompressibility and Zonal Techniques," Z. Flugwiss. Weltraumforsch, Vol. 13, p. 31.

WARFIELD, M. J., LAKSHMINARAYANA, B. (1987), "Computation of Rotating Turbulent Flow With an Algebraic Reynolds Stress Model," AIAA Journal, Vol. 25, No.7, p.957.

WEISS, J. M. (1991), personal communication.

WHITE, F. (1974), Viscous Fluid Flow, McGraw-Hill.

WILCOX, D. C. (1991), personal communication.

YOKOTA, J. W., CAUGHEY, D. A. (1987), "An L-U Implicit Multigrid Algorithm for the Three-Dimensional Euler Equations," AIAA Paper 87-0453.

ZHANG, J., LAKSHMINARAYANA, B. (1990), "Computation of Three-Dimensional Turbulent Boundary Layers in Internal Flows, Including Turbomachinery Rotor Blades," AIAA Journal, Vol. 28, No. 11, p. 1861.

ZIERKE, W. C., DEUTSCH, S. (1989), "The Measurement of Boundary Layers on a Compressor Blade in Cascade: Part 4 -- Flow Fields for Incidence Angles of -1.5 and -8.5 Degrees," ASME Paper 89-GT-72.

APPENDIX

NONCONSERVATIVE JACOBIAN MATRICES AND FOURIER MATRIX FOR HYPERBOLIC STABILITY

Nonconservative Jacobian Matrices

$$Q=\begin{pmatrix}\rho\\ u\\ v\\ w\\ p\\ k\\ \varepsilon\end{pmatrix},\ \hat{A}_1=\begin{bmatrix} U & \rho\xi_x & \rho\xi_y & \rho\xi_z & 0 & 0 & 0\\ 0 & U & 0 & 0 & \frac{1}{\rho}\xi_x & 0 & 0\\ 0 & 0 & U & 0 & \frac{1}{\rho}\xi_y & 0 & 0\\ 0 & 0 & 0 & U & \frac{1}{\rho}\xi_z & 0 & 0\\ 0 & \xi_x\rho c^2 & \xi_y\rho c^2 & \xi_z\rho c^2 & U & 0 & 0\\ 0 & 0 & 0 & 0 & 0 & U & 0\\ 0 & 0 & 0 & 0 & 0 & 0 & U \end{bmatrix},\ \hat{A}_2=\begin{bmatrix} V & \rho\eta_x & \rho\eta_y & \rho\eta_z & 0 & 0 & 0\\ 0 & V & 0 & 0 & \frac{1}{\rho}\eta_x & 0 & 0\\ 0 & 0 & V & 0 & \frac{1}{\rho}\eta_y & 0 & 0\\ 0 & 0 & 0 & V & \frac{1}{\rho}\eta_z & 0 & 0\\ 0 & \eta_x\rho c^2 & \eta_y\rho c^2 & \eta_z\rho c^2 & V & 0 & 0\\ 0 & 0 & 0 & 0 & 0 & V & 0\\ 0 & 0 & 0 & 0 & 0 & 0 & V \end{bmatrix}$$

$$\hat{A}_3=\begin{bmatrix} W & \rho\zeta_x & \rho\zeta_y & \rho\zeta_z & 0 & 0 & 0\\ 0 & W & 0 & 0 & \frac{1}{\rho}\zeta_x & 0 & 0\\ 0 & 0 & W & 0 & \frac{1}{\rho}\zeta_y & 0 & 0\\ 0 & 0 & 0 & W & \frac{1}{\rho}\zeta_z & 0 & 0\\ 0 & \zeta_x\rho c^2 & \zeta_y\rho c^2 & \zeta_z\rho c^2 & W & 0 & 0\\ 0 & 0 & 0 & 0 & 0 & W & 0\\ 0 & 0 & 0 & 0 & 0 & 0 & W \end{bmatrix},\ P=\begin{bmatrix} 1 & 0 & 0 & 0 & 0 & 0 & 0\\ 0 & \frac{1}{\rho} & 0 & 0 & 0 & 0 & 0\\ 0 & 0 & \frac{1}{\rho} & 0 & 0 & 0 & 0\\ 0 & 0 & 0 & \frac{1}{\rho} & 0 & 0 & 0\\ 0 & 0 & 0 & 0 & \gamma-1 & 0 & 0\\ 0 & 0 & 0 & 0 & 0 & \frac{1}{\rho} & 0\\ 0 & 0 & 0 & 0 & 0 & 0 & \frac{1}{\rho} \end{bmatrix}$$

$$\hat{S}_1 =$$

$$\begin{bmatrix}
0 & 0 & 0 & 0 & 0 & 0 & 0 \\
0 & \frac{\mu_e}{\rho}\left(\nabla\xi\cdot\nabla\xi + \frac{1}{3}\xi_x\xi_x\right) & \frac{\mu_e}{\rho}\frac{1}{3}\xi_x\xi_y & \frac{\mu_e}{\rho}\frac{1}{3}\xi_x\xi_z & 0 & 0 & 0 \\
0 & \frac{\mu_e}{\rho}\frac{1}{3}\xi_x\xi_y & \frac{\mu_e}{\rho}\left(\nabla\xi\cdot\nabla\xi + \frac{1}{3}\xi_y\xi_y\right) & \frac{\mu_e}{\rho}\frac{1}{3}\xi_y\xi_z & 0 & 0 & 0 \\
0 & \frac{\mu_e}{\rho}\frac{1}{3}\xi_x\xi_z & \frac{\mu_e}{\rho}\frac{1}{3}\xi_y\xi_z & \frac{\mu_e}{\rho}\left(\nabla\xi\cdot\nabla\xi + \frac{1}{3}\xi_z\xi_z\right) & 0 & 0 & 0 \\
\begin{matrix}\gamma\left(\frac{\mu_l}{Pr_l} + \frac{\mu_t}{Pr_t}\right)\left(\frac{-p}{\rho^2}\right)\cdot \\ \left(\nabla\xi\cdot\nabla\xi+\nabla\xi\cdot\nabla\eta+\nabla\xi\cdot\nabla\zeta\right)\end{matrix} & 0 & 0 & 0 & \begin{matrix}\gamma\left(\frac{\mu_l}{Pr_l} + \frac{\mu_t}{Pr_t}\right)\left(\frac{1}{\rho}\right)\cdot \\ \left(\nabla\xi\cdot\nabla\xi+\nabla\xi\cdot\nabla\eta+\nabla\xi\cdot\nabla\zeta\right)\end{matrix} & 0 & 0 \\
0 & 0 & 0 & 0 & 0 & \frac{1}{\rho}\left(\mu_l + \frac{\mu_t}{Pr_k}\right)\left(\nabla\xi\cdot\nabla\xi\right) & 0 \\
0 & 0 & 0 & 0 & 0 & 0 & \frac{1}{\rho}\left(\mu_l + \frac{\mu_t}{Pr_\varepsilon}\right)\left(\nabla\xi\cdot\nabla\xi\right)
\end{bmatrix}$$

With consistent expressions for $\hat{S}_2$, $\hat{S}_3$.

$$\hat{T}_1 = \begin{bmatrix} 0 & 0 & 0 & 0 & 0 & 0 & 0 \\ 0 & \frac{2\mu_e}{\rho}\left(\nabla\xi\cdot\nabla\eta + \frac{1}{3}\xi_x\eta_x\right) & \frac{\mu_e}{\rho}\frac{1}{3}\left(\xi_x\eta_y+\xi_y\eta_x\right) & \frac{\mu_e}{\rho}\frac{1}{3}\left(\xi_x\eta_z+\xi_z\eta_x\right) & 0 & 0 & 0 \\ 0 & \frac{\mu_e}{\rho}\frac{1}{3}\left(\xi_x\eta_y+\xi_y\eta_x\right) & \frac{2\mu_e}{\rho}\left(\nabla\xi\cdot\nabla\eta + \frac{1}{3}\xi_y\eta_y\right) & \frac{\mu_e}{\rho}\frac{1}{3}\left(\xi_y\eta_z+\xi_z\eta_y\right) & 0 & 0 & 0 \\ 0 & \frac{\mu_e}{\rho}\frac{1}{3}\left(\xi_x\eta_z+\xi_z\eta_x\right) & \frac{\mu_e}{\rho}\frac{1}{3}\left(\xi_y\eta_z+\xi_z\eta_y\right) & \frac{2\mu_e}{\rho}\left(\nabla\xi\cdot\nabla\eta + \frac{1}{3}\xi_z\eta_z\right) & 0 & 0 & 0 \\ 0 & 0 & 0 & 0 & 0 & 0 & 0 \\ 0 & 0 & 0 & 0 & 0 & \frac{2}{\rho}\left(\mu_l + \frac{\mu_t}{Pr_k}\right)\left(\nabla\xi\cdot\nabla\eta\right) & 0 \\ 0 & 0 & 0 & 0 & 0 & 0 & \frac{2}{\rho}\left(\mu_l + \frac{\mu_t}{Pr_\varepsilon}\right)\left(\nabla\xi\cdot\nabla\eta\right) \end{bmatrix}$$

With consistent expressions for $\hat{T}_2$, $\hat{T}_3$.

$$\hat{D}_I = \begin{bmatrix} 0 & 0 & 0 & 0 & 0 & 0 & 0 \\ 0 & 0 & 0 & 0 & 0 & 0 & 0 \\ 0 & 0 & 0 & 2\omega & 0 & 0 & 0 \\ 0 & 0 & -2\omega & 0 & 0 & 0 & 0 \\ 0 & 0 & 0 & 0 & 0 & 0 & 0 \\ 0 & 0 & 0 & 0 & 0 & 0 & -\left(\frac{P}{\rho\varepsilon} + 1\right) \\ 0 & 0 & 0 & 0 & 0 & \left(C_1 f_1 \frac{P\varepsilon}{\rho k^2} + C_2 f_2 \frac{\varepsilon^2}{k^2}\right) & 0 \end{bmatrix}$$

$$\hat{D}_R = \begin{bmatrix} 0 & 0 & 0 & 0 & 0 & 0 & 0 \\ 0 & 0 & 0 & 0 & 0 & 0 & 0 \\ 0 & 0 & 0 & 0 & 0 & 0 & 0 \\ 0 & 0 & 0 & 0 & 0 & 0 & 0 \\ 0 & 0 & 0 & 0 & 0 & 0 & 0 \\ 0 & 0 & 0 & 0 & 0 & \frac{2P}{\rho k} - \frac{2\mu_1}{\rho l^2} & 0 \\ 0 & 0 & 0 & 0 & 0 & 0 & \frac{-2C_2 f_2 \varepsilon}{k} - \frac{2\mu_1}{\rho l^2} e^{-y^+/2} \end{bmatrix}$$

where $\hat{D} = \hat{D}_I + \hat{D}_R$

Fourier Matrix for Hyperbolic Stability

$$
Z_1 = i\begin{bmatrix}
US_\xi+VS_\eta+WS_\zeta & \rho\left(\xi_x S_\xi+\eta_x S_\eta+\zeta_x S_\zeta\right) & \rho\left(\xi_y S_\xi+\eta_y S_\eta+\zeta_y S_\zeta\right) & \rho\left(\xi_z S_\xi+\eta_z S_\eta+\zeta_z S_\zeta\right) & 0 & 0 & 0 \\
0 & US_\xi+VS_\eta+WS_\zeta & 0 & 0 & \frac{1}{\rho}\left(\xi_x S_\xi+\eta_x S_\eta+\zeta_x S_\zeta\right) & 0 & 0 \\
0 & 0 & US_\xi+VS_\eta+WS_\zeta & -2i\omega & \frac{1}{\rho}\left(\xi_y S_\xi+\eta_y S_\eta+\zeta_y S_\zeta\right) & 0 & 0 \\
0 & 0 & 2i\omega & US_\xi+VS_\eta+WS_\zeta & \frac{1}{\rho}\left(\xi_z S_\xi+\eta_z S_\eta+\zeta_z S_\zeta\right) & 0 & 0 \\
0 & \rho c^2\left(\xi_x S_\xi+\eta_x S_\eta+\zeta_x S_\zeta\right) & \rho c^2\left(\xi_y S_\xi+\eta_y S_\eta+\zeta_y S_\zeta\right) & \rho c^2\left(\xi_z S_\xi+\eta_z S_\eta+\zeta_z S_\zeta\right) & US_\zeta+VS_\eta+WS_\zeta & 0 & 0 \\
0 & 0 & 0 & 0 & 0 & US_\xi+VS_\eta+WS_\zeta & i\left(\frac{P}{\rho\varepsilon}+1\right) \\
0 & 0 & 0 & 0 & 0 & -i\left(C_1 f_1\frac{P\varepsilon}{\rho k^2}+C_2 f_2\frac{\varepsilon^2}{k^2}\right) & US_\xi+VS_\eta+WS_\zeta
\end{bmatrix}
$$